

TRANSPORTATION RESEARCH  
**RECORD**

No. 1355

*Pavement Design, Management,  
and Performance*

---

**Nondestructive Structural  
Evaluation of  
Pavements**

*A peer-reviewed publication of the Transportation Research Board*

**TRANSPORTATION RESEARCH BOARD  
NATIONAL RESEARCH COUNCIL**

NATIONAL ACADEMY PRESS  
WASHINGTON, D.C. 1992

**Transportation Research Record 1355**

Price: \$22.00

Subscriber Category  
IIB pavement design, management, and performance

TRB Publications Staff  
*Director of Reports and Editorial Services:* Nancy A. Ackerman  
*Senior Editor:* Naomi C. Kassabian  
*Associate Editor:* Alison G. Tobias  
*Assistant Editors:* Luanne Crayton, Susan Gober,  
Norman Solomon  
*Office Manager:* Phyllis D. Barber  
*Production Assistant:* Betty L. Hawkins

Printed in the United States of America

**Library of Congress Cataloging-in-Publication Data**

National Research Council. Transportation Research Board.  
Nondestructive structural evaluation of pavements.  
p. cm.—(Transportation research record, ISSN 0361-1981 ;  
no. 1355)  
ISBN 0-309-05219-X  
1. Pavements—Testing. 2. Non-destructive testing.  
I. National Research Council (U.S.). Transportation Research  
Board. II. Series: Transportation research record ; 1355.  
TE7.H5 no. 1355  
[TE251.5]  
388 s—dc20  
[625.8'028'7]

92-31824  
CIP

**Sponsorship of Transportation Research Record 1355**

**GROUP 2—DESIGN AND CONSTRUCTION OF  
TRANSPORTATION FACILITIES**

*Chairman:* Charles T. Edson, New Jersey Department of Transportation

**Pavement Management Section**

*Chairman:* Joe P. Mahoney, University of Washington

**Committee on Rigid Pavement Design**

*Chairman:* Gary Wayne Sharpe, Kentucky Transportation Cabinet,  
Department of Highways  
*Don R. Alexander, Ernest J. Barenberg, Brian T. Bock, Kathleen  
Theresa Hall, Amir N. Hanna, John E. Hunt, Michael P. Jones,  
Walter P. Kilareski, Starr D. Kohn, Roger M. Larson, Jo A. Lary,  
Richard A. McComb, B. Frank McCullough, Theodore L. Neff,  
Maurico R. Poblete, Robert J. Risser, Jr., Shiraz D. Tayabji, Mang  
Tia, James H. Woodstrom, John P. Zaniewski, Terrence L. Zoller,  
Dan G. Zollinger*

**Committee on Strength and Deformation Characteristics of  
Pavement Sections**

*Chairman:* Albert J. Bush III, USAE Waterways Experiment Station  
*Gilbert Y. Baladi, Richard D. Barksdale, Robert C. Briggs,  
Stephen F. Brown, George R. Cochran, Ronald J. Cominsky, Billy  
G. Connor, Mark P. Gardner, John P. Hallin, Dennis R. Hiltunen,  
Lynne H. Irwin, Starr D. Kohn, Robert L. Lytton, Michael S.  
Mamlouk, Soheil Nazarian, Rasmus S. Nordal, Gonzalo Rada,  
J. Brent Rauhut, Byron E. Ruth, Larry A. Scofield, Tom Scullion,  
Stephen B. Seeds, R. N. Stubstad, Marshall R. Thompson, Per  
Ullidtz, Jacob Uzan, Thomas D. White, Haiping Zhou*

**Committee on Pavement Monitoring, Evaluation, and Data Storage**

*Chairman:* Freddy L. Roberts, Louisiana Tech University  
*Secretary:* Don H. Kobi, Paris, Ontario, Canada  
*A. T. Bergan, Frank V. Boielho, Billy G. Connor, Brian E. Cox,  
Jerome F. Daleiden, Wade L. Gramling, Jerry J. Hajek, Amir N.  
Hanna, Andris A. Jumikis, Scott A. Kutz, Kenneth J. Law, W. N.  
Lofroos, Kenneth H. McGhee, Amy L. Mueller, Edwin C. Novak,  
Jr., Dennis G. Richardson, Richard B. Rogers, Ivan F. Scazziga,  
Mohamed Y. Shahin, Robert M. Smith, Roger E. Smith, Herbert F.  
Southgate, Elson B. Spangler, John P. Zaniewski*

Frank R. McCullagh, Transportation Research Board staff

Sponsorship is indicated by a footnote at the end of each paper.  
The organizational units, officers, and members are as of  
December 31, 1991.

# Transportation Research Record 1355

---

## Contents

<b>Foreword</b>	<b>v</b>
<hr/>	
<b>Nonlinear Effects in Falling Weight Deflectometer Tests</b> <i>Der-Wen Chang, Jose M. Roesset, and Kenneth H. Stokoe II</i>	<b>1</b>
<hr/>	
<b>Effect of Depth to Bedrock on Deflection Basins Obtained with Dynaflect and Falling Weight Deflectometer Tests</b> <i>Der-Wen Chang, Yumin Vincent Kang, Jose M. Roesset, and Kenneth Stokoe II</i>	<b>8</b>
<hr/>	
<b>Variability in Estimation of Structural Capacity of Existing Pavements from Falling Weight Deflectometer Data</b> <i>Mustaque Hossain and John P. Zaniewski</i>	<b>17</b>
<hr/>	
<b>Comprehensive Evaluation of Five Sensors Used To Measure Pavement Deflection</b> <i>Vivek Tandon and Soheil Nazarian</i>	<b>27</b>
<hr/>	
<b>Effects of Buffers on Falling Weight Deflectometer Loadings and Deflections</b> <i>Erland O. Lukanen</i> <i>DISCUSSION, Carl Lemngren, 51</i>	<b>37</b>
<hr/>	
<b>Evaluation of a Dual-Load Nondestructive Testing System To Better Discriminate Near-Surface Layer Moduli</b> <i>Reynaldo Roque, Pedro Romero, and Byron E. Ruth</i>	<b>52</b>
<hr/>	
<b>Estimating Damage Effects of Dual versus Wide Base Tires with Multidepth Deflectometers</b> <i>Tayyeb Akram, Tom Scullion, Roger E. Smith, and Emmanuel G. Fernando</i>	<b>59</b>
<hr/>	

---

<b>Field and Laboratory Determination of Elastic Properties of Portland Cement Concrete Using Seismic Techniques</b> <i>J. A. Bay and K. H. Stokoe II</i>	67
<b>Alternative Method for Temperature Correction of Backcalculated Equivalent Pavement Moduli</b> <i>Andrew M. Johnson and Ronald L. Baus</i>	75
<b>Simplified, Rational Approach to Falling Weight Deflectometer Data Interpretation</b> <i>Dieter F. E. Stolle and Friedrich W. Jung</i>	82
<b>Radar Pavement Thickness Evaluations for Varying Base Conditions</b> <i>W. M. Kim Roddis, Kenneth Maser, and Andrew J. Gisi</i>	90
<b>Modeling of Ground-Penetrating Radar Wave Propagation in Pavement Systems</b> <i>Chun Lok Lau, Tom Scullion, and Paul Chan</i>	99

---

# Foreword

Chang et al. investigated the potential for nonlinear behavior in falling weight deflectometer (FWD) tests. They found that material nonlinearities are quite localized and important for FWD tests on flexible pavements with relatively soft subgrade and on thin pavements. In another study, Chang et al. investigated the effect of depth to bedrock on the amplitude of the deflections and the shape of the deflection basins obtained with dynaflect and FWD tests. The results show that the range of bedrock depths over which dynamic effects are important differs between the two tests and mainly depends on the stiffness of the subgrade. Hossain and Zaniewski present the variability in the calculation of existing pavement structural capacity in terms of 18-kip equivalent single axle load repetitions by the mechanistic empirical method with respect to FWD input data. Tandon and Nazarian present the results of a laboratory evaluation of five different sensors that can be used in deflection measurement and determined that geophones appear to be the optimum sensor.

Lukanen evaluated the effects that various buffers have on the loads and deflections of FWD test results. Roque et al. conducted theoretical analyses that illustrate the ability of a dual-load FWD to discriminate between near-surface layer moduli; they show that a set of relatively simple equations can be developed to backcalculate pavement layer moduli. Akram et al. evaluated the effects of dual versus wide base single tires on anticipated pavement life and found that wide base single tires will reduce the anticipated pavement life for both thick and thin pavements. Bay and Stokoe demonstrate the ability of seismic techniques to non-destructively monitor portland cement concrete from the earliest stages of curing throughout the life of the structure.

Johnson and Baus present an alternative temperature correction procedure to be used in the Direct Structural Capacity Method as described in the *AASHTO Guide for the Design of Pavement Structures*. When used with experimental field data, the alternative method is shown to provide more uniform results with varying temperatures. Stolle and Jung present a simple elastostatic approach to estimate a suitable subgrade modulus from FWD data. Roddis et al. investigated the capability of ground-penetrating radar to provide accurate subsurface pavement profile information and determined that it can provide an effective alternative to coring. Lau et al. proposed and tested a forward model capable of simulating the signature of ground-penetrating radar waveforms and found reasonable agreement between the theoretically calculated field-measured ground-penetrating radar traces.

# Nonlinear Effects in Falling Weight Deflectometer Tests

DER-WEN CHANG, JOSE M. ROESSET, AND KENNETH H. STOKOE II

The falling weight deflectometer (FWD) has been used in the evaluation of material properties of pavement systems for many years. The load amplitude and frequency content are intended to provide deformation levels similar to those induced by truck wheel loads. Interpretation of the in situ measured data is normally based on an elastic solution and therefore does not take into account the possible existence of localized nonlinearities. The objective of this work was to develop some understanding of the potential for nonlinear behavior in the FWD test. Analytical studies were conducted using both a linear iterative solution and a nonlinear solution with the generalized cap model to reproduce the nonlinear soil behavior. Three pavement sections in Texas were considered using the finite discrete model. By varying the level of loads FWD deflection basins, induced strains, and inelastic material properties were obtained. The results of this study indicate that material nonlinearities are localized and are important for FWD tests on flexible pavements where the subgrade is relatively soft or the pavement is thin. In these cases, nonlinear effects increase peak displacements by at least 50 percent under a 20,000-lb load but are negligible for receivers at 3 ft or more from the source. In general, a FWD test with a load of 2,000 lb or less would not result in any apparent nonlinear effects at any pavement site. For FWD tests on rigid pavements or flexible pavements with a relatively stiff subgrade, nonlinearities are also less pronounced.

Nondestructive testing techniques have been used by highway engineers for years to evaluate in the field the structural capacity and integrity of existing pavements. Among a number of available testing methods, the falling weight deflectometer (FWD) is commonly considered to provide estimates of material properties for levels of load similar to those exerted by truck wheels as discussed by Uddin et al. (1). In this method, a hydraulically lifted weight is dropped on top of a disc mounted on the surface of the pavement and outward by propagating wave motions are recorded by a set of velocity transducers placed on the surface (Figure 1). The peak displacements of these receivers form a deflection basin that is then used to backfigure the material profile on the basis of elastic multi-layer theory. In general, the peak of the FWD load ranges from 1,500 to 24,000 lb with frequencies between 0 and 60 Hz. An illustration of the idealized FWD loading function used for the present study is shown in Figure 2.

A number of research studies have been conducted recently to understand the effect of various factors on the FWD measurements such as the presence of much stiffer bedrock at a finite depth. Roesset and Shao (2), Davies and Mamlouk (3),

and Chang et al. in another paper in this Record have concentrated on the importance of dynamic effects. Kang et al. (4) investigated the effect of the finite width of the pavement. Dynamic wave phenomena were found to be important in some cases in which the effects ought to be taken into account to ensure appropriate backcalculations. Another concern in analyzing the measured data is the possible nonlinear behavior of the paving materials induced by large load levels. Such effects were reported by Nazarian and Stokoe (5), who performed a set of FWD measurements on a secondary road. Although the occurrence of nonlinear behavior has been considered an advantage in better simulating the levels of strain and stress caused by the truck wheels, it is necessary to account for the magnitude and spatial distribution of these nonlinearities under different loads for a proper interpretation of the data. The purpose of this work is to estimate the degree of nonlinearity that can be expected in different types of pavements as a function of the load magnitude, and to estimate associated errors in backfiguring the material moduli. The work is limited to analytical predictions intended to provide an expected order to magnitude. Experimental work is needed to validate these predictions.

## NONLINEAR CHARACTERISTICS OF THE PAVING MATERIALS

The most often used materials for the pavement surface layer are portland cement concrete and asphalt concrete. The load-dependent behavior of these materials is not of interest here because they are considerably stiffer than the base and subgrade materials (soils). Nevertheless, it is necessary to point out that loading rate would affect the dynamic modulus of the asphalt mixtures, particularly for high temperatures.

For the base, the focus of interest in the present study is on untreated granular materials. Deformational characteristics of granular materials depend on the strain level and the state of stress. Such relations are commonly expressed in highway engineering in terms of the resilient modulus and 1-D recoverable strain. Alternatively, they can be represented as the variation of shear modulus and damping with shear strain as normally done in earthquake engineering. Many factors have been found to affect the shear modulus ( $G$ ) and damping ratio of soils. Hardin and Drnevich (6) ranked several factors in order of their importance including state of stress, void ratio and strain amplitude. For a given material with known void ratio and state of stress, the nonlinear behavior is normally represented by plotting the modulus and damping versus shear strain. As a general rule of thumb, material response

D.-W. Chang, Department of Civil Engineering, Tamkang University, 180 Chung-An Street, Chung-Ho City, Taipei Hsien, Republic of China. J. M. Roesset and K. H. Stokoe II, Department of Civil Engineering, University of Texas at Austin, Austin, Tex. 78712-1076.

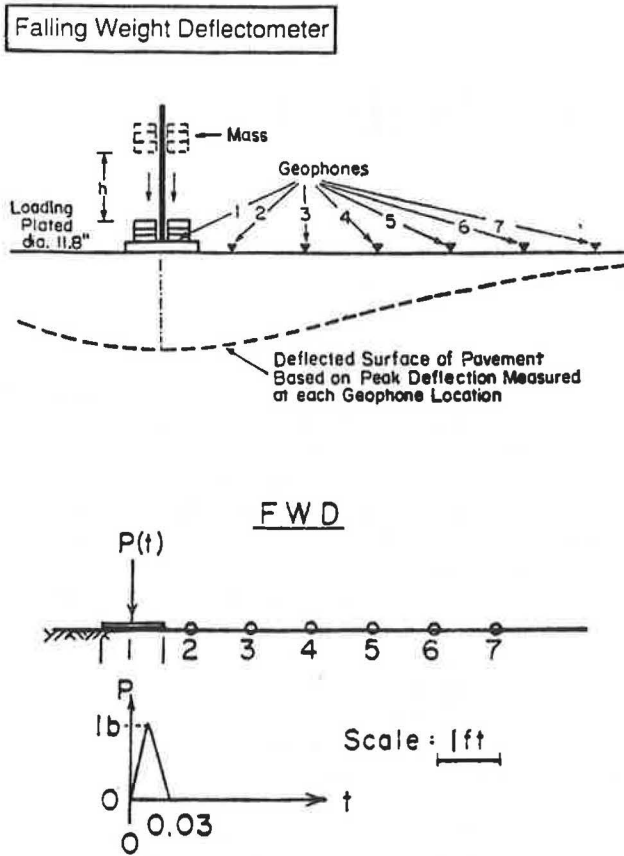


FIGURE 1 Layout of the in situ instrumentation and geometric configuration of the load and stations of FWD test (1).

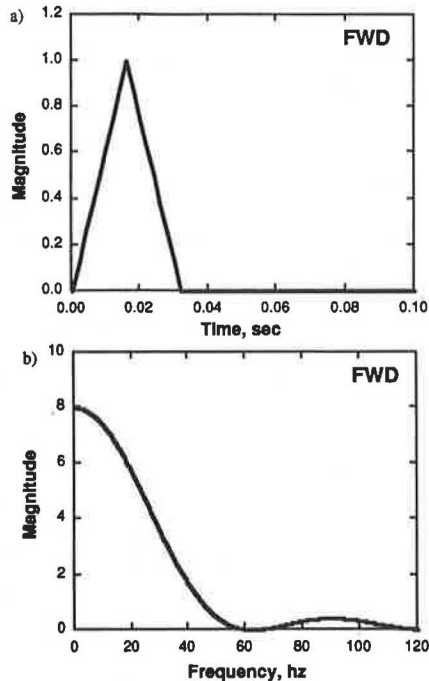


FIGURE 2 Simplified loading history of FWD test and corresponding load spectra.

is considered to be linear elastic for strain levels less than 0.001 percent, nonlinear elastic (reversible load-displacement relations) for shear strains between 0.001 percent and 0.01 percent, and inelastic for strains larger than 0.01 percent. A comprehensive review of the research on shearing characteristics of soils can be found in work by Ni (7).

The nonlinear material characteristics used in this study are based on laboratory data on clayey and sandy soils. Both rely on samples representing common materials collected at pavement sites in Texas. A typical plot of the variation of the shear modulus and damping with shear strain amplitude is shown in Figure 3. To simplify the material profiles at different sites, the curves for sandy soils are considered as representative of granular bases, and the data of clays are used to model the subgrade. Owing to the lack of more complete laboratory data on asphalt concrete, strain amplitude and rate dependence of its shear modulus and damping are neglected.

**ANALYTICAL MODEL AND APPROACHES**

Determination of the displacements, strains, and stresses created in a layered medium by dynamic loads has been a subject of considerable interest and research for the last 20 years in relation to the design of machine foundations and the seismic analyses of buildings and foundations. A number of procedures have been developed to solve the linear problem by modeling the ground with a discrete model and an absorbing boundary to reproduce the far-field or by applying analytical solutions with a Fourier series expansion in two or three dimensions. For the nonlinear problem, a model that has a core

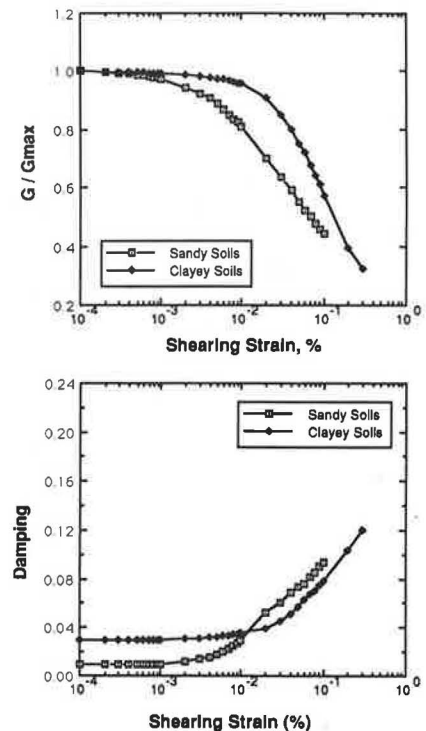


FIGURE 3 Nonlinear shear deformational characteristics of subgrade soils.

region discretized with finite elements and an appropriate set of boundary conditions at a finite distance is more attractive. Nonlinear analyses related to foundation engineering have been conducted by Lysmer et al. (8) and Roesset and Scaletti (9) assuming linear hysteretic soil properties, accounting approximately for the nonlinear soil behavior using the so-called linear iterative or equivalent linear approach. In this work, dynamic analyses were conducted using two approaches: the approximate nonlinear approach and a true nonlinear analysis.

The first approach, the linear iterative procedure, is conducted in the frequency domain, using prescribed nonlinear curves of modulus and damping versus strain to select in each cycle properties consistent with the levels of strain computed in the previous one; the time histories of the solutions are then obtained using fast Fourier transform. Corrections of the material properties are based on an equivalent measure of shear strain defined as the shearing strain intensity  $\Gamma = [(2\bar{J}_2)^{1/2}]$  where  $\bar{J}_2$  is the second invariant of the shear strain tensor. A lateral absorbing boundary is placed at an appropriate distance from the source to reproduce the energy dissipation in the far field as suggested by Kausel et al. (10).

Using the second approach, a true nonlinear analysis, the solution is obtained in the time domain integrating the equations of motion of the system. A generalized cap model proposed by Sandler et al. (11) is used to reproduce the nonlinear material behavior (Figure 4). The equations used in the model for failure envelope, hardening cap and the nonlinear moduli suggested by Chen and Baladi (12) are discussed in detail by Chang (13).

Because the data necessary to fit the parameters of the plasticity model were not available, no attempt was made to reproduce exactly the actual behavior of a specific site. The objective of the study was, instead, to get an idea of the degree of nonlinearity that could be expected using two different models with consistent values.

The discrete models used for both types of analyses are shown in Figure 5. The details of the formulation, compu-

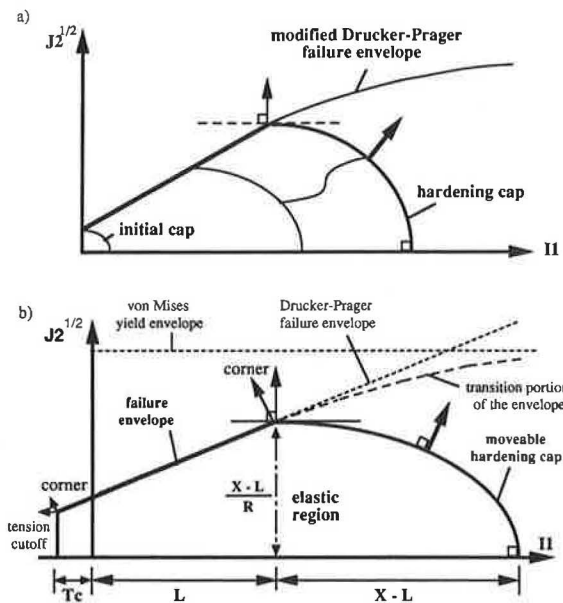
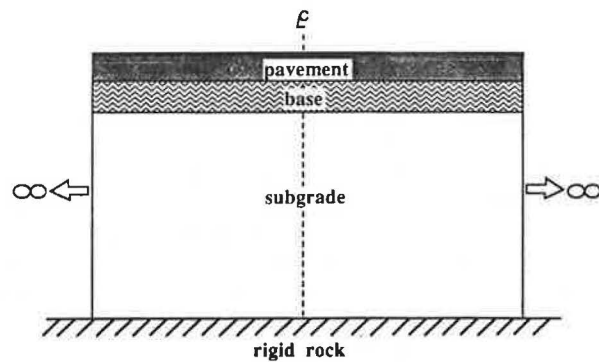
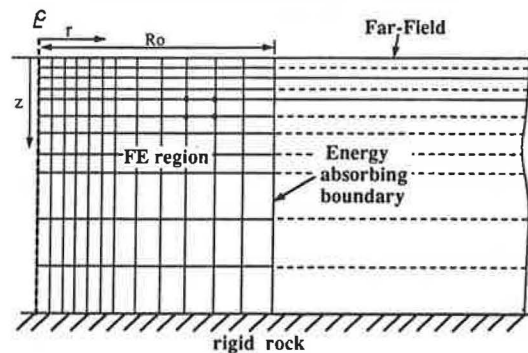


FIGURE 4 Configuration of the cap model in the II-J2 space.



Approximate Nonlinear Analysis



Nonlinear Analysis

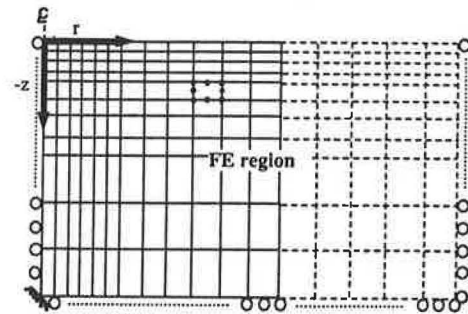


FIGURE 5 Simplified pavement systems and discrete models for analyses.

tational schemes, model behavior, and simulation as well as material correlations for the nonlinear analyses can be found in work by Chang (13).

## CASE STUDIES

### Site Description

To investigate the possible existence of nonlinearities and their localization at various typical pavement sites, three pavement sections were selected as material profiles for analysis. They correspond to farm-to-market road FM 195 in Paris, Texas; Route 1 in Austin, Texas; and Interstate 10 in El Paso, Texas. Road FM 195 was selected to represent a typical flexible pavement on relatively soft subgrade. Route 1 represents a flexible pavement where the subgrade is relatively stiff. Interstate highway 10 represents a typical rigid pavement. The

elastic material properties and layer thicknesses of each profile as reported to the authors from measurements are presented in Table 1. Rigid rock was placed at a depth of 20 ft in all cases to reduce the size of the finite element mesh and to save computational time. Clearly the depth to bedrock influences the dynamic amplification and therefore the strains.

The material parameters in the nonlinear gap model were selected to yield variation of modulus and damping curves similar to those used in the approximate approach. The values were reported by Chang (13). To generalize the initial state, a hydrostatic stress of 10 psi was preassigned to the soils in order to place the initial cap.

**Approximate Nonlinear Analyses**

*Deflection Basin*

The results of the deflection basin normalized with respect to the load (deflections per pound) for 1, 1,000, 2,000, 5,000, 10,000 and 20,000-lb loads and the corresponding deflection ratios with respect to the 1-lb load are plotted in Figures 6 and 7 for the approximate nonlinear analysis. Important nonlinearities on the peak displacements are found at the first two receivers (which are within 2 ft from the source) in site FM 195 for loads over 5,000 lb. These effects would cause an increase of approximately 56 percent in the peak displacements at site FM 195 with a 20,000-lb load. For Route 1 and I-10, nonlinear effects were found to be insignificant for all load levels.

*Variation of Nonlinear Material Moduli and Damping*

Variations of the material shear moduli (in the normalized form) and the damping using the 20,000-lb load at site FM

**TABLE 1 Material Properties and Thickness of Profile at Sites**

FM 195					
Layer	Thickness (ft)	Vs (fps)	$\nu$	E (ksi)	$\gamma$ (pcf)
ACP	0.333	2500	0.15	434	140
Base	0.50	800	0.25	43	125
Subgrade	19.167	500	0.33	16	110
Route 1					
Layer	Thickness (ft)	Vs (fps)	$\nu$	E (ksi)	$\gamma$ (pcf)
ACP	0.583	2000	0.27	318	145
Base	0.50	1000	0.25	76	130
Subgrade	18.917	1000	0.33	76	130
IH 10					
Layer	Thickness (ft)	Vs (fps)	$\nu$	E (ksi)	$\gamma$ (pcf)
CRC	0.833	8500	0.20	5423	145
AC	0.5	2000	0.27	318	145
Base	1.0	800	0.33	46	125
Subgrade	17.667	500	0.33	18	125

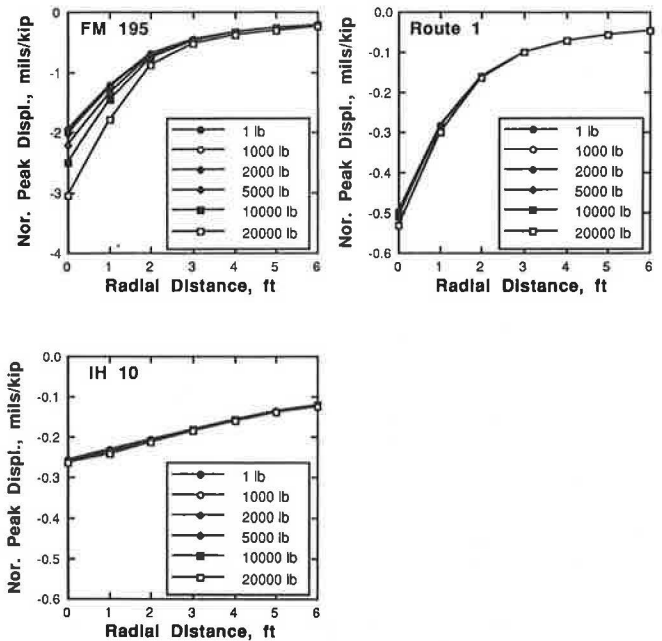


**FIGURE 6 Dynamic deflection basins at various sites from approximate nonlinear analysis.**

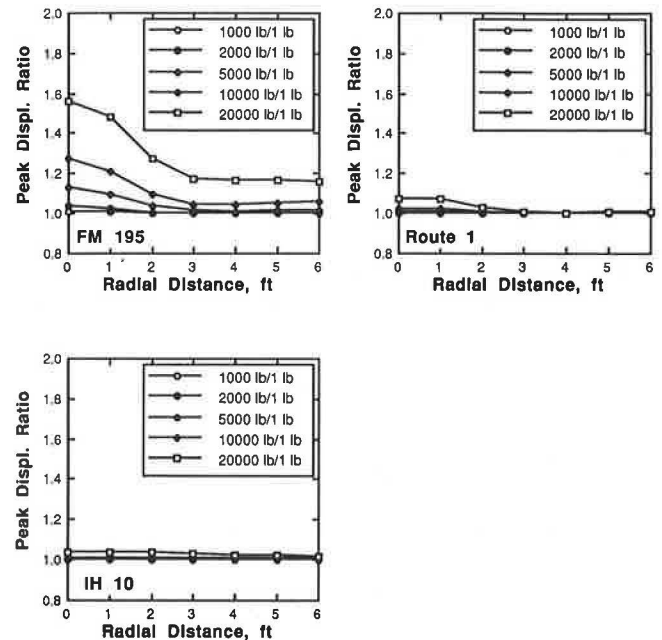


**FIGURE 7 Ratio of deflection basin at various sites from approximate nonlinear analysis.**

195 are presented in Tables 2 and 3. Note that the shear modulus of the base layer can be reduced to about 14 percent of its original value. The shear modulus in the upper portion of the subgrade layer decreases to 45 percent of its initial value. The associated maximum material damping at the site is 11 percent in the base layer and 9 percent in the upper subgrade layer. The localized nature of these nonlinearities are clearly illustrated and an assumption of lateral homogeneity, as is implicitly done in normal backcalculation procedures, is not appropriate.

**TABLE 2** Variation of  $G/G_{max}$  for FM 195 with 20,000-lb FWD Load

Depth, ft	Radial Distance, ft												
	.25	.75	1.25	1.75	2.25	2.75	3.25	3.75	4.25	4.75	5.25	5.75	6.25
.167	1.00	1.00	1.00	1.00	1.00	1.00	1.00	1.00	1.00	1.00	1.00	1.00	1.00
.583	.138	.162	.193	.232	.277	.326	.374	.420	.475	.521	.560	.596	.632
1.083	.451	.519	.590	.645	.726	.777	.819	.859	.897	.906	.913	.919	.925
1.583	.500	.568	.615	.684	.752	.796	.837	.876	.903	.909	.915	.921	.928
2.083	.541	.594	.646	.722	.773	.815	.856	.895	.906	.913	.919	.925	.931
2.583	.574	.614	.680	.750	.793	.835	.876	.903	.910	.916	.922	.928	.935
3.083	.590	.634	.711	.769	.812	.856	.897	.907	.914	.920	.926	.932	.938

**TABLE 3** Variation of Material Damping for FM 195 with 20,000-lb FWD Load

Depth, ft	Radial Distance, ft												
	.25	.75	1.25	1.75	2.25	2.75	3.25	3.75	4.25	4.75	5.25	5.75	6.25
.167	.020	.020	.020	.020	.020	.020	.020	.020	.020	.020	.020	.020	.020
.583	.110	.104	.096	.088	.080	.075	.071	.067	.063	.059	.056	.054	.051
1.083	.089	.083	.076	.070	.064	.057	.052	.049	.045	.043	.041	.039	.038
1.583	.085	.079	.073	.067	.061	.055	.050	.047	.044	.042	.040	.039	.038
2.083	.081	.076	.070	.064	.058	.053	.049	.045	.043	.041	.039	.039	.038
2.583	.079	.073	.068	.062	.056	.051	.047	.044	.042	.040	.039	.038	.038
3.083	.076	.070	.065	.059	.053	.049	.045	.043	.041	.039	.038	.038	.037

**Nonlinear Analyses**

*Deflection Basin*

The normalized deflection basins and their ratios are plotted in Figures 8 and 9 for the nonlinear analyses. In the case of FM 195, the nonlinear effects of a 20,000-lb load cause an increase of about 140 percent in the peak displacement at the first receiver. For Route 1, the same load results in an increase of the displacement of about 50 percent, much more signifi-

cant than the increase predicted by the previous solution. In general, the nonlinearities for relatively large loads (> 10,000 lb) are important within 3 ft from the source at these two sites. The displacements recorded at the farther receivers become smaller with increase in the load. For site I-10, nonlinear effects were again found. The true nonlinear displacement was about 50 percent larger than the approximate one (from 1.6 to 2.4 times the linear displacement at FM 195). This was expected and has been reported in the past.

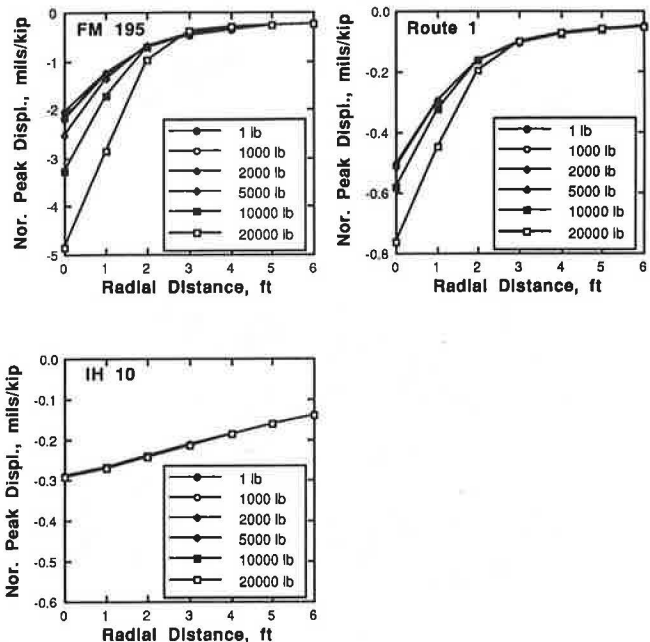


**FIGURE 8** Dynamic deflection basins at various sites from nonlinear analysis.

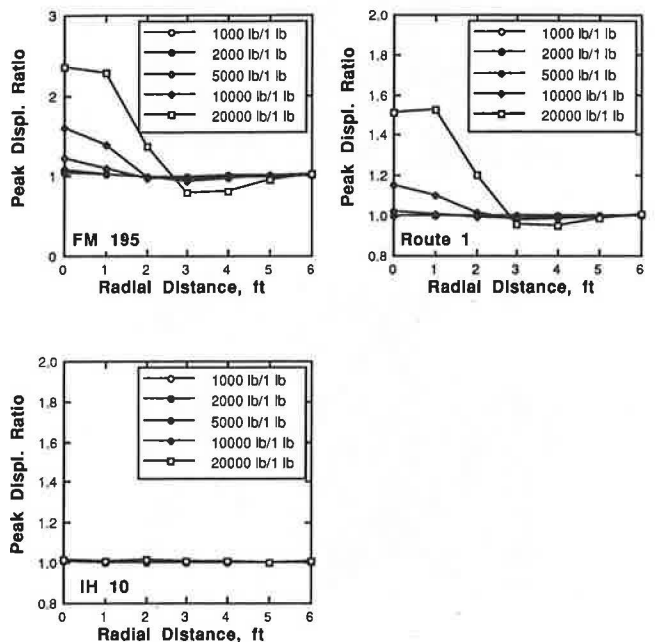


**FIGURE 9** Ratio of dynamic deflection basins at various sites from nonlinear analysis.

*Variation of Linear and Nonlinear Strain Field*

The variation of the shear strains underneath the pavements using 1 lb and 20,000 lb loads at all sites is plotted in Figures 10–12. The maximum strain is always found in the base layer. The levels of the strain distribution can be used to correlate the variation of the material properties that induce the inelastic phenomena.

**CONCLUSIONS**

Dynamic nondestructive tests for evaluating the structural capacity of pavements have become a popular tool for highway engineers in selecting rehabilitation and reconstruction strategies. A considerable amount of research has been conducted in recent years to improve the understanding of the factors affecting these tests from both the analytical and experimental points of view. Although some problems still have not yet been fully resolved specially in the interpretation of the measured data, a distinct nonlinear phenomenon (load dependence) has often been noticed in FWD measurements on light pavements. In this study investigations based on forward analyses modeling the nonlinear phenomena were conducted to predict the response of the pavements. A study was first conducted using an approximate nonlinear solution. Two sets of experimental nonlinear curves were used to model the

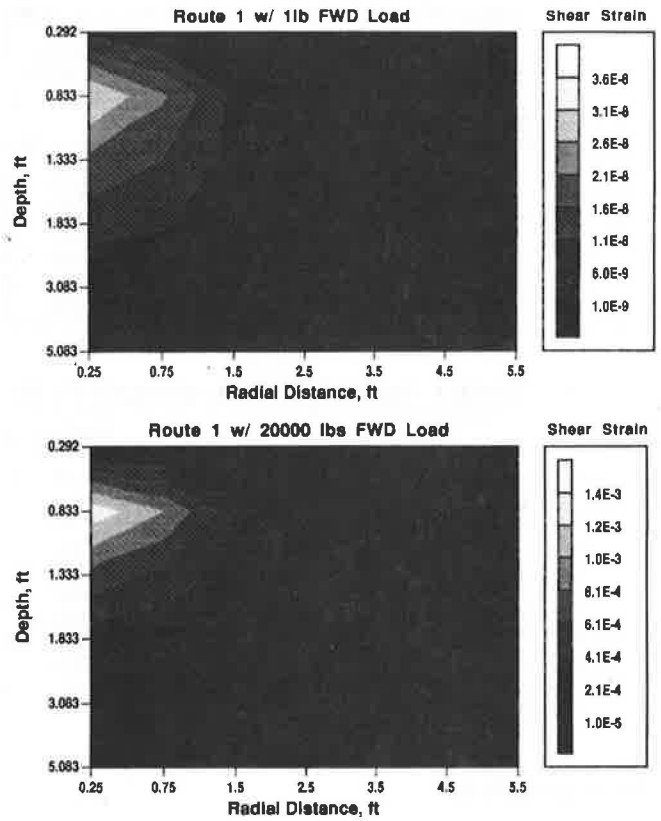


**FIGURE 11** Variation of shear strain at Route 1 using 116 and 20,000-lb FWD loads.

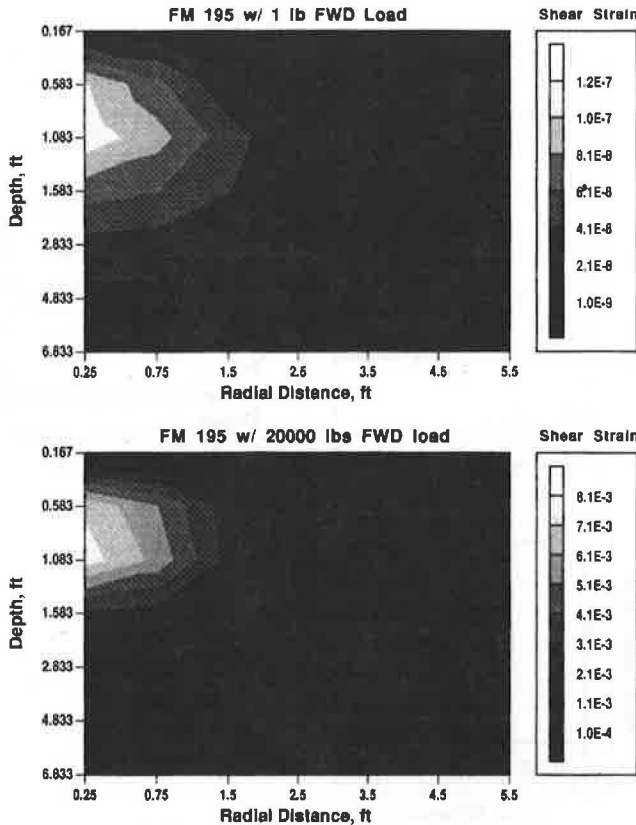


**FIGURE 10** Variation of shear strain at FM 195 using 116 and 20,000-lb FWD loads.

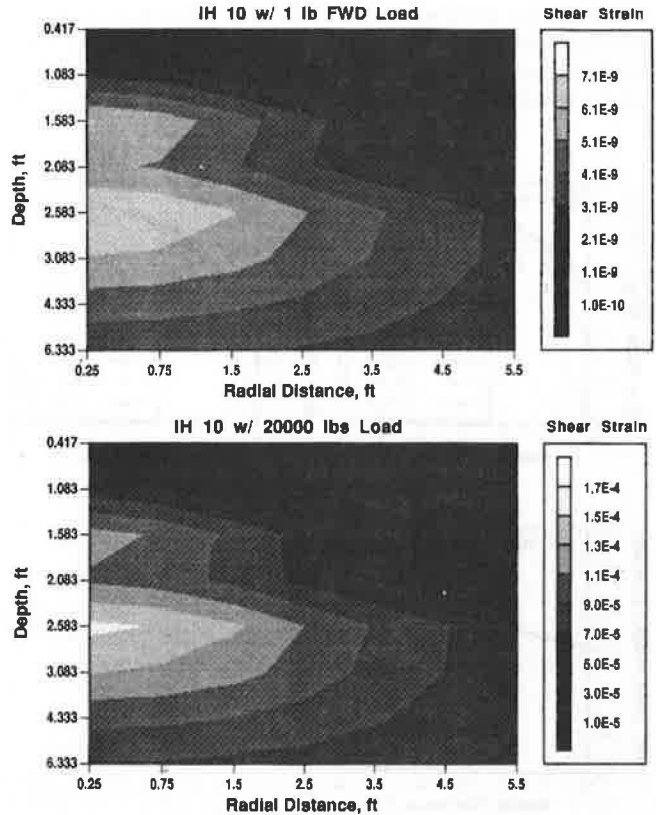


**FIGURE 12** Variations of shear strain at I-10 using 116 and 20,000-lb FWD loads.

shear deformational characteristics of the base and the subgrade materials. To simulate more realistically nonlinear response, analyses were also conducted integrating the equations of motion in time with the generalized cap model to reproduce material behavior. A set of analyses was conducted for three pavement sites using both methods. Solutions in terms of surface displacements, strain distribution and the modulus and damping spread were presented.

The results of these studies indicate that nonlinear effects on the measured deflections are directly related to (a) the magnitude of the load, (b) the type of pavement, (c) the stiffness of the subgrade, and (d) the thickness of the pavement surface. If the test is performed on a flexible pavement, a thin surface, a relatively soft subgrade, and with a large value of the load, large nonlinearities will take place near the source.

Results also indicate that for the FWD measurements at farm-to-market roads such as FM 195 where the nonlinearities are important, the maximum difference in peak displacements due to the nonlinear effects of a 20,000 lb load can be at least 50 percent. The nonlinear effects will be smaller for receivers at distances beyond 3 ft from the source.

The nonlinear effects obtained from the nonlinear analyses are greater than those from the approximate analyses. To resolve this problem more carefully, complete information of the material behavior under proper loading (using proper testing) must be obtained to calibrate the parameters used for the nonlinear material model.

The possible effects of material nonlinearities on FWD measurements were studied analytically in this work. Correlation of these results with field measurements is necessary. The approximate nonlinear analysis provides a better qualitative understanding of the material variations under the road. It also requires less data on the base and subgrade properties. It may underestimate strains, however, by about 50 percent. The true nonlinear analysis would provide more accurate results if the nonlinear constitutive equations were realistic and their parameters were known for the material in question. To fit these parameters would require a considerable amount of sample collection and laboratory testing. This type of analysis is thus more suited for research purposes than for actual use in practice on a regular basis. Both methods revealed the potential for nonlinearities using large FWD loads particularly for flexible pavements and soft subgrades. The question that must still be resolved is the meaning of the backfigured moduli when the properties change in the horizontal direction as will happen when there is nonlinear behavior. Both methods revealed the potential for nonlinearities using large FWD loads. At arbitrary sites, the degree of the nonlinear effects is indeed related to the actual thickness of the soil stratum and should be studied independently.

## ACKNOWLEDGMENTS

This work was supported by the Texas State Department of Highways and Public Transportation under contract 3-18-88/1-1175. The authors wish to express their appreciation for this support.

## REFERENCES

1. W. Uddin, A. H. Meyer, W. R. Hudson, and K. H. Stokoe II. *A Structural Evaluation Methodology for Pavements Based on the Dynamic Deflection*. Center for Transportation Research, University of Texas, 1983.
2. J. M. Roesset and K. Shao. Dynamic Interpretation of Dynaflect and Falling Weight Deflectometer Tests. In *Transportation Research Record 1022*, TRB, National Research Council, Washington, D.C., 1985, pp. 7-16.
3. T. G. Davies and M. S. Mamlouk. Theoretical Response of Multilayer Pavement Systems to Dynamic Nondestructive Testing. In *Transportation Research Record 1022*, TRB, National Research Council, Washington, D.C., 1985, pp. 1-7.
4. V. K. Kang, J. M. Roesset, and K. H. Stokoe II. Effect of the Finite Width of Pavements on Deflection Basins Obtained with Dynaflect and FWD Tests. Transportation Research Board, 1990, pp. 1-26.
5. S. Nazarian and K. H. Stokoe II. Effect of Seasonal Prediction on the Moduli of Farm-To-Market Roads. Technical Memorandum, Study No. 936-2. Center of Transportation Research, University of Texas at Austin, Aug. 1986.
6. B. O. Hardin and V. P. Drnevich. Shear Modulus and Damping in Soils: Measurement and Parameter Effects. *Journal of the Soil Mechanics and Foundations Division*, ASCE, Vol. 98, No. SM6, 1972, pp. 603-624.
7. S.-H. Ni. *Dynamic Response of Sand Under True Triaxial Stress State From Resonant/Column Torsional Shear Tests*. Ph.D. dissertation. University of Texas at Austin, Aug. 1987.
8. J. Lysmer, T. Udaka, C.-F. Tsai, and H. B. Seed. *FLUSH—A Computer Program for Approximate 3-D Analysis of Soil-Structure Interaction Problems*. Report EERC 75-30. University of California, Berkeley, Nov. 1975.
9. J. M. Roesset and H. Scaletti. Nonlinear Effects in Dynamic Soil Structure Interaction. In *Proc., Third Interaction Conference on Numerical Methods in Geomechanics*, Aachen, April 1979, pp. 1,457-1,470.
10. E. Kausel, J. M. Roesset, and G. Waas. Dynamic Analysis of Footings on Layered Media. *Journal of the Engineering Mechanics Division*, ASCE, Vol. 101, No. EM5, Oct. 1975, pp. 679-693.
11. I. S. Sandler, F. L. DiMaggio, and G. Y. Baladi. Generalized Cap Model for Geological Materials. *Journal of the Geotechnical Engineering Division*, ASCE, Vol. 102, No. GT7, 1976, pp. 638-699.
12. W. F. Chen and G. Y. Baladi. *Soil Plasticity—Theory and Implementation*. Developments in Geotechnical Engineering Series 38, Elsevier Science Publishing Co., New York, N.Y., 1985.
13. D. W. Chang. *Nonlinear Effects on Dynamic Response of Pavements Using the Non-Destructive Testing Technique*. Ph.D. Dissertation. University of Texas at Austin, May 1991.

*Publication of this paper sponsored by Committee on Strength and Deformation Characteristics of Pavement Sections.*

# Effect of Depth to Bedrock on Deflection Basins Obtained with Dynaflect and Falling Weight Deflectometer Tests

DER-WEN CHANG, YUMIN VINCENT KANG, JOSE M. ROESSET, AND  
KENNETH H. STOKOE II

The dynaflect and falling weight deflectometer (FWD) are commonly used for nondestructive testing of pavements. In both cases a dynamic load is imparted on the surface of the pavement, and deflections are measured at various points along the surface. Evaluation of the moduli of the surface layer, base, and subgrade is normally performed by comparing the experimental deflections with the results of static analyses. The moduli of the layers in the static model are then varied in an iterative procedure until a reasonable match between experimental and theoretical deflections is obtained. This solution ignores the dynamic nature of these nondestructive tests. In this paper the effect of depth to bedrock on the amplitude of the deflections and the shape of the deflection basins obtained with the dynaflect and the FWD tests is investigated analytically. Dynamic and static deflections at four different pavement profiles are compared. The results show that the range of bedrock depths over which dynamic effects are important differs between the two nondestructive tests because of the excitation frequencies and depends mainly on the stiffness of the subgrade. The results also show that, when dynamic effects occur in the measurements but are not taken into account in the analysis, the modulus of the subgrade is generally underestimated, sometimes by 50 percent or more, and the moduli of the base and surface layer are overestimated. Finally, a simple method is suggested for the FWD that makes it possible to estimate the depth to bedrock by recording the free vibration of the pavement system.

Reliable measurements of the in situ conditions of pavements are an important aspect in effectively managing pavement systems. The dynaflect and falling weight deflectometer (FWD) are two devices commonly used in practice for nondestructive determination of the values of Young's moduli for the various layers in a pavement profile.

The dynaflect consists of a force generator and five geophones housed in a small trailer that is towed by a light vehicle. The loading system consists of two counter-rotating eccentric masses. The resulting vertical force varies harmonically with time. At a frequency of 8 Hz, a 1,000-lb peak-to-peak oscillating force is transmitted to the pavement through the loading wheels. The resulting deflection basin is measured by five geophones mounted on the trailer draw bar at 12-in. intervals.

---

D.-W. Chang, Tam Kang University, 180 Chung-An Street, Chung-Ho City, Taipei Hsien, Republic of China. Y. V. Kang, Department of Civil Engineering, Feng Chai University, 100 Wenhwa Road, Taichung, Taiwan, Republic of China. J. M. Roesset and K. H. Stokoe II, Department of Civil Engineering, University of Texas, Austin, Tex. 78712-1076.

The position of the geophones (Stations 1 through 5) with respect to the wheels is shown schematically in Figure 1.

The FWD has a drop weight mounted on a vertical shaft and housed in a compact trailer that can easily be towed by most conventional vehicles. The drop weight is hydraulically lifted to predetermined heights ranging from about 2 to 20 in. The weight is then dropped onto a spring system that helps condition and distribute the load to the loading area. The resulting load is a force impulse with a duration of approximately 30 msec and a peak magnitude ranging from about 2,000 lbs to more than 20,000 lbs, depending on the drop height, drop weight, and pavement stiffness. The peak force and maximum deflections at various points along the surface are measured by a load cell and a set of velocity transducers. The applied pressure is measured in kilopascals and the deflections in micrometers. The positions of the load and recording stations are also shown in Figure 1, the dynaflect in plan and the FWD in profile views.

In the case of the dynaflect the deflections measured at the various stations represent the amplitudes of the steady-state displacements at a given frequency (8 Hz). For the FWD they are the peak displacements under a transient type excitation. In both cases the tests are dynamic in nature, but interpretation of the results to estimate the moduli of the surface layer, base, and subgrade relies on static analyses. Furthermore, these analyses assume that the soil in the subgrade is an elastic, uniform half-space or an elastic stratum of finite thickness. In many cases soil properties vary with depth, and the soil is underlain at some depth by much stiffer, rock-like material that causes reflections in the stress waves imparted during the dynamic tests.

The purpose of this work is to assess the effect of depth to bedrock on the amplitude of the deflections and the shape of the deflection basins that would be measured by the dynaflect and FWD for four different pavement profiles. The influence of the dynamic effects on backcalculated moduli is presented. Finally, the possibility of recognizing the existence of bedrock at a finite depth and estimating this depth from the measured data is discussed.

## FORMULATION

Static and dynamic analyses of pavement systems always assume the existence of horizontal layers with different material

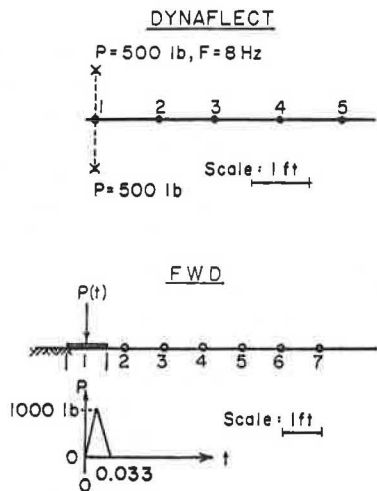


**FIGURE 1** Geometric configuration of loads and stations for dynaflect and FWD simulations.

properties that extend to infinity in the horizontal directions. The top layer represents the surface layer, the second represents the base, and the following layers represent the soil of the subgrade. An accurate solution requires consideration of the finite width of the pavement, but for the purpose of this work the above assumptions are not unreasonable. The effects of the finite width of the pavement and the position of the load with respect to the edge were the subject of a previous paper (1). Determination of the response of this system to dynamic loads applied at the surface falls mathematically into the area of wave propagation theory.

The formulation of these problems always starts by considering steady-state harmonic forces and displacements at a given frequency. For a harmonic excitation as applied by the dynaflect the solution at the desired frequency (typically 8 Hz) directly provides the desired results. For an arbitrary transient excitation as applied by the FWD the time history of the load must be first decomposed into different frequency components using a Fourier series, or more conveniently, a Fourier transform. Results are then obtained for each term of the series (each frequency) and are later combined to obtain the time history of displacements (inverse Fourier transform). When the frequency considered is zero, the results of the analysis are the static solution.

For a given frequency the solution proceeds by considering a uniform single layer with two horizontal surfaces, at the top and bottom. Due to a vertical load, displacements, stresses, and strains at any point will be independent of the angle  $q$  (circumferential direction) in cylindrical coordinates, and a function only of the radial distance from the vertical axis through the origin. They can then be expressed in a series of Bessel or modified Bessel functions. Each term of the series represents a wave number. For each wave number one can then develop a dynamic stiffness matrix for the layer relating stresses at the two interfaces to the displacements at the same elevations. By assembling the stiffness matrixes of the different layers (surface layer, base, and subgrade), one can form a total stiffness matrix for the pavement system and compute the displacements at any point due to the applied load (for each wave number). The actual displacements are then ob-

tained by performing an inverse Bessel (or Hankel) transform, involving an integral from zero to infinity of the displacements for each wave number multiplied by a Bessel function. This provides the steady-state solution for each frequency. In FWD tests the process is repeated for many different frequencies. The time history of the displacements is then obtained by applying an inverse Fourier transform. For the dynaflect the last step is not needed, and results are obtained only for one frequency (typically 8 Hz).

The terms of the dynamic stiffness matrixes of each layer involve transcendental functions (2). An alternative is to divide the physical layer into a number of thin sublayers. For these sublayers one can approximate the variation of the displacements with depth by a straight line (or higher order polynomial expansions if so desired). This approximation leads to much simpler algebraic expressions for the terms of the stiffness matrixes, which allows one to compute the wave numbers (eigenvalues) and mode shapes (eigenvectors) of the waves propagating through the pavement system by solving an algebraic eigenvalue problem (3,4). The displacements caused by harmonic dynamic loads can then be obtained in explicit form (without the need to compute the Bessel integrals) as shown by Kausel (5).

Each one of these two approaches (continuous and discrete formulations) has advantages and disadvantages from a computational point of view. Both have been implemented in computer programs that yield nearly identical results. In the discrete solution the division of the physical layers into sublayers is done automatically inside the program on the basis of a number of parametric studies conducted by Roesset and Shao (6), so that the input is the same for all the programs.

The results presented here were obtained using the computer programs UTDYNAF and UTFWD developed at the University of Texas at Austin to simulate the dynaflect and the FWD, respectively, using the discrete formulation.

## PARAMETRIC STUDY

Roesset and Shao (6) conducted a number of parametric studies on a hypothetical pavement profile, comparing the dynamic deflections with those that would be obtained from static analyses assuming that the subgrade extended to infinity (an elastic half space) and considering a rigid base at a finite depth (the same depth used for the dynamic analyses). Davies and Mamlouk (7) and Mamlouk (8) used the same formulation to conduct parametric studies and investigate the importance of dynamic effects and reached similar conclusions. Davies and Mamlouk (7) suggested in particular a formula for the frequency at which the maximum dynamic amplification takes place as a function of the thickness and shear wave velocity of the subgrade. In this study four actual sites were considered to conduct further analyses.

## Description of Test Sites

Four typical in-service pavement sections were selected as the models for the test sites in these analyses. The models are patterned after (but do not exactly match): FM 137 in Paris, Texas; FM 195 in Paris, Texas; Route 1 in Austin, Texas;

and Interstate highway 10 in El Paso, Texas. Detailed information used for the calculations on these test sites is presented in Table 1. The damping ratios were assumed to be 2 percent in all layers. Variation of the damping ratios from these assumed values will obviously alter the proportions of the results of this study. Each profile is modeled as a horizontally layered stratum resting over bedrock (rigid rock). The depth to bedrock, defined as the total depth measured from the surface to the bedrock, was varied by changing the thickness ( $h$ ) of the subgrade.

### Effect of Depth to Bedrock on Deflection Basins for Dynaflect Tests

Simulation of the dynaflect test was conducted on the four selected profiles, and the corresponding static solutions were obtained for comparison purposes. Figure 2a shows the ratio of dynamic to static deflections as a function of the assumed depth to bedrock for the first profile (FM 137). The dynamic deflection is the amplitude of the steady state response, which is also the peak deflection in this range. It can be seen that, for all stations, the deflection ratio initially starts from a value of nearly one at shallow depths, reaches its maximum at a critical depth of about 27.5 ft, and finally decreases to one as the depth increases. There is a second smaller peak at a depth of about 70 ft. The dynamic amplification factor is not constant at all receiver stations. The maximum deflection ratio occurs at the fifth station (farthest from the source) and reaches a maximum value of 2.23 at the critical depth (27.5 ft). The depths at which resonance would occur for pure shear and compression waves due to a harmonic excitation at a frequency of 8 Hz are indicated in Figure 2a by symbols  $d_s$  and

$d_p$ , respectively. It can be seen that the critical depth is located between  $d_s$  and  $d_p$  but is quite close to the depth corresponding to resonance associated with compression waves,  $d_p$ .

Figures 2b, 2c, and 2d show the deflection ratios for the FM 195, Route 1, and I-10 profiles. The results for the second and fourth sites (FM 195 and I-10) are similar to those of Site 1, with important dynamic amplification occurring when the depth to bedrock is from 15 to 35 ft. On the other hand, for the third profile (Route 1), large amplifications occur when the depth to bedrock is between 30 and 65 ft. It is interesting to notice that the only difference between the first two sites is the thickness of the surface layer (1 in. versus 4 in.). The thickness of the base and the elastic moduli of the surface layer, base, and subgrade are otherwise identical. The fourth site has different moduli and thicknesses for the pavement and base, in addition to having an additional subbase layer. However, the properties of the subgrade are the same as Profiles 1 and 2. On the other hand, the subgrade at Profile 3 has a shear wave velocity that is twice that of the other sites (Young's modulus is about 4 times higher than that of the other sites). Comparison of the four sites indicates that the dynamic effects are primarily influenced by the stiffness and thickness of the subgrade.

Dynamic effects have been traditionally represented in structural dynamics by amplification factors that represent the ratio of peak dynamic to static displacements (or forces). This is the approach followed in Figure 2. The advantage of this approach is that it shows clearly at what frequency, or for what depth to bedrock in the case of a fixed frequency, dynamic effects are important. For the present application it is interesting, however, to look also at the difference between dynamic and static deflections, instead of their ratio. This is shown in Figure 3 for the four sites. The differential deflections are measured in mils (thousandths of inches). It can be observed that, in general, the deflection differences are fairly uniform over the 5 stations for a given depth to bedrock. (The exceptions are at 30 ft for Profiles 1, 2, and 4, and 60 ft for Profile 3, where the difference increases with distance from the source.) From a physical point of view these results imply that the dynamic effects can be interpreted as a train of plane compressional waves traveling down the profile, reflecting at the rigid bottom and then at the (free) pavement surface. From a practical point of view this implies that the deflection basin obtained experimentally could be corrected for dynamic effects by subtracting a constant quantity from the deflections measured at all five stations. Unfortunately the amount to be subtracted is a function of the thickness and modulus of the subgrade and of the effective damping. Therefore, it is difficult to estimate this additional increment without previous knowledge of the properties of the pavement system. Moreover, application of a correction to obtain a static basin is of limited interest because dynamic analysis of a layered pavement system at a fixed frequency is no more expensive nor time-consuming than the usual static analysis.

The main limitation of the dynaflect is that the test is conducted at a single frequency and that only the amplitudes of the steady-state vibrations are used. If one were to conduct the test at two different frequencies (e.g., 8 and 16 Hz), it would at least allow a comparison of the measured deflection basins. If the results were almost identical for the two frequencies, one could conclude that dynamic effects are not

TABLE 1 Properties of Four Test Sites Used as Models

Site	Layer	Thickness (in.)	S-Wave	P-Wave	Unit Weight (pcf)	Damping Ratio (%)
			Velocity (fps)	Velocity (fps)		
FM 137 Paris, Texas	AC	1	2500	3900	140	2
	base	12	1000	1730	125	2
	subgrade	$h^*$	500	1000	110	2
FM 195 Paris, Texas	AC	4	2500	3900	140	2
	base	12	1000	1730	125	2
	subgrade	$h$	500	1000	110	2
Route 1 Austin, Texas	AC	7	3000	5200	145	2
	base	6	1000	2080	130	2
	subgrade	$h$	1000	2080	130	2
Interstate Highway 10, El Paso, Texas	CRC	10	9000	14030	145	2
	base	6	2500	3900	145	2
	subbase	12	800	1600	125	2
	subgrade	$h$	500	1000	125	2

\*  $h$  is a variable

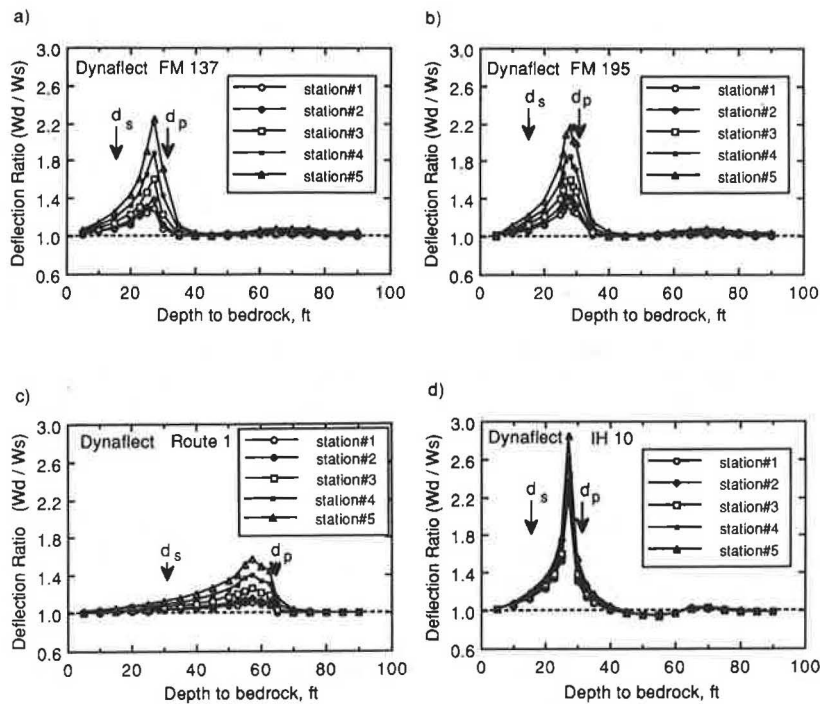


FIGURE 2 Deflection ratios versus depth to bedrock for dynaflect testing.

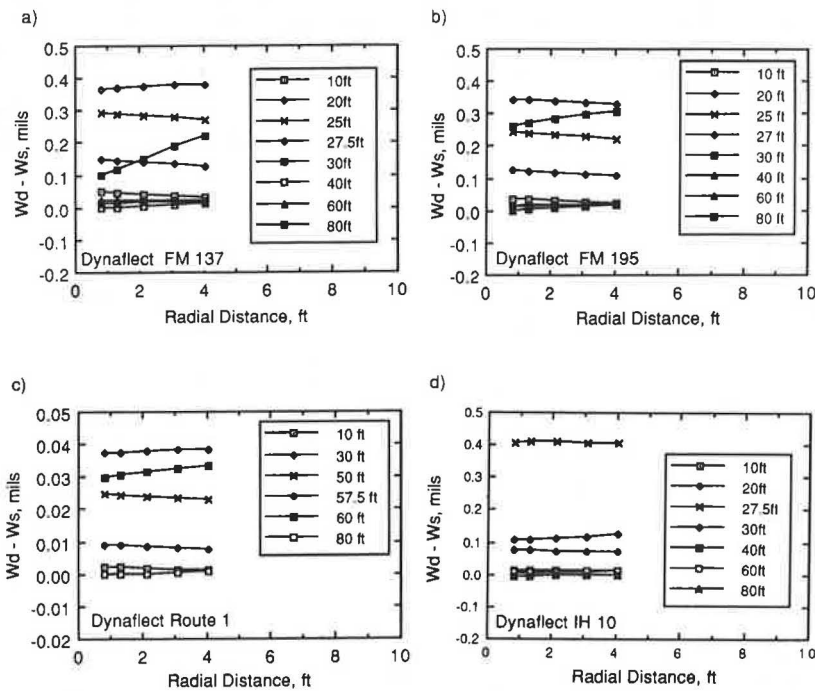


FIGURE 3 Difference in deflections versus radial distance for dynaflect testing.

important, that bedrock is located at a sufficient depth (of the order of 70 ft or more), and that a static analysis would be appropriate to backcalculate the elastic properties of the layers. On the other hand, if the results showed clear differences, it would be apparent that dynamic effects are important. In this case testing at other frequencies would be needed

in order to define the peak of the amplification function and to permit estimation of the depth to bedrock. A simpler alternative might be to continue recording the motions at the different stations after the excitation has ceased in order to obtain the free vibrations of the pavement system. In this case a procedure similar to the one proposed for the FWD in the

following section could be used to estimate, relatively simply, the depth to bedrock.

### Effect of Depth to Bedrock on Deflection Basins for FWD Tests

The results of the simulations of the FWD tests are presented again in terms of deflection ratio (dynamic amplification factor) as a function of the assumed depth to bedrock in Figure 4. The dynamic deflection is the peak deflection. Two main points are notable. First, the critical depth to bedrock for the FWD (depth at which the maximum amplification occurs) is always less than for the dynaflect. This result is because the FWD generates higher frequencies than the dynaflect. If one defines a characteristic or predominant frequency as the natural frequency of the pavement system in compression for the depth to bedrock at which the maximum dynamic amplification takes place, the predominant frequency of the FWD test is between 30 and 35 Hz (versus 8 Hz for the dynaflect). Second, the deflection ratio can become less than one for the FWD, especially for the deeper subgrade, whereas for the dynaflect, the ratio is almost always greater than one. It should be noted that when the deflection ratio is less than one, the use of an inversion process based on a static analysis will lead to overestimating the Young's moduli of the layers as discussed in the next section.

For Profile 1 (Figure 4a) the maximum amplification occurs for a depth to bedrock of about 5 ft (between 5 and 7.5 ft). The critical depth is about 7.5 ft for Profile 2 (Figure 4b) and Profile 4 (Figure 4d) and becomes of the order of 15 ft for Profile 3 (Figure 4c). This trend is consistent with that observed for the dynaflect and reflects the higher modulus of

the subgrade in Route 1 (third profile). At the third site the amplification is higher than one over the complete range of depths to bedrock studied. At Profile 1 the amplification is slightly less than one at all stations for depths to bedrock of 60 ft or more and is smaller than one over most of the range of depths under the load (Station 1). The results are similar for Profile 2, although the deamplification is slightly more pronounced. For Profile 4 the dynamic deflections are smaller than the static ones at all stations for depths to bedrock greater than 20 ft. It is interesting to notice that in this range the ratio of dynamic to static deflection is essentially the same at all stations (the deflection basin is multiplied by a constant factor).

Figure 5a shows the differences between dynamic and static deflections for the FWD and Profile 1. It can be seen that in this case the differences are not constant for all stations as in the case of the dynaflect. This implies that the dynamic effects are more complex because of the many frequencies involved and can no longer be explained on the basis of plane waves. Similar results are obtained at the other sites (Figures 5b, 5c, and 5d).

### Effects of Bedrock Depth on Moduli Backcalculated from FWD Data

Knowledge of the effects of bedrock at a finite depth on the FWD deflection measurements can be used to investigate the resulting effects on backcalculated layer moduli. This was done by presuming that the peak dynamic deflections could be equated to the static FWD deflections. The peak dynamic deflections were then used with conventional interpretation procedures to backcalculate layer moduli. For simplicity the following study was conducted by choosing two cases for each

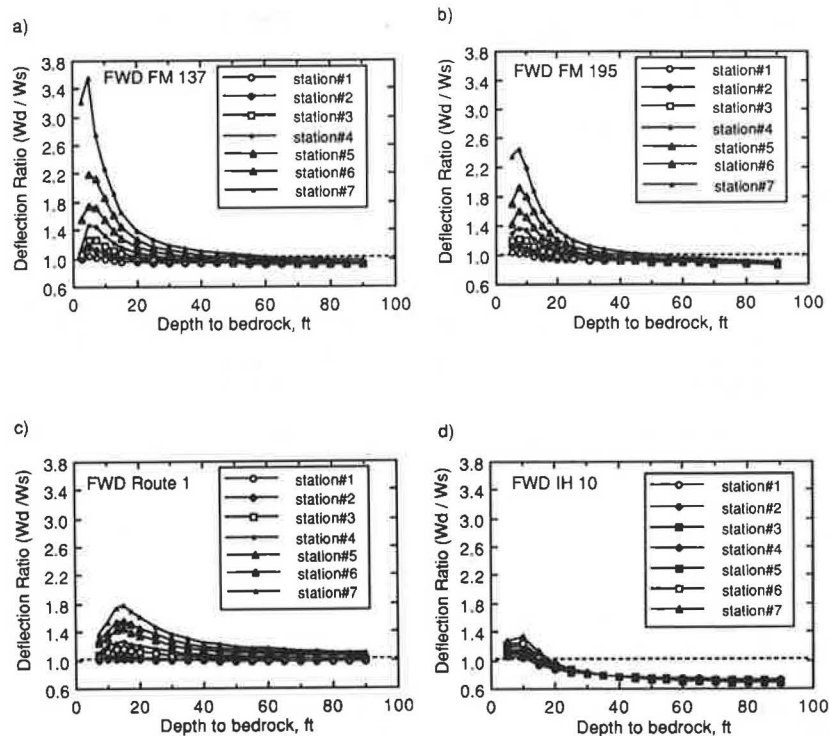


FIGURE 4 Deflection ratios versus depth to bedrock for FWD testing.

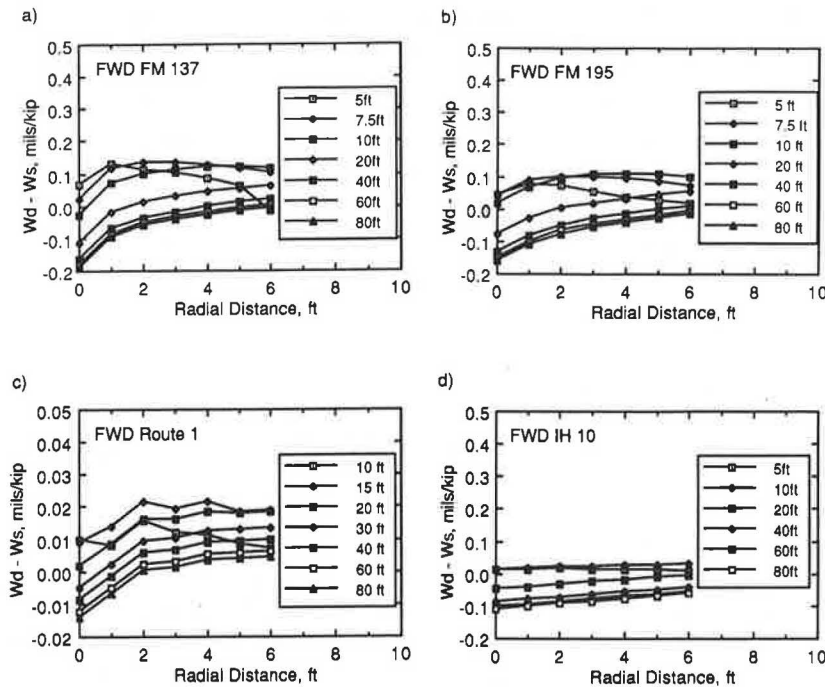


FIGURE 5 Difference in deflections versus radial distance for FWD testing.

site (see Table 2) in which the associated depth to rock results in either (a) peak dynamic amplification or (b) an insignificant amount of dynamic amplification or possibly even some deamplification (such as the bedrock at 80 ft). By assigning the dynamic FWD deflection basin to the basin-fitting program MODULUS (9), layer moduli were backcalculated and compared with their original values. The resulting errors in terms of the ratio of backcalculated moduli to their original values are summarized in Table 3.

For the FM 137 site deflections at peak amplification result in a 50 percent underestimation of the subgrade modulus,

TABLE 2 Estimated Depth to Bedrock for Four Study Sites with Various Bedrock Depths

Site	Measured Period (sec) ( $T_n$ )	Estimated Depth to Bedrock (ft)	Actual Depth to Bedrock (ft)
1	0.02	6	5
	0.03	9	7.5
	0.04	12	10
2	0.08	24	20
	0.02	6	5
	0.03	9	7.5
3	0.04	12	10
	0.06	18	20
	0.02	6	10
	0.03	9	15
4	0.04	12	20
	0.07	21	30
	0.02	6	5
	0.04	12	10
	0.09	27	20

NOTE: Estimated depth to bedrock based on  $h = 300 T_n$ . Compression wave velocity in the subgrade is assumed to be 1200 fps. Accuracy of the estimated depth increases in direct proportion with the accuracy of the assumed compression wave velocity of the subgrade.

whereas the moduli of the surface and base layer are overestimated by about 100 percent. When the depth to bedrock is 80 ft at the same site the modulus of the surface layer is greatly overestimated whereas the moduli of the base and subgrade are only overestimated by 6 percent, an insignificant amount. For the FM 195 site the peak amplification results in a 37 percent underestimation of the subgrade modulus, about a 60 percent overestimation for both the surface layer and base moduli. When the depth to the bedrock is 80 ft, overestimations of the moduli of the surface, base, and subgrade layers are all less than 20 percent. For Route 1 use of peak displacements gives 3 percent and 21 percent underestimations for the surface and subgrade layers. However it gives a 107 percent overestimation for the base moduli. In the case in which the dynamic amplification ratio is nearly one dynamic effects are found to give -1 percent, +33 percent, and -3 percent errors in layer moduli for Route 1. It is interesting to note that even in this case, the static analyses give results in error in the modulus of the base layer. For the I-10 site the peak amplification results in 25 percent and 135 percent overestimations of the surface and subbase moduli and 4 percent and 33 percent underestimations for the moduli of the base and subgrade. In the case in which the depth to the bedrock is as deep as 80 ft the significant dynamic deamplification phenomenon results in 8 percent, 31 percent, 115 percent, and 44 percent overestimations for the moduli of the surface, base, subbase, and subgrade layers, respectively. All these results are based on the assumed 2 percent damping.

Generally speaking, conventional (static) interpretation of the FWD data appears to yield overpredictions of the material stiffness for the surface and base layers. This is particularly true in the cases in which the dynamic effects on the measured response are important (shallow depth to the rock). In this case the stiffness of the subgrade is significantly underpre-

**TABLE 3 Comparison of Backcalculated Layer Moduli Using Computer Program Modulus with Actual Moduli Used to Generate Dynamic Deflections**

Site	Depth (ft)	AC Surface				Base				Subgrade			
		True E <sub>o</sub>	Input E <sub>x</sub>	Comp. E <sub>c</sub>	E <sub>c</sub> /E <sub>o</sub>	True E <sub>o</sub>	Input E <sub>x</sub>	Comp. E <sub>c</sub>	E <sub>c</sub> /E <sub>o</sub>	True E <sub>o</sub>	Input E <sub>x</sub>	Comp. E <sub>c</sub>	E <sub>c</sub> /E <sub>o</sub>
FM 195	5	434	200 to 1000	803	1.85	57	25 to 200	145	2.16	16	16	8.0	0.5
	80	434	200 to 1000	5082	11.71	67	25 to 200	59	0.88	16	16	17	1.06
FM 137	7.5	434	200 to 1000	700	1.61	67	25 to 200	111	1.66	16	16	10	0.63
	80	434	200 to 1000	443	1.02	67	25 to 200	80	1.19	16	16	18	1.13
Route 1	15	704	200 to 1000	680	0.97	76	25 to 200	157	2.07	76	76	60	0.79
	80	704	200 to 1000	699	0.99	76	25 to 200	101	1.33	76	76	74	0.97

Site	Depth (ft)	CRC Surface				AC Base				Subbase				Subgrade			
		True	Input	Comp.	E <sub>c</sub> /E <sub>o</sub>	True	Input	Comp.	E <sub>c</sub> /E <sub>o</sub>	True	Input	Comp.	E <sub>c</sub> /E <sub>o</sub>	True	Input	Comp.	E <sub>c</sub> /E <sub>o</sub>
IH 10	10		1000 to 10000	7263	1.25	450	200 to 1000	431	0.96	46	25 to 200	108	2.35	18	18	12	0.67
	80	5826	1000 to 10000	6286	1.08	450	200 to 1000	591	1.31	46	25 to 200	99	2.15	18	18	26	1.44

dicted. If the dynamic response of the FWD test is significantly less than the presumable static response, such as the cases of the I-10 site at which depths to the rock are greater than 20 ft, the stiffness of the subgrade can be overpredicted significantly.

To overcome the uncertainties involved in using the static FWD interpretation procedure knowledge of the depth to bedrock and materials damping is important as is the dynamic nature of the test. A simple way of assessing bedrock depth is described in the next section.

**Estimation of Bedrock Depth from FWD Tests**

Although in the normal use of the FWD only the peak deflections are kept to construct the deflection basin and then backfigure the elastic moduli, one can obtain at each station the complete history of the motions as a function of time. Figure 6a shows the deflection time histories at the first station (under the load) for the fourth site (I-10) assuming a deep subgrade (simulating a half space) and bedrock at a depth of 10 ft. In the case of the half-space (dotted line) there is basically a displacement pulse similar in shape to the applied load. In the case of bedrock at a depth of 10 ft, on the other hand, the main pulse is followed by several oscillations, with decaying amplitude, which represent the free vibrations of the pavement system and the subgrade layer in particular. These residual vibrations have a well-defined period that corresponds approximately to the natural period of the profile in compression. Moreover, as shown in Figure 6b, this period

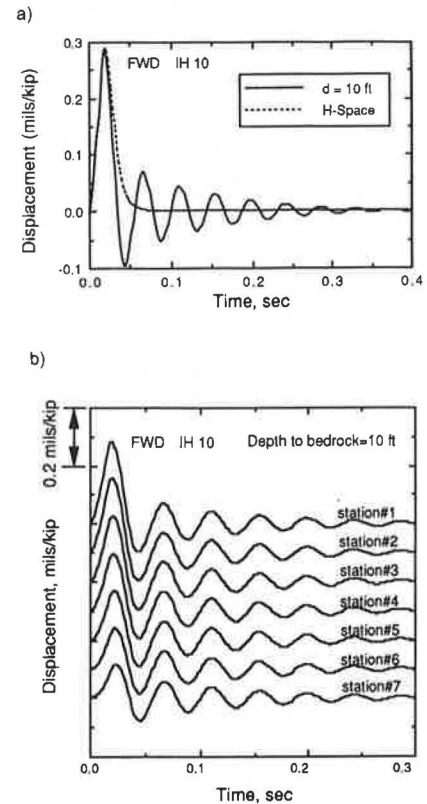


**FIGURE 6 Time histories of FWD displacements for Profile 4 (I-10).**

is essentially the same at all recording stations. For the I-10 site with a depth to bedrock of 10 ft the period is about 0.04 sec. Similar results were obtained for different depths to bedrock (with the corresponding change in the period) and for the other sites. This suggests that the depth to bedrock can be easily estimated from a simple observation of the displacement-time records. The natural frequency of interest is approximately

$$f_n = 1/T_n \cong c_p/4h \quad (1)$$

where  $c_p$  is the compressional wave velocity of the subgrade and  $h$  is the depth to bedrock. As a first approximation and before any inversion is performed one can assume a shear wave velocity for typical subgrades on the order of 600 ft/sec. (For the sites considered here the shear wave velocity of the subgrade varied from 500 ft/sec for Sites 1, 2, and 4 to 1,000 ft/sec for Site 3.) By assuming an average Poisson's ratio of 0.33, the compressional wave velocity would be  $c_p = 1,200$  ft/sec. Then

$$h \cong c_p/4T_n \cong 300 T_n \quad (2)$$

with the period in seconds and the depth to bedrock  $h$  in feet, or

$$h \cong 90 T_n \quad (3)$$

with  $h$  in meters.

Davies and Mamlouk's (7) formula would yield  $h = 0.2 c_p T_n$ , which differs only by 20 percent.

By applying this formula to the free vibrations shown in Figure 6, one would obtain a depth to bedrock of 12 ft instead of the actual 10 ft used for the analyses. Table 2 presents the measured periods from time records, estimated depths, and actual depths for various other cases. Because the shear wave velocity of the subgrade is 500 ft/sec for Profiles 1, 2, and 4, the formula should overestimate the depth to bedrock by about 20 percent. For Profile 3 the shear wave velocity was 1,000 ft/sec, and the formula should underestimate the depth to bedrock by about 40 percent. It is important to notice that this preliminary estimate can be obtained directly in the field without any need for computer processing of the data. It can then be used in the inversion process to obtain improved estimates of the moduli. Once Young's modulus of elasticity of the subgrade has been determined, an improved estimate of the depth to bedrock can be obtained as

$$h \cong 60 \sqrt{E} T_n \quad (4)$$

with  $E$  in ksi,  $T_n$  in seconds, and  $h$  in ft, or

$$h \cong \frac{1}{4} \sqrt{E} T_n \quad (5)$$

with  $E$  in kN/m<sup>2</sup> and  $h$  in meters.

These formulas assume an average unit weight of 120 lb/ft<sup>3</sup> (20000 N/m<sup>3</sup>) for the subgrade and an average Poisson's ratio of 0.33. They are, therefore, approximations intended primarily to obtain an order of magnitude estimate. The value of the Poisson's ratio assumed for all the formulas is appropriate for average subgrades that are not 100 percent saturated.

Additional studies are being conducted to select more appropriate coefficients when the subgrade is fully saturated. However, the general approach is simple and should be helpful in evaluating bedrock depth for all subgrade materials.

## CONCLUSIONS

The results of the studies presented in this paper show clearly that dynamic effects can influence the magnitude of the deflections and the shape of the deflection basin obtained in the dynaflect and FWD tests. The importance of these effects is a function of the depth to bedrock and the material properties (including material damping) when there is a sharp discontinuity in the values of the elastic modulus of the subgrade and that of the underlying rock. For the dynaflect test these effects lead to significant dynamic amplification when bedrock is at a depth ranging from about 20 to 60 ft for small values of damping, depending on the properties of the subgrade. Determination of the moduli of the surface layer, base and subgrade using static analyses, as is the current practice, may then lead to a significant underestimation of the modulus of the subgrade and an overestimation of the moduli of the base and surface layer. For the FWD dynamic amplifications occur only for much smaller depths to bedrock, on the order of one-fourth of the dynaflect's (5 to 15 ft typically). On the other hand, there can be deamplifications (dynamic deflections smaller than the static ones) over a wide range of depths for the FWD. In this case static analyses would generally overestimate the elastic moduli of all layers in the pavement.

It appears that using only the maximum deflections recorded at each station fails to use the true potential of the FWD. Recording the complete time history of the deflections, at least at one station, allows a simple and fast estimation of the depth to bedrock, which can be performed in the field simply by measuring the period of the residual vibrations after the first pulse. From the decay of these residual vibrations, one could also estimate an effective damping. This same concept could be extended to the dynaflect.

## ACKNOWLEDGMENTS

The work described in this paper was conducted at the University of Texas at Austin under a research grant from the Texas State Department of Highways and Public Transportation and is part of a comprehensive study on the potential of the dynaflect and FWD to estimate moduli of pavement systems.

## REFERENCES

1. Y. V. Kang, J. M. Roesset and K. H. Stokoe II. Effect of Loading Position on Deflection Basins Obtained with Dynaflect and FWD Tests. Presented at 70th Annual Meeting of the Transportation Research Board, Washington, D.C., 1991.
2. E. Kausel and J. M. Roesset. Stiffness Matrices for Layered Soils. *Bulletin of the Seismological Society of America*, Vol. 71, No. 6., Dec. 1981.
3. G. Waas. *Linear Two Dimensional Analysis of Soil Dynamics Problems on Semi-Infinite Layered Media*. Ph.D. thesis. University of California, Berkeley, 1972.

4. E. Kausel. *Forced Vibrations of Circular Foundations on Layered Media*. Research Report R74-11. Department of Civil Engineering, Massachusetts Institute of Technology, Cambridge, 1974.
5. E. Kausel. *An Explicit Solution for the Green Functions for Dynamic Loads in Layered Media*. Research Report R81-13. Department of Civil Engineering, Massachusetts Institute of Technology, Cambridge, 1981.
6. J. M. Roesset and K. Shao. Dynamic Interpretation of Dynaflect and Falling Weight Deflectometer Tests. In *Transportation Research Record 1022*, TRB, National Research Council, Washington, D.C., 1985, pp. 7-16.
7. T. G. Davies and M. S. Mamlouk. Theoretical Response of Multilayer Pavement Systems to Dynamic Nondestructive Testing. In *Transportation Research Record 1022*, TRB, National Research Council, Washington, D.C., 1985, pp. 1-7.
8. M. S. Mamlouk. Use of Dynamic Analysis in Predicting Field Multilayer Pavement Moduli. In *Transportation Research Record 1043*, TRB, National Research Council, Washington, D.C., 1986, pp. 113-119.
9. J. Uzan, R. L. Lytton, and F. P. Germann. General Procedures for Backcalculating Layer Moduli. First Symposium on NDT of Pavements and Backcalculation of Moduli, American Society for Testing and Materials, Baltimore, Md., July, 1988.

---

*Publication of this paper sponsored by Committee on Strength and Deformation Characteristics of Pavement Sections.*

# Variability in Estimation of Structural Capacity of Existing Pavements from Falling Weight Deflectometer Data

MUSTAQUE HOSSAIN AND JOHN P. ZANIEWSKI

The calculation of existing pavement structural capacity in terms of 18-kip equivalent single axle load (18-kip ESAL) repetitions by the mechanistic-empirical method is a multistep analysis process. The variability in this calculation process is presented with respect to falling weight deflectometer (FWD) input deflection data in the backcalculation scheme, backcalculated layer moduli, and the number of FWD tests over a section of the road. As can be expected, the sensor readings of FWD on a long section of the road show more variability than on a short section. This variability in sensor readings is magnified when the layer moduli are backcalculated (i.e., small variability in sensor data over a section of a pavement will result in high variability of calculated layer moduli). However, this variability is independent of the length of the section of the roadway over which deflection testing is done. All the layer moduli and their interaction affect the calculated structural capacity. The variation in backcalculated layer moduli is magnified when the number of 18-kip ESALs the pavement can carry before fatigue failure is estimated. Interaction of high asphalt concrete modulus and base modulus tends to produce low asphalt concrete strain and consequently a high number of 18-kip ESAL applications. The opposite is true for interaction of low asphalt concrete modulus and low base modulus. As a result, the computed structural capacity becomes highly variable, especially when the number of tests done on a long section of the pavement is small. The frequency of testing does not affect the estimated 18-kip ESALs over a short section of pavement. However, for long sections it affects the mean estimated 18-kip ESALs. For a mile-long section, five FWD tests were found to be a viable choice for estimation of 18-kip ESALs. However, the coefficient of variation of estimated 18-kip ESALs over a long section may or may not decrease with increasing number of tests.

Nondestructive testing (NDT) is widely recognized as an important tool for pavement structural evaluation. State-of-the-art NDT evaluation measures a pavement's deflection response to a known load. The load generated by an NDT device may be static (Benkelman beam), steady-state vibratory (dynaflect and road rater), or impulse [falling weight deflectometer (FWD)]. Though surface deflection data analysis is a matter of continuing research, NDT for measuring surface deflection is accepted by most highway agencies as standard practice because it is fast and reliable in most cases.

---

M. Hossain, Department of Civil Engineering, Seaton Hall, Kansas State University, Manhattan, Kans. 66506-2905. J. Zaniewski, Department of Civil Engineering, College of Engineering and Applied Sciences, Arizona State University, Tempe, Ariz. 85287.

## PROBLEM DEFINITION

Calculation of pavement structural capacity, in terms of the ability to carry 18-kip equivalent single axle load (18-kip ESAL) repetitions, from FWD data is a three-step procedure. First, the layer moduli are backcalculated from the FWD, layer type, and thickness data. Second, the critical pavement response, usually the tensile strain at the bottom of asphalt concrete layer, is calculated. Third, empirical relationships are used for estimating the number of 18-kip ESALs based on the critical pavement response. The relationship estimates the number of 18-kip ESAL repetitions the pavement can carry before fatigue failure. Variability in any stage of the analysis affects the estimation of structural capacity by the mechanistic-empirical method.

## OBJECTIVES

The objectives of this study were (a) to find the variability of calculated 18-kip ESALs with respect to the variability in input FWD data and corresponding backcalculated layer moduli over short and long sections of pavements and (b) to find the effect of number of FWD tests over a short section (90 ft) and a long section (1 mi) of pavement on the estimated structural capacity.

## DATA COLLECTION

A list of the 16 sites selected for this study is presented in Table 1, and the pavement sections of these sites are presented in Table 2. The sites were selected in the Arizona State University Overlay Study (1) for Arizona Department of Transportation (ADOT) on the basis of a number of preselected criteria. All deflection data were collected with a Dynatest model 8002 FWD. The sensors were spaced at 12-in. intervals with the first sensor located at the center of the load. The target load was 9,000 lb. At Sites 1 through 13 deflection data were measured in the outer wheel path at 10 locations at 10-ft intervals. For Sites 14 to 16, deflection data were collected every 0.1 mi.

## ANALYSIS METHOD

The analysis process requires backcalculation of layer moduli of the pavements from FWD data and computation of struc-

TABLE 1 Location of Test Sites and Pavement Types

Site/Station	Location	Route	Milepost	Pavement Type	Test Type
1	Benson	I10W	300.07	5-layer	10 tests/90 ft.
2	Winslow	I40E	260.21	4-layer	10 tests/90 ft.
3	Minnetonka	I40E	261.78	4-layer	10 tests/90 ft.
4	Dead River	I40E	317.06	4-layer	10 tests/90 ft.
5	Flagstaff	I17N	337.00	4-layer	10 tests/90 ft.
6	Crazy Creek	I40E	323.78	4-layer	10 tests/90 ft.
7	Sunset Point	I17N	251.41	5-layer	10 tests/90 ft.
8	Seligman	I40W	131.71	4-layer	10 tests/90 ft.
9	Benson East	I10W	303.00	4-layer	10 tests/90 ft.
10	Jacob Lake	US89A	578.00	4-layer	10 tests/90 ft.
11	Morristown	US60W	120.00	4-layer	10 tests/90 ft.
12	McNary	US260E	369.00	5-layer	10 tests/90 ft.
13	Kingman I	I40E	59.00	4-layer	10 tests/90 ft.
14	Yucca	I40W	33.00	4-layer	10 tests/mile
15	Kingman II	I40E	24.00	4-layer	10 tests/mile
16	Tombstone	U80E	316.50	4-layer	10 tests/mile

TABLE 2 Layer Type and Thickness at Different Sites

Site/ Sta.	Layer 1		Layer 2		Layer 3		Layer 4		Layer 5	
	Mat	Thk (in)	Mat	Thk (in)	Mat	Thk (in)	Mat	Thk (in)	Mat	Thk (in)
1/1	AC	7	HB	2.5	AB	2	SB	12	SC-SM*	-
2/1	AC	12	BT B	3	SB	5	SM*	-	-	-
3/1	AC	11.5	BT B	2	SB	3	SM*	-	-	-
4/1	AC	8	CT B	4.5	SB	7	SM*	-	-	-
5/1	AC	9	AB	4	SB	12	-	-	-	-
6/1	AC	8	CT B	6	SB	6	SM*	-	-	-
7/1	AC	6	BS	4	SB	26	SGS	6	CL- CH*	-
8/1	AC	6	AB	6	SB	24	CH*	-	-	-
9/1	AC	6	AB	6	SB	18	SC-SM*	-	-	-
10/1	AC	9	HB	4	AB	4	SC-CH*	-	-	-
11/1	AC	4.25	AB	4	SB	15	-	-	-	-
12/1	AC	4.8	HB	2.2	AB	3	SB	6	-	-
13/1	AC	9.5	AB	4	SB	15	-	-	-	-
14/1	AC	4.0	AB	4	SB	9	-	-	-	-
15/1	AC	4.0	AB	4	SB	9	-	-	-	-
16/1	AC	3.0	AB	4	SB	15	-	-	-	-

\* Subgrade Classification based on Unified Method.

Note: AC: Asphalt Concrete, HB: HMAC Base, BTB: Bituminous Treated Base, CTB: Cement Treated Base, AB: Aggregate Base, SGS: Subgrade Seal, SB: Sub Base (Select Material)

tural capacity of the existing pavement through fatigue analysis. Backcalculation of layer moduli was done with the Arizona Deflection Analysis Method (ADAM) developed by Hossain (2). ADAM uses the CHEVRON (3,4) computer program for pavement response analysis. A robust optimization routine iterates the moduli values to minimize the squared error between the peak measured deflections and calculated deflections at the same offsets. The backcalculated layer moduli were used to determine the tensile strain at the bottom of the asphalt concrete layer. The structural capacity of the pavement in terms of theoretical number of 18-kip ESALs was

determined using the following equation for fatigue analysis. Hossain developed the analysis by modifying the ADOT overlay design fatigue relationship (2).

$$N = (2.265 \times 10^{-7}) (1/e_{ac})^{3.84} \quad (1)$$

where  $N$  is the theoretical number of 18-kip ESAL repetitions to fatigue failure and  $e_{ac}$  is the tensile strain at the bottom of the asphalt concrete layer (micro inch<sup>2</sup>). Equation 1 is valid for an asphalt concrete temperature of 70°F. Figure 1 shows the flow chart of the analysis process.

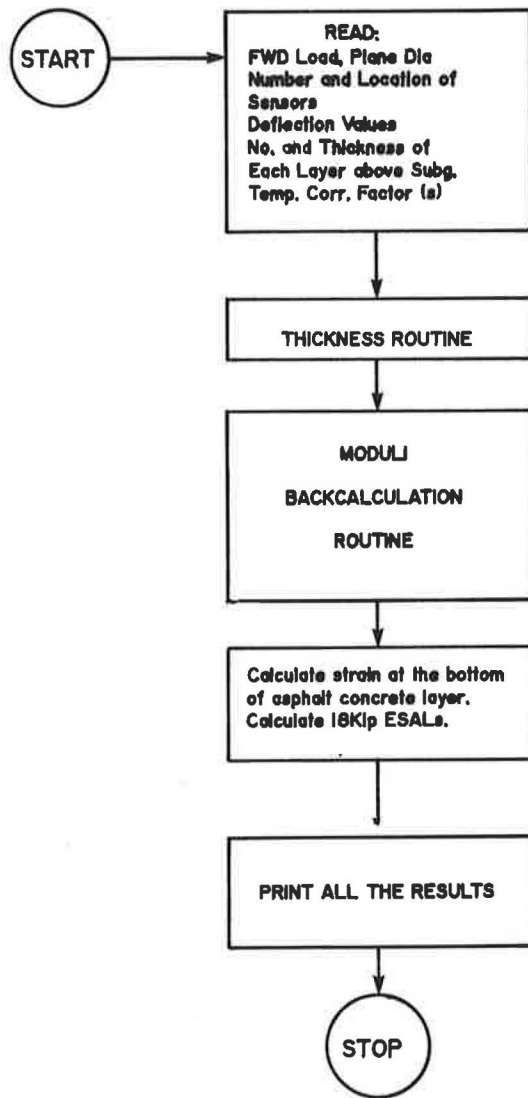


FIGURE 1 Flow chart of the analysis process.

**SPATIAL VARIABILITY OF FWD DEFLECTION DATA**

The estimated structural capacity of an existing pavement is affected by the spatial variability of the measured deflections. This variability is the result of equipment repeatability and spatial characteristics of the pavement structure and materials. Mamlouk et al. (1) concluded that equipment variability is insignificant compared with spatial variability. In this section, the spatial variability of FWD deflection data along a 90-ft section of 13 sites and along a 1-mi section of 3 sites is presented. The variation in sensor readings for the sites listed in Table 1 is presented in Table 3. The coefficients of variation for all the sensors varies from 2.80 percent to 41.7 percent for the 90-ft sections and 27 percent to 57 percent for the 1-mi sections. Variations of sensor readings are higher for the 1-mi section of the road than for the short road section. This spatial variability of deflection measurements reflects the variability of the structural response of the existing pavement sections and varying subgrade support along the roadway.

TABLE 3 Spatial Variability of Sensor Readings at Different Sites

Sensor	Mean Deflection (mils)	Standard Deviation (mils)	C.V. (%)	Average C.V. (%)
<b>Site 1</b>				
1	15.32	4.02	26.3	31.5
2	9.67	2.43	25.1	
3	4.92	1.25	25.5	
4	2.49	0.74	29.6	
5	1.44	0.51	35.4	
6	0.99	0.41	41.7	
7	0.70	0.26	36.9	
<b>Site 2</b>				
1	8.74	1.31	15.0	10.9
2	6.65	0.82	12.4	
3	4.74	0.47	9.90	
4	3.44	0.35	10.1	
5	2.63	0.24	9.20	
6	2.08	0.20	9.80	
7	1.70	0.17	9.90	
<b>Site 3</b>				
1	8.98	0.79	8.80	9.56
2	6.58	0.74	11.2	
3	4.64	0.49	10.60	
4	3.46	0.36	10.5	
5	2.69	0.25	9.40	
6	2.18	0.18	8.30	
7	1.80	0.15	8.10	
<b>Site 4</b>				
1	8.39	0.42	5.00	6.93
2	6.75	0.39	5.70	
3	5.10	0.29	5.60	
4	3.77	0.26	7.00	
5	2.74	0.17	6.20	
6	2.01	0.17	8.30	
7	1.45	0.16	10.7	
<b>Site 5</b>				
1	6.74	0.19	2.80	10.1
2	5.76	0.18	3.20	
3	4.48	0.25	5.60	
4	3.29	0.29	8.90	
5	2.33	0.28	12.1	
6	1.66	0.26	15.9	
7	1.11	0.25	22.2	
<b>Site 6</b>				
1	15.37	2.50	16.3	10.97
2	11.39	1.77	15.5	
3	7.62	0.93	12.2	
4	5.19	0.54	10.5	
5	3.73	0.28	7.40	
6	2.85	0.22	7.60	
7	2.34	0.17	7.30	
<b>Site 7</b>				
1	12.16	0.45	3.70	7.4
2	9.08	0.32	3.50	
3	5.96	0.21	3.50	
4	3.67	0.17	4.70	
5	2.25	0.15	6.70	
6	1.44	0.17	11.7	
7	0.98	0.18	18.1	

(continued on next page)

TABLE 3 (continued)

Sensor	Mean Deflection (mils)	Standard Deviation (mils)	C.V. (%)	Average C.V. (%)
Site 8				
1	18.93	6.13	32.4	18.9
2	13.71	3.23	23.5	
3	8.09	1.22	15.1	
4	4.96	0.71	14.4	
5	3.22	0.39	12.1	
6	2.36	0.38	16.2	
7	1.80	0.33	18.5	
Site 9				
1	16.96	1.40	8.20	7.5
2	11.23	0.70	6.20	
3	6.20	0.29	4.70	
4	3.32	0.13	3.90	
5	1.91	0.16	8.20	
6	1.31	0.10	7.90	
7	0.98	0.13	13.7	
Site 10				
1	26.70	6.14	23.0	12.5
2	6.31	1.34	21.2	
3	2.01	0.23	11.6	
4	1.18	0.10	8.90	
5	0.92	0.07	8.10	
6	0.72	0.05	7.60	
7	0.57	0.04	7.00	
Site 11				
1	13.98	1.62	11.6	11.1
2	6.47	0.76	11.7	
3	2.35	0.40	17.0	
4	1.25	0.16	13.1	
5	0.92	0.08	8.20	
6	0.74	0.07	8.70	
7	0.61	0.05	7.40	
Site 12				
1	18.29	1.66	9.10	11.2
2	13.31	1.29	9.70	
3	8.57	0.91	10.6	
4	5.45	0.61	11.2	
5	3.52	0.41	11.7	
6	2.54	0.31	12.2	
7	2.00	0.275	13.7	
Site 13				
1	12.28	2.00	16.2	13.84
2	6.91	1.09	15.8	
3	3.05	0.52	16.9	
4	1.48	0.23	15.3	
5	0.91	0.11	11.9	
6	0.68	0.07	10.4	
7	0.55	0.06	10.4	
Site 14				
1	9.56	2.84	29.7	35.44
2	6.81	2.17	31.8	
3	3.61	1.22	33.7	
4	1.99	0.70	34.9	
5	1.19	0.46	38.3	
6	0.82	0.31	38.1	
7	0.58	0.24	41.6	

TABLE 3 (continued)

Sensor	Mean Deflection (mils)	Standard Deviation (mils)	C.V. (%)	Average C.V. (%)
Site 15				
1	6.62	2.54	38.4	49.30
2	4.62	2.00	43.3	
3	2.57	1.30	50.6	
4	1.48	0.83	56.0	
5	0.94	0.54	57.0	
6	0.68	0.35	52.0	
7	0.52	0.25	47.6	
Site 16				
1	13.71	3.64	26.6	32.20
2	5.01	1.42	28.3	
3	2.33	0.76	32.5	
4	1.47	0.48	32.5	
5	1.10	0.37	33.6	
6	0.88	0.32	36.4	
7	0.72	0.26	35.5	

As shown in Table 4, spatial variability for different sites was compared with several factors, including surface condition expressed in terms of percent cracking, coefficients of variation of backcalculated asphalt concrete moduli over the section, and calculated theoretical number of 18-kip ESALs the sections can carry before fatigue failure.

The percent of cracking data was extracted from the ADOT pavement management system inventory data base. These crack data are for 1,000 ft<sup>2</sup> at the milepost location and not for the entire pavement area. The validity of these data with respect to the pavement condition at the point where the deflection measurements were made is questionable. Variability in deflection measurements over a section of the road cannot be explained by the distress condition on the surface only and may depend on the other factors, such as subgrade type and moisture content and properties of other layers.

Because the deflection measurements were used to compute moduli and subsequently the number of allowable applications, variability in deflection measurements produced variability in the computed parameters. However, as shown in Table 4, the variability of the computed parameters actually increased at each step in the process. In every case, the coefficient of variability of the asphalt modulus was greater than for the measured deflections. The coefficient of variability of the computed allowable axle loads was greater than the variability in the moduli values.

#### EFFECT OF VARIATION IN LAYER MODULI ON STRUCTURAL CAPACITY

The variability in the backcalculated layer moduli affects the estimated structural capacity. In order to study and quantify the effect of layer moduli on the estimated structural capacity, the factorial design shown in Figure 2 with the levels of layer moduli presented in Table 5 was analyzed. Five levels of AC (surface), AB (aggregate base), and SM (select material/sub-base) modulus were selected for each of the three predefined pavement categories: weak, medium, and stiff. Figure 3 shows

**TABLE 4 Comparison of Spatial Variability of Measured Deflections with Estimated Structural Capacity**

Base Type	Average Cracking (%)	Avg. C.V. All Sensors (%)	Avg. C.V. EAC (%)	Avg. C.V. Calculated N18 (%)
AB	2.40	12.2	28.0	69.7
AB (long span)	20.3	39.0	22.3	57.7
HB	0.25	15.6	31.0	56.4
BTB	0.00	10.2	20.0	47.3
CTB	0.00	9.00	31.0	60.4

Note: AC: Asphalt Concrete, HB: HMAC Base, BTB: Bituminous Treated Base, CTB: Cement Treated Base, AB: Aggregate Base

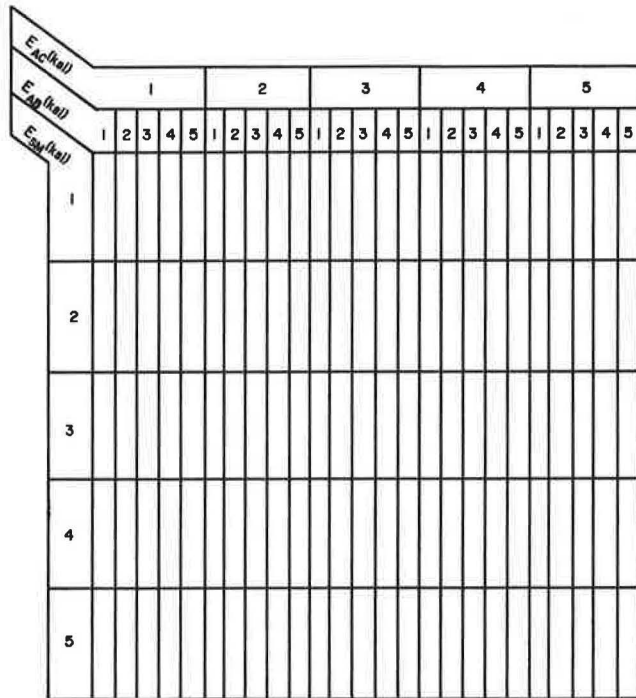


**FIGURE 2 Factorial to study the effect of layer moduli on the structural capacity of the pavements.**

the cross-section for each type of pavement. The CHEVRON program (4,5) was run for each of the  $3 \times 5^3 = 625$  pavements. Tensile strain at the bottom of the asphalt concrete layer was calculated for a 9,000-lb wheel load and 100 psi tire pressure.

The tensile strain was substituted in Equation 1 to estimate the number of 18-kip ESALs the pavement can carry before fatigue failure. The correlation coefficients between layer moduli and 18-kip ESAL for weak, medium, and stiff pavements were developed. Significance of correlations were evaluated with the Student's *t*-tests. The moduli for all the layers are significantly correlated with the estimated 18-kip ESALs for each pavement type. The correlation coefficients are higher than 0.5 for the AC and AB layers. For the weak pavement, the AB modulus appears to have a stronger effect than the AC modulus on the calculated 18-kip ESALs, whereas for medium and stiff pavement, the AC modulus appears to affect the calculation of 18-kip ESALs more than any other layer

moduli. To study the effect of interaction of layer moduli, the factorial in Figure 4 was developed for medium stiff pavement.

The following model was proposed for the analysis of variance (ANOVA) to describe the variation in calculated 18-kip ESALs:

$$\begin{aligned}
 N18_{ijk} = & \mu + ACE_i + ABE_j + SME_k \\
 & + ACEABE_{ij} + ACESME_{ik} \\
 & + ABESME_{jk} + ACEABESME_{ijk} \\
 & + \varepsilon_{(ijk)}
 \end{aligned} \tag{2}$$

$$i = 1, \dots, 3$$

$$j = 1, \dots, 3$$

$$k = 1, \dots, 3$$

where

$N18_{ijk}$  = theoretical 18-kip ESALs calculated at *i*th level of AC modulus, *j*th level of AB modulus, and *k*th level of SM modulus;

$\mu$  = overall mean;

$ACE_i$  = effect of *i*th level of (fixed) treatment AC modulus;

$ABE_j$  = effect of *j*th level of (fixed) treatment AB modulus;

$SME_k$  = effect of *k*th level of (fixed) treatment AB modulus;

$ACEABE_{ij}$  = interaction effect between *i*th level of AC modulus and *j*th level of AB modulus;

$ACESME_{ik}$  = interaction effect between *i*th level of AC modulus and *k*th level of SM modulus;

$ABESME_{jk}$  = interaction effect between *j*th level of AB modulus and *k*th level of SM modulus;

$ACEABESME_{(ijk)}$  = interaction effect between *i*th level of AC modulus, *j*th level of AB modulus, and *k*th level of SM modulus; and

$\varepsilon_{(ijk)}$  = random within error.  $\varepsilon_{(ijk)}$  is assumed to be normally and independently distributed with mean zero and variance  $\sigma^2$ .

TABLE 5 Levels of Layer Moduli Used to Study Modulus Variability Effect

Pavement Type	Layer Type	Modulus (ksi) at Level				
		1	2	3	4	5
STIFF	AC	325	488	650	819	975
	AB	20	30	40	50	60
	SM	12.5	19	25	32.5	37.5
MEDIUM	AC	225	337.5	450	562.5	675
	AB	15	22.5	30	37.5	35
	SM	10	15	20	25	30
WEAK	AC	125	187.5	250	312.5	375
	AB	10	15	20	25	30
	SM	5	7.5	10	12.5	15

Note: AC: Asphalt Concrete, AB: Aggregate Base, SM: Select Material

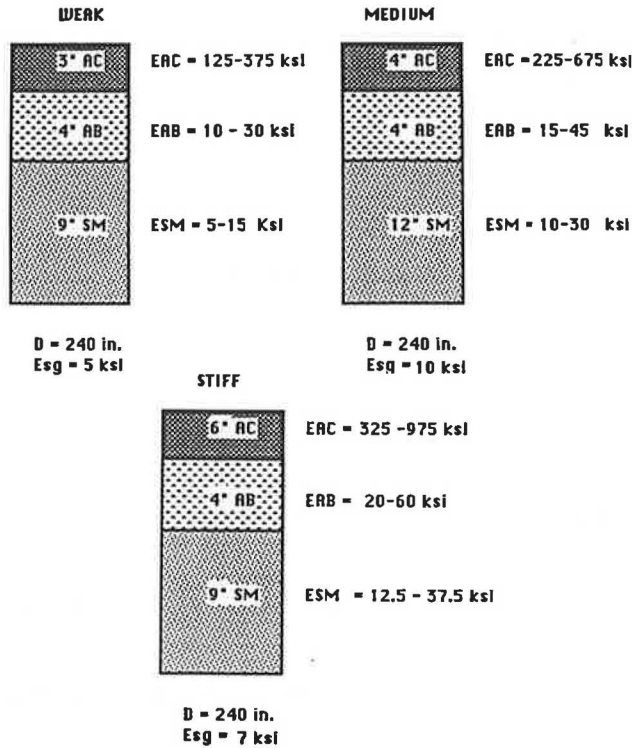


FIGURE 3 Cross-sections for different pavement types.

It is important to note that in Equation 2 the subscripts for *ACEABESME* and  $\epsilon$  are the same, indicating the effects due to interaction of all the layer moduli and the error are confounded. This is necessary because of absence of any replication.

From the ANOVA all the main factors or layer moduli and two factor interactions (or interaction between two layer moduli) were significant at 5 percent. The three-way interaction among layer moduli, which was used as the error term, might be significant. Thus the model described in Equation 2 is not adequate to capture all the variation. However, physical interpretation of response of the flexible pavement system to the applied load also supports the assertion that not only the layer moduli but also the interactions between the layer moduli dictate the structural response of a multilayer system. The precision needed for resilient moduli test of pavement materials to determine the effect of test variance on estimated structural capacity should be examined in further research.

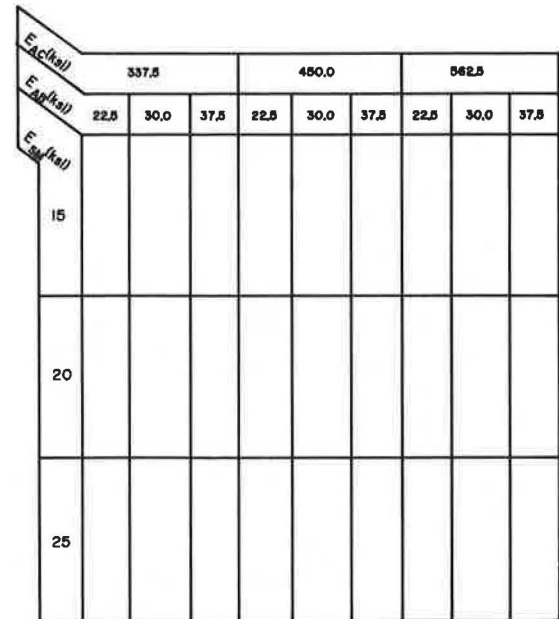


FIGURE 4 Factorial for medium stiff pavement.

In the backcalculation of layer moduli variation in estimated layer modulus from actual values is compensated by the variations in the moduli of other layers in the structure, providing a compensating effect. The resultant capacity of the pavement system with backcalculated layer moduli remains essentially unchanged (5). The significant interactions of layer moduli in the ANOVA analysis supports the compensating effect concept in the backcalculation analysis.

### SPATIAL VARIABILITY OF BACKCALCULATED LAYER MODULI

Deflection data from each station of the sites listed in Table 1 were analyzed to define the spatial variability of the backcalculated layer moduli. The mean, standard deviation, and coefficient of variation of the layer moduli are presented in Table 6. The average coefficient of variation for layer moduli for the short-span sections varies from 15 percent to 46 percent with a mean value of 29 percent. The average coefficient of variation for layer moduli for three sites with ten deflection

**TABLE 6 Spatial Variability of Backcalculated Layer Moduli**

Site	Layer	Mean (ksi)	St. Dev. (ksi)	C.V. (%)	Avg. CV (%)	Range	
						Min.	Max.
1	AC	155	79.5	50		110	343
	BS	66	10.5	16		60	87
	AB	24	11.8	49	29	10	38
	SM	11	1.3	12		10	14
	SG	14	2.4	16		12	19
2	AC	200	51.5	26		125	253
	BTB	205	83	40	35	152	433
	SM	21	10.9	51		10	46
	SG	19	4	21		12	23
3	AC	217	28.3	13		186	274
	BTB	189	14.3	7.5	15	171	224
	SM	37	10.8	29		13	46
	SG	19	1.8	9		17	23
4	AC	389	60	15		362	516
	CTB	438	143	33	15	254	692
	SM	29	1.4	5		27	31
	SG	12	0.81	7		11	13
5	AC	349	52	15		287	390
	AB	65	2.7	41	18	61	69
	SM	34	3.0	9		27	38
	SG	14	1.1	7.5		13	15
6	AC	142	65	46		64	271
	CTB	87	67	76	46	60	275
	SM	13	5	42		10	24
	SG	13	3	20		10	14
7	AC	419	11	31		402	436
	BS	101	21	20	19	77	125
	SM	17	2.0	12		15	20
	SG	13	1.4	14		10	15
8	AC	180	100	56		41	302
	AB	38	13	34	32	12	48
	SM	15	4	25		10	23
	SG	9	1.2	14		7	10
9	AC	237	56	23	23	126	309
	AB	32	14	45		17	58
	SM	14	2.5	18		12	18
	SG	14	0.8	6		13	16
10	AC	265	23	9		233	279
	BS	270	38	14		230	358
	SM	12	6	50	24	10	27
	SG	48	10	21		32	60
11	AC	227	38	17		181	307
	AB	66	25	38	29	33	96
	SM	26	11	42		15	52
	SG	47	9	18		31	60
12	AC	199	63	32		141	332
	BS	60	25	42		20	94
	AB	18	13	74	43	10	41
	SM	15	7	44		10	24
	SG	12	3	25		9	16
13	AC	88	26	30		54	125
	AB	31	18	58	45	10	56
	SM	22	13	60		10	55
	SG	44	14	32		26	60
14	AC	1028*	194	19		814	1371
	AB	80	13	16	22	62	1002
	SM	41	17	42		10	78
	SG	32	13	40		19	60
15	AC	1229*	160	13		1059	1523
	AB	77	8	10	22	56	85
	SM	28	15	54		10	48
	SG	24	2.5	10		21	26
16	AC	232*	82	35		175	423
	AB	49	20	40	34	30	915
	SM	38	15	39		22	72
	SG	37	7	20		29	53

\* Modulus was not corrected due to very high correction factor

Note: AC: Asphalt Concrete, BS: Bituminous Surface, BTB: Bituminous Treated Base, CTB: Cement Treated Base, AB: Aggregate Base, SM: Select Material

tests per mile varies from 22 percent to 34 percent with a mean value of 28 percent. Interestingly the average coefficients of variation for the two data sets are almost equal.

The average coefficient of variation of the AC modulus for nine sites is 28 percent, whereas for the base modulus the average coefficient of variation is 36 percent. These variations strongly affect the structural capacity determined from fatigue analysis. The interaction of high asphalt concrete modulus and base modulus tends to produce low asphalt concrete tensile strain and consequently a high number of 18-kip ESAL applications. The opposite is true for the interaction of low asphalt concrete modulus and low base modulus. As a result, the computed structural capacity is highly variable.

Table 7 compares average coefficient of variation of layer moduli to the estimated structural capacity for the 1-mi section sites listed in Table 1. Variation of asphalt concrete and base moduli is highly magnified in the calculation of structural capacity.

It is to be noted that there are inherent sources of errors in the backcalculation of the moduli itself. Layer thicknesses are variable and sometimes spatially unknown, as are depths to effective rigid layers. Both affect the relative magnitudes of the backcalculated layer moduli. However, in this analysis, actual layer thicknesses determined from the cores were used and the depths to rigid layer were estimated (6).

#### EFFECT OF TESTING FREQUENCY ON ESTIMATED STRUCTURAL CAPACITY

Researchers differ on the issue of required number of FWD tests needed for structural characterization of existing pavements. The AASHTO Guide for the Design of Pavement Structures (7) recommends a spacing of 300 to 500 ft when accurate historic data for a section are unavailable. When accurate historic data are available, the guide recommends 10 to 15 test points per mile. No analysis was presented in the guide to support this recommendation. ARE Inc. (8) recommended dynaflect tests every 100 ft when the subgrade is nonuniform. For uniform subgrade, the spacing can be extended to 250 ft. Karan et al. (9) used a spacing of 6 deflection tests per kilometer (roughly 10 per mile). Koole (10) proposed a spacing of 66 ft for an overlay design method. ADOT studied the variability of dynaflect deflection data and concluded that one measurement per mile is required for network level pavement management system (11). Shell Research (12) recommends one FWD test per 85 to 165 ft. Lytton et al. (13) concluded that a minimum of 5 tests per mile is required at the network level to rank pavement sections. Project level evaluation requires one test every 100 to 300 ft in each wheel path.

**TABLE 7 Effect of Variation of Backcalculated Layer Moduli on Estimated Structural Capacity**

Site	Average Coefficient of Variation (%)				
	EAC	EAB	ESM	ESG	N18
14	13	10	54	10	23
15	19	16	42	40	44
16	35	40	39	20	106

#### Effect of Testing Frequency Over a Short Section

Of the projects listed in Table 1, FWD data collected on 9 projects were analyzed to determine the effect of the number of FWD tests over a 90-ft section of the pavement. The number of tests were sorted in the following fixed fashion.

Number of Tests	Location
10	Beginning of project and 10-ft intervals
5	Beginning of project and 20-ft intervals
3	Beginning of project and 30-ft intervals
1	Beginning of project

It was assumed that 10 FWD tests per 90 ft represented the standard or truth for this particular experiment. It was also inherently assumed that the samples were a random selection from the population of pavements.

The backcalculated asphalt concrete modulus (EAC) and the structural capacity in terms of estimated number of 18-kip ESALs (N18) the sections can carry were selected as the response parameters. Table 8 summarizes the mean, pooled standard deviation, and coefficient of variation for the above parameters for each sample size.

The size of the coefficients of variation for the backcalculated asphalt concrete moduli is much smaller than anticipated. Linear regressions were conducted between the mean 18-kip ESALs derived by taking different sample sizes. The coefficient of determination  $R^2$  for the linear regression between estimated 18-kip ESALs from one test per 90 ft and average estimated 18-kip ESALs from ten tests per 90 ft was 0.94. It appears that estimated 18-kip ESALs from 1 FWD test per 90 ft closely approximate the average of estimated 18-kip ESALs from 10 tests per 90 ft.

The assumed linear relationship between backcalculated asphalt concrete modulus and 18-kip ESALs from one FWD test per 90 ft and from ten FWD tests per mile was verified by the ANOVA. The relationship appeared to be significant at a 5 percent level of significance. In addition, paired  $t$ -tests were conducted between the values of this parameter from 1 test per 90 ft and 10 tests per 90 ft. No significant difference was detected at a 5 percent level of significance. It appears

**TABLE 8 Summary Statistics of Backcalculated AC Modulus and Structural Capacity Corresponding to Different Testing Frequency**

No. of Tests per Site	EAC (ksi)	N18 (millions)
Mean		
10	222	41.7
5	221	42.8
3	212	42.9
1	234	42.4
Pooled Standard Deviation of Group		
10	48.3	65.2
5	57.2	17.0
3	55.4	21.8
Coefficient of Variation		
10	21.7	156.3
5	25.9	39.70
3	26.1	50.80

NOTE:  $N = 9$ .

that the number of tests does not affect the estimated structural capacity for a short section of the pavement (up to 90 ft).

### Effect of Testing Frequency Over a Long Section

FWD deflection measurements were taken at the beginning of the project and at nine locations at a uniform interval of 0.1 mi for Sites 14 through 16 listed in Table 1. To determine the effect of testing frequency, 7, 5, and 3 tests were randomly selected out of 10 tests. The current ADOT practice is to take three tests per mile for overlay design.

The FWD data were used to backcalculate the layer moduli and estimate the number of 18-kip ESALs based on fatigue criteria. Table 9 shows the mean, standard deviation, and coefficient of variation of the number of 18-kip ESALs (N18) for the three sites for each random selection. The coefficient of variation is nearly equal for seven and five tests per mile. However, for three tests per mile the variation is high.

It is apparent that the Kolmogorov-Smirnov (K-S) (14) test verified that the data were normally distributed. Student's *t*-tests were conducted to detect the difference in means of 18-kip ESALs calculated at each site corresponding to different testing frequency. No significant difference was detected between means of 18-kip ESALs calculated from 10, 7, 5, or 3 tests. It may be noted that because of the high standard deviation associated with each mean, the pooled standard deviation during the *t*-tests was also high. This high standard deviation was responsible for the low *t*-statistic during mean testing.

The results of the *t*-test suggest that 3 tests per mile are as good as 10 tests per mile to characterize the pavement structurally. However, the coefficients of variation of 18-kip ESALs for three tests per mile appeared to fluctuate widely compared with those for five tests per mile. Student's *t*-tests were also conducted between means of 18-kip ESALs from seven, five, and three tests per mile. Significant difference was observed between means of 18-kip ESALs computed from five and three test results for a single run for Site 15. However, in two other runs for Site 15, no difference was detected.

Results suggest that 18-kip ESALs estimated from five tests per mile would be a viable choice for a project level decision on structural capacity estimation for the existing pavements. The failure of the Student's *t*-test to detect a statistically significant difference between three and five tests per mile is due to the variability associated with three tests per mile. Hence, this level of testing was rejected in favor of five tests per mile. However, FWD data collected on a larger number of sections should be analyzed to further support or reject this conclusion. Other statistical methods can also be employed in the data analysis.

### CONCLUSIONS

In this paper the variability of the structural capacity determination by the mechanistic-empirical method was presented with respect to FWD input deflection data in the backcalculation scheme, backcalculated layer moduli, and the number of FWD tests over a section of the road.

As can be expected, sensor readings on a longer section of the road show more variability than on a shorter section. This variability in sensor readings was magnified when the layer moduli were backcalculated (i.e., small variability in sensor data over a section of a pavement would result in high variability of calculated layer moduli). However, this variability was independent of the length of the section of the roadway over which deflection testing was done.

All the layer moduli and their interaction affect the calculated structural capacity. The variation in backcalculated layer moduli was magnified when the number of 18-kip ESALs the pavement can carry before fatigue failure was estimated. Interaction of high asphalt concrete modulus and base modulus tends to produce low asphalt concrete strain and consequently a high number of 18-kip ESAL applications. The opposite is true for interaction of low asphalt concrete modulus and base modulus. As a result, the computed structural capacity becomes highly variable, especially when the number of tests done on a long section of the pavement is small.

TABLE 9 Effect of Testing Frequency on Variation of Structural Capacity

Site	No. of Tests/Mile	N18 (millions)								
		X	Run 1 $\sigma$	CV (%)	X	Run 2 $\sigma$	CV (%)	X	Run 3 $\sigma$	CV (%)
14	10	1862	810	44	1862	810	44	1862	810	44
	7	1858	805	43	2180	686	32	2179	688	32
	5	2184	826	38	2126	904	43	1598	696	44
	3	1574	1155	73	2729	184	7	2061	1008	49
15	10	1197	275	23	1197	275	23	1197	275	23
	7	1170	292	25	1159	300	26	1232	306	25
	5	1008	195	19	1205	332	28	1166	300	26
	3	1460	134	9	1450	145	10	1283	408	32
16	10	18	19	106	18	19	106	18	19	106
	7	18	23	128	18	23	128	17	23	135
	5	26	25	96	15	8	53	10	5	50
	3	31	33	107	8	3	38	13	5	39

The frequency of testing did not affect the estimated 18-kip ESALs over a short section of the pavement. However, for long sections it affects the mean estimated 18-kip ESALs. For a mile-long section, five FWD tests were found to be a viable choice for estimation of 18-kip ESALs. However, the coefficient of variation of estimated 18-kip ESALs over a long section may or may not decrease with an increasing number of tests.

#### ACKNOWLEDGMENTS

The authors wish to acknowledge the financial support for this study provided by the ADOT's Arizona Transportation Research Center. The computing facilities were provided by Arizona State University. Thanks are due to Larry Scofield and John Eisenberg of ADOT and Dwayne Rollier and Rohan Perera of Arizona State University for their help in this study.

#### REFERENCES

1. M. S. Mamlouk, W. N. Houston, S. L. Houston, and J.P. Zaniewski. *Rational Characterization of Pavement Structures Using Deflection Analysis*. Report FHWA-AZ88-254, Vol. 1. Arizona Department of Transportation, Phoenix, 1988.
2. A. S. M. M. Hossain. *Deflection Analysis of Flexible Pavements Using Nondestructive Test Data*. Ph.D. dissertation. Department of Civil Engineering, Arizona State University, Tempe, July 1990.
3. L. J. Painter. *CHEVRON N-layer—Program Improved Accuracy*. California Research Corporation, Richmond, Calif., 1980.
4. J. Michelow. *Analysis of Stresses and Displacements in an N-layered Elastic System Under a Uniformly Distributed Load On a Circular Area*. California Research Corporation, Richmond, Calif., 1963.
5. F. W. Jung. Interpretation of Deflection Basin for Real-World Layer Materials of Flexible Pavements. Presented at 69th Annual Meeting of the Transportation Research Board, Washington, D.C., 1990.
6. A. S. M. M. Hossain and J. P. Zaniewski. Detection and Determination of Depth of Rigid Bottom from Falling Weight Deflectometer Data. In *Transportation Research Record 1293*, TRB, National Research Council, Washington, D.C., 1991.
7. *Guide for Design of Pavement Structures*. AASHTO, Washington, D.C., 1986.
8. ARE Inc. *Asphalt Concrete Overlays of Flexible Pavements*, Report FHWA A-RD-75-76, Vol. II. FHWA, U.S. Department of Transportation, June 1976.
9. M. A. Karan, R. Haas, and T. Walker. Illustration of Pavement Management: From Data Inventory to Priority Analysis. In *Transportation Research Record 814*, TRB, National Research Council, Washington, D.C., 1981.
10. R. C. Koole. Overlay Design Based on Falling Weight Deflectometer Measurements. In *Transportation Research Record 700*, TRB, National Research Council, Washington, D.C., 1979.
11. G. B. Way, J. F. Eisenberg, and J. P. Delton. *Arizona's Pavement Management System, Phase II: Analysis of Testing Frequency for Pavement Evaluation*, Report FHWA/AZ-81/169-1. FHWA, U.S. Department of Transportation.
12. A. I. M. Classen and R. Ditmarsch. Pavement Evaluation and Overlay Design. *Proc., 4th International Conference on Structural Design of Asphalt Pavements*, Vol. 1, University of Michigan, Ann Arbor, 1977, pp. 649-661.
13. R. L. Lytton, F. L. Roberts, and S. Stoffels. *NCHRP Report 327: Determining Asphaltic Concrete Pavement Structural Properties by Nondestructive Testing*. TRB, National Research Council, Washington, D.C., Feb. 1990, 105 pp.
14. D. C. Montgomery. *Design and Analysis of Experiments*, 2nd ed. John Wiley and Sons, New York, N.Y., 1984.

---

*Publication of this paper sponsored by Committee on Strength and Deformation Characteristics of Pavement Sections.*

# Comprehensive Evaluation of Five Sensors Used To Measure Pavement Deflection

VIVEK TANDON AND SOHEIL NAZARIAN

The results of a comprehensive evaluation of five sensors used in pavement instrumentation are discussed. These five sensors are velocity transducer (geophone), accelerometer, linear variable differential transformer, laser optocator, and proximeter probe. The sensors were selected because of their commercial availability and their potential effectiveness in deflection measurement. The main two parameters studied were the accuracy and precision of each sensor. These parameters were studied in a laboratory environment to minimize the effects of uncertainties that may affect the results. Various impact shapes and duration were investigated. The magnitude of deflection was also varied over a wide range. In addition, factors such as cost and field-worthiness were also considered. It was found that for pavement evaluation, geophones appear to be the optimum sensors. Geophones, if used properly, will provide adequate accuracy and precision at minimal cost.

The use of mechanistic pavement design methodologies is increasingly emphasized. To successfully implement these methodologies, the response of pavement to applied loads should be accurately determined. Among the major response parameters to be considered are the deflections, deformations, and strains within the pavement system.

The state-of-practice in determining these parameters is the employment of deflection-based nondestructive testing (NDT) devices. Unfortunately, because of inherent theoretical and experimental problems with the NDT methods, the levels of accuracy and precision with which displacements and strains within the pavement are measured are not known.

To determine these uncertainties, pavements are typically instrumented. Three of the most popular sensors are linear variable differential transformers (LVDTs), velocity transducers (geophones), and accelerometers. Two other promising sensors are the laser devices and the noncontact proximeter probes. The limitations and advantages of these sensors as applied to pavement instrumentation are not well known.

The results of a comprehensive study conducted to determine the suitability and accuracy of these sensors are discussed here. The working principles and specifications of each sensor are discussed. The setup used for evaluating the precision and accuracy of different sensors and the evaluation process involved in determining the most suitable sensor are described. Finally, based on this evaluation process, the most appropriate sensor is selected.

## DESCRIPTION OF SENSORS

The nature, specifications, and accuracy of each sensor are extensively reported elsewhere by Tandon and Nazarian (1). A brief description of each sensor is presented next.

### Accelerometers

Accelerometers are important vibration measurement sensors that are available in wide ranges of sizes and response characteristics. As shown in Figure 1a, accelerometers use a sensing mechanism to measure the acceleration that acts upon a mass. Under a dynamic motion, the mass is accelerated at a certain rate as a result of force exerted on the spring. Because the spring deflection is proportional to the force applied to the mass and the force is proportional to the acceleration of the mass, the spring deflection is a measure of acceleration.

There are several advantages to the use of accelerometers. Piezoelectric accelerometers generate large output-voltage signals, are compact, and possess high natural frequencies. These properties make an accelerometer a good tool for accurate shock and vibration measurements.

There are also disadvantages associated with accelerometers, however. Piezoelectric accelerometers are not reliable at low frequencies. The lowest frequency that can be accurately measured with an accelerometer depends on the value of discharge time constant ( $I$ ).

### Linear Variable Differential Transformers

LVDTs use the principle of change in magnetic coupling (or reluctance) to determine deflection. Basically, an LVDT consists of a case and a core (Figure 1b). The case of an LVDT contains three coils: one primary and two secondary. The basic function of secondary coils is to produce opposing voltages. When the core is in a neutral or zero position the voltages induced in the secondary windings are equal and the net output is zero. The output voltage will be nonzero when the core is moved. The output voltage will be positive or negative depending on the relative position of the case and the core rod.

As the core rod penetrates farther into the core, magnetic coupling between the primary and one of the secondary coils increases; meanwhile the coupling between the primary and the other secondary coil decreases. Therefore, the net voltage increases as the core is moved away from the neutral position.

The advantages of the LVDT are several. There is no physical contact between the case and the core; thus there is no

V. Tandon, Pennsylvania State University, Department of Civil Engineering, University Park, Pa. 16802. S. Nazarian, University of Texas at El Paso, Department of Civil Engineering, El Paso, Tex. 79968-0516.

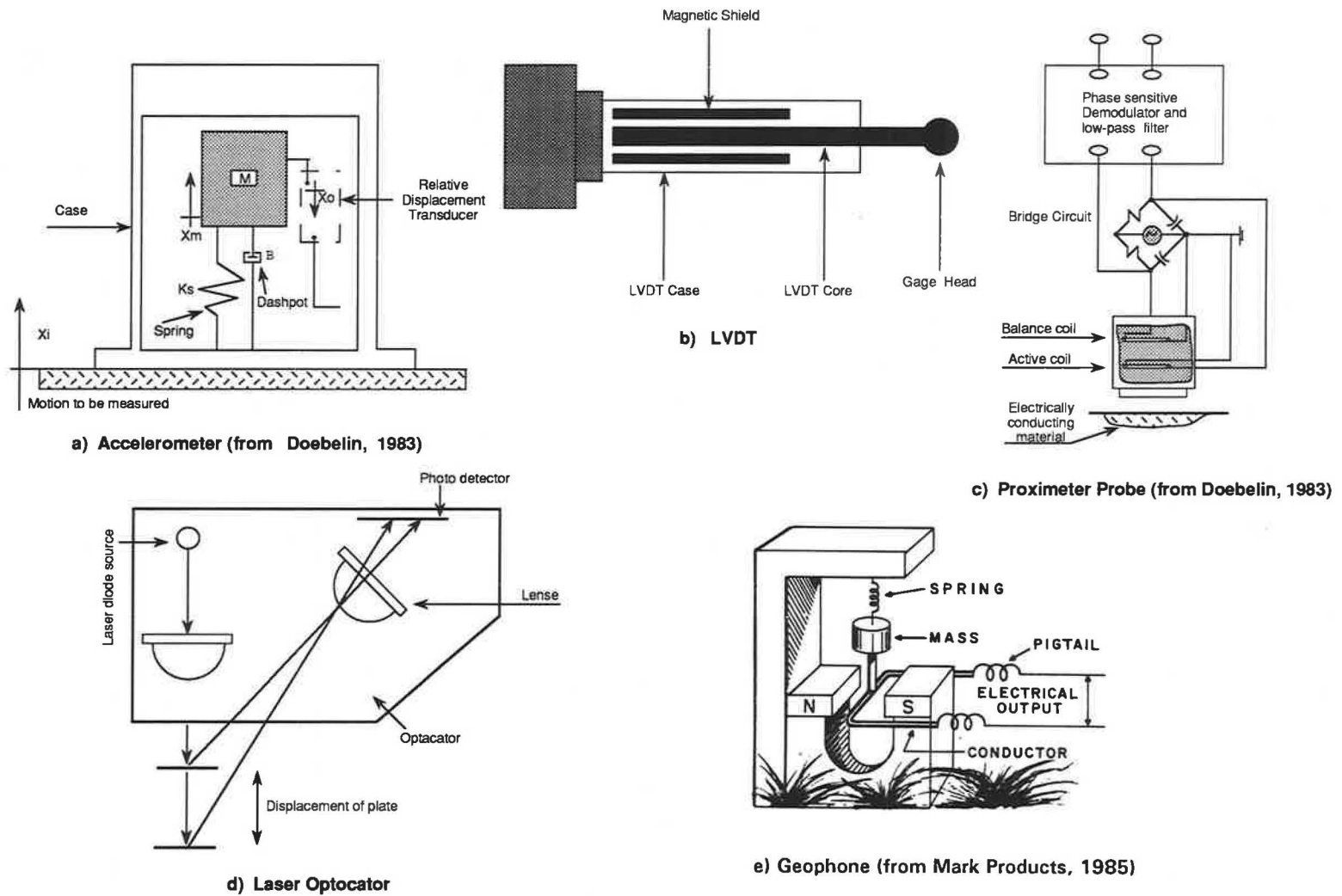


FIGURE 1 Schematic of sensors used.

friction or wear. As a result of the introduction of DC-DC circuitry, LVDTs have become highly sensitive and extremely rugged at the expense of reduced reliability.

There are also several disadvantages associated with the LVDT setup. Dynamic response of an LVDT is limited. Therefore, motions with high frequency contents cannot be detected by an LVDT. There are small radial and longitudinal magnetic forces in the core if it is not centered radially and at the null position, which results in less reliability of measured deflection. The use of LVDTs in the field is difficult and expensive. The output of the LVDT is linear only in a certain range, near the neutral position of the core. Therefore, the LVDT should be mounted such that the core is positioned near the neutral position.

### Proximeter Probes

Proximeter probes are noncontact inductive displacement transducers. Generally, the transducer system consists of a proximeter, a probe, and an extension cable (Figure 1c).

The proximeter performs two functions within the transducer system. The first is to generate a high-frequency signal and transmit the signal to the probe tip. The second is to receive the signal from the probe tip and process it to produce a DC output proportional to the displacement of the material being observed.

Major advantages of proximeters are as follows. Proximeter output can be read easily with any type of DC voltmeter. Application of high frequency radio signals yields a higher signal-to-noise ratio because more energy is transferred in less time, which immunizes the system from noise. The probe can be connected to the proximeter with a long cable; therefore the probe can be conveniently located near the (conductive) target material.

There are, however, some drawbacks associated with proximeters. The calibration of a proximeter varies based on the target material used. The input voltage must also be constant and equal to the input voltage supply used when calibrating the proximeter. Proximeters can measure deflections accurately only if the probe is in the close vicinity of the target (within 2 mm). As such, the chances of damaging the probe as a result of a sudden increase in the deflection of the target material is high. It is not always easy to maintain a 2 mm gap between the target and probe under field conditions. It is also difficult to mount a proximeter perpendicular to the target in the field. For accurate measurement, the probe should be exactly perpendicular to the target; otherwise the deflection obtained may not be reliable.

### Laser Optocator

The laser optocator is a noncontact displacement transducer. As shown in Figure 1d, it consists of a light source (either ultraviolet or infrared) and a photodetector (or light-sensitive transistor) to receive the reflected signal. A beam of light from the light source is aimed at the surface. The beam of light is reflected back and is focused on the photodetector through a lens. The photodetector sends a signal to the signal

processors according to the position of the focused beam on the photodetector.

The laser used in this study is an accurate deflection measuring tool. However, it is not a practical instrument, especially for field use. To avoid scatter of infrared laser rays, the observed target should be smooth, which is not characteristic of pavements. In addition, good resolution at very low deflections (about 1 mil) could not be obtained in this experiment.

### Velocity Transducers (Geophones)

Geophones are coil-magnet systems, as shown in Figure 1e. A mass is attached to a spring, and a coil is connected to the mass. The coil is located such that it crosses the magnetic field. An impact causes the magnet to move, but the mass remains more or less stationary, causing a relative motion between the coil and magnet. This relative motion generates voltage in the coil that is proportional to the relative velocity between the coil and magnet.

Geophones are small in size, light in weight, and inexpensive compared to other transducers. The output of a geophone can be connected to any recording device without using an amplifier. Geophones are rugged and can withstand both high and low temperatures.

### LABORATORY SETUP

In the setup for determining the accuracy and precision of deflections of all sensors, a thick concrete block was selected and leveled perfectly. Such a structure results in minimal differential movement among different components in the system. An exciter was kept between the two walls of the block. A circular aluminum plate, 8 in. in diameter, was screwed securely to the exciter. The geophones were rigidly fastened to the plate using a specially designed casing. An accelerometer was fastened to the top of the casing of each geophone. To place the LVDT and proximeter, a square aluminum plate was fastened to two beams connected rigidly to two steel plates (Figure 2a). The two steel plates were securely connected to the concrete. Two holes were bored in this aluminum plate for mounting the LVDT and proximeter. The LVDT was fixed to the top plate so that the gage head of the LVDT was touching the bottom plate attached to the shaker. Because the proximeter had been calibrated using 4140 steel as a target material, a small circular piece of 4140 was screwed in the lower plate, providing proper target material for the probe. The proximeter was also attached to the top plate in a similar manner as used for the LVDT, using an adjustable connector.

The second half portion of the bottom plate was reserved for the laser optocator. The laser required sufficient unobstructed area for sending and receiving laser beams. The laser was fixed to the top steel plate with the help of another vertical plate, as shown in Figure 2b.

The accuracy and precision of sensors were determined for four different waveforms (sine, half-sine, square, and triangular). Sine waves were generated using the HP 3562A analyzer; the other waveforms were generated using model 75

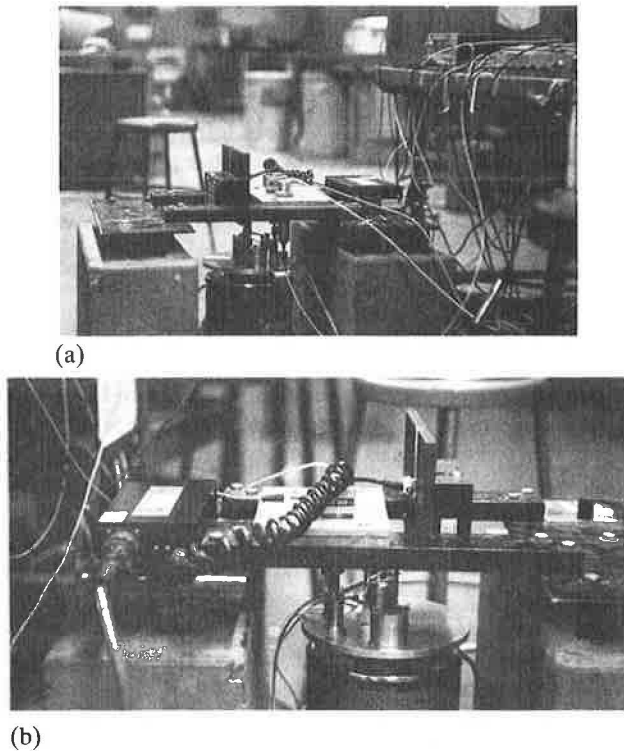


FIGURE 2 Experimental setup: (a) layout and (b) close-up.

Wavetek arbitrary waveform generator. The procedure used to obtain deflections is different for each device and each waveform. For an in-depth understanding of procedures used to determine deflections from each sensor, the reader may refer to other work by the authors (1).

### EVALUATION OF SENSORS

To evaluate fully the five candidate sensors, several parameters were considered. The parameters studied were amplitude of vibration, type of excitation, and frequency content of vibration. Tests were carried out in the laboratory environment so that these variables could be easily controlled.

The amplitude of vibration was varied from 1 to 25 mils. Such a broad range of amplitude was studied to ensure proper response of the sensors to small and large amplitudes. Small amplitudes of vibration allowed examination of the effects of background noise (signal-to-noise ratio) for each sensor. Tests at large vibration amplitudes were carried out to determine the range of usefulness of each sensor.

Different types of excitation were investigated to determine the versatility of each sensor for use with different types of NDT devices. The steady-state vibration and impulse (transient) motions were examined. Three types of impulses—half-sine, triangular, and square—were used. The steady-state vibration is used by several NDT devices such as the dynaflect and road rater. Falling weight deflectometers (FWDs) impart impulse, or transient, loads to pavements.

The effect of frequency content on the behavior of each sensor was also studied. For the steady-state tests, the frequency of vibration was varied between 5 and 100 Hz. The

lower frequency signifies the lower limit of operation of the shaker's amplifier. The amplifier cannot adequately amplify steady-state signals below 5 Hz. The upper frequency limit (100 Hz) is practically the highest frequency of interest in the deflection-based tests. For the impulse tests, the duration of impulse was varied from 12.5 to 175 msec, to cover the frequency ranges of interest in NDT methods.

### Steady-State Tests

Two series of tests were carried out using the steady-state vibration setup. The laser device was not used in the first series because it is expensive to rent the device. It was added to the testing sequence of the second series. Because of time limitations, the extent of deflection data collected with the laser device is relatively limited.

All combinations of frequency and amplitude evaluated in the steady-state tests are presented in Table 1. Typically, at each frequency measurements in the range of amplitudes of 1 to 25 mils were carried out. The amplitude of vibration was limited to about 20 to 25 mils. At a frequency of 100 Hz, displacements larger than 5 mils could not be generated because of the shaker's characteristics.

An example of data collected at each frequency and each amplitude is shown in Table 2. Two geophones (Geo 1 and Geo 2), two accelerometers (Acc 1 and Acc 2), an LVDT, and a proximeter (Prox) were used in all tests.

The recording device used in this experiment was a two-channel spectral analyzer. Therefore, only two devices could be compared at one time. To remove any bias in the data as a result of sequence of testing, deflections were compared in random order. This sequence is depicted in the second and third columns of Table 2. Each sensor was compared twice with the other five sensors. The actual deflections from each pair of sensors are reflected in the fourth and fifth columns of Table 2. The difference between the deflections of the two sensors was calculated and is presented in the sixth column.

The proximeter was selected as the reference sensor to facilitate the evaluation process. The proximeter sensors can

TABLE 1 Summary of Steady-State Tests

Frequency (Hz)	Approximate Deflection (mils)				
	1	5	10	18	25
5	1	5	10	18	25
10	1	5	10	18	25
15	5	8	10	15	18*
20	5	10	14	18*	22
30	5	15	18*	22	--
40	1	5	10	18*	22
50	1	5	10	18	25
75	1	5	10	18	--
100	1	5	--	--	--

Shaded Cells correspond to tests performed with and without laser device

\*Only tested when laser was present

**TABLE 2 Testing Sequence Used in Steady-State Deflection Measurements at Each Frequency and Amplitude (Without Laser Device)**

Frequency Used : 05 Hz			Source Level: 0.020 Volts		
File No.	Device Used		Deflection (mil)		Difference (percent) <sup>+</sup>
	Channel 1	Channel 2	Channel 1	Channel 2	
1	Acc 1	Geo 1	1.48	1.51	-1.75
3	Prox	Acc 2	1.53	1.53	-0.13
5	LVDT	Acc 2	1.49	1.51	-1.34
7	Geo 2	Geo 1	1.50	1.50	-0.07
9	Prox	Geo 2	1.53	1.49	2.71
11	LVDT	Acc 1	1.50	1.47	2.33
13	Prox	LVDT	1.53	1.49	2.61
15	LVDT	Acc 1	1.51	1.48	1.99
17	Acc 1	Geo 2	1.50	1.49	0.40
19	Prox	Geo 1	1.53	1.51	1.50
21	Acc 1	Geo 1	1.49	1.51	-1.34
23	LVDT	Prox	1.50	1.53	-2.00
25	Geo 2	Acc 1	1.52	1.51	0.66
27	Prox	Acc 1	1.54	1.49	3.12
29	Acc 1	Acc 2	1.48	1.52	-2.70
31	Acc 2	Prox	1.54	1.53	0.46
33	Prox	Geo 2	1.54	1.50	2.34
35	Acc 2	Geo 2	1.52	1.51	0.66
37	Acc 1	Prox	1.50	1.54	-2.40
39	LVDT	Geo 1	1.51	1.52	-0.93
41	Acc 2	Geo 1	1.56	1.53	1.99
43	LVDT	Acc 2	1.51	1.54	-1.99
45	Geo 2	Geo 1	1.53	1.52	0.33
47	Acc 2	Geo 2	1.54	1.51	2.21
49	Acc 1	Acc 2	1.50	1.53	-1.73
51	Acc 2	Geo 1	1.54	1.52	1.30
53	Prox	Geo 1	1.55	1.52	1.94
55	LVDT	Geo 2	1.52	1.51	0.59
57	LVDT	Geo 1	1.51	1.52	-0.93
59	Geo 2	LVDT	1.53	1.51	1.31

$$^+ \text{Difference} = \{ \text{Channel 1} - \text{Channel 2} \} * 100 / \text{Channel 1}$$

accurately measure small deflections in the laboratory environment because of their noncontact nature. An example of comparison of deflections obtained from the proximeter and other sensors is shown in Table 3 for the data presented in Table 2.

In the next step, the average, standard deviation, and variance of deflections were calculated for each sensor. As reflected in Table 2, each device was used 10 times for comparison purposes. As an example, the statistical information obtained from data in Table 2 is presented in Table 4. It can be seen that the average varies between 1.49 mils and 1.53 mils, about 0.04 mils difference, and the overall variance is less than 0.02 percent.

**TABLE 3 Accuracy Determined from Data in Table 2**

File No.	Device Used		Deflection (mil)		Difference (percent) <sup>+</sup>
	Channel 1	Channel 2	Channel 1	Channel 2	
3	Prox	Acc 2	1.53	1.53	-0.13
9	Prox	Geo 2	1.53	1.49	2.71
13	Prox	LVDT	1.53	1.49	2.61
19	Prox	Geo 1	1.53	1.51	1.50
23	LVDT	Prox	1.50	1.53	1.96
27	Prox	Acc 1	1.54	1.49	3.12
31	Acc 2	Prox	1.54	1.53	-0.46
33	Prox	Geo 2	1.54	1.50	2.34
37	Acc 1	Prox	1.50	1.54	2.34
53	Prox	Geo 1	1.55	1.52	1.94

$$^+ \text{Difference} = \{ (\text{Prox. defl.}) - (\text{Other Device defl.}) \} * 100 / (\text{Prox. defl.})$$

A laser device was added to the second series of tests. The laser device was rented for 2 weeks. Therefore, the number of tests had to be modified and reduced. The compilation of all steady-state tests carried out in the presence of the laser device is presented in Table 1.

An example of data collected at one frequency and one amplitude in the presence of the laser device is presented in Table 5. In these tests, each device was compared with the laser once. As such, six deflections were obtained from the laser device for each setup. The statistical information on these six measurements was calculated for evaluation purposes. This information is presented in Table 5. As before, the two devices that were compared are shown in the second and third columns; measured deflections with the corresponding sensors are shown in the fourth and fifth columns; and finally, the differences in deflections are reflected in the sixth column.

**TABLE 4 Precision Determined from Data in Table 2**

Test No.	Device Used	Average Deflection (mil)	Standard Deviation (mil)	Variance (percent)
1	Accelerometer 1	1.49	0.01	0.02
2	Accelerometer 2	1.53	0.01	0.02
3	Geophone 1	1.52	0.01	0.01
4	Geophone 2	1.51	0.01	0.02
5	Proximeter	1.53	0.01	0.00
6	LVDT	1.51	0.01	0.01

**TABLE 5 Testing Sequence Used in Steady-State Deflection Measurements at Each Frequency and Amplitude (With Laser Device)**

Frequency Used : 10 Hz		Source Level: 0.045 Volts			
Test No.	Device Used		Deflection (mil)		Difference (percent) <sup>+</sup>
	Channel 1*	Channel 2	Channel 1	Channel 2	
1	Laser	Geo 1	5.19	5.13	1.16
2	Laser	Prox.	5.20	5.12	1.54
3	Laser	Acc 2	5.19	5.23	-0.77
4	Laser	LVDT	5.19	5.12	1.35
5	Laser	Geo 2	5.19	5.13	1.16
6	Laser	Acc 1	5.20	5.08	2.23

\* Average = 5.19 mil  
 Standard Deviation = 0.00 mil  
 Variance = 0.00 percent

<sup>+</sup>Difference = {Channel 1 - Channel 2}\*100/Channel 1

### Impulse Tests

Each sensor was subjected to three different types of impulse for evaluation purposes. These impulse types were half-sine, square, and triangular. The pulse width was varied from 12.5 msec to 175 msec to cover a wide range of frequencies. Typically, the pulse width for loads applied with the FWD varies between 25 msec and 75 msec. Therefore, this experiment should cover all ranges of interest in pavement evaluation. Normally, as the pulse width increases the dominant frequency content of the pulse decreases. As an example, a pulse width of 25 msec corresponds to frequencies in the range of 0 to about 25 Hz. However a pulse of 175 msec corresponds to frequency range of 0 to 2 Hz.

Nominal deflections used were 5, 15, and 25 mils. As for the steady-state tests, the lower limit (5 mils) was used to evaluate the effects of undesirable, external, electrical, and environmental noise, whereas the upper limit was used to evaluate the working range of each sensor.

Tests with the impulse motion were carried out in two phases: without the laser device and with the laser device. A matrix of all tests carried out with the half-sine impulse in the absence of the laser device is shown in Table 6. The half-sine impulse

**TABLE 6 Summary of Impulse Tests**

Pulse Width (msec)	Deflection (mils)			Type of Impulse <sup>a</sup>
12.5	5	15	25	1
25	5	15	25	1,2,3
50	5	15	25	1,2,3
75	5	15	25	1,2,3
100	5	15	25	1,2,3
112.5	5	15	25	1
125	5	15	25	1,2
150	5	15	25	1
175	5	15	25	1,2

Shaded areas correspond to tests performed with and without laser device.

<sup>a</sup>Type of Impulse: 1 = Half-Sine, 2 = Square, 3 = Triangular

tests are quite comprehensive because this is the shape of the pulse typically used in NDT devices.

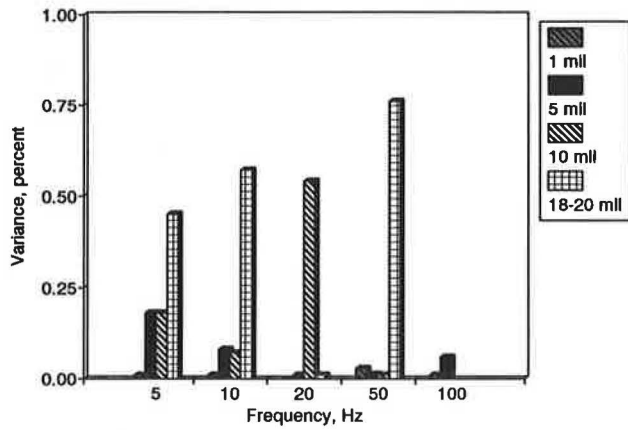
In the absence of laser device, the sequence of tests carried out at any given impulse width and amplitude was identical to that of the steady-state tests. Once again, the proximeter was used as the reference source to demonstrate the differences in the measured deflections. In the last step, the statistical information on measurements made by each device was determined. The mean, standard deviation, and variance for each device were obtained for the steady-state tests.

### PRECISION AND ACCURACY OF SENSORS

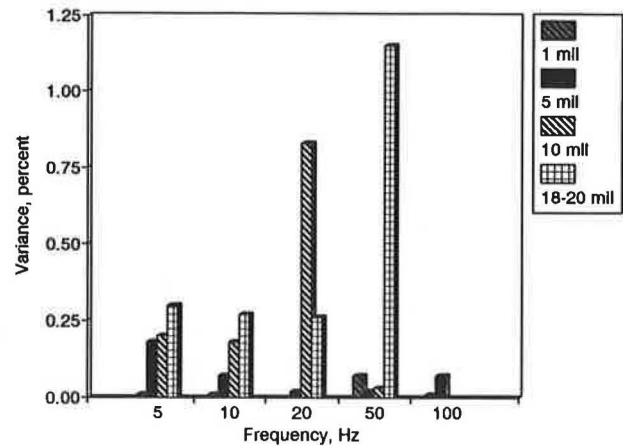
In this section the accuracy and precision of the sensors as measured in an ideal laboratory setting are compared. It is understood that the level of precision and accuracy realized in the field may be significantly greater (worse) than those reported herein. The values reported herein can be considered as minimum acceptable levels. Based on the experience of the authors, the accuracy and precision of the geophones and accelerometers in the normal field condition can be 50 percent greater (worse) than those reported herein. For the other devices the normal levels of accuracy and precision can be two to three times greater (worse) than those reported herein. It is intuitive that the accuracy and precision expected in the field depends directly on the level of care and sophistication in the installation of the equipment.

### Steady-State Motion

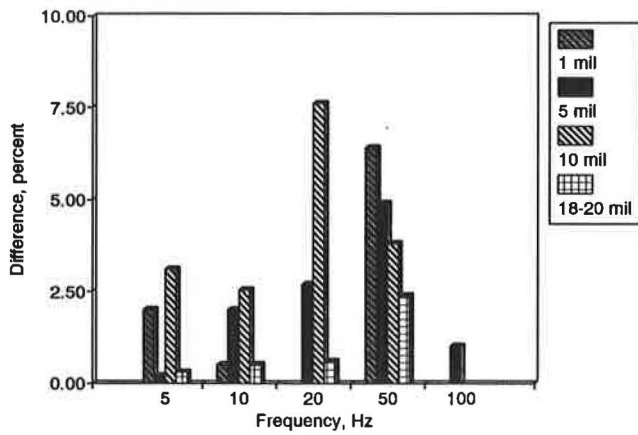
As mentioned in the previous section, for each frequency and each amplitude, deflections were measured 10 times. The precision of each sensor in terms of variance of the 10 repetitions (only 6 repetitions were performed when the laser device was used) at any given frequency and nominal deflection was determined. The variances determined in this manner are illustrated as a function of frequency in Figure 3 for the geophone and Figure 4 for the LVDT. As seen in Figure 3, the variance for deflections from the geophone is less than 0.75 percent. As a result, the variation in deflections from geophones is well within background noise. The LVDT device also performs well under the steady-state loads (Figure 4).



a) Variance



a) Variance



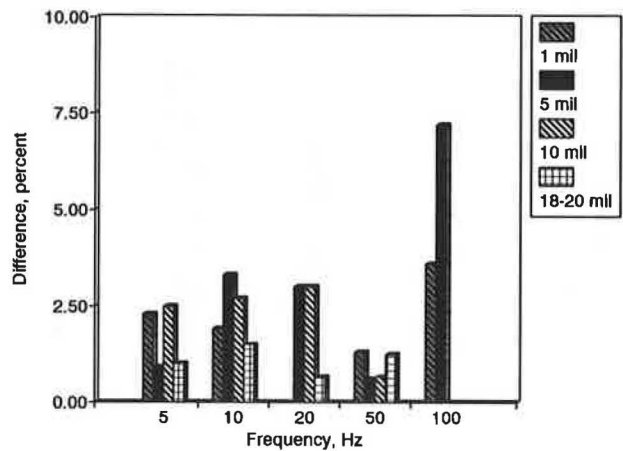
b) Difference from Proximeter Deflections

FIGURE 3 Evaluation of accuracy and precision of geophone under steady-state loading.

The variances are usually less than 0.5 percent, except two cases in which the variances were about 1 percent.

The results for the other three devices are not included here. These results are comprehensively reported elsewhere by the authors (1). The variances at all deflection levels for accelerometers are less than 1 percent, which translates to a maximum standard deviation of 0.2 mils. This deviation is well within the level of background noise. The laser device exhibits little variance. In most cases the variance is almost zero. The precision of the proximeter is quite good on the order of 0.5 percent. At high amplitudes of vibration, the variance is about 0.75 percent, which is still quite small.

The accuracy of each device was determined by comparing deflections measured with each device against those measured with the proximeter. The maximum difference between deflections measured by the accelerometers and the proximeter is about 5 percent. The accuracy of geophones is generally within 4 percent (Figure 3). The LVDT has similar accuracy when compared with the proximeter (Figure 4). The laser



b) Difference from Proximeter Deflections

FIGURE 4 Evaluation of accuracy and precision of LVDT under steady-state loading.

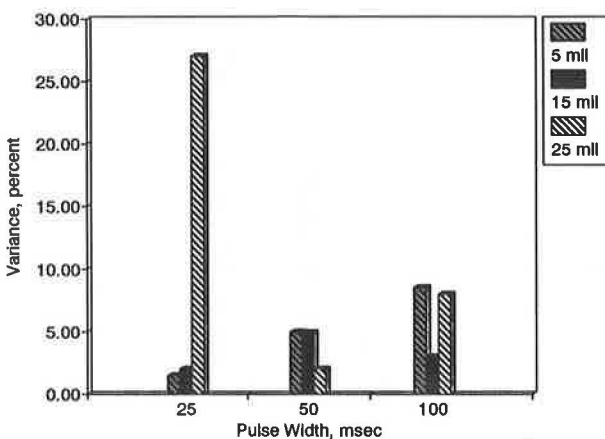
device compared favorably with the proximeter. In all cases, deflections from the two devices do not differ more than 1.5 percent.

**Impulse Motion**

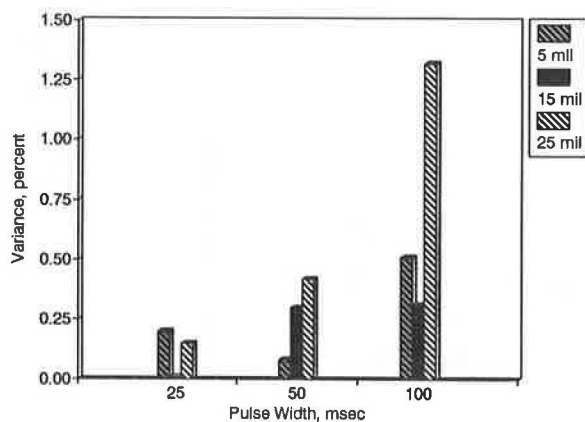
Precision and accuracy of the five sensors were also evaluated under half-sine, square, and triangular impulses. Shown in Figures 5 through 9 are the evaluation of the precision and accuracy of the five sensors under half-sine impulse. The accelerometer exhibited a large variation in deflections. Variances greater than 5 percent were not uncommon.

Contrary to the accelerometer, the variances measured with the geophone are less than 2 percent in all cases. Such a small variation can easily be attributed to background noise. In most cases the variance is below 0.5 percent.

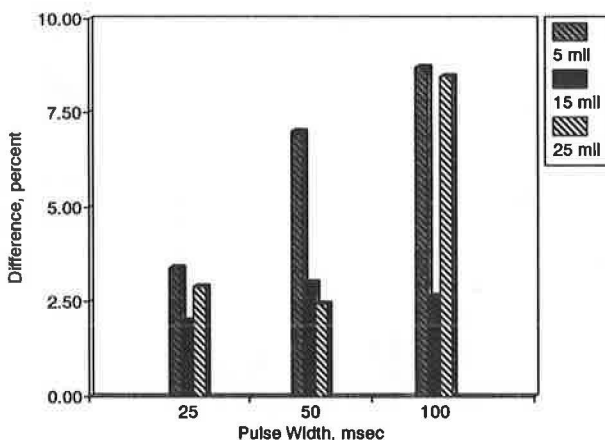
The LVDT also is quite precise. The maximum variance is about 1.25 percent and is typically less than 0.5 percent. The



a) Variance

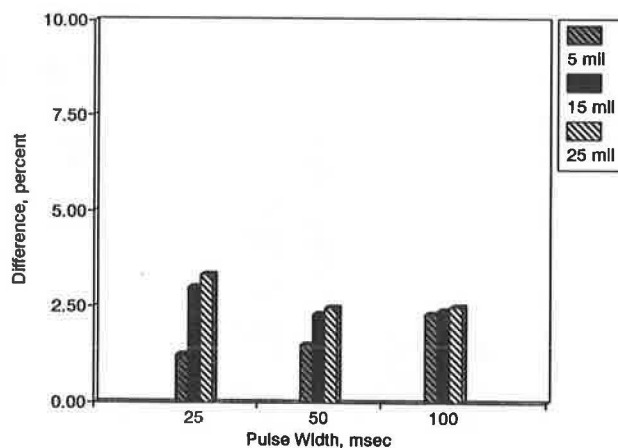


a) Variance



b) Difference from Proximeter Deflections

**FIGURE 5** Evaluation of accuracy and precision of accelerometer under half-sine pulse loading.



b) Difference from Proximeter Deflections

**FIGURE 6** Evaluation of accuracy and precision of geophone under half-sine pulse loading.

laser device is not as repeatable as it was under the steady-state conditions. However, in all conditions (but one) the repeatability of data is within 1.5 percent. For all the experiments carried out with proximeter device the maximum variance is only about 0.60 percent.

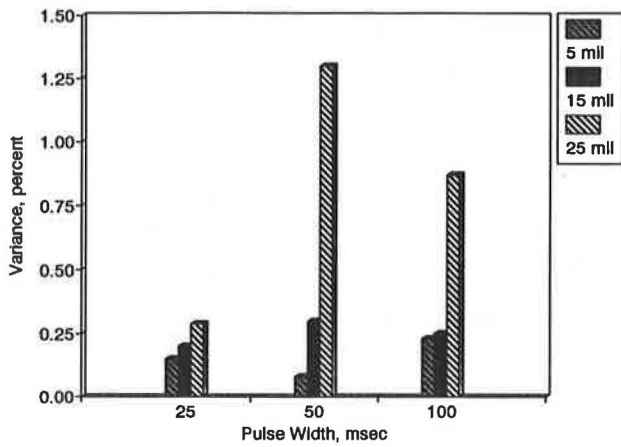
The accuracy of the accelerometer is unacceptably low for an impulse width of 100 msec. For large pulse widths, vibrations are not accurately measured with an accelerometer. The accuracy of the accelerometer at shorter pulse widths is within 3 percent. The accuracy of the geophones and the LVDT is quite good; deflections measured with both sensors are within 2.5 percent of deflections measured with a proximeter in almost all cases. Therefore, one may confidently use a geophone or an LVDT for accurate measurement of deflections under impulse loading.

The accuracy of the laser device as compared with a proximeter normally varies between 0.5 and 4 percent. Therefore, it seems that a geophone or an LVDT may produce more consistent and accurate results.

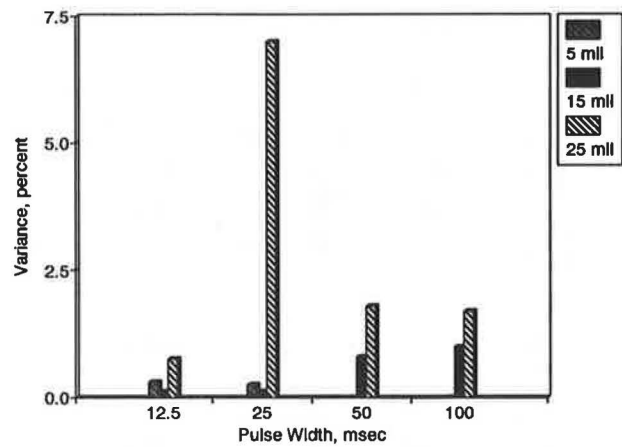
## OVERALL EVALUATION AND CONCLUSIONS

The advantages and disadvantages of all sensors as well as their direct and indirect costs are presented in Table 7. In general, accelerometers are well-calibrated sensors because their calibration curves can be traced to the National Bureau of Standards. However, piezoelectric accelerometers are not capable of accurately measuring motions of large duration (1). Accelerometers used in this study function in the frequency range of 10 Hz to 10 kHz. A significant portion of the energy imparted to a pavement by an impulsive NDT device is below 10 Hz limit; the dynaflect device vibrates at a frequency of 8 Hz. The original cost of the accelerometers is high and the connecting microdot coaxial cables used for connecting the accelerometers to the amplifiers are not very field-worthy. The cost of the coaxial cable itself is almost the same as the cost of a geophone.

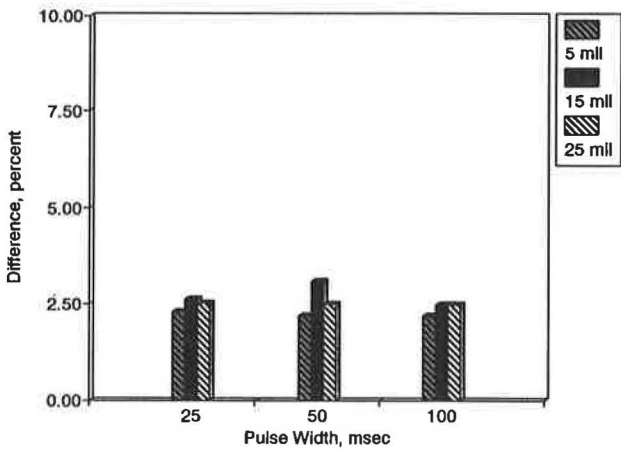
A proximeter probe is a good tool for measuring deflection in the laboratory. However, the mounting of a proximeter is



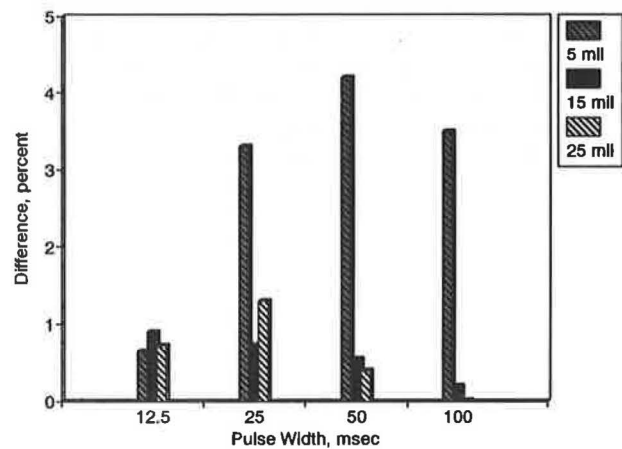
a) Variance



a) Variance



b) Difference from Proximeter Deflections



b) Difference from Proximeter Deflections

**FIGURE 7 Evaluation of accuracy and precision of LVDT under half-sine pulse loading.**

**FIGURE 8 Evaluation of accuracy and precision of laser under half-sine pulse loading.**

a problem in the field. In other words, the gap between the proximeter probe and target material should be well controlled throughout the experiment. Also, the input power supply should be of high quality to maintain a constant voltage. The gap between the proximeter and probe is small (about 2 mm); therefore, the chances of damaging the probe in the field are high. The proximeter probe should be mounted perfectly horizontal, which may be difficult in the field.

The LVDT is a good sensing device because of its infinitesimal resolution. However, it has mounting problems similar to those of the proximeter. It is possible to design and construct a mounting system. However, the cost may be prohibitive.

The laser device is an accurate and precise sensor. However, its target must be an extremely smooth surface (which a pavement is not). In the laboratory, a properly machined plate was used. Even under this condition, the data obtained from the laser for 1 mil deflection had a very poor resolution. Once again, the mounting problems must be addressed. In addition, the cost of a laser is high compared with the costs of the other devices.

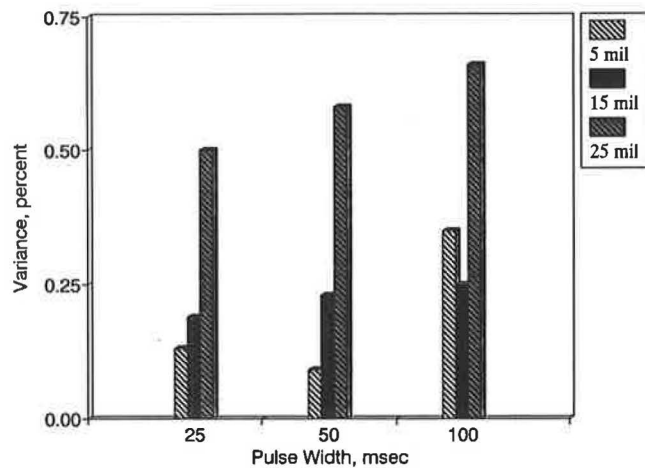


**FIGURE 9 Variability in deflection measured with proximeter as a function of half-sine impulse.**

**TABLE 7 Comparison of Different Characteristics of Sensors Evaluated**

Sensor	Accelerometer	LVDT	Geophone	Proxi-meter	Laser
Cost	\$350	\$350	\$40	\$400	> \$10,000
Supporting Device(s)	Power Amplifier (\$300)	Power Supply (\$400)	--	Power Supply (\$400)	--
Precision, Steady-State	Moderate	Good	Good	V. Good	Excellent
Precision, Impulse	Poor	Good	Good	V. Good	Good
Accuracy, Steady-State	Moderate	Good	Good	Excellent	Excellent
Accuracy Impulse	Poor	Good	Good	Good	Good
Field Worthiness	Good	Moderate	V. Good	Moderate	Poor
Mounting	Very Easy	Difficult	Very Easy	Difficult	Difficult

In contrast with the other sensors, geophones do not have mounting problems, but the data reduction process is rather complicated. The geophone is rugged enough for field testing and costs less than any other sensor. The geophone does not need any special type of mounting fixture: it can be attached to the pavement anywhere with modeling clay. No post- or

pre-amplification or signal conditioning is needed for data collection. This results in large savings.

#### ACKNOWLEDGMENTS

This work was funded by the Texas Department of Transportation. The financial assistance and cooperation of this organization is gratefully acknowledged. Special thanks are extended to project managers Richard Rogers and Bob Briggs for their trust and enthusiasm.

#### REFERENCES

1. V. Tandon and S. Nazarian. *Comprehensive Evaluation of Sensors Used for Pavement Monitoring*. Research Report 913-1F. Center for Geotechnical and Highway Materials Research, University of Texas at El Paso, 1991.
2. *Geophone General Information*. Mark Products, Inc., Houston, Tex., 1985.
3. E. O. Doebelin. *Measurement System Application and Design*, 3rd ed. McGraw-Hill Book Co., New York, N.Y., 1983.

*Publication of this paper sponsored by Committee on Strength and Deformation Characteristics of Pavement Sections.*

# Effects of Buffers on Falling Weight Deflectometer Loadings and Deflections

ERLAND O. LUKANEN

Falling weight deflectometers (FWDs) apply a load to the pavement surface that is generated by dropping a mass onto a hit bracket. The resulting impact generates the force that is transmitted to the pavement through a contact plate. A spring set between the falling mass and the hit bracket buffers the impact by decelerating the mass. The greater the deceleration, the greater the force generated. The amount of force generated is a function of the stiffness of the spring set, the amount of mass, and its velocity when it strikes the spring set, plus any dampening that may be part of the system. The Dynatest Model 8000E FWD is used for monitoring pavement sections in the Strategic Highway Research Program (SHRP) Long-Term Pavement Performance (LTPP) study. During the course of the study, several buffer changes were made. To evaluate the effects the buffers have on the loads and deflections, tests were conducted using each buffer set on three pavement structures near the SHRP North Central Regional Office. The results show the various buffer shapes had an effect on the test results. The differences observed are not considered significant for routine production testing but are expected to be relevant in research work involving viscoelastic materials (asphalt) and dynamic deflection analysis.

A key activity of the Long-Term Pavement Performance (LTPP) program of the Strategic Highway Research Program (SHRP) is to monitor the condition of a number of pavement sections throughout the United States and Canada (1). Part of the monitoring includes deflection measurements. To measure the deflections, four Model 8000E Dynatest falling weight deflectometers (FWDs) were purchased by SHRP and assigned to each of the four LTPP regions. During the first two years, deflection data were gathered with three different types of buffers. Information is provided here on how the buffers affect the shape of the load pulse. Information on sensitivities of deflection measurements to the form or shape of the load pulse is also provided, as is a description of how the three buffer shapes were used for LTPP testing. Comparison deflection data from all three buffers are presented, and deflection results and backcalculated layer modulus results are compared.

## BACKGROUND

To conduct deflection testing, one of the pavement monitoring techniques of the LTPP program, SHRP assigned a Dynatest Model 8000E FWD to each of its four regions (2). The regional contractors operate the FWDs to periodically collect deflection data from each LTPP test section. In the first 2

years of deflection testing, three different buffer shapes, as shown in Figure 1, were used.

Deflection data from all three buffer shapes are stored in the SHRP LTPP data base. The type of buffer used at a particular time of test must be determined from the date of test. The buffer shape is not a part of the data base.

## FWD OPERATION

The FWD applies a load to the pavement surface through a plate 11.9 in. in diameter. The bottom of the plate has a ribbed neoprene isolation pad that is intended to equally distribute the pressure under the load plate. The plate is attached to a load cell that measures the amount of load that is applied to the pavement (see Figure 2). Seven velocity transducers are placed on the pavement to measure the vertical movement of the pavement when the load is applied.

A computerized system controls the operation of the FWD and records the load and the pavement deflection data. The load information is recorded as a voltage output of the load cell and is converted to load force or pressure. The pavement deflection is calculated from the vertical pavement velocity data that are measured by the velocity transducers. The output of the velocity transducers is converted to deflection data.

The computer system records the load and deflection data once every 0.2 msec (3). All the data collected during a 60-msec period may be saved, or the operator may select to save only the peak readings. The complete load-deflection-time history data set is called a "whole history" in the Dynatest operators manual and field software (3).

The load applied by the FWD is generated when a falling mass is decelerated by a set of rubber buffers (springs) between the mass and hit bracket mounted above the load cell (Figure 2). The buffers used for the SHRP testing are cylindrical. They are about 100 mm in diameter and 80 mm in length. The amount of mass, the drop height, and the stiffness of the buffers control the form of the load pulse and the magnitude of load applied to the pavement. The SHRP FWDs were originally delivered with cylindrical rubber buffers; the bottom end of the buffer that struck the hit bracket was flat. Several buffer sets are supplied with the FWD. The buffer set used depends on the amount of mass dropped. Only the 440-lb mass set and corresponding buffer set is used for LTPP testing.

The shape of the load versus time pulse curve for the flat buffers often had two load peaks about 6 to 6.5 msec apart, as shown in Figure 3, instead of the ideal haversine-shaped pulse. This may be due to the resonant frequency of the

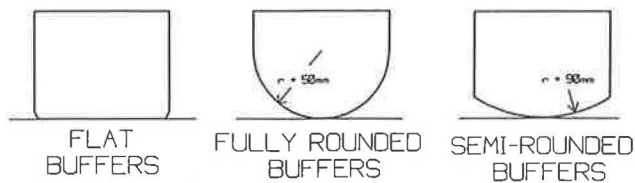


FIGURE 1 Shape of cross section of buffers used.

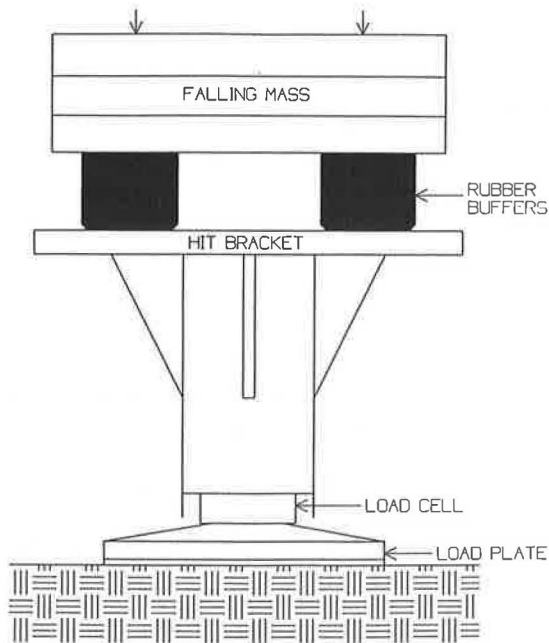


FIGURE 2 Side view sketch of load generation subassembly.

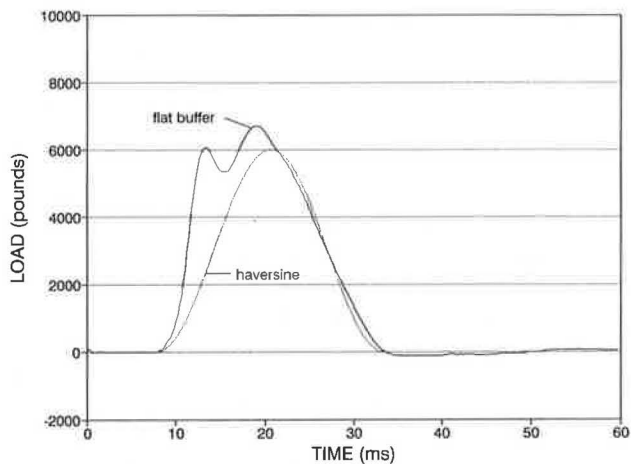


FIGURE 3 Ideal load pulse and load pulse generated by flat buffer set.

loading system, substructure, and isolation pad, which would be in the 150 to 170 Hz range. During testing, most of the time the second peak, at 12 to 13 msec into the load pulse, is the largest peak. Occasionally, there were two peaks of approximately the same magnitude, and on rare occasions the first peak was the highest. The double peak, and its effect on pavement deflection, was a concern.

After the first year of testing, Dynatest supplied a different set of buffers with a rounded contact surface at the bottom (Figure 1). The contact surfaces of the new buffers were rounded to a 50-mm radius, resulting in a hemispherical shape. The effect of the rounding is to create a variable rate spring. (This 50-mm configuration is also referred to as “fully rounded buffers” in the text and figures.) At initial contact, only a small section of the rubber buffer is compressed. At the highest drop height, the rounded end would compress so that the final contact surface on the hit bracket has a diameter of about 100 mm. The lower spring constant under partial compression would reduce the magnitude of the first load peak. Ideally, the spring set could be varied to allow the peak load to occur about 12 to 13 msec after the beginning of the load pulse, which would coincide with the second cycle of the apparent resonance frequency of the subassembly. The second peak, then, would always be the largest of the two peaks that develop during the rise time of the load pulse. If the rise time of the load pulse was reduced to about 9 msec, it would coincide with the unloading side of the cycle of the subassembly, which could result in two nearly equal pulses at about 6 to 7 msec and at 12 to 13 msec. The rounding of the buffers created a variable spring that has a lower spring constant when first compressed; the spring constant then increases as the effective contact radius of the buffer increases to a maximum value.

Shortly after the new 50-mm buffers were installed, it was noticed that the rebound of the mass assembly had increased and was impacting the lift mechanism at the lower drop heights. The impact was causing damage to the lift mechanism. Dynatest, after diagnosing the problem, recalled the 50-mm buffers and supplied a new set of buffers (see Figure 1) rounded to a radius of 90 mm. (This 90-mm configuration is also called “semi-rounded buffers” in the text and figures.) The 50-mm buffers, however, had been in service for some time and field data were collected with them. Including the 90-mm buffers, SHRP has collected deflection data with three different buffer sets on the FWDs.

What effect do the different buffers have on the deflections that were measured on the SHRP sections? Researchers in the North Central Region had an opportunity to obtain deflection measurements on several pavement sections using all three buffer types. To do this, a testing setup with pauses was used that allowed the buffers to be changed without lifting the load plate off the pavement. Using this setup, tests were conducted on three pavement sections:

- The garage floor at the North Central Regional office, estimated to consist of 4 in. of concrete on 12 in. of fill on grade;
- Concordia Avenue, a street in front of the regional office that was constructed as a composite pavement with 3 in. of asphalt over 6 in. of concrete; and
- Pascal Avenue, a new pavement near the regional office that was constructed with approximately 10 in. of asphalt over 6 in. of aggregate base.

The setup used for deflection testing used all four drop heights and saved a whole history for the last drop at each drop height. The data files and a hard copy of the peak deflections were sent to SHRP on June 27, 1990.

## COMPARISON OF BUFFER EFFECTS ON DEFLECTIONS

The whole histories were used to compare the load pulses and resulting deflections for each of the buffer sets. The whole histories were graphed to display the load and deflection pulses for each of the drop heights on each of the pavement sections tested. The three pavement sections and four drop heights resulted in 36 different graphs shown in Figure 4. The load pulse plots were scaled to achieve a load plot with the same amplitude on each of the graphs; the deflection data were also scaled to achieve the same amplitude for the center sensor deflections for each of the graphs. The plots may be overlaid on each other to compare the shape of the pulses on a common basis, regardless of the amount of load or deflection. Each graph also has the peak deflection values listed in the upper right corner and a scaled plot of the deflection basin on the right side. In the lower right corner of each graph, the time of occurrence of the load peak and the deflection peak of the center sensor are listed. The values do not reflect the rise time of the pulse, but are included to show the delay time between the load peak and the deflection peak.

Some observations on the buffer effects from the data follow:

- The rounded buffers did reduce the magnitude of the first peak in the load pulse, as shown in the whole history plots in Figure 4.

- The flat buffers have approximately the same dwell time for all four drop heights—about 25 msec.

- The rounded buffers had longer load pulses for the lower drop heights. The 90-mm buffers had load pulses of about 31.5 msec at drop height 1 and about 26.5 msec at drop height 4. The 50-mm buffers had load pulse dwell times of about 36 msec at drop height 1 and 29 msec at drop height 4.

- The rise times (see Table 1) of the load pulses varied with drop height for the rounded buffers but were relatively constant for the flat buffers as long as the first peak was not the highest. The 50-mm buffers showed the most change in rise time over the different drop heights, ranging from a low of 12.8 msec at drop height 4 to 15.6 msec at drop height 1 on the flexible section. The 90-mm buffers ranged from 11.1 msec to 12.8 msec for drop heights 4 and 1, respectively, on the portland cement concrete (PCC) section. The rise time for flat buffers ranged from 10.2 (except for the 8.4 rise time for drop height 4 on the composite pavement, which was influenced by the first peak) to 11.1 msec for drop heights 4 and 1, respectively, on PCC; the rise times went the other way, from 11.0 to 10.4 msec, on the flexible section. The times listed here are the largest differences observed for a particular pavement type.

The rise time is thought to be an important part of the load pulse since the strength of asphalt is known to be dependent on the rate of loading. If pavements were truly elastic and without mass, the load/deflection ratio would not be influenced by the rate of loading.

The effect of this rise time on deflections is presented in Table 2. This table expresses the normalized deflections for each buffer set as a percentage of the normalized deflections of the flat buffers. At lower drop heights, it can be seen that considerably more deflection was measured on the composite

bituminous over concrete (BOC) pavement with the rounded buffers than with the flat buffers. On the other hand, both the 50- and 90-mm buffers measured less deflection on the thin PCC garage floor than the flat buffers did. On the BOC and flexible sections, the difference in deflections and rise time diminished as the drop height increased.

- The impulse stiffness modulus (ISM) is used to describe the overall stiffness of the pavement section. The ISM is calculated by dividing the load by the deflection at the center of the load area and is expressed in kips per inch. The ISM increases as the overall pavement strength increases. The ISM values for the flat buffers on the composite and flexible sections show the pavements are stress softening; that is, the ISM decreases as the load increases, whereas the rounded buffers show the opposite trend (Table 1 and Figure 5). The PCC garage floor shows little change in ISM as a result of drop height, but shows some increase in ISM from the flat to 90-mm to 50-mm buffers. This may correspond to the increase in rise time from flat to 90-mm to 50-mm buffers, which is roughly 11, 12, and 13 msec, respectively.

It can thus be seen that buffer shape affects the measured deflections for a given load.

## MODULUS RESULTS

Modulus values were determined for the pavement layers using MODULUS, Version 4.0 (4). The parameters used for analysis were Poisson ratios of 0.15 for concrete, 0.35 for asphalt and aggregate base, and 0.40 for subgrade. The modulus limits were set at 2,000,000 to 9,000,000 psi for concrete, 100,000 to 2,000,000 psi for asphalt, and 5,000 to 150,000 psi for base. The depth of subgrade was set to infinity, and the deflection weight factors were all set to 1.0. The results are summarized in Table 3. The results are reasonably consistent over the range of drop heights and buffer types. The basin fits were good for all three buffer shapes and pavement types. The absolute sum of percentage error was in the 4 to 8 percent range for all three buffer shapes. The results, however, for the flexible pavement show the rate of loading may affect the modulus of the asphalt. This is an expected behavior of asphaltic concrete, and it may be possible to use variable buffer rates on an FWD to measure the effect loading rates have on stiffness.

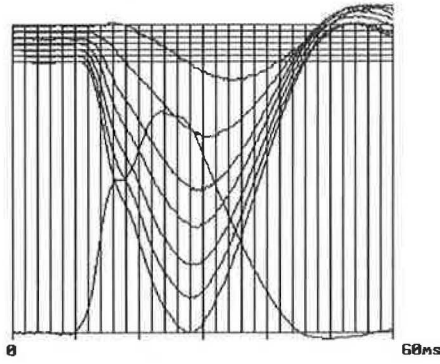
The results for drop height 1 on the BOC pavement show quite a bit of variation, which cannot be explained. It may be that the low load was not enough to fully seat the concrete on the underlying material; slip between the layers at low load is another possible explanation.

## CONCLUSIONS

Conclusions that can be drawn from the limited amount of data available are as follows:

- It appears that by varying the mass, drop height, and spring sets, some degree of control of the forcing function or load pulse of the FWD can be provided.

THIN PCC: FULLY ROUNDED BUFFERS

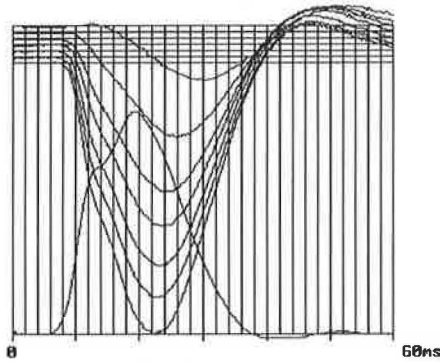


Load = 5232  
 D 0 = 8.63  
 D +8 = 7.73  
 D +12 = 6.86  
 D +18 = 5.85  
 D +24 = 4.91  
 D +36 = 3.38  
 D +60 = 1.76

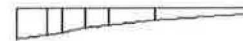


LOAD PK = 23.4 ms  
 DEFL PK = 27.4 ms

THIN PCC: SEMIROUNDED BUFFERS

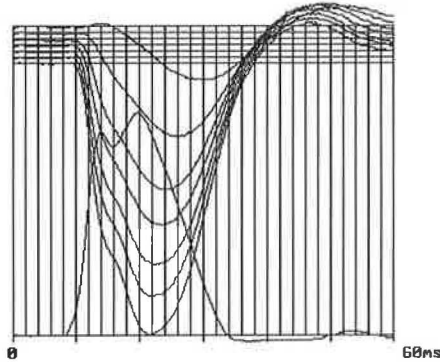


Load = 5920  
 D 0 = 9.80  
 D +8 = 8.76  
 D +12 = 7.86  
 D +18 = 6.60  
 D +24 = 5.58  
 D +36 = 3.81  
 D +60 = 1.98

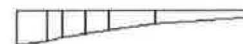


LOAD PK = 19.8 ms  
 DEFL PK = 22.2 ms

THIN PCC: FLAT BUFFERS

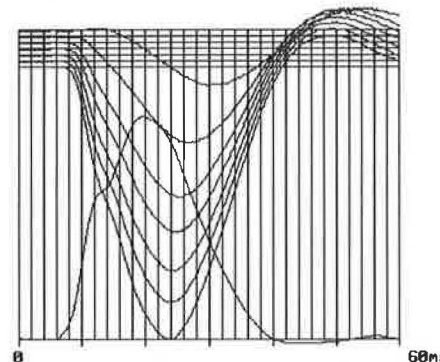


Load = 6400  
 D 0 = 11.39  
 D +8 = 10.05  
 D +12 = 8.94  
 D +18 = 7.56  
 D +24 = 6.34  
 D +36 = 4.37  
 D +60 = 2.24

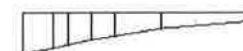


LOAD PK = 19.6 ms  
 DEFL PK = 21.6 ms

THIN PCC: FULLY ROUNDED BUFFERS



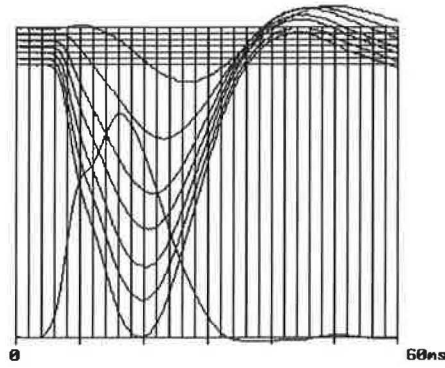
Load = 7968  
 D 0 = 13.07  
 D +8 = 11.59  
 D +12 = 10.40  
 D +18 = 8.82  
 D +24 = 7.40  
 D +36 = 5.11  
 D +60 = 2.60



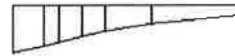
LOAD PK = 19.4 ms  
 DEFL PK = 23.6 ms

FIGURE 4 Whole history plots and peak deflection information (continued on next page).

THIN PCC : SEMIROUNDED BUFFERS

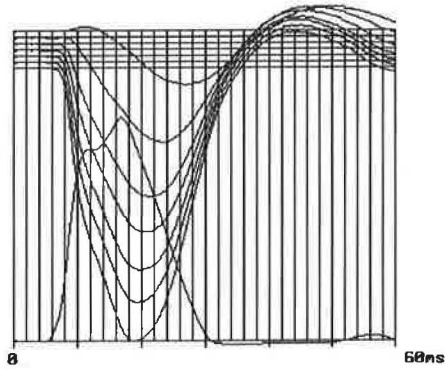


Load =	9064
D 0 =	15.12
D +8 =	13.38
D +12 =	11.94
D +18 =	10.15
D +24 =	8.54
D +36 =	5.85
D +60 =	3.83

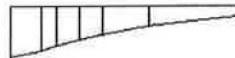


LOAD PK = 15.8 ns  
DEFL PK = 20.0 ns

THIN PCC : FLAT BUFFERS

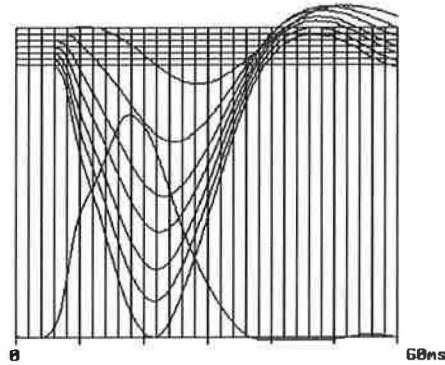


Load =	9536
D 0 =	16.37
D +8 =	14.41
D +12 =	12.89
D +18 =	10.95
D +24 =	9.22
D +36 =	6.32
D +60 =	3.25

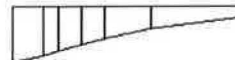


LOAD PK = 16.6 ns  
DEFL PK = 19.8 ns

THIN PCC : FULLY ROUNDED BUFFERS

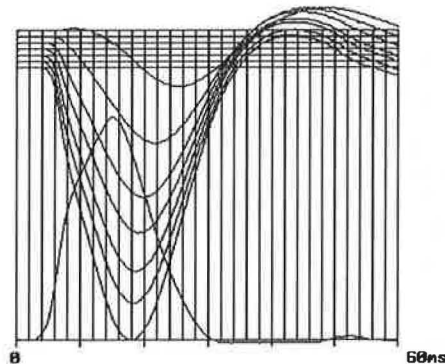


Load =	11032
D 0 =	17.92
D +8 =	15.95
D +12 =	14.31
D +18 =	12.24
D +24 =	10.28
D +36 =	7.18
D +60 =	3.69

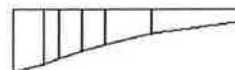


LOAD PK = 17.6 ns  
DEFL PK = 21.4 ns

THIN PCC : SEMIROUNDED BUFFERS



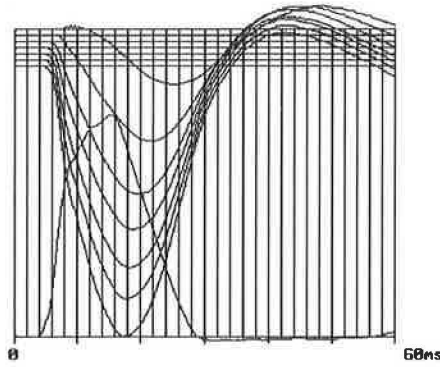
Load =	12448
D 0 =	20.35
D +8 =	18.03
D +12 =	16.14
D +18 =	13.75
D +24 =	11.55
D +36 =	7.92
D +60 =	4.17



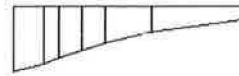
LOAD PK = 15.8 ns  
DEFL PK = 17.6 ns

FIGURE 4 (continued).

THIN PCC: FLAT BUFFERS

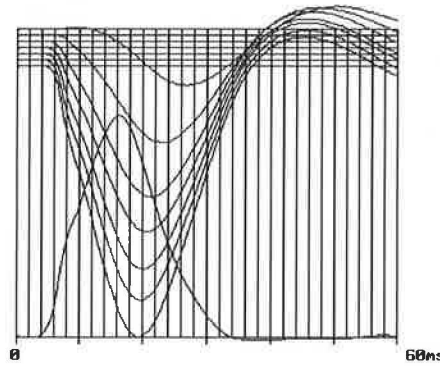


Load	=	12320
D 0	=	21.40
D +8	=	18.90
D +12	=	16.93
D +18	=	14.37
D +24	=	12.10
D +36	=	8.40
D +60	=	4.39

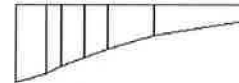


LOAD PK = 15.2 ns  
DEFL PK = 17.2 ns

THIN PCC: FULLY ROUNDED BUFFERS

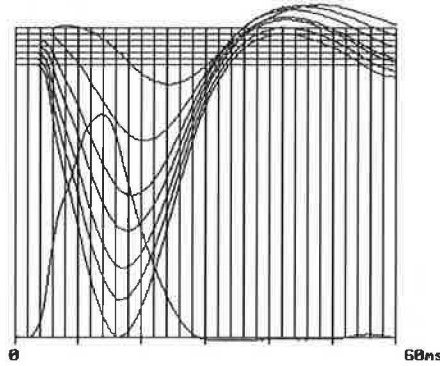


Load	=	15424
D 0	=	25.17
D +8	=	22.27
D +12	=	20.00
D +18	=	17.09
D +24	=	14.42
D +36	=	9.96
D +60	=	5.23

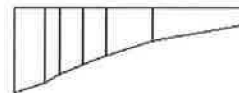


LOAD PK = 16.2 ns  
DEFL PK = 19.4 ns

THIN PCC: SEMI-ROUNDED BUFFERS

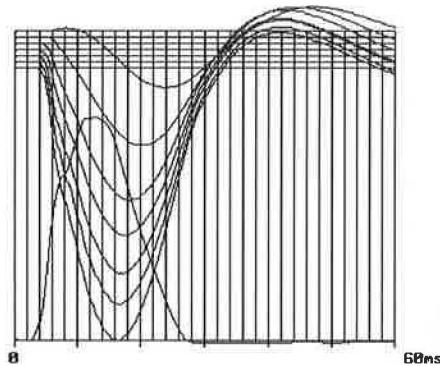


Load	=	16600
D 0	=	27.47
D +8	=	24.30
D +12	=	21.71
D +18	=	18.59
D +24	=	15.69
D +36	=	10.70
D +60	=	5.71

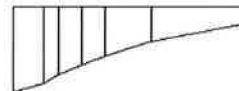


LOAD PK = 13.6 ns  
DEFL PK = 16.6 ns

THIN PCC: FLAT BUFFERS



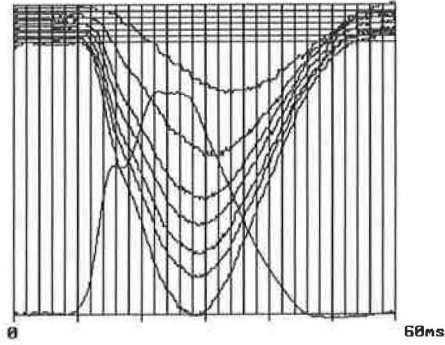
Load	=	16024
D 0	=	27.72
D +8	=	24.67
D +12	=	22.12
D +18	=	18.89
D +24	=	15.99
D +36	=	11.00
D +60	=	5.00



LOAD PK = 13.0 ns  
DEFL PK = 16.6 ns

FIGURE 4 (continued).

COMPOSITE SECTION: FULLY ROUNDED BUFFERS.

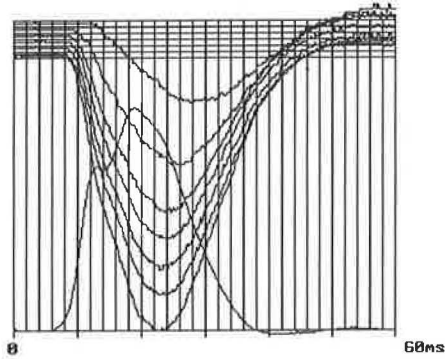


Load = 5872  
 D 0 = 3.77  
 D +8 = 3.36  
 D +12 = 3.12  
 D +18 = 2.80  
 D +24 = 2.54  
 D +36 = 1.99  
 D +60 = 1.23



LOAD PK = 22.8 ms  
 DEFL PK = 27.6 ms

COMPOSITE SECTION: SEMIROUNDED BUFFERS.

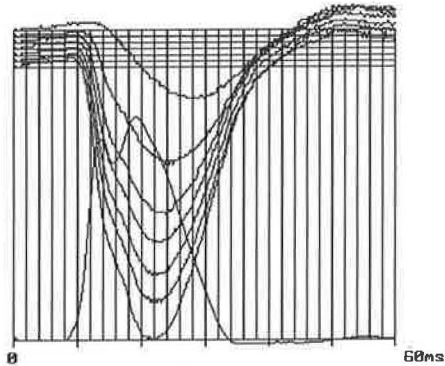


Load = 5896  
 D 0 = 4.06  
 D +8 = 3.61  
 D +12 = 3.33  
 D +18 = 3.01  
 D +24 = 2.66  
 D +36 = 2.04  
 D +60 = 1.23



LOAD PK = 18.8 ms  
 DEFL PK = 22.2 ms

COMPOSITE SECTION: FLAT BUFFERS.

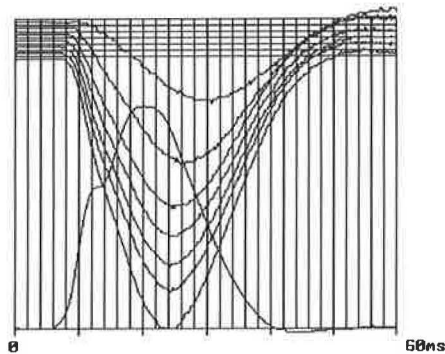


Load = 6712  
 D 0 = 4.23  
 D +8 = 3.74  
 D +12 = 3.41  
 D +18 = 3.01  
 D +24 = 2.66  
 D +36 = 1.99  
 D +60 = 1.05



LOAD PK = 19.0 ms  
 DEFL PK = 21.0 ms

COMPOSITE SECTION: FULLY ROUNDED BUFFERS.



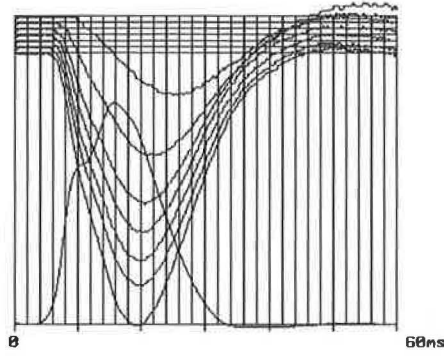
Load = 7744  
 D 0 = 5.74  
 D +8 = 5.07  
 D +12 = 4.70  
 D +18 = 4.18  
 D +24 = 3.72  
 D +36 = 2.90  
 D +60 = 1.76



LOAD PK = 28.2 ms  
 DEFL PK = 23.6 ms

FIGURE 4 (continued).

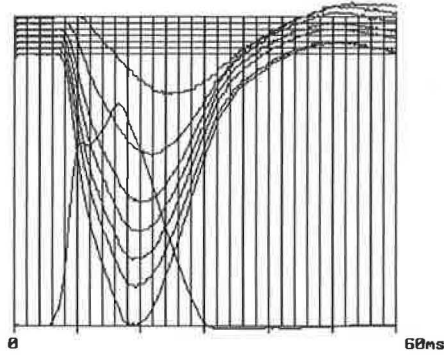
COMPOSITE SECTION: SEMIROUNDED BUFFERS.



Load =	8976
D 0 =	6.32
D +8 =	5.61
D +12 =	5.12
D +18 =	4.68
D +24 =	4.18
D +36 =	3.12
D +60 =	1.84

LOAD PK = 15.8 ms  
DEFL PK = 18.8 ms

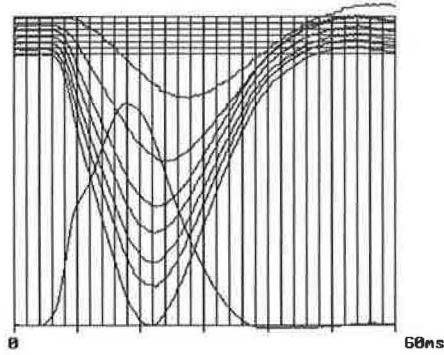
COMPOSITE SECTION: FLAT BUFFERS.



Load =	9680
D 0 =	6.62
D +8 =	5.82
D +12 =	5.32
D +18 =	4.76
D +24 =	4.23
D +36 =	3.25
D +60 =	1.89

LOAD PK = 16.6 ms  
DEFL PK = 18.6 ms

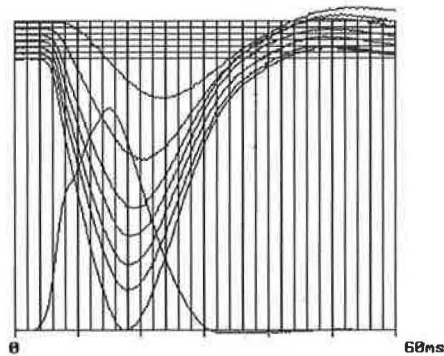
COMPOSITE SECTION: FULLY ROUNDED BUFFERS.



Load =	10040
D 0 =	7.83
D +8 =	6.90
D +12 =	6.36
D +18 =	5.72
D +24 =	5.12
D +36 =	3.98
D +60 =	2.37

LOAD PK = 17.8 ms  
DEFL PK = 21.6 ms

COMPOSITE SECTION: SEMIROUNDED BUFFERS.

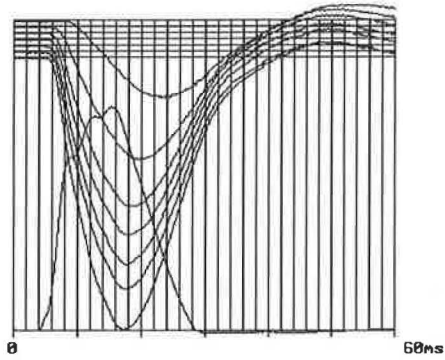


Load =	12280
D 0 =	8.63
D +8 =	7.56
D +12 =	6.95
D +18 =	6.23
D +24 =	5.58
D +36 =	4.28
D +60 =	2.46

LOAD PK = 15.8 ms  
DEFL PK = 17.2 ms

FIGURE 4 (continued).

COMPOSITE SECTION: FLAT BUFFERS.

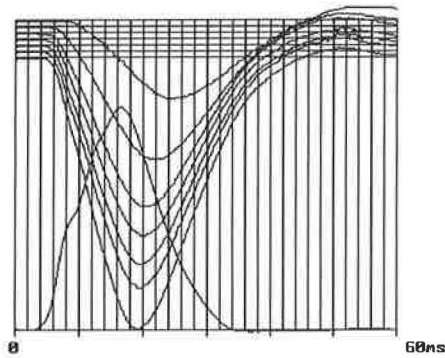


Load = 12424  
 D 0 = 8.84  
 D +8 = 7.73  
 D +12 = 7.11  
 D +18 = 6.35  
 D +24 = 5.63  
 D +36 = 4.33  
 D +60 = 2.50

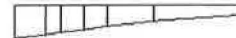


LOAD PK = 15.2 ms  
 DEFL PK = 17.0 ms

COMPOSITE SECTION: FULLY ROUNDED BUFFERS.

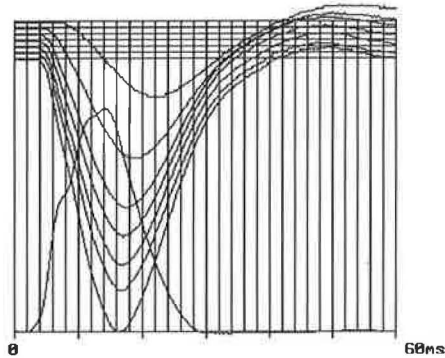


Load = 15440  
 D 0 = 10.89  
 D +8 = 9.47  
 D +12 = 8.78  
 D +18 = 7.86  
 D +24 = 6.98  
 D +36 = 5.33  
 D +60 = 3.16

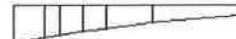


LOAD PK = 16.4 ms  
 DEFL PK = 19.4 ms

COMPOSITE SECTION: SEMIROUNDED BUFFERS.

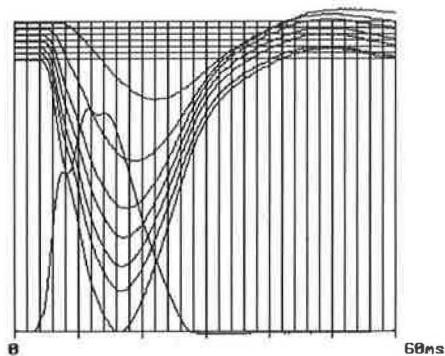


Load = 16784  
 D 0 = 11.85  
 D +8 = 10.38  
 D +12 = 9.48  
 D +18 = 8.52  
 D +24 = 7.53  
 D +36 = 5.67  
 D +60 = 3.29

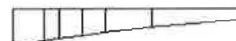


LOAD PK = 14.0 ms  
 DEFL PK = 16.2 ms

COMPOSITE SECTION: FLAT BUFFERS.



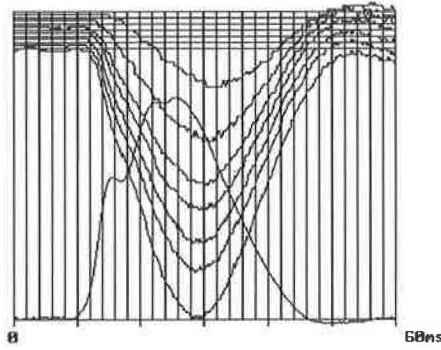
Load = 16376  
 D 0 = 11.93  
 D +8 = 10.43  
 D +12 = 9.61  
 D +18 = 8.61  
 D +24 = 7.61  
 D +36 = 5.85  
 D +60 = 3.42



LOAD PK = 11.6 ms  
 DEFL PK = 16.0 ms

FIGURE 4 (continued).

FLEXIBLE SECTION: FULLY ROUNDED BUFFERS.

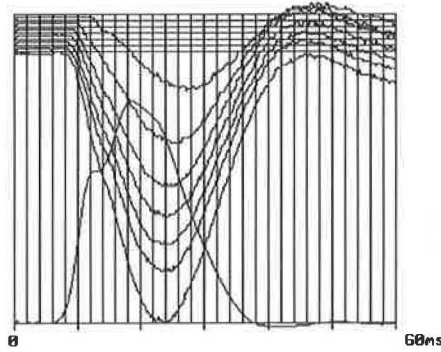


Load =	5088
D 0 =	3.56
D +8 =	3.03
D +12 =	2.70
D +18 =	2.38
D +24 =	2.11
D +36 =	1.60
D +60 =	0.97



LOAD PK = 25.2 ms  
DEFL PK = 28.2 ms

FLEXIBLE SECTION: SEMI-ROUNDED BUFFERS.

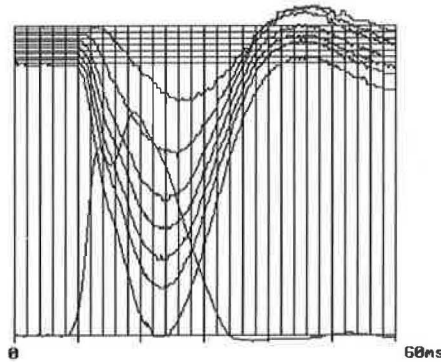


Load =	5816
D 0 =	4.02
D +8 =	3.36
D +12 =	3.04
D +18 =	2.72
D +24 =	2.37
D +36 =	1.82
D +60 =	1.14



LOAD PK = 18.4 ms  
DEFL PK = 23.6 ms

FLEXIBLE SECTION: FLAT BUFFERS.

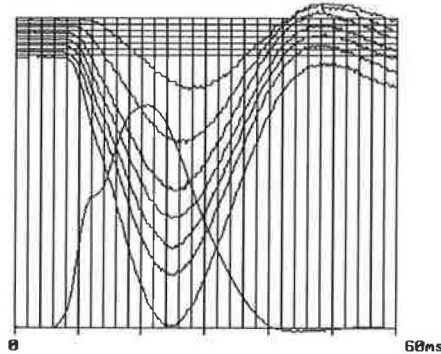


Load =	6584
D 0 =	4.36
D +8 =	3.70
D +12 =	3.33
D +18 =	2.97
D +24 =	2.58
D +36 =	1.99
D +60 =	1.19



LOAD PK = 18.8 ms  
DEFL PK = 22.2 ms

FLEXIBLE SECTION: FULLY ROUNDED BUFFERS.



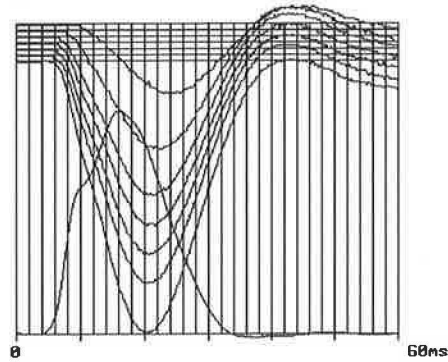
Load =	7776
D 0 =	5.57
D +8 =	4.61
D +12 =	4.20
D +18 =	3.72
D +24 =	3.26
D +36 =	2.42
D +60 =	1.45



LOAD PK = 28.8 ms  
DEFL PK = 24.6 ms

FIGURE 4 (continued).

## FLEXIBLE SECTION: SEMI-ROUNDED BUFFERS.

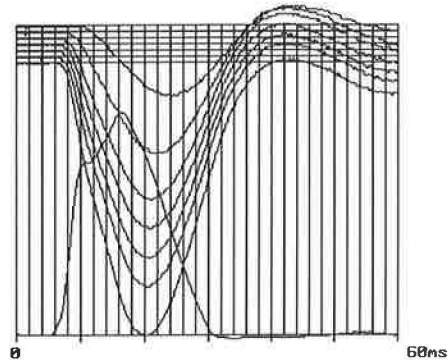


Load = 8896  
 D 0 = 6.16  
 D +8 = 5.15  
 D +12 = 4.66  
 D +18 = 4.14  
 D +24 = 3.68  
 D +36 = 2.68  
 D +60 = 1.58



LOAD PK = 16.8 ms  
 DEFL PK = 28.4 ms

## FLEXIBLE SECTION: FLAT BUFFERS.

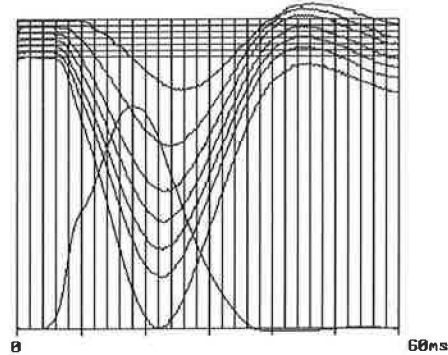


Load = 9552  
 D 0 = 6.53  
 D +8 = 5.52  
 D +12 = 4.99  
 D +18 = 4.43  
 D +24 = 3.89  
 D +36 = 2.98  
 D +60 = 1.71

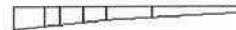


LOAD PK = 16.4 ms  
 DEFL PK = 28.8 ms

## FLEXIBLE SECTION: FULLY ROUNDED BUFFERS.

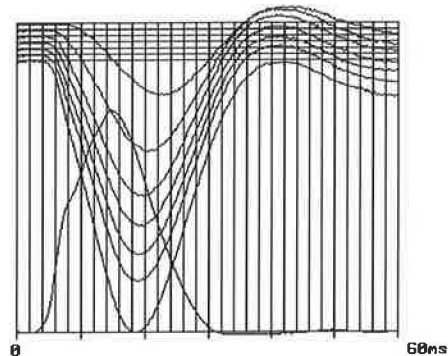


Load = 10768  
 D 0 = 7.75  
 D +8 = 6.48  
 D +12 = 5.86  
 D +18 = 5.22  
 D +24 = 4.53  
 D +36 = 3.42  
 D +60 = 2.82



LOAD PK = 17.6 ms  
 DEFL PK = 22.8 ms

## FLEXIBLE SECTION: SEMI-ROUNDED BUFFERS.



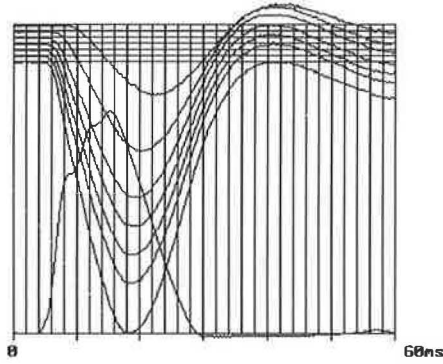
Load = 12232  
 D 0 = 8.58  
 D +8 = 7.14  
 D +12 = 6.45  
 D +18 = 5.77  
 D +24 = 5.09  
 D +36 = 3.81  
 D +60 = 2.24



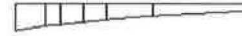
LOAD PK = 14.8 ms  
 DEFL PK = 18.8 ms

FIGURE 4 (continued).

FLEXIBLE SECTION: FLAT BUFFERS.

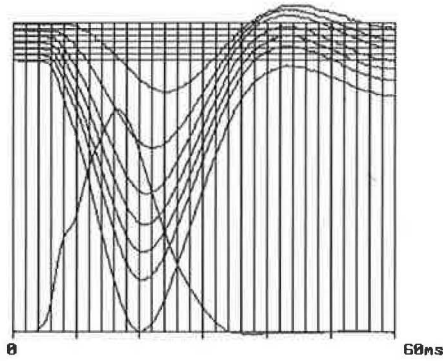


Load	=	12416
D 0	=	8.75
D +8	=	7.31
D +12	=	6.61
D +18	=	5.89
D +24	=	5.16
D +36	=	3.98
D +60	=	2.28

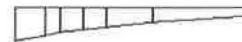


LOAD PK = 15.2 ms  
DEFL PK = 18.8 ms

FLEXIBLE SECTION: FULLY ROUNDED BUFFERS.

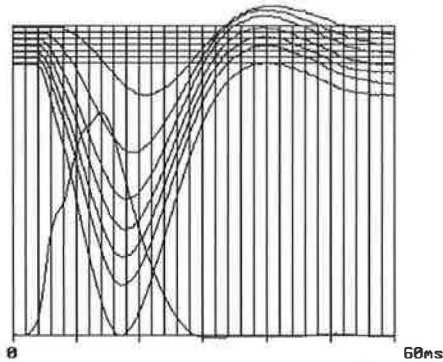


Load	=	15384
D 0	=	10.89
D +8	=	9.06
D +12	=	8.19
D +18	=	7.31
D +24	=	6.34
D +36	=	4.76
D +60	=	2.81

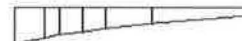


LOAD PK = 16.6 ms  
DEFL PK = 20.8 ms

FLEXIBLE SECTION: SEMI-ROUNDED BUFFERS.

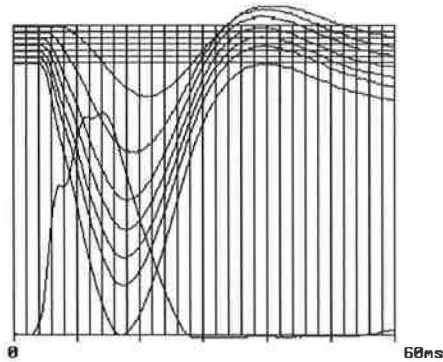


Load	=	16720
D 0	=	11.73
D +8	=	9.84
D +12	=	8.98
D +18	=	7.98
D +24	=	6.94
D +36	=	5.20
D +60	=	2.99

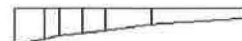


LOAD PK = 13.8 ms  
DEFL PK = 16.8 ms

FLEXIBLE SECTION: FLAT BUFFERS.



Load	=	16224
D 0	=	11.77
D +8	=	9.89
D +12	=	8.98
D +18	=	8.02
D +24	=	7.02
D +36	=	5.24
D +60	=	3.07



LOAD PK = 14.8 ms  
DEFL PK = 16.8 ms

FIGURE 4 (continued).

**TABLE 1 Rise Times and ISM Results by Buffer Type**

Impulse Stiffness Modulus (Kips per inch)				Load Pulse Rise Time (milliseconds)		
<b>Flexible Section:</b>						
	Flat	90mm	50mm	Flat	90mm	50mm
Drop 1	1510	1447	1429	10.4	12.2	15.6
2	1462	1444	1396	10.6	12.0	14.8
3	1419	1439	1389	11.2	11.8	13.4
4	1378	1425	1413	11.0	11.8	13.0
<b>Composite Section:</b>						
	Flat	90mm	50mm	Flat	90mm	50mm
Drop 1	1587	1452	1345	10.9	12.8	13.8
2	1462	1420	1349	10.8	12.0	14.2
3	1405	1423	1385	11.1	11.8	13.4
4	1373	1410	1417	8.4	11.6	13.0
<b>Thin PCC Section:</b>						
	Flat	90mm	50mm	Flat	90mm	50mm
Drop 1	569	599	606	11.1	12.8	13.5
2	583	599	609	11.1	11.8	13.3
3	576	611	616	11.2	11.8	13.1
4	578	604	613	10.2	11.1	12.4

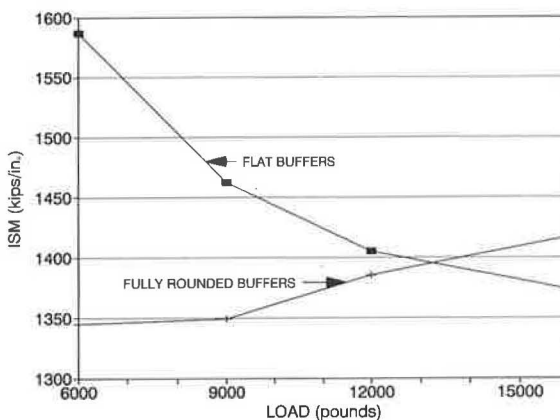


**FIGURE 5 ISM on composite section.**

**TABLE 2 Percentage Change in Deflection From Flat Buffers**

Pvm't	Buffer Type	Drop Height	Percent Change From Flat Buffers						
			D (offset in inches)						
			D(0)	D(8)	D(12)	D(18)	D(24)	D(36)	D(60)
<b>BOC</b>	ROUND	1	17.9%	18.9%	21.1%	23.1%	26.4%	32.3%	55.0%
	SEMI	1	9.3%	9.9%	11.2%	13.8%	13.8%	16.7%	33.4%
	ROUND	2	8.4%	8.9%	10.4%	9.8%	9.9%	11.5%	16.4%
	SEMI	2	3.0%	4.0%	3.8%	4.2%	4.5%	3.5%	5.0%
	ROUND	3	1.4%	2.2%	2.4%	3.2%	4.2%	5.3%	8.6%
	SEMI	3	-1.2%	-1.1%	-1.1%	-0.7%	-1.2%	-1.9%	-0.4%
	ROUND	4	-3.2%	-3.7%	-3.1%	-3.2%	-2.7%	-3.4%	-2.0%
	SEMI	4	-2.6%	-3.2%	-3.3%	-3.0%	-3.0%	-5.0%	-5.7%
<b>FLEX</b>	ROUND	1	5.7%	6.0%	4.9%	3.7%	5.8%	4.0%	5.5%
	SEMI	1	4.4%	2.8%	3.3%	3.7%	4.0%	3.5%	8.4%
	ROUND	2	4.8%	2.6%	3.4%	3.2%	2.9%	2.5%	4.2%
	SEMI	2	1.3%	0.2%	0.3%	0.3%	-0.6%	-0.8%	-0.8%
	ROUND	3	2.1%	4.8%	2.2%	2.2%	1.2%	1.1%	2.2%
	SEMI	3	-1.4%	1.6%	-1.0%	-0.6%	-1.1%	-0.8%	-0.3%
	ROUND	4	-2.4%	-3.4%	-3.8%	-3.9%	-4.8%	-4.2%	-3.5%
	SEMI	4	-3.3%	-3.5%	-3.8%	-3.5%	-4.1%	-3.7%	-5.5%
<b>PCC</b>	ROUND	1	-6.2%	-4.7%	-5.0%	-4.2%	-4.1%	-4.2%	-2.7%
	SEMI	1	-5.1%	-4.6%	-3.8%	-4.4%	-3.7%	-4.6%	-3.2%
	ROUND	2	-4.4%	-3.6%	-3.3%	-3.5%	-3.8%	-3.1%	-1.2%
	SEMI	2	-2.8%	-2.3%	-2.5%	-2.5%	-2.6%	-2.6%	-1.9%
	ROUND	3	-6.5%	-5.8%	-5.6%	-4.9%	-5.9%	-5.6%	-6.1%
	SEMI	3	-5.8%	-5.5%	-5.6%	-5.2%	-5.5%	-6.6%	-5.9%
	ROUND	4	-5.7%	-6.2%	-6.1%	-6.0%	-6.3%	-6.6%	-6.3%
	SEMI	4	-4.3%	-4.9%	-5.3%	-5.0%	-5.3%	-6.1%	-5.0%

TABLE 3 Modulus Backcalculation Results

Buffer Type	Drop Height	Modulus (psi)					
		Mean and Standard Deviation					
		E1		E2		Subgrade	
		Avg	StD	Avg	StD	Avg	StD
<b>Asphaltic Concrete:</b>							
50mm	1	726,023	22,075	110,229	17,587	25,108	378
90mm	1	769,002	42,213	110,441	25,012	25,616	571
flat	1	814,434	29,730	99,796	8,505	26,483	381
50mm	2	724,904	42,810	90,891	22,618	25,417	570
90mm	2	795,538	24,288	81,170	16,500	26,072	672
flat	2	844,738	31,873	69,128	12,140	26,199	429
50mm	3	754,251	7,973	76,698	4,535	25,650	300
90mm	3	821,911	22,962	69,960	7,266	26,093	134
flat	3	816,486	20,520	66,824	7,463	25,689	267
50mm	4	782,433	22,963	68,758	6,763	26,087	137
90mm	4	874,617	35,012	47,902	9,908	26,392	329
flat	4	849,474	17,421	47,156	6,359	25,340	279
<b>Asphalt Over Concrete:</b>							
50mm	1	388,539	24,369	4,384,293	377,297	21,287	415
90mm	1	680,371	175,288	3,177,245	475,285	23,590	469
flat	1	543,888	62,498	2,983,933	526,719	27,118	1,664
50mm	2	356,995	14,957	4,110,469	110,899	22,261	295
90mm	2	454,346	35,275	3,426,804	248,724	24,295	268
flat	2	403,908	26,442	3,855,991	243,590	24,890	273
50mm	3	389,053	8,922	3,944,405	59,896	23,072	150
90mm	3	419,324	21,778	3,527,551	97,856	24,586	209
flat	3	391,915	11,246	3,598,230	159,869	24,205	388
50mm	4	380,123	9,790	3,801,212	76,751	24,394	260
90mm	4	409,118	9,360	3,345,549	106,942	24,769	178
flat	4	378,759	7,785	3,514,400	85,426	23,882	129
<b>Concrete:</b>							
50mm	1	4,240,671	121,503	11,031	630	13,917	221
90mm	1	4,306,675	111,792	9,861	476	14,108	130
flat	1	3,868,785	116,369	10,298	832	13,603	163
50mm	2	4,159,983	101,371	11,772	897	13,784	259
90mm	2	4,177,051	86,820	10,790	739	13,932	227
flat	2	4,125,816	82,800	9,907	556	13,736	200
50mm	3	4,436,835	100,511	11,202	1,120	13,983	236
90mm	3	4,205,421	44,918	11,873	373	13,869	157
flat	3	3,983,088	60,705	10,909	400	13,173	133
50mm	4	4,516,514	66,573	11,122	365	13,923	99
90mm	4	4,321,860	56,777	11,562	70	13,689	32
flat	4	4,302,819	62,650	10,094	608	13,152	98

• Changing the shape of the load pulse and its rise and dwell time does affect the magnitude of the measured deflections. This change, however, is not considered to be significant for routine production testing and analysis, but may be of interest to pavement researchers.

As the knowledge of system behavior advances, it is likely that some of this information will be important in understand-

ing the behavior of pavement systems and predicting their performance. With the equipment available, different loading rates may be applied to pavements, and the corresponding deflection response may be measured. If a change in response occurs, it may be possible to associate it with the viscoelastic characteristics of asphalt or with the dynamic forces associated with the mass and internal dampening of the pavement system.

## ACKNOWLEDGMENT

This paper was prepared for SHRP to document the information available on the use of various rubber buffers during operation of the Dynatest FWDs.

## REFERENCES

1. *Strategic Highway Research Program: Research Plans*. TRB, National Research Council, Washington, D.C., 1986.
2. *SHRP-LTPP Manual for FWD Testing, Operational Field Guidelines, Version 1.0*. Operational Guide SHRP-LTPP-OG-002. SHRP, National Research Council, Washington, D.C., Jan. 1989.
3. *Dynatest 8000 FWD Test System, Owners Manual—Part 1, Operating Instructions*. Dynatest Engineering, Ojai, Calif., 1988.
4. *SHRP LTPP Evaluation of Backcalculation Software, Data Forms, Software, and User's Manual*. SHRP, National Research Council, Washington, D.C., Jan. 1991.

## DISCUSSION

CARL LENNGREN

University of Minnesota, Department of Civil and Mineral Engineering, 500 Pillsbury Drive, S.E., Minneapolis, Minn. 55455.

The author has shown the importance of using the appropriate buffers in the falling weight deflectometer (FWD). Because similar research is under way at the University of Minnesota, it seems fitting to make a few comments on the subject.

Like the author, we at the University of Minnesota have noted a change in the stiffness of asphalt concrete through the changing of buffers, but we would also point out the great influence temperature has on the material. Further, the backcalculation procedure produces some uncertainty about the moduli that may not always reflect statistically significant effects of the loading time (i.e., more than a few tests are usually necessary). However, strain gauges at the bottom of the asphalt layer have confirmed our findings of a change in modulus due to loading time.

It should be mentioned that the problems discussed in the paper of controlling the loading curve have been thoroughly investigated by Tholén. The solution he offered was a dual-mass loading system (1,2). The dual-mass system results in a much smoother application of the load without any bumps or flattened tops in the loading time curve. The loading time of the dual-mass system may be varied without affecting the shape of the curve. Thus, by changing buffers one is capable of varying the loading time without otherwise changing the characteristics of the load. A time history of a load from a dual-mass FWD that was equipped with standard buffers for highway testing is shown in Figure 6. Shown in Figure 7 is a test at the same site for which stiffer buffers, intended for airport pavement testing, were used, yielding a shorter loading time. As shown, the shape of the curves are practically the same.

In this particular case, the pavement consisted of 12-in., full-depth asphalt concrete. The shorter load application resulted in an asphalt concrete modulus increase of about 10 percent. However, some tests at this site showed little or no difference in stiffness. Other pavements and load levels rendered a difference in stiffness of as much as 20 percent. Thus,

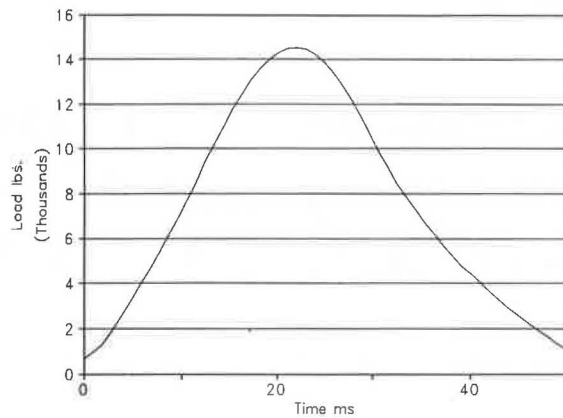


FIGURE 6 Time history of load from dual-mass FWD equipped with standard buffers for highway testing.

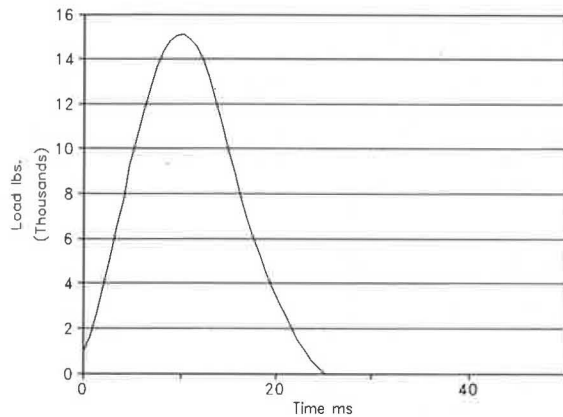


FIGURE 7 Test for which stiffer buffers, intended for airport pavement testing, were used, yielding a shorter loading time.

it seems possible to assess this important property of asphalt concrete. Actually, as the change of loading time mimics a change in temperature, testing with different loading times appears to be a way to overcome the problems of assessing an appropriate temperature correction for the material tested. Two FWDs operating in tandem could be a strong alternative for critical work.

## REFERENCES

1. O. Tholén. *Falling Weight Deflectometer—A Device for Bearing Capacity Measurement: Properties and Performance*. Bulletin 1980:1. Department of Highway Engineering, Royal Institute of Technology, Stockholm, Sweden, 1980.
2. O. Tholén. *Testing Different FWD Loading Times*. Bulletin 1980:8. Department of Highway Engineering, Royal Institute of Technology, Stockholm, Sweden, 1980.

# Evaluation of a Dual-Load Nondestructive Testing System To Better Discriminate Near-Surface Layer Moduli

REYNALDO ROQUE, PEDRO ROMERO, AND BYRON E. RUTH

Theoretical analyses were conducted to illustrate the inability of the existing single-load falling weight deflectometer (FWD) to discriminate among near-surface layer moduli of flexible pavement systems. Comprehensive analyses were also conducted to show that this deficiency can be overcome by using a dual-load FWD when the loads are spaced sufficiently apart to induce a concave downward curvature in the pavement surface between the loads (transverse deflection basin). The analyses showed that the asphalt concrete modulus is strongly, and almost uniquely, related to the curvature of this transverse deflection basin, whereas the base course modulus is strongly, and almost uniquely, related to the shape of the longitudinal deflection basin. This strong correspondence was shown to hold true for a broad range of pavement geometries and layer moduli. Stress and deformation analyses were conducted to show that the dual-load system works because the shape of the transverse deflection basin is most strongly influenced by the bending moments induced within the asphalt concrete layer between the loads, and by the relatively large changes in vertical compression that are induced in the asphalt concrete layer within this zone. Neither of these effects is observed in the base course, which explains the lack of influence of the base course on the shape of the transverse deflection basin. Finally, an analysis was conducted to select load radii and spacing, and deflection sensor positions that optimize the capabilities of a dual-load system to discriminate among near-surface layer moduli. It was shown that a set of relatively simple equations can be developed to determine (backcalculate) pavement layer moduli obtained from surface deflection measurements using the dual-load system proposed.

Nondestructive testing is now a commonly accepted method for pavement structural evaluation. The surface deflections produced under a load are routinely used for determining pavement layer moduli in analysis and design. Of the numerous devices that have been developed for this purpose, the falling weight deflectometer (FWD) is probably the most widely used. Its advantages include simplicity, capability to use variable loads, and the claim that the loading induced by the instrument closely simulates a moving wheel load. However, several disadvantages are also associated with the instrument.

Ruth et al. (1) and Badu-Tweneboah et al. (2) showed that the deflection basin resulting from the single-load FWD did not allow for accurate discrimination of different pavement layer moduli, particularly the moduli of near-surface layers.

---

R. Roque and P. Romero, The Pennsylvania Transportation Institute, Pennsylvania State University, Research Office Building, University Park, Pa. 16802. B. E. Ruth, University of Florida, 346 Weil Hall, Gainesville, Fla. 32611.

They also showed that deflections resulting from a dual-load system such as the dynaflect allowed for better discrimination of near-surface layer moduli when appropriate deflection measurements were obtained. They used a modified sensor configuration that defines deflection basins in both the longitudinal and transverse directions. However, the relatively small and fixed load levels used by the dynaflect system are a distinct disadvantage, particularly when determining effective layer moduli, which may depend on the load level used. In addition, the semirigid, noncircular loads are hard to model with existing analysis programs and prevent measurements from being obtained directly under the load.

These observations imply, however, that a superior system can and should be designed to provide optimal discrimination for each layer. A dual-load FWD would have these capabilities. The two loads would result in improved discrimination of pavement layer moduli while maintaining the advantage of using variable load levels similar to design wheel loads.

## OBJECTIVES

The work reported in this paper was part of a comprehensive study conducted for the Florida Department of Transportation. The objectives were as follows:

1. To determine whether a dual-load nondestructive testing system provides for better discrimination of near-surface layer moduli than the existing single-load FWD;
2. To identify a dual-load system configuration (load radii and spacing, and deflection sensor positions) that optimizes the capabilities of the dual-load system to discriminate among near-surface layer moduli;
3. To develop analysis procedures (backcalculation) to determine layer moduli using surface deflection measurements that would be obtained from the dual-load system configured.

All three objectives were met, but this paper deals primarily with the first two objectives. The development of relationships for modulus prediction and their integration into a computer program was a study in itself and was considered beyond the scope of this paper. The specific objectives of this paper are as follows:

1. To illustrate the inability of the existing single-load FWD to discriminate among the near-surface layer moduli of flexible pavement systems (asphalt concrete, base, and subbase);

2. To show that this deficiency can be overcome by using a dual-load FWD where the loads are spaced sufficiently apart to induce a concave downward curvature in the pavement surface between the loads;

3. To show why the dual-load system is more effective in isolating the effects of the asphalt concrete from the effects of the base course on the surface deflections;

4. To show that the improved discrimination of the dual-load system holds true for a broad range of pavement geometries and pavement layer moduli; and

5. To present the analyses and rationale used to select the dual-load system configuration (load radii and spacing, and deflection sensor positions) that optimizes the capabilities of the dual-load system to discriminate among near-surface layer moduli.

**SCOPE**

Only flexible pavement systems were considered in this study. All analyses were conducted using the elastic layer computer program BISAR (3). Therefore, the layer moduli being considered for determination are effective layer moduli for response prediction using elastic layer analysis. The evaluations reported here are based on analyses performed on a range of pavement geometries and layer moduli typically encountered in North America. The range of pavement geometries were identified using the Strategic Highway Research Program general pavement sections data base. A broad range of pavement layer moduli was selected.

**EVALUATION OF EXISTING FWD**

An evaluation of the deflection basins for a typical pavement structure clearly illustrates the inability of the existing single-load FWD to discriminate among the near-surface layer moduli of flexible pavement systems (asphalt concrete, base, and subbase). Figures 1 and 2 show that for a typical pavement structure (6-in. asphalt concrete, 10-in. base course, 10-in.

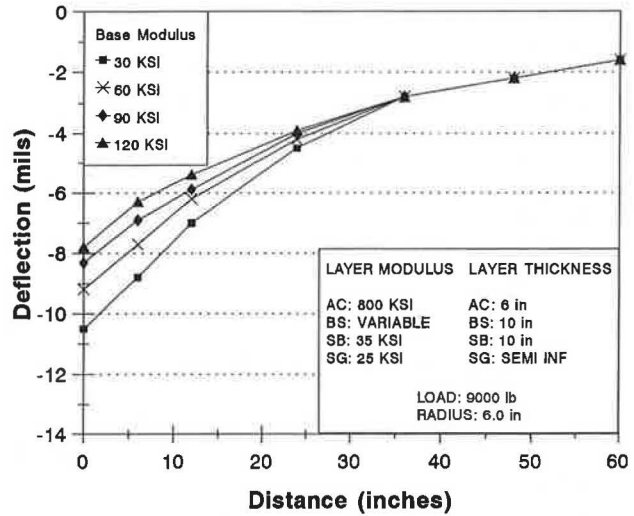


**FIGURE 2** Effect of changes in the base course modulus on predicted deflections for a single-load system.

subbase, and semi-infinite subgrade), changes in the asphalt concrete modulus affect the same portion of the deflection basin as changes in the base course modulus. Therefore, two different combinations of asphalt concrete and base course moduli may result in the same deflection basin. Figure 3 shows that reducing the base course modulus for a specific pavement structure by one-third has roughly the same effect on the deflection basin as does reducing the asphalt concrete modulus by one-half. It would be difficult to reliably determine the correct moduli of these near-surface layers on the basis of the measured surface deflections from the single-load FWD. One could attempt to use an asphalt concrete-temperature relationship to bound the problem, but temperature relationships are extremely rough at best because the modulus of the asphalt concrete will depend heavily on many other factors, including the degree of age-hardening and the characteristics of the specific mixture.

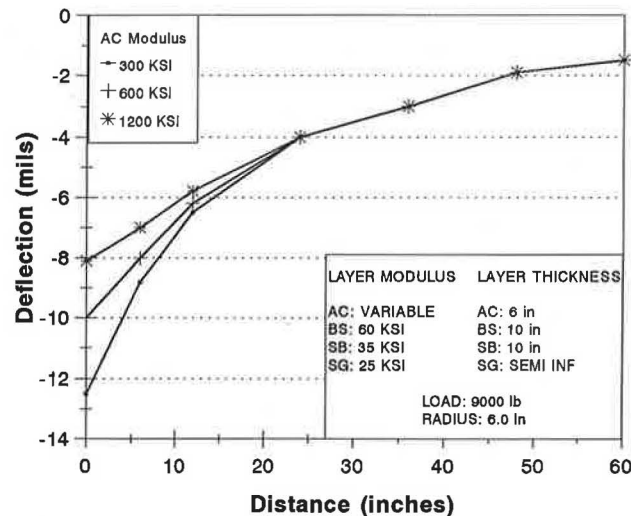


**FIGURE 1** Effect of changes in the asphalt concrete modulus on predicted deflections for a single-load system.

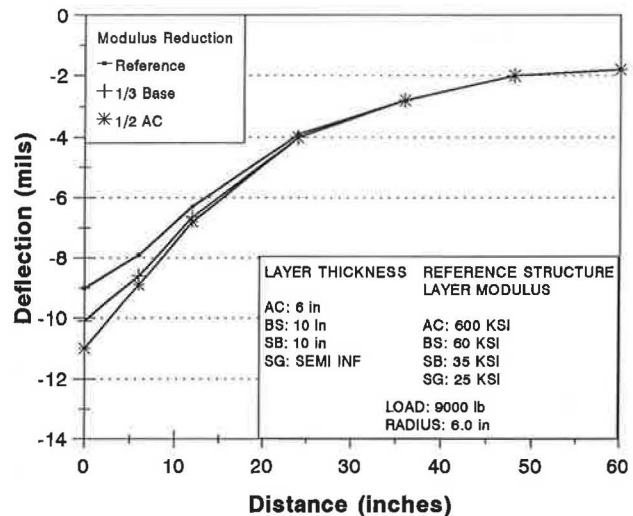


**FIGURE 3** Deflection basins caused by reducing the asphalt concrete or base course modulus for single-load system.

Although the results in this example are specific to the pavement structure used (i.e., the effect of changing the layer moduli on the deflection basin will be different for different pavement structures), they are fairly representative of what occurs for the range of pavement structures typically encountered (asphalt concrete from 3 to 9 in.; base course from 8 to 16 in.). The problem of discriminating near-surface layer moduli using the single-load FWD becomes more difficult for asphalt concrete layers thinner than the 6-in. layer used in the example.

**EVALUATION OF DUAL-LOAD SYSTEMS**

An evaluation of the transverse and longitudinal deflection basins for a dual-load system on the same pavement structure mentioned previously (see Figure 1) clearly illustrates the superiority of the dual-load system in independently isolating the effects of the asphalt concrete modulus and the base course modulus on the surface deflections. Figure 4 shows a plan view of the dual-load system. A load spacing of 40 in. was chosen for the analysis. The effects of varying the asphalt concrete modulus and the base course modulus on the transverse deflection basin are shown in Figures 5 and 6. Figure 5

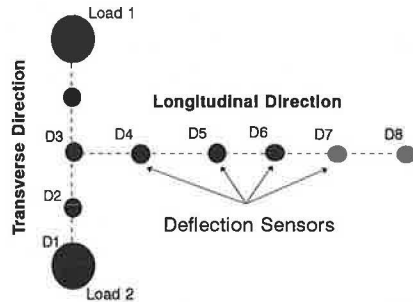


**FIGURE 4** Plan view of the dual-load system.

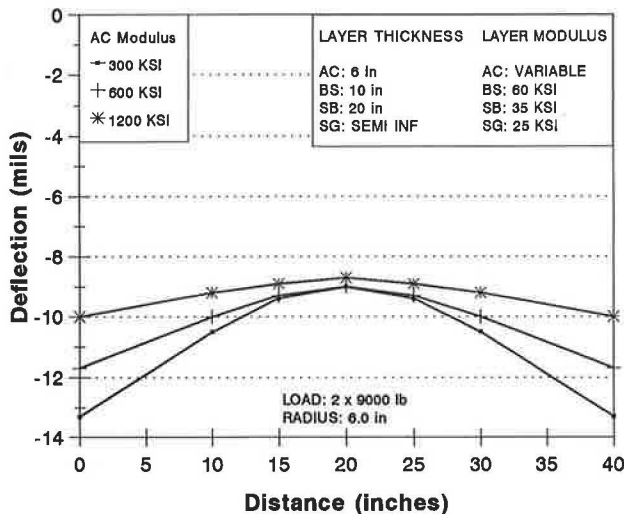


**FIGURE 5** Effect of changes in asphalt concrete modulus on transverse deflection basin for dual-load system: 40-in. spacing.

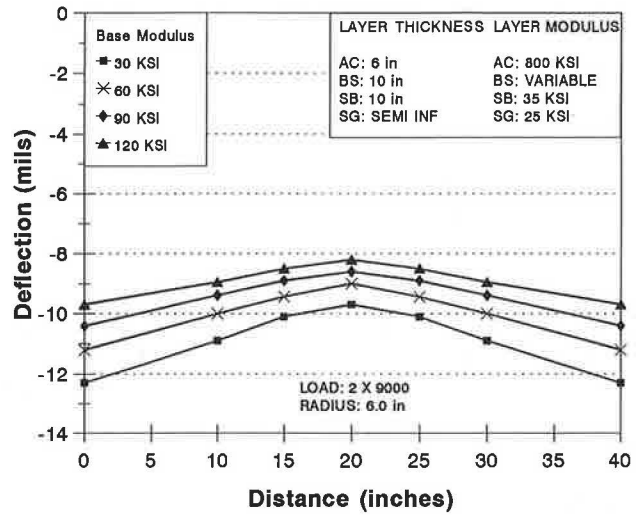


**FIGURE 6** Effect of changes in base course modulus on transverse deflection basin for dual-load system: 40-in. spacing.

clearly shows that the asphalt concrete modulus is strongly reflected in the shape of the transverse deflection basin of the dual-load system. As the asphalt concrete modulus varies from 300,000 psi to 1,200,000 psi, the deflection underneath the loads changes significantly, whereas the deflection immediately between the two loads remains constant. On the other hand, Figure 6 shows that the base course modulus has a relatively small influence on the shape of the transverse deflection basin. As the base course modulus varies from 30,000 psi to 120,000 psi the deflection change is relatively uniform at all points along the deflection basin. Therefore, the shape of the transverse deflection basin appears to provide a clear way to discriminate between the effects of the asphalt concrete modulus and the base course modulus. Later in this paper it will be shown that the strong relationship between the asphalt concrete modulus and the shape of the transverse deflection basin for a dual-load system was found to hold true for a broad range of pavement geometries and layer moduli.

An evaluation of the longitudinal deflection basins shown in Figures 7 and 8 clearly demonstrates that the base course modulus is strongly reflected in the shape of the longitudinal deflection basin, whereas the asphalt concrete modulus has a relatively small effect on the longitudinal deflections. Figure 7 shows that there is almost no change in the longitudinal deflection basin as the asphalt concrete modulus varies from 300,000 psi to 1,200,000 psi. Figure 8 shows that the deflections near the transverse centerline between the two loads decrease as the base course modulus varies from 30,000 psi to 120,000 psi. The figure also shows that the deflections beyond 30 in. away from the loads remain relatively constant as the base course modulus changes. Therefore, the shape of the longitudinal deflection basin appears to provide a clear way to discriminate between the effects of the asphalt concrete modulus and the base course modulus. Later in this paper it will be shown that the relationship between the base course modulus and the shape of the longitudinal deflection basin for a dual-load system was found to hold true for a broad range of pavement geometries and layer moduli.

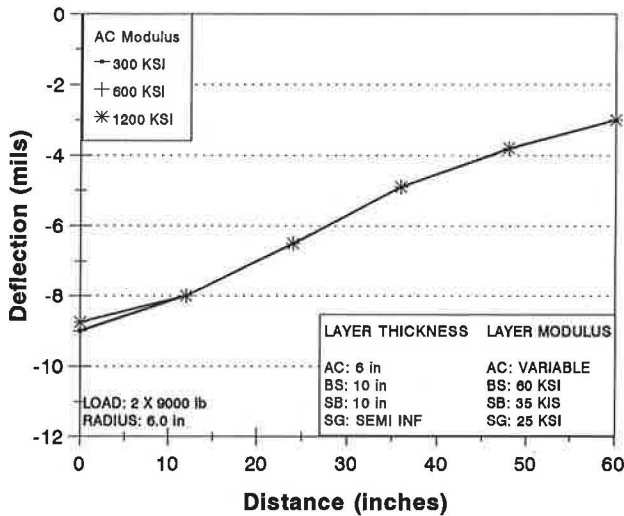


FIGURE 7 Effect of changes in asphalt concrete modulus on longitudinal deflection basin for dual-load system: 40-in. spacing.

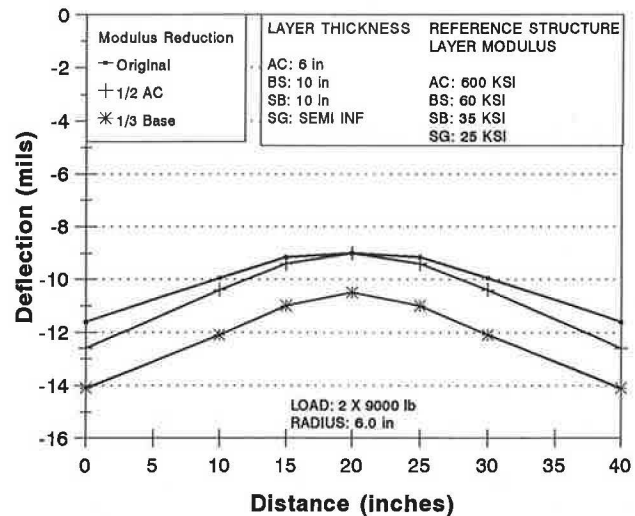


FIGURE 9 Transverse deflection basin caused by reducing asphalt concrete or base course modulus for dual-load system: 40-in. spacing.

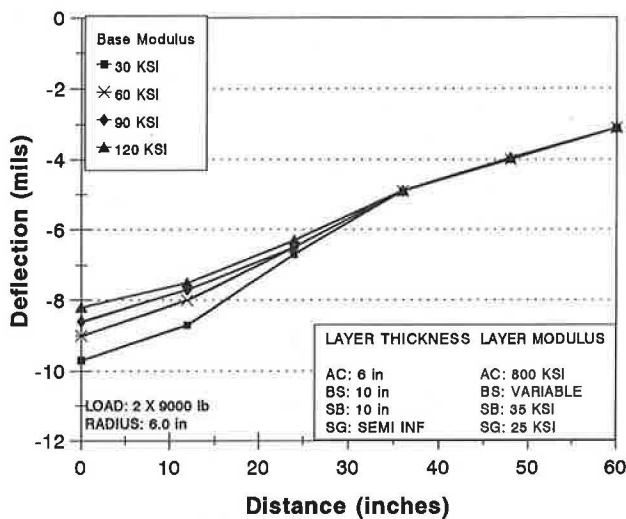


FIGURE 8 Effect of changes in base course modulus on longitudinal deflection basin for dual-load system: 40-in. spacing.

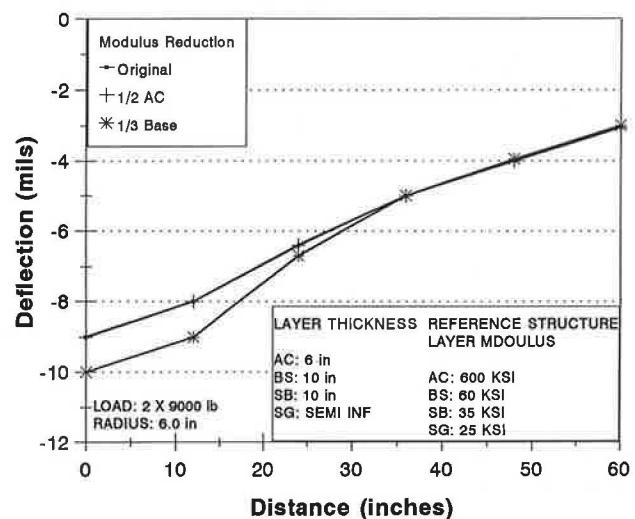


FIGURE 10 Longitudinal deflection basin caused by reducing the asphalt concrete modulus or base course modulus for dual-load system: 40-in. spacing.

In sharp contrast to the single-load FWD, Figures 9 and 10 show that two different combinations of asphalt concrete and base course moduli will not result in the same deflection basins for a dual-load system. Whereas for the single-load FWD, reducing the base course modulus by one-third had roughly the same effect on the deflection basin as reducing the asphalt concrete modulus by one-half (see Figure 3), the same modulus changes resulted in distinctly different changes in the transverse and longitudinal deflection basins for the dual-load system. Figure 9 shows that reducing the asphalt concrete modulus by one-half increased the deflections only under the load, whereas a reduction in base course modulus of one-third increased the transverse deflections uniformly. Figure 10 shows that only the reduction in base course modulus affected the longitudinal deflection basin.

#### ANALYSIS OF PAVEMENT RESPONSE INDUCED BY DUAL-LOAD SYSTEM

Stress and deformation analyses were conducted on a typical pavement structure to determine why the dual-load system works so well in isolating the independent effects of the asphalt concrete modulus and the base course modulus. An understanding of the system would allow configuration of a system that optimizes the capabilities to discriminate among the effects of near surface layer moduli. Deflection measurements obtained from such a system would optimize our chances of determining near-surface layer moduli accurately and reliably.

An evaluation of the stresses and deformations induced along a transverse cross-section of a typical pavement sub-

jected to a dual-load system demonstrates why the system works. Figure 11 shows that when the loads are spaced 40-in. apart, the surface deformations between the loads result in a concave downward deflection basin. As shown in the figure, this results in significant bending moments in the asphalt concrete layer between loads. Basic mechanics demonstrates that the curvature resulting from these bending moments depends on the stiffness (modulus and thickness) of the asphalt concrete layer. Figure 11 also shows that the bending moments induced in the base course are negligible so that the stiffness of the base course should have a negligible influence on the curvature of the surface, which agrees with the findings presented previously.

An evaluation of the vertical compressive stress distribution in the asphalt concrete and the base course layers shows that the effect of the base course modulus on the shape of the surface deflection basin should be negligible compared to the effect of the asphalt concrete modulus. Figures 12 and 13 show vertical stress distributions at different depths along the transverse cross-section of the pavement for base moduli of 30,000

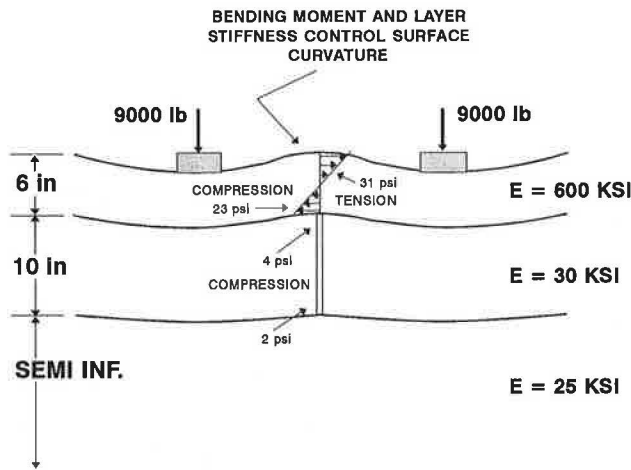


FIGURE 11 Stresses and deformations induced by a dual-load system.

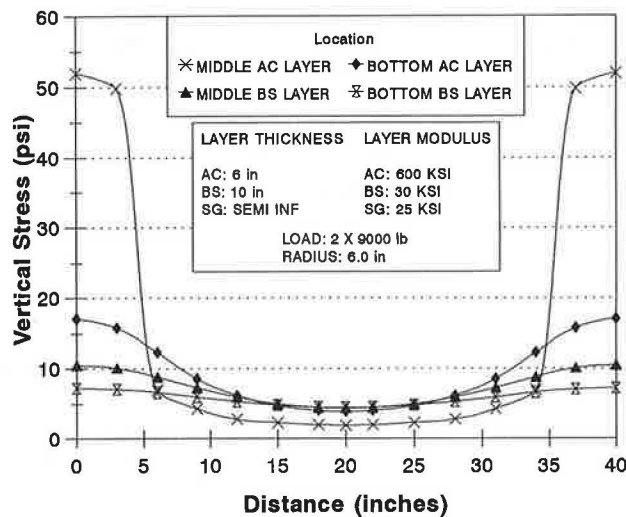


FIGURE 12 Vertical stress distributions induced by a dual-load system: 40-in. spacing, low-modulus base.

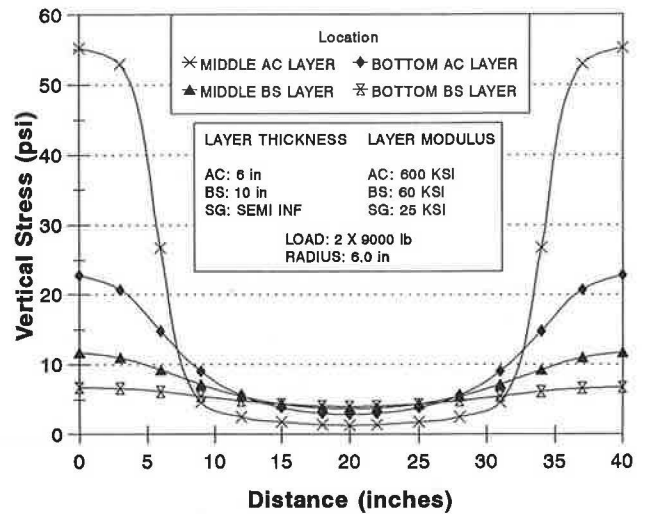


FIGURE 13 Vertical stress distributions induced by a dual-load system: 40-in. spacing, high modulus base.

psi and 60,000 psi, respectively. In both cases, the transverse stress distribution within the base layer is relatively uniform compared with the stress distribution within the asphalt concrete layer. Note that it is the variation in stresses that results in changes in the shape of the deflection basin. Changes in the base modulus will result in changes in total deflections, but the stress distributions imply that these changes should be uniform. Once again, this agrees with the findings presented earlier.

**DETERMINATION OF OPTIMAL LOAD-SPACING AND LOAD RADIUS**

The analyses presented previously clearly indicate that the asphalt concrete modulus is and should be strongly related to the shape of the transverse deflection basin for a dual-load system. This implies that load spacings, which produce sharper (rather than flatter) concave downward transverse deflection basins between the loads, will optimize the system's capability to discriminate among the effects of the near-surface layer moduli. This will allow for more accurate and reliable determination of these moduli. Furthermore, the system's deflection sensors must be positioned to define both the transverse and longitudinal deflection basins accurately enough to detect the independent changes caused by the different pavement layers.

The key to obtaining sharper deflection basins for optimal discrimination among the surface layer moduli is to position the loads sufficiently far apart to cause significant bending moments in the region immediately between the loads. If the loads are too close, such that strong interactions develop between the loads, these moments may never develop or the entire surface between the two loads may be in a state of horizontal compression. On the other hand, if the loads are spaced too far apart, the loads may act independently of each other, which would essentially result in two single-load systems. In either case, the advantages of the dual-load system would be lost.

Given that the shape of the transverse deflection basin would be influenced not only by the load spacing, but also by the pavement geometry and layer moduli, a comprehensive analysis was conducted to determine an optimal load spacing that would result in appropriate deflection basins for a broad range of pavement structures. The values shown in Table 1 were considered in the analysis.

The following constraints limited the ranges of acceptable load radii and spacings:

- The load levels used for testing should be representative of the load levels attained in the field. The load level chosen will govern the radii used to obtain average pressures similar to the ones obtained in the field.
- The center-to-center spacing of the loads should be kept as close as possible to make the construction of a dual-load system possible. A spacing greater than 40 in. was considered impractical.

Assuming 9,000 lbs per load, the resulting average stress under each load would be as follows:

- 179 psi for a 4.0 in. radius,
- 114 psi for a 5.0 in. radius, and
- 79.5 psi for a 6.0 in. radius.

These ranges were considered to be acceptable in pressures, such that radii less than 4.0 in. or greater than 6.0 in. were not considered for evaluation.

Elastic layer analyses were conducted for the range of pavement structures listed in Table 1, using load spacings of 20, 30, and 40 in. and load radii of 4 and 6 in. Typical results of the analyses are shown in Figures 14 and 15, which show transverse deflection basins for a 4-in. and 8-in. asphalt concrete pavement, respectively. Both figures indicate that load radius had little effect on the shape of the deflection basin. Figure 14 shows that for the thinner pavement section, all three load spacings resulted in fairly sharp transverse deflection basins, which would allow for accurate discrimination among near-surface layer moduli. This was typical for the thinner (lower stiffness) sections investigated, and indicated that there was no advantage of using one load spacing over another.

For the thicker (higher stiffness) sections investigated, it was found that wider load spacings were required to obtain deflection basins with reasonably sharp curvatures. A typical example is shown in Figure 15, which shows that the 40-in. spacing offers a slight advantage over the 30-in. spacing and a significant advantage over the 20-in. spacing in producing measurable deflection differences along the transverse axis.

**TABLE 1 Pavement Layer Thickness and Moduli Considered for Analysis**

Layer	Moduli (ksi)	Thicknesses (in)
Asphalt Concrete	200, 400, 600, 800, 1200	4, 6, 8, 12
Base Course	20, 40, 60, 80, 120	5, 10, 20
Subbase	**	5, 10, 15
Subgrade	5, 15, 25, 50	semi-infinite

\*\*The subbase modulus was varied between the subgrade modulus and the base modulus (i.e. it was never allowed to be greater than the base modulus or less than the subgrade modulus).

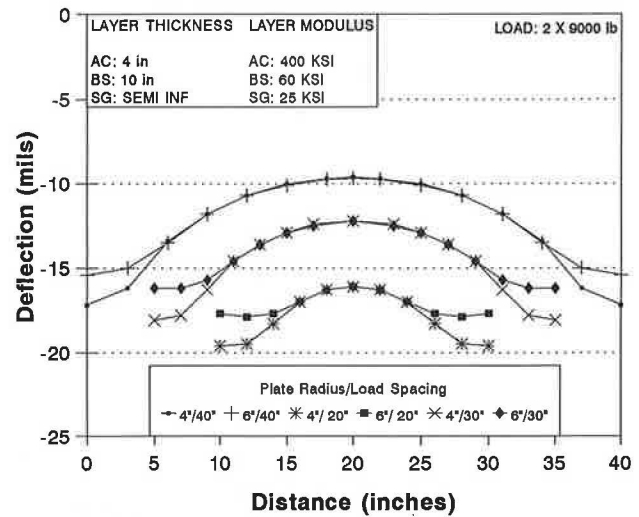


**FIGURE 14 Comparison of transverse deflection basins induced by different load-spacing and radii on 4-in. pavement section.**

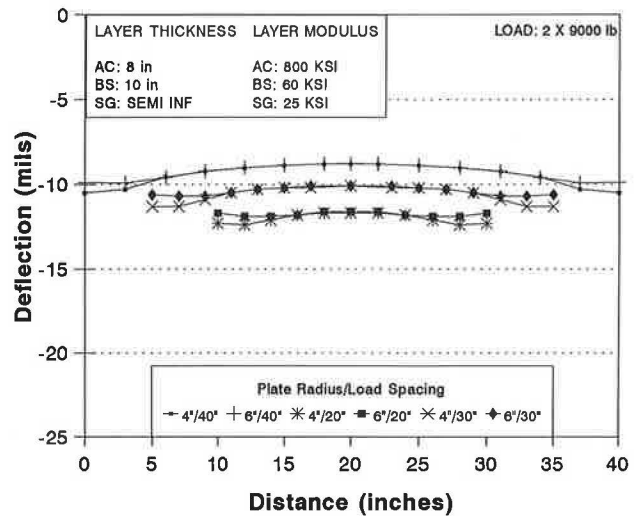


**FIGURE 15 Comparison of transverse deflection basins induced by different load spacing and radii on 8-in. pavement section.**

Based on these analyses, and the fact that spacings greater than 40 in. were considered impractical, a spacing of 40 in. was selected for the optimal system configuration. A load radius of 6 in. was selected for further evaluation. However, any load radius from 4 to 6 in. may be considered acceptable, because the radius of the load was found to have little influ-

ence on the shape of the deflection basins. A 6-in. radius would allow for larger loads to be used without overstressing and possibly damaging the surface layer during testing.

### EVALUATION OF THE DUAL-LOAD SYSTEM CONFIGURATION

An evaluation of the deflection basins resulting from the dual-load system configured previously (40-in. load spacing, 6-in. radius loads) was conducted for the range in pavement structures and layer moduli generally encountered in North America. These analyses showed that the relationships between the shape of the transverse deflection basin and the asphalt concrete modulus, and between the shape of the longitudinal deflection basin and the base course modulus, held true for almost all pavement structures investigated.

Elastic layer analyses were conducted using BISAR to determine the transverse and longitudinal deflection basins resulting from the dual-load system configured previously for every combination of the layer thicknesses and of layer moduli shown in Table 1. An analysis was conducted to determine whether there was a strong correspondence between the shape of the transverse deflection basin and the asphalt concrete modulus. The difference in deflections between the point immediately underneath the load (D1) and the point immediately between the loads (D3) was used as the parameter to represent the shape of the transverse deflection basin. The following relationship was found for a typical pavement structure (6-in. asphalt concrete, 10-in. base, 10-in. subbase, semi-infinite subgrade).

$$EAC = e^{[7.22 - 0.55(D1 - D3)]} \quad R^2 = 84.4 \text{ percent} \quad (1)$$

where

- $EAC$  = asphalt concrete modulus (ksi),
- $D1$  = surface deflection directly under one of the loads ( $\times 10^{-3}$  in.),
- $D3$  = surface deflection exactly between the two loads ( $\times 10^{-3}$  in.).

Similarly, the base course modulus was found to be related to the shape of the longitudinal deflection basin for the range of pavement structures investigated. The relationship involved interactions with the subbase and subgrade moduli, such that a simple correlation as shown in Equation 1 could not be obtained.

It should be emphasized that Equation 1 is not intended to predict asphalt concrete modulus directly but only to show the strong correlation between the asphalt concrete and the shape of the transverse deflection basin as would be measured

by the dual-load system. Predictive equations for all layer moduli, which account for the effects of layer thicknesses and interactions among layer moduli, were developed successfully based these analyses. However, presentation and development of these equations is beyond the scope of this paper.

### CONCLUSIONS AND RECOMMENDATIONS

The following conclusions were reached on the basis of the results of the analyses presented in this paper:

1. A dual-load nondestructive testing system provides for better discrimination of near-surface layer moduli than the existing single-load FWD.
2. The dual-load system works because the shape of the transverse deflection basin induced between the two loads is most strongly influenced by the bending moments induced within the asphalt concrete layer between the loads and by the relatively large changes in vertical compression which are induced in the asphalt concrete layer between the loads.
3. A dual-load spacing of 40 in. was found to provide for optimal discrimination of near-surface layer moduli for the broad range of pavement geometries and layer moduli generally encountered in North America.
4. Because of the relatively strong and direct correlations between different layer moduli and surface deflections for a dual-load system, it appears that a set of relatively simple regression equations can be developed to determine layer moduli.

It is recommended that the dual-load system configured in this paper be constructed and implemented for field testing.

### REFERENCES

1. B. E. Ruth, M. Tia, K. Badu-Tweneboah. *Structural Characterization and Stress Analysis of Flexible Pavement Systems*. Final report, State Project 99700-7351-010. Florida Department of Transportation; University of Florida, Gainesville, July 1987.
2. K. Badu-Tweneboah, C. W. Manzione, B. E. Ruth, and W. G. Miley. Prediction of Flexible Pavement Layer Moduli from Dynaflect and FWD Deflections. In *Nondestructive Testing of Pavements and Backcalculation of Moduli* (A. J. Bush and G. Y. Baladi, eds.), ASTM STP 1026, ASTM, Philadelphia, Pa., 1989.
3. D. L. DeJong, M. G. F. Peutz, and A. R. Korswagen. *Computer Program BISAR, Layered Systems Under Normal and Tangential Loads*. Kononklijke-Shell Laboratorium, Amsterdam, The Netherlands, 1973.

---

*Publication of this paper sponsored by Committee on Strength and Deformation Characteristics of Pavement Sections.*

# Estimating Damage Effects of Dual versus Wide Base Tires with Multidepth Deflectometers

TAYYEB AKRAM, TOM SCULLION, ROGER E. SMITH, AND  
EMMANUEL G. FERNANDO

Multidepth deflectometers (MDDs) were successfully used to assess the relative damage of dual and wide base single tires. In this study MDDs were installed in two in-service asphaltic concrete highways (one thick, one thin) to measure the pavement response to vehicle loading. A specially configured 3S2 truck was used in the study. It is an 18-wheel water tanker that was converted to a 14-wheel tanker for this study. For the first set of data collection, dual tires were used on the tandem drive axle with wide base single tires on the tandem trailer axle. For the second set, wide base single tires were used on the tandem drive axle and dual tires on the trailer axle. Deflections measured at several depths within the pavement by MDD under dual and wide base single tires were used to calculate average vertical compressive strains. The Asphalt Institute subgrade limiting strain criteria were used to estimate the reduction in pavement life that will occur by using the wide base single tires in place of duals. Wide base single tires were found to be more damaging on both tandem drive and tandem trailer axle positions. At a speed of 55 mph and equivalent axle loading, it was found that the wide base single tires (trailer axle) reduced the anticipated pavement life on the thin and thick sections by a factor of between 2.5 and 2.8 over that predicted for standard dual tires.

Since the AASHO Road Test (1) several new tire types, sizes and configurations have been used by the trucking industry. Changes in tires and wheel configuration for heavy trucks have generated concern about the potential increase in highway pavement damage. Early concerns were related to an increase in tire inflation pressure that accompanied the change from bias-ply tires to radial-ply tires. Of particular current concern is the use of single wide base tires (super single) (2-6). In a conversion application, a single wide base tire replaces the conventional dual tire assembly, thereby reducing the typical "18 wheeler" to a "10 wheeler."

Proponents claim that using wide base single tires on truck tractors and trailers improves fuel consumption, ride, handling, and braking while reducing tire cost and increasing payload. Replacing duals also releases the vehicle designer from the requirements for demountable wheel or rim assemblies for access to the inside tire (7).

However, a major concern of highway agencies regarding using wide base single tires is their impact on pavement de-

terioration. A technique developed to monitor transient relative deflection and permanent deformation in pavement layers under moving vehicular loading is described here. The device developed for this purpose is called a multidepth deflectometer (MDD) (8). From the deflections measured at various depths, typically measured at the layer interfaces, it is possible to backcalculate the elastic moduli of the layers.

The aim of this paper is to present and compare pavement responses under dual and wide base single tires on tandem axles for different speeds. The deflection measurements were made on two in-service asphaltic concrete pavement sections. Measurements were made at vehicle speeds between 4 and 55 mph. Peak deflection profiles under the two tire types at different lateral offsets were compared. Vertical compressive strains measured near the top of the subgrade were used to estimate and compare the allowable number of equivalent single axle load (ESAL) repetitions for dual and wide base single tires.

## MEASUREMENT SYSTEM

The MDD is made up of modules with linear variable differential transformers (LVDTs) as shown in Figure 1. The modules are locked into the different pavement layers to measure the relative movement in these layers with respect to an anchor point located approximately 8 ft below the pavement surface (9). A typical setup is shown schematically in Figure 2. The detailed description, installation techniques, and precautions for the installation of the MDD system are described in detail elsewhere (8,9).

A specialized data acquisition system has been developed at the Texas Transportation Institute to record the MDD pulse under both falling weight deflectometer (FWD) and truck loadings. A Compaq 386/20 microcomputer is used with a Data Translation (DT 2814) circuit board to provide a maximum sampling rate of 5,000 readings per channel per second. For recording truck data, the truck length is the input, the sampling rate is automatically calculated, and the data collection is automatically started by a response of any sensor greater than a preset trigger level. For trucks typically 1,000 data points per channel are stored. The files created are read directly into a spreadsheet software package for display and analysis.

Texas Transportation Institute, Highway Materials Division, Texas Transportation Institute, Texas A&M University, College Station, Tex. 77843.

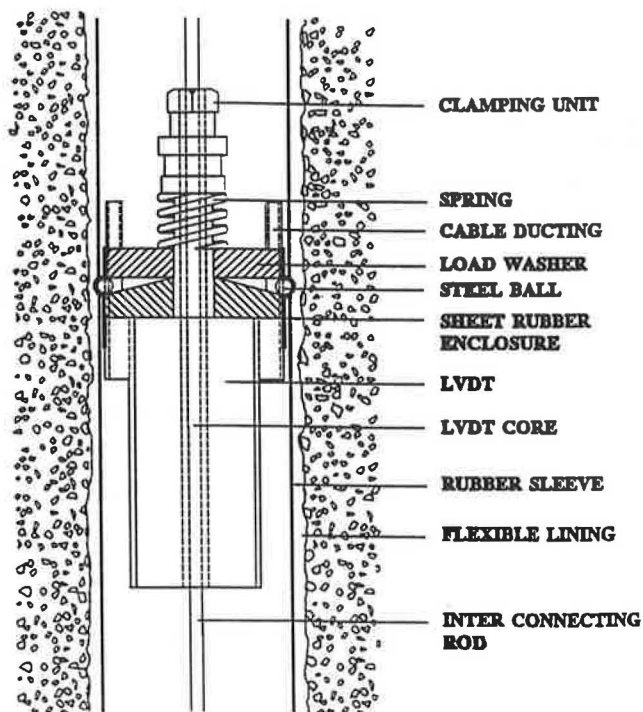


FIGURE 1 MDD module.

#### LAYOUT OF TEST SECTIONS AND INSTRUMENTATION

Two test sites were selected on in-service highways to investigate the effects of truck tire type and speed on both thick and thin asphaltic concrete pavements. MDDs with four LVDT modules each were installed in the outer wheel path at each site. The cross-sections of the test sections showing the locations of MDD sensors are shown in Figure 3.

Section I has a hot-mix asphalt concrete (HMAC) thickness of 1.5 in. and a crushed limestone base course thickness of 10 in. overlaying a sandy clay subgrade. The average value of the international roughness index (IRI) for Section I is 95.82 in./mi. Section II has an HMAC thickness of 7 in., a crushed limestone base course thickness of 14 in., and a 6-in. lime stabilized subbase overlaying a sandy clay subgrade. The average value of the IRI for Section II is 85.87 in./mi. In situ properties measured are presented in Table 1.

#### TEST VEHICLE

The test vehicle is a specially prepared 3S2 truck consisting of a steering axle, tandem drive axles, and tandem trailer axles. It is an 18-wheel water tanker that was converted to a 14-wheel vehicle by replacing dual wheels on one set of tandem axles with wide base single tires. Figure 4 shows the truck and the axle spacings.

To check if the loading sequence had any significant effect on the pavement response, two data sets were collected. The first set of data was collected with dual tires on the tandem drive axles and wide base single tires on the tandem trailer axles. The second data set was collected with the wide base

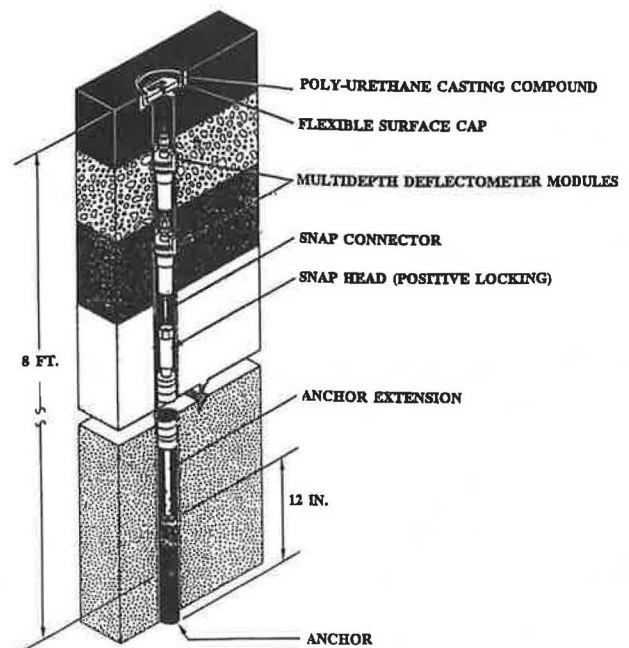


FIGURE 2 Typical cross-section of MDD after installation.

single tires on the drive axles and dual tires on the trailer axles.

The dual tires were 11R22.5, inflated to 120 psi (cold). The wide base singles were 425/65R22.5, inflated to 130 psi (cold). The tanker was filled with water to develop the desired load. The loads on the tandem drive and trailer axles and other test conditions are presented in Table 2.

#### TRUCK DATA COLLECTION

MDD response to the truck loading was recorded for four speed groups: less than 10 mph, 10–20 mph, 30–40 mph, and 40–60 mph. Four runs were made for each speed group. A typical plot of the MDD response from Section I under the passing test vehicle (five axles) at 10 mph speed is presented in Figure 5.

To determine the transverse position of the right side tires relative to the MDD location, a grid (6 in. × 6 in.) was painted on the pavement surface next to the MDD hole. As the test vehicle passed over the MDD, the transverse (or lateral) position of the outer tires (toward the shoulder) relative to the MDD position was recorded by a video camera. Using the width of the tires, the transverse positions of the centerline of the single tire and dual tire assemblies relative to the MDD location were determined.

Deflections at various depths within the pavement structure caused by each loading condition under the two tire types were recorded at truck speeds ranging from approximately 4 to 55 mph. Comparisons between the magnitude of the vertical compressive strains at top of the subgrade were made for both tire types at different speeds. The predicted allowable ESAL repetitions are solely dependent on the test conditions

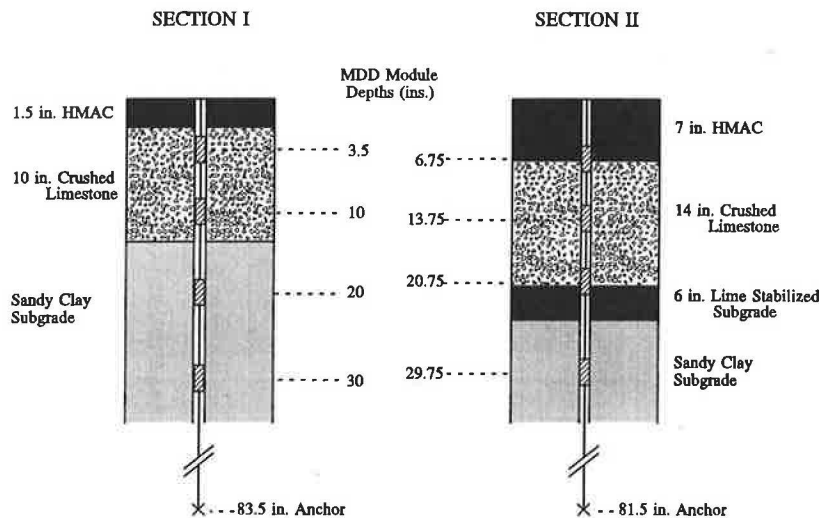


FIGURE 3 MDD location in test pavements.

TABLE 1 In Situ Soils Data for the Test Sections

Section	Base (B) or Subgrade (S)	Moisture Content (%)	Dry Density (pcf)
I	B	6.0	132.9
I	S	33.2	84.5
II	B	6.0	131.7
II	S	14.1	109.1

and should be viewed solely as the relative damage difference due to the effects of dual and wide base single tires.

**MOVING TANDEM AXLE LOAD PULSE DURATION**

As the moving truck approaches a point in the pavement, such as where the MDD is located, that point experiences vertical deflection, which increases until the wheel is directly over the point at which the deflection reaches its maximum value and then decreases as the wheel moves away. Typical MDD responses for the vehicle traveling at speeds of 10 and 55 mph on Section I are shown in Figures 5 and 6. The curves

represent the relative deflection response at depths of 3.5, 10, 20, and 30 in. The pulse width is much narrower for the faster vehicle loading. The measured pulse durations for speeds of 10 and 55 mph under the tandem axle loading are 1,053 msec and 180 msec, respectively.

The duration of the load pulse under the truck loading for a tandem axle at 55 mph speed is about 6 times the pulse duration for the FWD (28–30 msec). The duration of the pulse is related to the loading rate, which may affect the material properties.

**DEFLECTIONS UNDER DUAL AND WIDE BASE SINGLE TIRES**

Higher deflections were measured under the wide base single tires in both drive and trailer axle positions, under similar test conditions. The plot of peak deflections (Figure 7) at the bottom of asphalt layer (MDD1) shows that the dual tires cause less deflection than the wide base single tires.

The maximum deflection under the wide base single tire generally occurs under the tire centerline, whereas the maximum deflection under dual tires can occur under either of the tires. The same phenomenon was observed by Sharp et

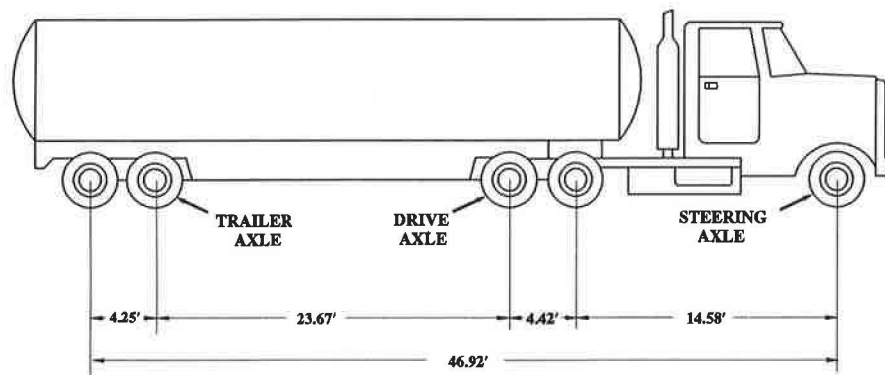


FIGURE 4 3S2 water tanker used for testing.

TABLE 2 Summary of Test Conditions

Section	Tire Type	Tandem Axle	Load (Kips)	Test Date		AC Temperature (°F)		
				From	To	Top	Middle	Bottom
I	Dual	Drive	33	11-13-90	11-13-90	80		79
I	Super Single	Trailer	33	11-13-90	11-13-90	80		79
I	Super Single	Drive	37	5-30-91	5-30-91	95		96
I	Dual	Trailer	37	5-30-91	5-30-91	95		96
II	Dual	Drive	33	10-15-90	10-16-90	80	76	73
II	Super Single	Trailer	33	10-15-90	10-16-90	80	76	73
II	Super Single	Drive	33	7-12-91	7-12-91	103	97	85
II	Dual	Trailer	33	7-12-91	7-12-91	103	97	85

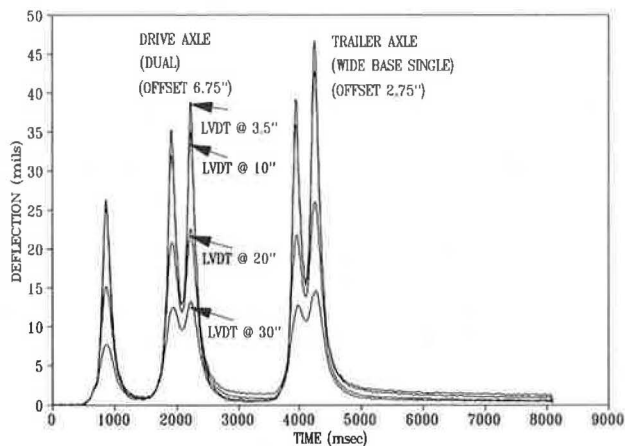


FIGURE 5 Typical MDD response from Section I under test vehicle (5 axles) passing at 10 mph.

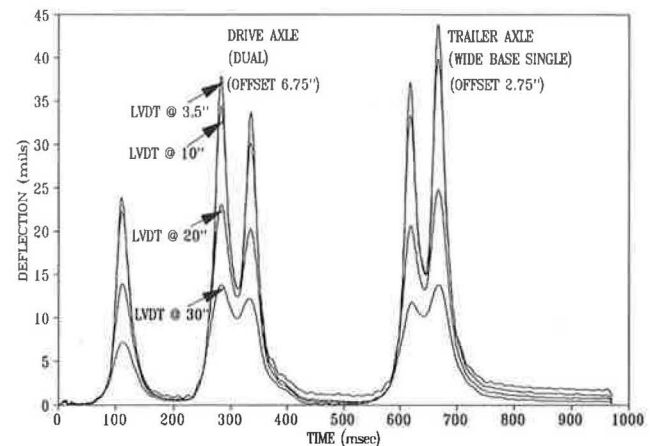


FIGURE 6 Typical MDD response from Section I under test vehicle (5 axles) passing at 55 mph.

al. (4). Another interesting feature of this plot is the rapid decrease in deflection at the edge of the wide base single. This is more significant in Section I (thin) than in Section II (thick), which indicates high shear forces at the edge of the wide base single tire. The deflection basin generated by the wide base single tires is deeper and more concentrated than that of regular dual tires. This phenomenon is no doubt detrimental to the pavement life. Although the focus of this paper is on induced rutting damage, these results indicate that wide base single tires may also generate more surface cracking.

#### VERTICAL COMPRESSIVE STRAIN MEASUREMENT IN BASE COURSE LAYER AND TOP OF SUBGRADE

The average vertical compressive strains within the pavement layers are calculated simply by subtracting the maximum deflection between two consecutive MDDs and dividing by the spacing between them. Compressive strains at top of the subgrade at different speeds for both sections are presented in Table 3.

#### Strain in the Base Course Layer

Response curves for strains in the base course material are shown in Figures 8 and 9. These response curves show dilation or extension in the base course material for both sections. Figure 8 indicates that in Section I (thin), the dilation occurs immediately before and after the wheel passes over the MDD. For Section II (thick), the dilation occurs only in front of each axle before the tire passes over the MDD, as shown in Figure 9. For the thin section the dilation is 7 times greater than the thick section. Uzan and Scullion (10) observed similar behavior in the base course layer for thin sections under FWD loadings.

#### Strain on Top of Subgrade and Effect of Speed

The effect of speed on vertical strain at top of the subgrade is shown in Figure 10. Increasing the speed from 10 to 55 mph decreased the measured strains on top of the subgrade for both sections. The wide base single tires were found to be more damaging than the dual tires in both drive and trailer axle positions.

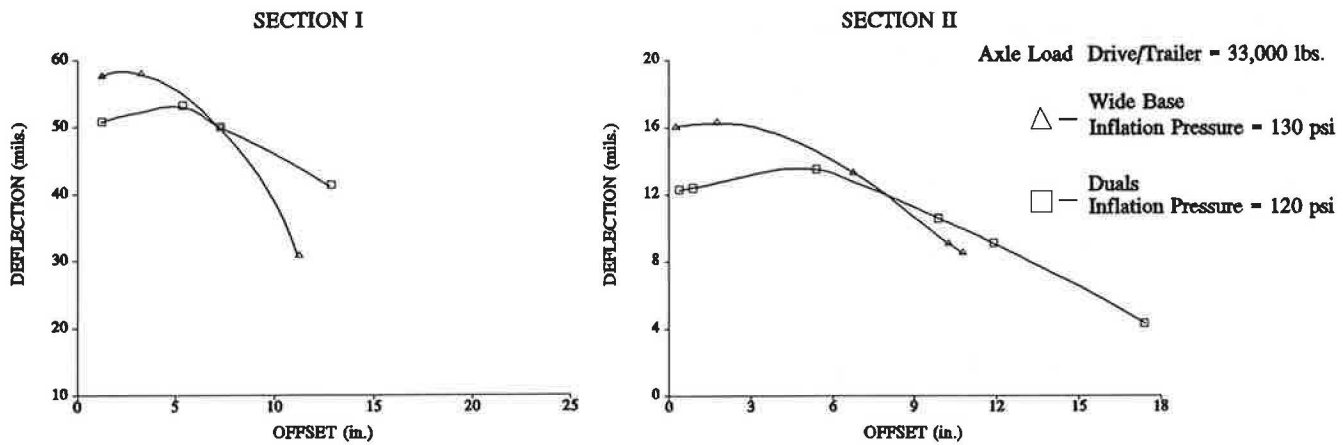


FIGURE 7 Peak deflections under dual and wide base single on MDD1 (speed 40–60 mph) at bottom of asphalt layer.

For the same loading conditions, with an increase of speed from 10 to 55 mph, the strain at the top of the subgrade at Section I decreased by 8 percent for dual tires and by 7 percent for wide base single tires. For similar conditions on Section II, the strain at top of the subgrade decreased by 13 percent under dual tires and 5 percent under wide base single tires.

At a speed of 55 mph, the measured vertical compressive strains under similar loading conditions at the top of the subgrade for Section I are found to be 26 percent higher under wide base single tires than for the dual tires. In Section II (thick), the strains under the wide base single tires are found to be approximately 23 percent higher than under the dual tires.

#### ESTIMATING REDUCTION IN PAVEMENT LIFE

The Asphalt Institute rutting criteria are widely used in pavement design (11). They provide the allowable number of ESAL repetitions for various levels of compressive strain at the surface of the subgrade and are expressed in the form

$$\epsilon_v = L(1/N)^m$$

where

$$\begin{aligned} N &= \text{permissible number of ESALs,} \\ \epsilon_v &= \text{subgrade vertical strain,} \\ L &= 1.05 \times 10^{-2}, \text{ and} \\ m &= 0.223. \end{aligned}$$

The allowable number of ESAL repetitions at different speeds and strain levels for both sections is tabulated in Table 3. Figures 11 and 12 show that the number of repetitions increases with speed for both tire types. On Section I, with an increase of speed from 10 to 55 mph, the predicted allowable number of dual and wide base single tire repetitions increased by approximately 45 percent and 39 percent, respectively. For the same speed increase on Section II, the number of dual and wide base single tire repetitions increased by approximately 87 percent and 26 percent, respectively.

At a speed of 55 mph under similar test conditions the wide base single tires were found to be 2.8 times more damaging

than the dual tires on Section I. Under similar test conditions on Section II, the wide base single tires were found to be 2.5 times more damaging. This indicates that wide base single tires are more damaging to thin bituminous pavements than to thick pavements.

#### PREDICTION OF SURFACE CRACKING

The main focus of this paper is estimating damage caused by increasing vertical compressive strain at the top of the subgrade. However, it appears that the wide base single tires may produce more surface cracking than standard dual tires.

The results in Figure 7 show the transverse deflection patterns for both tires. Figure 13 shows typical longitudinal deflection patterns measured by the MDD at the bottom of the asphalt layer on Section I for each tire under the same test conditions. Using Figure 13, and assuming these deflections to be the same at the top of the asphalt layer for the thin section, it is possible to calculate a surface curvature index (SCI), which has been related by many authors to the tensile strain at the bottom of the asphalt layer (12). The SCI is defined as the difference between the maximum deflection underneath the load and the deflection at a distance of 12 in. preceding the maximum. The SCI is shown schematically in Figure 13. The following equation relating SCI to tensile strain was proposed by Scullion (13):

$$\epsilon_t = -38.9 + 28.7 \text{ SCI}$$

Using that relationship, the data presented in Figure 13 can be used to estimate the tensile strains presented in Table 4. Results show that the tensile strains in the asphalt layer for Section I under wide base single tires are about 1.5 times higher than those for dual tires.

#### CONCLUSION AND FUTURE WORK

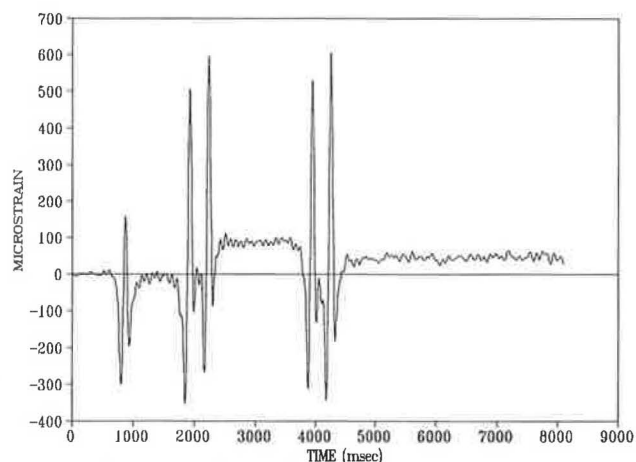
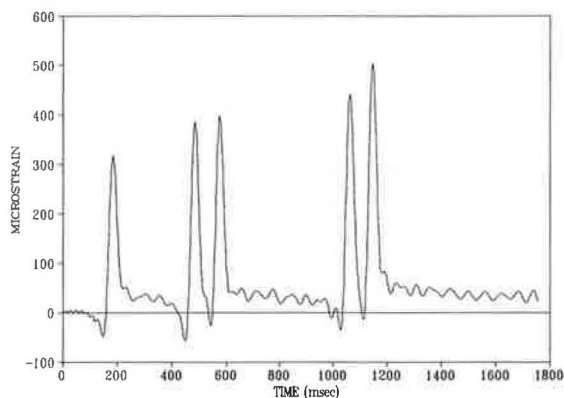
The overall aim of this study is to compare pavement response under dual and wide base single tires for various conditions of speed, load, and inflation pressure, taking into account the

**TABLE 3 Average Vertical Compressive Strain Measured at Top of Subgrade and Allowable ESAL Repetitions**

Section	Tire	Axle	Speed (mph)	$\mu$ Strain	Allowable ESAL Repetitions
I	Dual	Drive	10	1355	9719
I	Dual	Drive	20	1332	10495
I	Dual	Drive	35	1294	11950
I	Dual	Drive	55	1246	14157
I	Super Single	Trailer	10	1690	3609
I	Super Single	Trailer	20	1665	3858
I	Super Single	Trailer	35	1623	4327
I	Super Single	Trailer	55	1570	5021
II	Dual	Drive	10	297	8782890
II	Dual	Drive	20	289	9926930
II	Dual	Drive	35	275	12402795
II	Dual	Drive	55	258	16511743
II	Super Single	Trailer	10	334	5187796
II	Super Single	Trailer	20	330	5475794
II	Super Single	Trailer	35	325	5863820
II	Super Single	Trailer	55	317	6557210
I	Super Single	Drive	10	2087	1401
I	Super Single	Drive	20	2081	1419
I	Super Single	Drive	35	2071	1450
I	Super Single	Drive	55	2060	1485
I	Dual	Trailer	10	1626	4291
I	Dual	Trailer	20	1617	4399
I	Dual	Trailer	35	1601	4600
I	Dual	Trailer	55	1581	4866
II	Super Single	Drive	10	390	2588858
II	Super Single	Drive	20	385	2743075
II	Super Single	Drive	35	382	2841008
II	Super Single	Drive	55	376	3050031
II	Dual	Trailer	10	361	3660915
II	Dual	Trailer	20	358	3800507
II	Dual	Trailer	35	354	3996905
II	Dual	Trailer	55	348	4315343

transverse position with respect to the MDD. The effect of speed on pavement response under dual and wide base single tires for one set of loading and tire pressure conditions was examined. The major conclusions follow.

1. The MDD is an excellent tool to measure vertical strains and deflections in the pavement structure under different conditions of actual truck loading.

**FIGURE 8 Vertical strain in granular base layer for Section I at speed of 10 mph.****FIGURE 9 Vertical strain in granular base layer for Section II at speed of 34 mph.**

2. Under similar test conditions, wide base single tires produced higher deflections than dual tires, whether fitted to tandem drive axles or tandem trailer axles.

3. The maximum deflection under the wide base single tire generally occurs under the tire centerline, whereas the maximum deflection under dual tires occurs under either of the two tires.

4. The duration of load pulse under truck loading for a tandem axle at 55 mph speed is about 6 times (180 msec) the pulse duration for a FWD (28–30 msec). The duration of the pulse is related to the loading rate, which may affect the material properties. This aspect requires further research.

5. The apparent dilation in the base course layer under the moving load requires further attention and investigation.

6. The measured pavement deflections under both dual tires and wide base single tires in all the layers decreased with increase in speed.

7. Under similar test conditions wide base single tires are 2.8 times more damaging than dual tires on the thin pavement section and 2.5 times more damaging on the thick section for a speed of 55 mph based on design equations using vertical compressive strain.

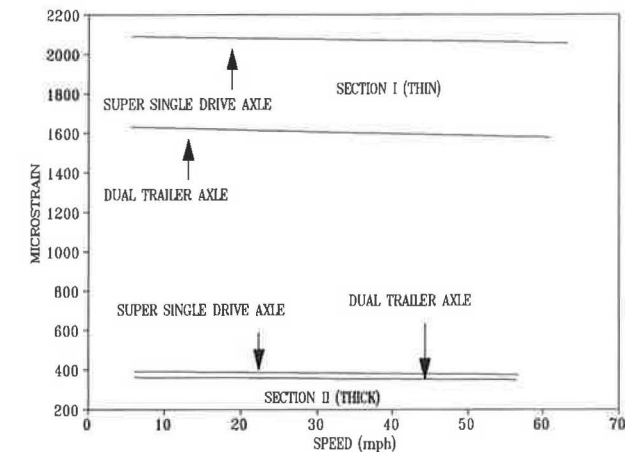
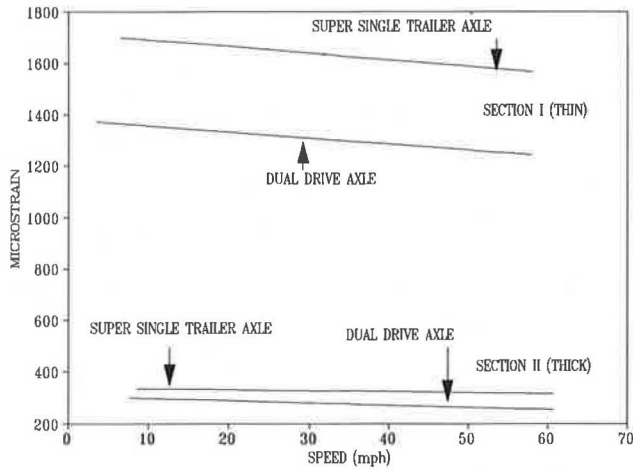


FIGURE 10 Effect of speed on vertical strain at top of subgrade (Sections I and II).

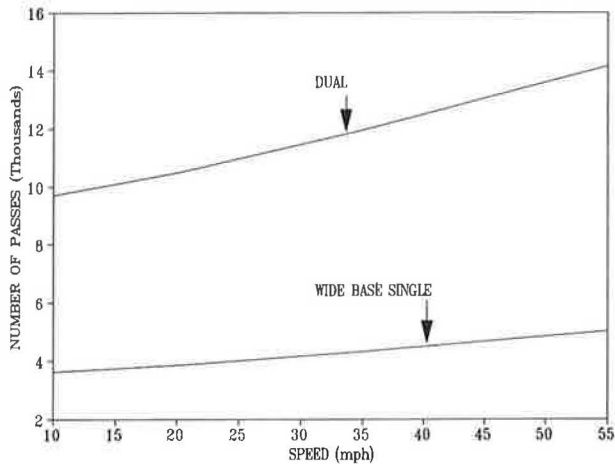


FIGURE 11 Effect of speed on allowable number of passes for Section I.

The plan for future work includes pavement material characterization under FWD and vehicular loading using linear and nonlinear elastic backcalculation techniques. Testing under different loadings and inflation pressures is planned. Analysis

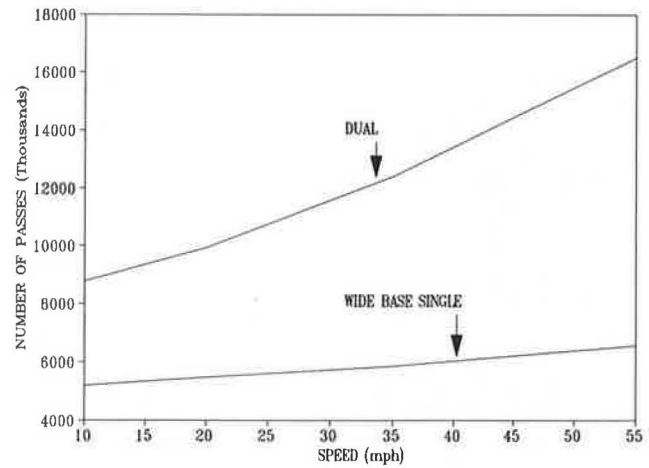


FIGURE 12 Effect of speed on allowable number of passes for Section II.

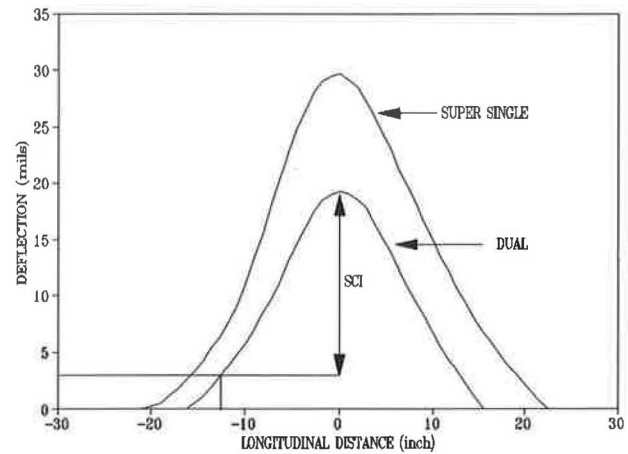


FIGURE 13 Measured peak longitudinal deflections profile under dual and wide base tire on Section I.

TABLE 4 Tensile Strain in the Asphalt Layer for Section I

Tire Type	Load (kips)	Tire Pressure (psi)	SCI	Tensile Strain ( $\mu$ Strain)
Wide base Single tires	33	130	19.078	592.73
Dual tires	33	120	15.835	405.23

of the measured data will be used to estimate the amount of pavement damage caused by the variation in these characteristics and their effects on thin and thick asphaltic concrete pavements service life.

ACKNOWLEDGMENTS

This work is part of ongoing research sponsored by the Texas State Department of Transportation (DOT). The authors wish to thank Bob Briggs of Texas DOT for his support.

## REFERENCES

1. *Special Report 73: The AASHO Road Test*. HRB, National Research Council, Washington, D.C., 1962.
2. M. Huhtala, J. Pihlajamaki, and M. Pienimaki. The Effects of Tires and Tire Pressures on Road Pavements. Presented at 68th Annual Meeting of the Transportation Research Board, Washington, D.C., 1989.
3. J. T. Christison and B. P. Shields. Evaluation of the Relative Damaging Effects of Wide Base Tire Loads on Pavements. Presented at Annual Conference of the Roads and Transportation Association of Canada, Toronto, Ontario, 1980.
4. K. G. Sharp, P. F. Sweatman, and D. W. Potter. The Comparative Effects of The Dual and Wide Single Tires on Pavement Response. *Pavements and Construction*, Vol. 13, Part 4, Proc., 13th ARRB/5th REAA Combined Conference, Australian Road Research Board, 1986.
5. P. Sebaaly and N. Tabatabaee. Effect of Tire Pressure and Type on Response of Flexible Pavement. In *Transportation Research Record 1227*, TRB, National Research Council, Washington, D.C., 1989.
6. H. A. Smith. Synopsis of Tire-Pavement Interaction Research. SAE Truck and Bus Meeting, Charlotte, N.C., SAE, Warrendale, Pa., 1989.
7. W. L. Giles. Expanded Applications Wide Base Radial Truck Tire. SAE Truck and Bus Meeting, Ft. Wayne, Ind., SAE, Warrendale, Pa., 1979.
8. J. E. B. Basson, O. J. Wijnberger, and Skultely. *A Multistage Sensor for Measurement of Resilient Deflections and Permanent Deformation at Various Depths in Road Pavements*. NITRR RP/3/81. Council for Scientific and Industrial Research, Pretoria, South Africa, 1981.
9. T. Scullion, J. Uzan, J. I. Yazdani, and P. Chan. *Field Evaluation of the Multidepth Deflectometers*. Report 1123-1. Texas Transportation Institute, Texas A&M University, College Station, 1988.
10. J. Uzan and T. Scullion. Verification of Backcalculation Procedures. Third International Conference on Bearing Capacity of Roads and Airfields, Trondheim, Norway, 1990.
11. *Documentation of the Asphalt Institute's Thickness Design Manual*. Research Series No. 14 (RS-14), 7th ed. Asphalt Institute, College Park, Md., 1964.
12. A. A. A. Molenaar. *Structural Performance and Design of Flexible Road Construction and Asphalt Overlays*. Ph.D. thesis. Delft University of Technology, The Netherlands, 1983.
13. T. Scullion. *Incorporating a Structural Strength Index into PES*. Report 409-3F. Texas Transportation Institute, Texas A&M University, College Station, 1987.

---

*Publication of this paper sponsored by Committee on Strength and Deformation Characteristics of Pavement Sections.*

# Field and Laboratory Determination of Elastic Properties of Portland Cement Concrete Using Seismic Techniques

J. A. BAY AND K. H. STOKOE II

Seismic techniques, including the Spectral-Analysis-of-Surface-Waves test, direct and interval compression wave tests, and resonance tests, provide reliable techniques for determining the elastic properties of portland cement concrete (PCC). These techniques can be applied to pavement structures, such as slabs, and to laboratory specimens, such as cylinders. The nondestructive nature of these tests makes them ideal for monitoring PCC from the earliest stages of curing and continuing throughout the life of the structure. Elastic properties, typically expressed as Young's modulus and shear modulus, provide an easy way to compare the similarity of laboratory specimens with each other and with the structures they are intended to represent. The results of different seismic tests on curing slabs and field-curing cylinders demonstrate the applicability of the tests and show that, in these tests, the field-cured cylinders did not obtain the stiffnesses of the slabs. Small-strain static tests performed on cylinders are also shown to be consistent with moduli determined by dynamic (seismic) tests on the same cylinders when both types of tests are performed at similar strain levels. However, these small-strain moduli are shown to be about 10 percent greater than Young's moduli measured in conventional static tests at 40 percent of the unconfined strength, because of the decrease in modulus with increasing strain.

Seismic wave velocity measurements provide nondestructive techniques for determining the elastic properties of portland cement concrete (PCC). These techniques can be applied to PCC structures, such as slabs or beams, and to laboratory specimens, such as cylinders. The nondestructive nature of seismic tests makes them ideal for monitoring PCC, beginning immediately after placement of the concrete and continuing throughout the life of the structure.

A number of different techniques that employ different types of seismic waves can be used. These tests include Spectral-Analysis-of-Surface-Waves (SASW), direct and interval compression waves, and resonance. Because velocities of seismic waves differ, it is important to know which type of wave is being measured. Once velocities of two types of seismic waves have been measured, all elastic properties of a homogeneous, isotropic material can be determined.

A brief overview of the relationships between seismic wave velocities and elastic properties is presented here. Methods that can be employed to measure the various wave velocities in different situations are then discussed. The results of tests performed on curing PCC slabs and cylinders are used to illustrate the measurement methods. Seismic wave velocities are also used as a means of comparing the similarities of slabs and field-cured cylinders. Finally, values of Young's moduli

obtained seismically, or dynamically, are compared with values obtained in low-strain static tests and conventional static tests on the same specimens.

## ELASTIC PROPERTIES AND SEISMIC WAVE VELOCITIES

Seismic wave velocities are a function of the elastic properties and mass density of the material through which the stress waves are propagating. This characteristic makes seismic testing a powerful tool in the measurement of elastic material properties. The velocities of different stress (seismic) waves are controlled by different elastic moduli. If the material can be characterized as elastic, homogeneous, and isotropic, only two elastic constants are required to describe the material, and these constants can be determined by measuring the velocity of two types of seismic waves. The PCC materials tested in this work can be so described. On the other hand, if more elastic constants were required to characterize the material (such as for an elastic, homogeneous, cross-anisotropic material that requires five elastic constants), then additional stress wave measurements would have to be performed.

To understand which elastic modulus controls which type of seismic wave, one must look at the deformation of an element during stress wave loading. The deformation resulting from a shear wave is represented in Figure 1a. The only deformation in this case is in shear, so that shear modulus ( $G$ ) controls the wave velocity. The equation relating shear wave velocity ( $V_s$ ) and shear modulus is as follows:

$$G = \rho V_s^2 \quad (1)$$

where  $\rho$  is the mass density (unit weight divided by gravity) of the material.

The deformation caused by an unconstrained compression wave (also called a rod wave) is represented in Figure 1b. In this case the wave deforms the material in the direction of wave propagation and also in the lateral directions. Unconstrained modulus, or Young's modulus ( $E$ ), controls the wave velocity in this case. The equation relating unconstrained compression wave velocity ( $V_c$ ) and Young's modulus is as follows:

$$E = \rho V_c^2 \quad (2)$$

The deformation caused by a constrained compression wave is represented in Figure 1c. In this case, the element is re-

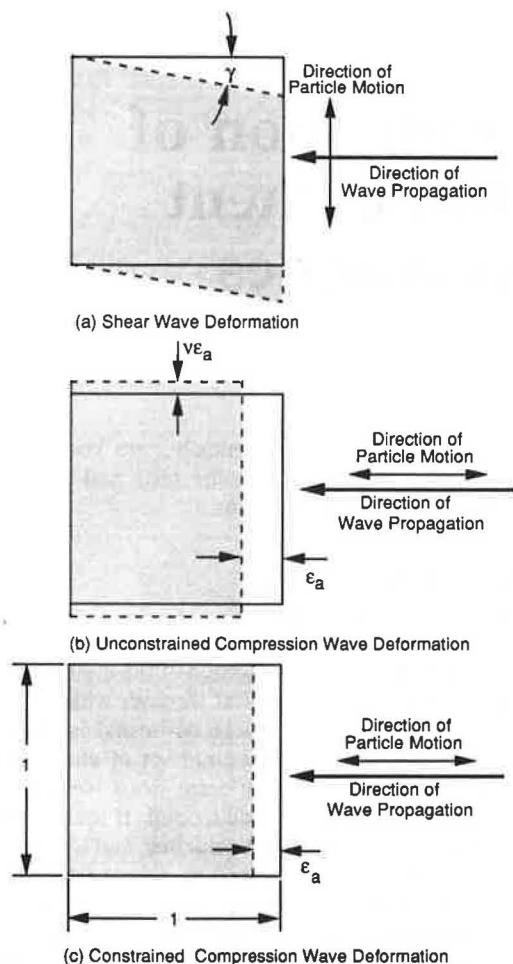


**FIGURE 1** Deformation of a unit element of material loaded by a shear wave or compression waves.

strained from deforming in the lateral directions. This wave velocity is controlled by the constrained modulus ( $M$ ). Because the constrained modulus has the largest value of the elastic moduli, this type of stress wave, known as a primary or  $P$ -wave, has the fastest wave velocity. The equation relating constrained modulus and  $P$ -wave velocity ( $V_p$ ) is as follows:

$$M = \rho V_p^2 \quad (3)$$

For an elastic, homogeneous, isotropic material like the PCC material tested in this work, all of the above moduli ( $G$ ,  $E$ , and  $M$ ) can be related to each other using the following equations:

$$M = \frac{(1 - \nu)}{(1 + \nu)(1 - 2\nu)} E \quad (4)$$

$$E = 2(1 + \nu)G \quad (5)$$

$$M = \frac{2(1 - \nu)}{1 - 2\nu} G \quad (6)$$

where  $\nu$  is Poisson's ratio.

One additional type of stress wave measured in this work is a Rayleigh-type surface wave. This type of wave travels along the air-solid interface and causes a complex deformation pattern that varies with depth beneath the interface. The deformation pattern contains both distortion and volume-change (shear and compression) components, which results in both horizontal and vertical motions that decay with depth. Because of this combination of distortion and volume change, the velocity of Rayleigh-type surface waves cannot be related to one modulus as simply as compression and shear waves. The velocity of the Rayleigh wave ( $V_R$ ) is always slightly less than the shear wave velocity. However, it is strongly controlled by the shear modulus of the material. Rayleigh wave velocity can be approximately related to  $V_s$  using the following equation:

$$V_R \approx \frac{0.862 + 1.14\nu}{1 + \nu} V_s \quad (7)$$

A crude estimate of  $V_R$  for values of Poisson's ratio between 0.1 and 0.3 is

$$V_R \approx 0.9 V_s \quad (8)$$

The type of wave that is excited and measured depends on the source, the receiver orientation, and the source/receiver location on the specimen being tested as described below.

#### SEISMIC MEASUREMENTS ON CURING PCC SLABS

Nondestructive seismic techniques can be employed to monitor the quality of PCC slabs beginning immediately after the concrete is placed, during curing, and throughout the life of the structure ( $t$ ). Measured wave velocities are only functions of the elastic moduli and mass density of the slab. Hence, velocities can be used to calculate moduli directly. The seismic techniques used on the surface layer of concrete pavements include SASW, direct and interval compression waves, impulse-response, and impact-echo. However, the last two techniques require that the thickness of the slab be known to determine the velocity or stiffness of the concrete (2,3).

#### SASW Method

The SASW method is a nondestructive, nonintrusive seismic technique that uses the dispersive nature of surface waves to determine the stiffness profile of layered systems. Because all testing is done on a single exposed surface, the SASW technique is particularly effective for evaluating the pavement surface layer and for repeated monitoring of pavements. A more complete treatment of the SASW method applied to pavements can be found elsewhere (4-7).

The SASW method involves measuring the velocities of Rayleigh-type surface waves over a wide range of frequencies. Surface waves propagate along the air-solid interface with particle motion limited primarily to depths less than about one wavelength. Thus, lower-frequency waves with longer wavelengths sample material deeper. Higher-frequency

waves with shorter wavelengths only sample shallow material. To measure the stiffness of a concrete surface layer, the velocity of wavelengths shorter than the concrete thickness are evaluated.

*SASW Testing Procedure*

The SASW source and receiver configuration is shown in Figure 2. A vertically oriented piezoelectric shaker on the concrete surface is used as the source, and two vertically oriented accelerometers positioned linearly from the source are used as receivers. The accelerometers are coupled to the slab immediately after the surface is finished using a fast-setting cement. The waveforms from the two accelerometers are transformed into their frequency spectra using the fast Fourier transform (FFT). The velocities of the various frequencies (which are related to the wavelengths) are determined by comparing the phase of the two spectra at each frequency. These operations are performed in real time using a FFT signal analyzer.

*Typical SASW Results*

A typical dispersion curve, a plot of surface wave velocity versus wavelength, for a 0.8-ft thick slab is shown in Figure 3. It can be seen that wave velocities for wavelengths less than 0.8 ft oscillate about a constant value. These oscillations are caused by surface waves that reflect off various boundaries of the slab and by the influence of additional compression

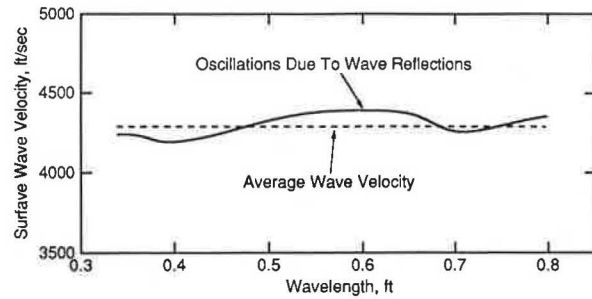


**FIGURE 3** Dispersion curve for SASW testing of 0.8-ft-thick PCC slab 14.5 hr after water was added to concrete mix.

and shear waves. The average velocity of the wavelengths that are shorter than the slab thickness closely represents the surface wave velocity of a uniform layer (5-7).

**Constrained Compression Wave Velocity Measurements**

Compression wave velocities can also be measured in PCC slabs. This type of measurement requires one or more accelerometers oriented in line with the source. In theory, testing can be performed on one exposed surface. However, in the authors' experience, the tests are best performed between two parallel surfaces or between boreholes extending into the slab. If this procedure is not followed, a velocity somewhat below the constrained wave velocity will likely be measured. The constrained compression wave velocity can be measured in either a direct or an interval test. The direct test involves measuring the travel time between the source and receiver. The interval test involves measuring the travel time between two identical receivers. The interval test is preferable because some period of time (delay) will always result at the generation and reception points, which can be difficult to calibrate. In an interval test, this delay time can be assumed identical for the two receivers, and therefore can be neglected. However, the delay time must be accounted for in a direct test and becomes especially critical when the travel time is short. This is the case when the velocity of stiff materials like PCC are measured over short travel paths on the order of 1 or 2 ft. The constrained compression wave is the fastest seismic wave. Therefore, to measure  $V_p$ , with both direct and interval compression wave tests, the first wave arrival is measured.

*Constrained Compression Wave Testing Procedure*

The source and receiver configuration is shown in Figure 2. A horizontally oriented piezoelectric shaker was mounted on the slab edge. Two steel casings were cast in the slab. An accelerometer was positioned in each casing at the center of the slab and in line with the source. Interval measurements were then performed between the two accelerometers.

*Typical Compression Wave Results*

Typical wave traces from an interval test are shown in Figure 4. The constrained compression wave is the initial wave arrival

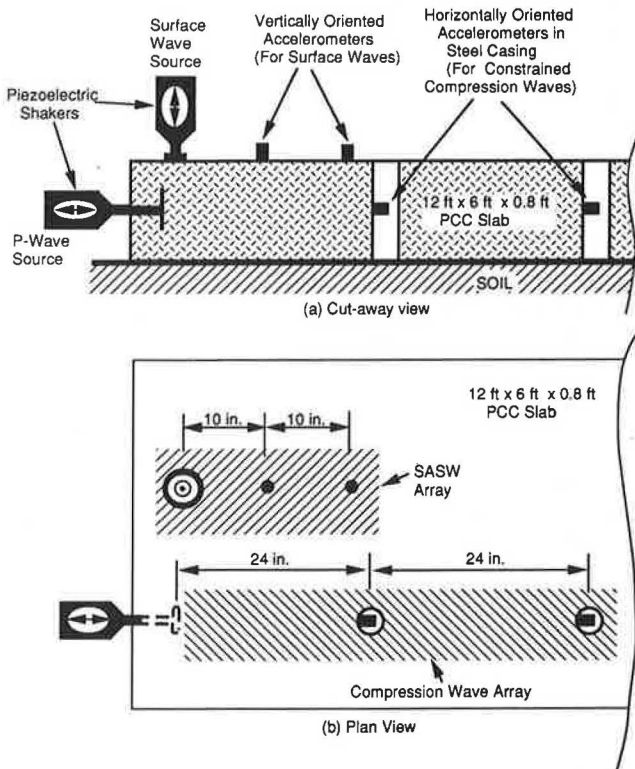


**FIGURE 2** Test configuration for measuring compression and surface waves on PCC slabs.

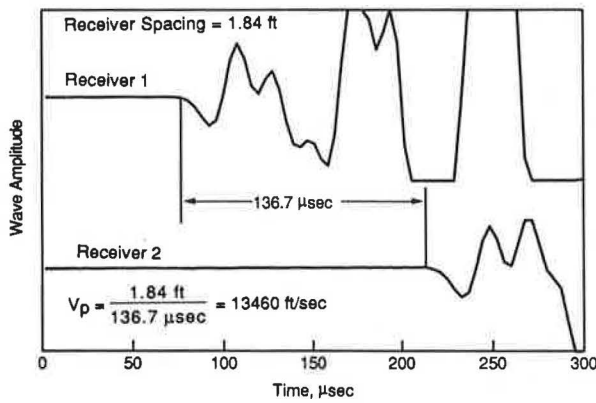


**FIGURE 4** Wave traces from an interval compression wave test performed on PCC slab 24 hr after water was added to concrete mix.

on each trace. The velocity is determined simply by dividing the distance between the two receivers by the time difference between the first arrivals.

### SEISMIC MEASUREMENTS ON PCC CYLINDERS

Seismic techniques can also be used to determine the properties of PCC cylinders. The SASW method has not yet been adapted for use on small specimens with reflecting boundaries close to the receivers. However, compression wave tests and resonance tests are readily employed (8,9).

#### Direct Constrained Compression Wave Measurements

Because of space and geometric limitations, it is not practical to use interval compression wave tests on small cylinders. Therefore, direct compression wave measurements are performed following ASTM C-597. This test configuration is shown in Figure 5a. Measurements are performed with the source and receiver centered on opposite ends of the cylinder. It is important that the source and receiver are centered as shown, because the *P*-wave in cylinders has a curved wave front with the leading point at the center.

Care must be exercised in direct *P*-wave measurements to determine the proper delay time in the source/receiver system. Calibrated specimens, with known elastic properties, were tested to determine the delay time. A delay time of 20.5 msec was found, which was about 20 percent of the total measured travel time in a cured, 1-ft-long cylinder. As a result, neglecting or using the wrong delay time can result in a significant error. Typical wave traces for a 1-ft cylinder are shown in Figure 6.

#### Resonance Tests

Another approach to determine the seismic wave velocity of small specimens is to use resonance tests (ASTM C-215). By exciting the end of a cylinder in compression or shear, waves will move up and down the cylinder, reflecting off the ends. As the waves reflect off the ends of the cylinder, some wave-

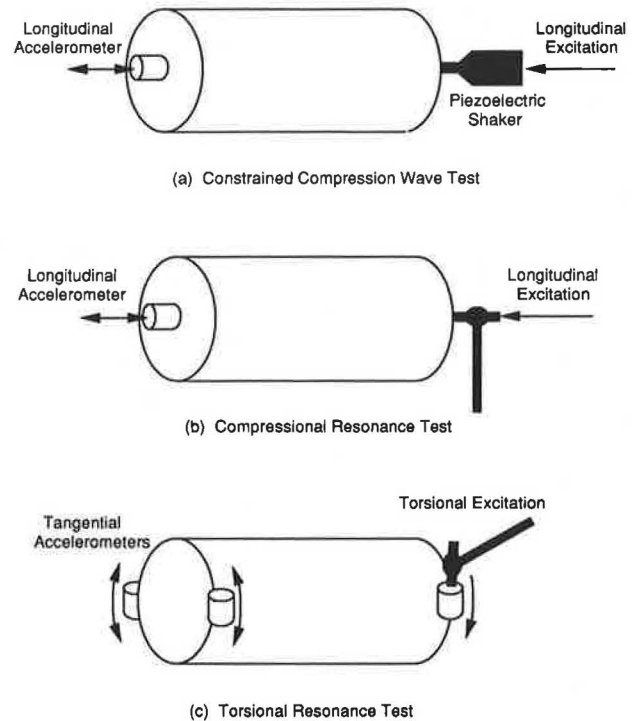


**FIGURE 5** Configuration of direct compression and resonance tests on cylindrical specimens.

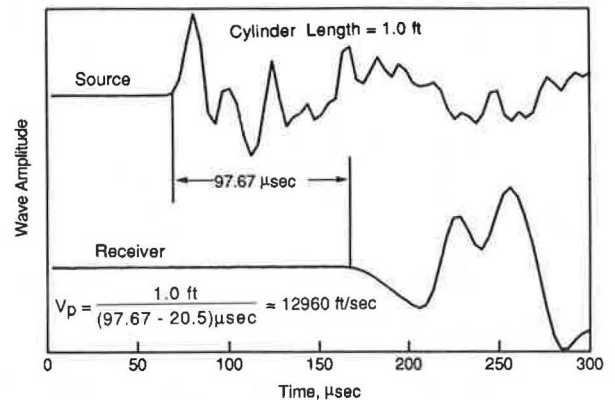


**FIGURE 6** Wave traces from direct compression wave test performed on 1.0-ft-long PCC cylinder.

lengths will add destructively, and those wavelengths will die out quickly. Other wavelengths will add constructively, and they will persist so that the cylinder resonates at those wavelengths. For a cylinder with two free ends, the wavelengths at which the cylinder resonates can be calculated as follows:

$$\lambda_n = \frac{2L}{n}, n = 1, 2, 3, \dots, \text{etc.} \quad (9)$$

where

$$\begin{aligned} \lambda_n &= \text{wavelength of } n\text{th mode,} \\ L &= \text{length of cylinder, and} \\ n &= \text{mode number.} \end{aligned}$$

The frequencies of the various resonant modes appear as peaks in the transfer function spectrum, which is calculated by dividing the FFT of the accelerometer output by the FFT of the input force. The wave velocity can be determined by

$$V = f_n \cdot \lambda_n \tag{10}$$

where

- $V$  = wave velocity,
- $f_n$  = frequency of  $n$ th mode, and
- $\lambda_n$  = corresponding wavelength of  $n$ th mode.

The peak strain in resonating cylinders can be determined using the following equation:

$$\epsilon_p = \frac{\dot{u}}{V} \tag{11}$$

where  $\dot{u}$  is peak particle velocity and  $V$  is wave velocity.

### Resonant Compression Tests

By striking a cylinder parallel to its longitudinal axis, as shown in Figure 5b, and measuring numerous reflections of the wave moving up and down the cylinder, an unconstrained compression wave can be measured. This measurement represents that of a plane compression wave because the wave has traveled numerous times up and down the cylinder. Hence, the wave is not constrained against lateral deformation.

A typical transfer function spectrum from a resonant compression test of a 1.0-ft-long cylinder is shown in Figure 7a. Notice the close agreement between velocities determined by the first and second modes, which adds validity to the measurement. The authors, however, use the results from the first-mode measurement because this mode most closely corresponds to plane-wave theory.

### Resonant Torsional Tests

By striking a cylinder tangentially at its circumference, a torsional shear wave can be generated. The resulting wave motion can be measured with one or more tangentially oriented accelerometers, as shown in Figure 5c. A typical transfer function spectrum from a resonant torsional test of a 1.0-ft-long cylinder is shown in Figure 7b.

### Comparison of Wave Velocities on Cylinders

The same concrete cylinder was used for the direct compression test shown in Figure 6 and the resonance tests shown in Figure 7. The velocity of any two types of seismic waves is sufficient to determine all elastic properties of a homogeneous, isotropic material. For example, by combining Equations 1-6 one can calculate Poisson's ratio from any two wave velocities as follows:

$$\frac{V_p}{V_c} = \sqrt{\frac{(1 - \nu)}{(1 + \nu)(1 - 2\nu)}} \tag{12}$$

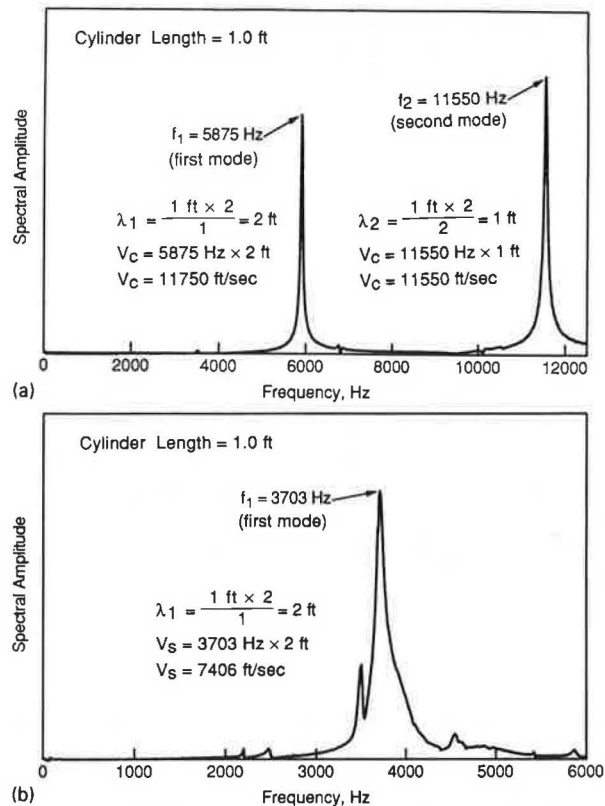


FIGURE 7 Response spectra from resonant testing of 1.0-ft-long PCC cylinder: a, compression test; b, torsional test.

$$\frac{V_c}{V_s} = \sqrt{2(1 + \nu)} \tag{13}$$

$$\frac{V_p}{V_s} = \sqrt{\frac{2(1 - \nu)}{(1 - 2\nu)}} \tag{14}$$

By applying these equations to the velocities from Figures 6 and 7, Poisson's ratio of the cylinder can be determined as shown in Table 1. The fact that any two wave velocities give essentially the same value for Poisson's ratio indicates that the different tests are consistent and that PCC does act as a homogeneous isotropic material at the strain levels and wavelengths generated.

### ELASTIC PROPERTIES OF CURING PCC SLABS

Two prototype PCC slabs were constructed at the Balcones Research Center of the University of Texas at Austin. The slabs were not reinforced and had dimensions of 6 ft x 12 ft and a thickness of 0.8 ft. The slabs were cast directly on a silty clay subgrade. The mixes had a maximum aggregate size of 1.5 in., 5 sacks of cement per cubic yard with fly ash for 25 percent of the cementitious material, and an air entraining admixture. SASW tests and interval P-wave tests were performed on the slabs, beginning immediately after the final surface finishing was completed. Direct constrained compression wave measurements were performed on 6- x 12-in. cyl-

**TABLE 1 Poisson's Ratio of a PCC Cylinder Based on Different Combinations of Wave Velocities**

Types of Seismic Wave Velocities Used in Calculation	Poisson's Ratio
$V_p, V_c$	0.257
$V_c, V_s$	0.259
$V_p, V_s$	0.258

inders that were prepared according to ASTM C-31 and field cured next to the slabs. Because there are no radial deformations associated with *P*-wave motion, testing results are unaffected by the confinement of a cylinder mold. Therefore, early *P*-wave tests on cylinders were performed on cylinders still in their molds with an accelerometer protruding through the bottom of the cylinder to be in direct contact with the concrete.

#### Variations in Seismic Wave Velocities with Time

Monitoring the seismic wave velocity of curing concrete shows how concrete increases in stiffness during curing. Because seismic techniques are effective over an extremely wide range of stiffnesses, testing can begin on freshly placed plastic concrete and can continue through curing and at subsequent times. Testing during early stages can be used to give an early indication of concrete quality. Continued seismic testing can also be used as a means of monitoring the quality of the concrete throughout its design life.

A typical plot of surface wave and constrained compression wave velocities with time is shown in Figure 8a. The error bars on the plot of the *P*-wave results indicate the maximum error due to the resolution of the recording equipment. The plot of surface wave results shows the average wave velocity of all of the surface waves measured with wavelengths less than the slab thickness, with error bars indicating plus or minus one standard deviation of those wave velocities. The curves fit through the data indicate the probable wave velocities during curing.

#### Variations in Elastic Moduli with Time

By applying Equations 1–7 to the seismic wave velocities, the elastic properties of curing PCC can be determined. A typical plot of *E*, *G*, and  $\nu$  with time is shown in Figure 8b. It is interesting to note that the value of  $\nu$  in freshly placed concrete approaches the theoretical limit of 0.5, which would indicate an incompressible fluid.

#### CURING PCC SLABS AND FIELD-CURED CYLINDERS

In addition to measurements on the slabs, constrained compression wave measurements were also conducted on field-cured cylinders during curing. A comparison of *P*-wave ve-

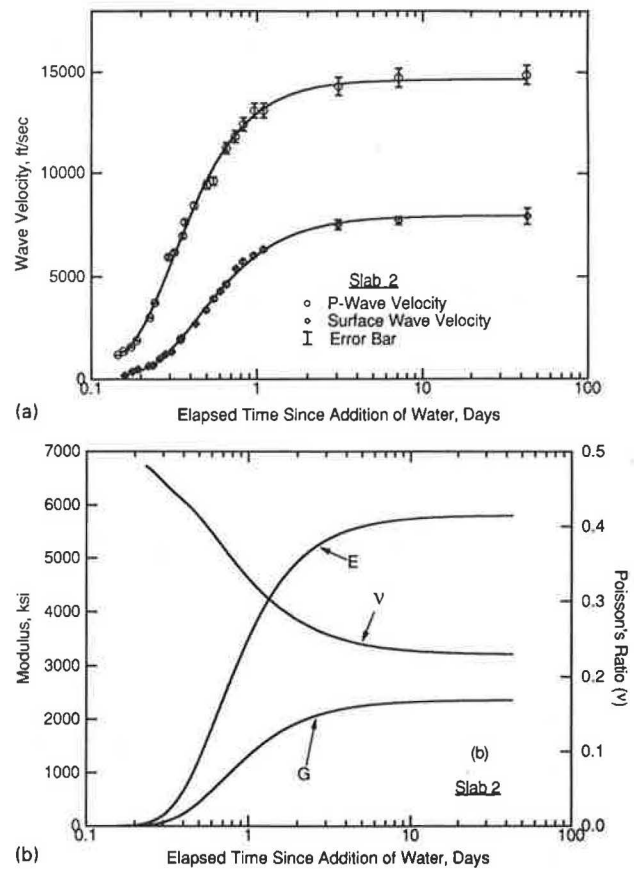


**FIGURE 8 Wave velocities and resulting elastic properties from stress wave measurements on a curing PCC slab: a, constrained compression and surface wave velocities; b, typical plot of *E*, *G*, and  $\nu$ .**

locities in the slab and in the cylinders indicates how well the cylinders represent the properties of the slab. The *P*-wave velocity of two cylinders along with the *P*-wave velocities of the associated slabs are shown in Figure 9. Again the error bars on the slab measurements indicate the resolution of the recording equipment and the error bars on the cylinders measurements indicate the resolution of the recording equipment plus the uncertainty of the delay time used.

It is evident by the error bars that the quality of direct *P*-wave measurements on short cylinders decreases as the velocity increases. This occurs because the equipment delay time and the sampling interval of the equipment becomes a larger percentage of the measured travel time. However, interesting points can still be determined about how closely the field-cured cylinders represent the slab. The cylinder associated with Slab 1 was slightly stiffer than the slab in the initial stages of curing whereas the cylinder associated with Slab 2 was slightly softer. Later in the curing process, both slabs became considerably stiffer than the cylinders; this difference continued during the approximately 40 days of monitoring.

These results clearly indicate that the cylinder properties are somewhat different than the slabs. It is hypothesized that cylinder breaks at 7 and 28 days would underestimate the strengths of the slabs. Unfortunately, no cores of the slabs were taken so that no strength measurements of slab cores could be performed. The difference in properties of the slab

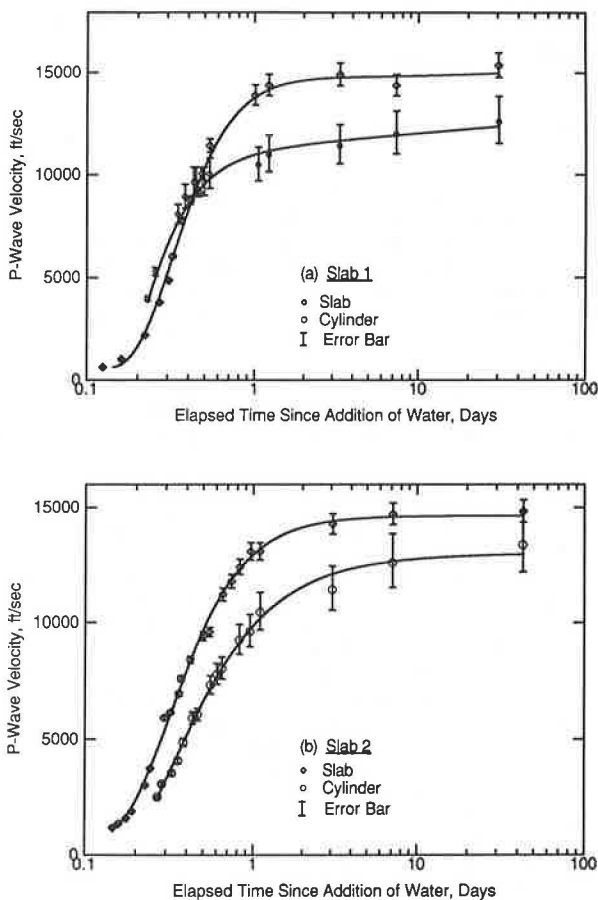


**FIGURE 9** Comparison of constrained compression wave velocities measured on curing slabs and field-cured cylinders.

and the cylinders highlights the importance of using nondestructive testing techniques, such as the SASW and *P*-wave methods, on actual structures. The relative wave velocities of a structure and its cylinders might also be used to more accurately infer material properties in the structure from cylinder tests.

**MODULI MEASURED STATICALLY AND DYNAMICALLY**

To determine how statically and dynamically measured moduli compare, four cylinders were cast and cured for two weeks in 180°F water to ensure that all curing was complete. Low-strain unconfined compression tests were then performed on the cylinders using micro-proximeter extensometers to measure the deflection between third points of the cylinders. Additional tests were performed according to ASTM C469 up to 40 percent of the ultimate strength of the cylinders. Resonant compression wave tests were also performed to determine values of *E* dynamically. The peak strain level of the dynamic tests was determined using Equation 11. A plot of modulus versus strain level for both static and dynamic tests on one cylinder is shown in Figure 10. It is quite clear that moduli measured statically and dynamically compare closely when the tests are performed at the same strain levels.

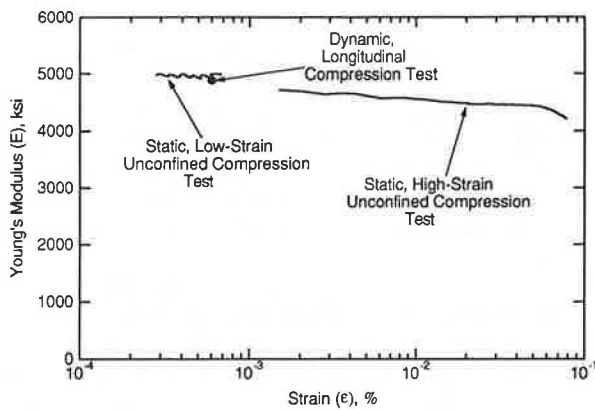


**FIGURE 10** Variation of Young's modulus with strain for static and dynamic tests on PCC cylinder.

The results of static and dynamic tests on four cylinders are tabulated in Table 2. Again the modulus from the low-strain static tests agrees closely with the dynamic tests; however tests performed up to 40 percent of the ultimate strength yielded moduli about 11 percent lower. Other researchers have found the difference between moduli determined by conventional static tests and dynamic tests to be as great as 20 percent to 30 percent (10). Caution must be used in evaluating such results to be sure that the proper wave velocities are used in determining Young's modulus. If constrained wave velocity is used, a constrained modulus rather than Young's modulus will be determined. Constrained modulus is about 10 percent higher than Young's modulus for cured PCC (Equation 4).

**CONCLUSIONS**

Measurement of the velocities of seismic (stress) waves is an effective method of determining the elastic properties of PCC in structures and laboratory specimens. Because seismic techniques are nondestructive and effective over any range of stiffness, they provide a means of monitoring PCC from the earliest stages of curing and continuing throughout the life of the structure. This was demonstrated by monitoring the stiffness of PCC slabs beginning just hours after the concrete was placed until after curing was complete.

The SASW method and direct or interval compression wave methods are especially effective for slabs or large structures.

**TABLE 2** Statically and Dynamically Measured Low-Strain Young's Modulus

Cylinder No.	"Static" <i>E</i> ( $\epsilon = 6 \times 10^{-4}\%$ ) ksi	"Dynamic" <i>E</i> ( $\epsilon = 6 \times 10^{-4}\%$ ) ksi	High Strain "Static" <i>E</i> * ( $\epsilon = 6 \times 10^{-2}\%$ ) ksi
1	4860	4830	4260
2	5040	4870	4410
3	4860	4880	4410
4	4900	4890	4280

\* Conventional measurement at about 40% of unconfined strength

On the other hand, resonance methods are effective on small prismatic members and laboratory specimens. Direct compression wave tests may be less reliable on small specimens than resonance or interval measurements unless equipment calibration is carefully controlled. Direct or interval compression wave tests measure the velocity of the constrained compression wave, whereas resonance tests can measure the unconstrained compression wave and shear wave velocities.

All of the elastic properties of a homogeneous, isotropic material can be determined by measuring the velocity of two different seismic waves. Redundant seismic tests on PCC cylinders show a high degree of consistency between tests, and indicate that this concrete behaves as an isotropic, homogeneous material at the strain levels and wavelengths generated in this testing. Values of Young's modulus, which were determined from dynamic tests, agreed closely with values measured statically at the same strain levels as the dynamic tests. Static tests that were performed at 40 percent of the ultimate strength of the concrete yielded values of Young's moduli that were about 11 percent lower than the values determined dynamically and the values determined in low-strain static tests.

Seismic techniques provide a means of comparing the similarity of laboratory specimens with the field structures they are intended to represent. Comparisons between slabs and field-cured cylinders showed that the stiffness of the cylinders was considerably less than the slab stiffness. This demonstrates the importance of using nondestructive techniques to determine the properties of actual structures. The relative seismic wave velocities of structures and cylinders could also be used to more accurately relate cylinder properties to the properties of the structure.

#### ACKNOWLEDGMENTS

This work was supported by the Texas Advanced Technology Program and the Texas State Department of Highways and

Public Transportation. The authors wish to express their appreciation for this support.

#### REFERENCES

1. G. J. Rix, J. A. Bay, and K. H. Stokoe II. Assessing In Situ Stiffness of Curing Portland Cement Concrete with Seismic Tests. In *Transportation Research Record 1284*, TRB, National Research Council, Washington, D.C., 1990, pp. 8–15.
2. M. Sansalone and N. J. Carino. Detecting Delaminations in Concrete Slabs With and Without Overlays Using the Impact-Echo Method. *ACI Materials Journal*, Vol. 86, No. 2, March–April 1989.
3. H. S. Limaye and G. J. Klein. Investigation of Concrete Arch Bridges Using The Impact-Echo Method. In *Proc., Nondestructive Evaluation of Civil Structures and Materials*, University of Colorado, 1990, pp. 221–231.
4. S. Nazarian. *In Situ Determination of Elastic Moduli of Soil Deposits and Pavement Systems by Spectral-Analysis-of-Surface-Wave Method*. Ph.D. dissertation. University of Texas at Austin, Dec. 1984.
5. J. A. Bay and K. H. Stokoe II. Field Determination of Stiffness and Integrity of PCC Slabs Using the SASW Method. In *Proc., Nondestructive Evaluation of Civil Structures and Materials*, University of Colorado, 1990, pp. 71–85.
6. J. M. Roesset, D.-W. Chang, K. H. Stokoe II, and M. Aouad. Modulus and Thickness of the Pavement Surface Layer from SASW Tests. In *Transportation Research Record 1260*, TRB, National Research Council, Washington, D.C., 1990, pp. 53–63.
7. J.-C. Sheu. *Applications and Limitations of the Spectral-Analysis-of-Surface-Waves Method*. Ph.D. dissertation. University of Texas at Austin, Dec. 1987.
8. V. M. Malhotra. *In Situ/Nondestructive Testing of Concrete*. Publication SP-82. American Concrete Institute, Detroit, Mich., 1984.
9. E. A. Whitehurst. *Evaluation of Concrete Properties from Sonic Tests*. ACI Monograph 2. American Concrete Institute, Detroit, Mich., 1966.
10. S. Mindess and J. F. Young. *Concrete*. Prentice-Hall, Inc., Englewood Cliffs, N.J., 1981.

---

*Publication of this paper sponsored by Committee on Rigid Pavement Design.*

# Alternative Method for Temperature Correction of Backcalculated Equivalent Pavement Moduli

ANDREW M. JOHNSON AND RONALD L. BAUS

The Direct Structural Capacity Method as described in the AASHTO *Guide for the Design of Pavement Structures* provides a quick and simple method for analyzing pavement deflections that are collected from nondestructive testing. However, results taken from 13 sites tested bimonthly during an 18-month period showed considerable variation with temperature even after the recommended AASHTO temperature correction procedures were applied. An alternative temperature correction procedure is derived from asphalt cement (AC) concrete temperature-modulus relationships and elasticity equations used to calculate composite pavement modulus. The alternative correction procedure requires knowledge of the ratio of AC bound layer thickness to non-AC bound layer thickness, the estimated average pavement temperature, and the ratio of AC bound layer stiffness to non-AC bound layer stiffness. Although the stiffness ratio is not known before temperature correction in a Direct Structural Capacity Method analysis, it is shown that the correction procedure is relatively insensitive to errors in the estimated stiffness ratio. Therefore, an estimate of the stiffness ratio is sufficiently precise for most pavement analyses. When the alternative procedure is applied to the data from the 13 test sites, it is shown to provide more uniform results with varying temperature.

The AASHTO *Guide for the Design of Pavement Structures* (1) introduces the Direct Structural Capacity Method to determine composite pavement stiffness from the analysis of flexible pavement deflections obtained through nondestructive testing (NDT). Integral to the analysis of flexible pavement using NDT data is the correction of the results to account for the temperature sensitivity of asphalt cement (AC) concrete. The AASHTO guide recommends the use of curves derived from studies conducted by Southgate and Deen (2) to correct the measured deflection at the test temperature to a deflection at a standard temperature of 70°F. The curves correspond to various pavement types and were determined empirically using AASHO Road Test data for the purpose of correcting Benkelman beam deflections. This correction method was applied to deflections collected with a falling weight deflectometer (FWD) during an 18-month period at various test sites in South Carolina. Even after the AASHTO temperature corrections were applied to the deflection data, the backcalculated pavement stiffnesses were observed to vary considerably in relation to the estimated pavement temperature at the time of FWD testing.

A. M. Johnson, South Carolina Department of Highways and Public Transportation, Research and Materials Laboratory, P. O. Box 191, Columbia, S.C. 29202. R. L. Baus, University of South Carolina, Department of Civil Engineering, Columbia, S.C. 29208.

To achieve more stable backcalculated pavement stiffnesses with varying pavement test temperature and to make such stiffnesses more representative of the standard pavement temperature of 70°F, an alternative temperature correction technique is proposed. The alternative technique is derived from AC concrete temperature-stiffness relationships and the elasticity relations used to calculate composite modulus. This alternative technique applies a correction factor to the calculated composite modulus.

## DIRECT STRUCTURAL CAPACITY METHOD

The Direct Structural Capacity Method is derived in Appendix PP of the AASHTO guide (1). This method is also referred to as NDT Method 2 in the guide. Presented here is a brief overview of the procedure. The Direct Structural Capacity Method models a flexible pavement structure as a multilayered linear elastic system, having layer characteristics of thickness ( $h_i$ ), Young's modulus ( $E_i$ ), and Poisson's ratio ( $\mu_i$ ). The total pavement thickness ( $h_t$ ) is transformed into one equivalent layer with an equivalent, or composite, Young's modulus ( $E_e$ ), creating a two-layer (pavement/subgrade) system. Using temperature-corrected underplate surface deflections obtained through field measurements with an FWD or other NDT device, the value of  $E_e$  is calculated iteratively using a Bummister linear elastic solution. The values of  $E_e$  and  $h_t$  are then converted to a structural number (SN) value using a simple transfer function (1). The SN value is used to evaluate the pavement's in situ structural capacity using the AASHTO pavement design equations. The recommended AASHTO technique to correct for temperature alters the total underplate (at load center) deflection value before analysis according to the estimated average pavement temperature and pavement type. The temperatures at different depths of the pavement are derived from the pavement surface temperature at the time of the test and the average air temperature for the 5 days preceding the test date using Figure 1. Once the mean temperature of the AC bound layer has been estimated using the average of the surface, midpoint, and bottom layer temperatures, Figure 2 is used to determine the deflection-temperature adjustment factor for the appropriate pavement type. The product of this factor and the observed underplate deflection is an estimate of the deflection at 70°F. The pavement stiffness is then backcalculated using the corrected deflection.

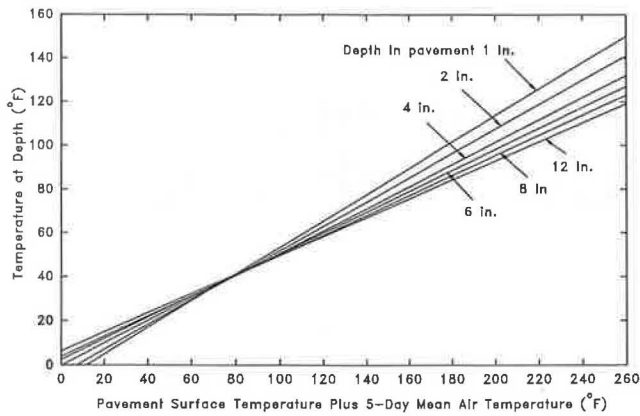
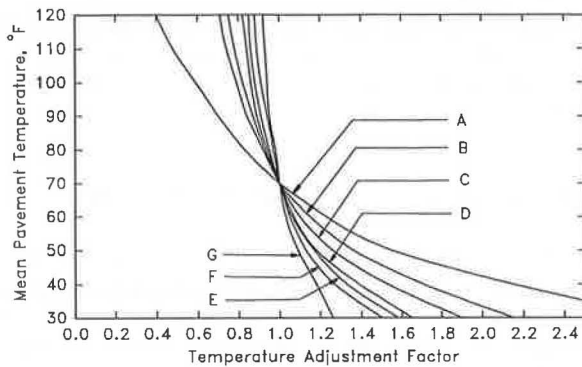


FIGURE 1 Variation of pavement temperature with depth and surface temperature plus 5-day mean air temperature (1, Appendix L).



Base Material	Curve (Base Thickness)
Asphalt (Full Depth)	A (All thicknesses)
Asphalt (Deep Strength)	B (4" of granular subbase)*
Portland Cement Concrete	G
Granular (Non-Stabilized)	C (6"); D (12"); E (20"); F (25")
Cement Treated Base	
Sound	D (4"); E (8")
Cracked	C (4"); D (8")

\* If more than 4" of granular material present use "Granular (Non-Stabilized)" base material category.

FIGURE 2 AASHTO recommended temperature adjustment factors (1, Appendix L).

### ALTERNATIVE TEMPERATURE CORRECTION METHOD

It is important to note that Figure 2 does not differentiate between pavements with different AC bound layer thicknesses. For instance, if a pavement has 2 in. of AC concrete over a 6 in. granular base or 8 in. of AC concrete over a 6 in. granular base, Curve C on Figure 2 is the recommended correction curve. To improve the AASHTO procedure an adjustment factor was developed that estimates the change in the overall pavement stiffness from the change in the AC bound layer stiffness and the geometry of the pavement. To calculate this factor the average pavement temperature, the ratio of AC bound layer thickness to non-AC bound thickness, and the modular ratio of AC bound to non-AC bound layers are used.

The composite modulus of an  $n$ -layer pavement system is calculated with the following equation (1, Appendix PP).

$$E_e = \left[ \sum_{i=1}^n \frac{h_i}{h_t} \times \sqrt[3]{\frac{E_i(1 - \mu_e^2)}{(1 - \mu_i^2)}} \right]^3 \quad (1)$$

For a three-layer system, (AC bound layer, non-AC bound layer, and subgrade), Equation 1 may be written as

$$E_e = \left[ \frac{\sqrt[3]{\frac{E_1(1 - \mu_e^2)}{(1 - \mu_1^2)}} + \frac{1}{x} \sqrt[3]{\frac{E_1}{z} \frac{(1 - \mu_e^2)}{(1 - \mu_2^2)}}}{\left(1 + \frac{1}{x}\right)} \right]^3 \quad (2)$$

where

- $\mu_1$  = Poisson's ratio of AC bound layer,
- $\mu_2$  = Poisson's ratio of non-AC bound layer,
- $\mu_e$  = Poisson's ratio of the equivalent (or composite) layer,
- $E_1$  = Young's modulus of AC bound layer,
- $x$  = ratio of AC bound layer thickness to non-AC bound layer thickness ( $h_1/h_2$ ), and
- $z$  = ratio of Young's modulus of the AC bound layer to Young's modulus of the non-AC bound layer ( $E_1/E_2$ ).

Several functions have been developed to estimate the variation of the modulus of AC concrete with temperature. An approximation taken from the Asphalt Institute (3) and recommended for correction of NDT results (4) is

$$\begin{aligned} \text{Log} E_{\text{std}} = & \text{log} E_{\text{field}} + 0.028829 P_{200} \left[ \frac{1}{(f_o)^\lambda} - \frac{1}{(f)^\lambda} \right] \\ & + 0.000005 \sqrt{P_{\text{ac}}} [(t_o)^{r_o} - (t)^r] \\ & - 0.00189 \sqrt{P_{\text{ac}}} \left[ \frac{(t_o)^{r_o}}{(f_o)^{1.1}} - \frac{(t)^r}{(f)^{1.1}} \right] \\ & + 0.931757 \left[ \frac{1}{(f_o)^n} - \frac{1}{(f)^n} \right] \end{aligned} \quad (3)$$

where

- $\lambda = 0.17033$ ,
- $n = 0.02774$ ,
- $t$  = test temperature (degrees Fahrenheit),
- $f$  = loading frequency (hertz),
- $t_o$  = standard temperature,
- $f_o$  = standard frequency,
- $P_{\text{ac}}$  = percent AC by weight of the mix,
- $E_{\text{field}}$  = AC concrete modulus at the standard temperature and frequency,
- $r_o = 1.3 + 0.49825 \log(f_o)$ ,
- $r = 1.3 + 0.49825 \log(f)$ , and
- $P_{200}$  = percent aggregate passing the No. 200 sieve.

Equation 3 may be simplified. A value of  $P_{\text{ac}} = 5.7$  percent was selected as typical (5). Typical FWD load duration is approximately 30 to 40 msec (6). Using the approximation

$$f = \frac{1}{2t} \tag{4}$$

where  $t$  = FWD load duration, an approximate typical frequency of 15 Hz is indicated for both test and standard conditions (4). Using these values and a reference temperature of 70°F, Equation 3 can be reduced to the following equation.

$$\text{Log}E_{\text{std}} = \text{log}E_{\text{field}} - 0.0002175[(t_0)^{1.886} - (t)^{1.886}] \tag{5}$$

Rewriting Equation 5 results in the following:

$$\frac{E_{\text{std}}}{E_{\text{field}}} = 10^{-0.0002175[(t_0)^{1.886} - (t)^{1.886}]} \tag{6}$$

Another correction, developed by Ullidtz (7), is based on backcalculation of moduli from AASHTO Road Test deflections. This relationship for asphalt temperatures above 35°F is given by

$$E(t) = 2.18 \times 10^6 \text{ psi} - 1.15 \times 10^6 \text{ psi} \times \log\left(\frac{(t^\circ\text{F} - 32)}{1.8}\right) \tag{7}$$

where  $E(t)$  is the AC concrete modulus (pounds per square inch) at the test temperature ( $t$ ) (degrees Fahrenheit). After solving for  $E(70^\circ\text{F}) = E_{\text{std}}$  and setting  $E(t) = E_{\text{field}}$ , Equation 7 may be rewritten as

$$\frac{E_{\text{std}}}{E_{\text{field}}} = \left[ 3.319 - 1.751 \times \log\left(\frac{(t^\circ\text{F} - 32)}{1.8}\right) \right]^{-1} \tag{8}$$

Ullidtz (7) notes that some AC concrete modulus-temperature relationships developed from laboratory tests indicate unrealistically low modulus values at high temperatures, whereas in the field the lower limit of AC concrete modulus is determined by the unbound modulus of the aggregate. A comparison of modular ratios derived from Equations 6 and 8 is shown in Figure 3. The values derived from Equation 6 are considerably lower than those predicted by Equation 8 at temperatures higher than 100°F. However, as the pavement

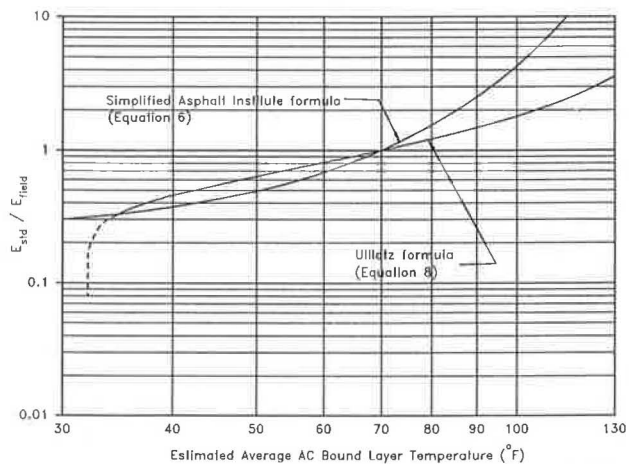


FIGURE 3 Variation of AC concrete modular ratio with temperature.

temperature approaches 32°F, the asphalt modulus predicted by Equation 8 approaches infinity. The Ullidtz formula (7) is not recommended when the pavement temperature is below approximately 35°F. Based on the authors' experience in the backcalculation of pavement stiffness, Equation 8 appears to provide the best prediction of in situ pavement stiffness for this type of analysis for AC bound layer temperatures above 35°F. Lytton et al. (4) discuss several other AC modulus temperature correction relationships that could also be used with this procedure.

The ratio of AC bound layer modulus at the reference temperature (70°F) to AC bound layer modulus at field temperature may be applied in a dimensionless form of Equation 2. To derive this ratio, Equation 2 is evaluated twice. The first evaluation sets  $E_e = E_{e \text{ std}} =$  the composite pavement modulus at the reference temperature and  $E_1 = E_{\text{std}} =$  AC bound layer modulus at 70°F. The second evaluation sets  $E_e = E_{e \text{ field}} =$  the composite pavement modulus at the field temperature and  $E_1 = E_{\text{field}} =$  AC bound layer modulus at the field temperature. The ratio of these two evaluations of Equation 2 may be written as

$$\frac{E_{e \text{ std}}}{E_{e \text{ field}}} = \frac{\left[ 1 + \sqrt[3]{\frac{E_{\text{std}}}{E_{\text{field}}} z x^3 \left( \frac{1 - \mu_2^2}{1 - \mu_1^2} \right)} \right]^3}{\left[ 1 + \sqrt[3]{z x^3 \left( \frac{1 - \mu_2^2}{1 - \mu_1^2} \right)} \right]^3} \tag{9}$$

The derivation of Equation 9 assumes that neither the base course stiffness ( $E_2$ ) nor the Poisson's ratios of the layers ( $\mu_1$  and  $\mu_2$ ) vary with temperature.

The use of Equation 9 with the Direct Structural Capacity Method requires that the modular ratio of the AC bound layer to the non-AC bound layer be specified. However, the Direct Structural Capacity Method (1) combines all layers before analysis and therefore provides no information on modular ratio. Fortunately, Equation 9 can be shown to be rather insensitive to variation in modular ratio. Figure 4 shows that at the bounds of thickness ratio ( $x$ ) typically encountered in the field, estimations of  $z$  will be inaccurate by a factor of 10 and will result in errors in  $E_{e \text{ std}}$  of approximately 10 percent.

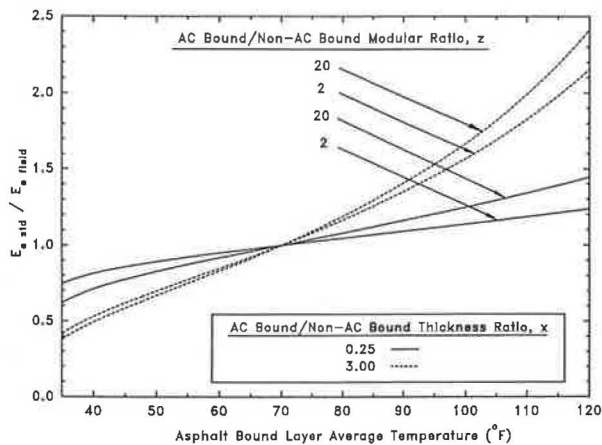


FIGURE 4 Variation of  $E_{e \text{ std}}/E_{e \text{ field}}$  ratio calculated using Equation 9 with temperature.

Therefore, it is suggested that a reasonable estimate of modular ratio is adequate for most pavement deflection analyses.

To simplify the use of Equation 9, the ratio of AC bound to non-AC bound layer stiffness ( $z$ ) may be estimated at 70°F and adjusted for temperature using Equation 8. Rewriting Equation 9 using this refinement gives

$$\frac{E_{e \text{ std}}}{E_{e \text{ field}}} = \left[ \frac{1 + \sqrt[3]{\frac{E_{\text{std}}}{E_{\text{field}}} z_{\text{std}}^3 \left( \frac{1 - \mu_2^2}{1 - \mu_1^2} \right)}}{1 + \sqrt[3]{\frac{E_{\text{std}}}{E_{\text{field}}} z_{\text{std}}^3 \left( \frac{1 - \mu_2^2}{1 - \mu_1^2} \right)}} \right]^3 \quad (10)$$

where  $z_{\text{std}} = z$  at 70°F. The variation with temperature in composite modulus temperature adjustment factor ( $E_{e \text{ std}}/E_{e \text{ field}}$ ) calculated using Equation 10 is shown in Figure 5. Equation 10 may also be written as

$$\frac{E_{e \text{ std}}}{E_{e \text{ field}}} = \left[ \frac{1 + \sqrt[3]{z_{\text{std}}^3 \left( \frac{1 - \mu_2^2}{1 - \mu_1^2} \right)}}{1 + \sqrt[3]{\frac{E_{\text{field}}}{E_{\text{std}}} z_{\text{std}}^3 \left( \frac{1 - \mu_2^2}{1 - \mu_1^2} \right)}} \right]^3 \quad (11)$$

The use of Equation 10 in lieu of the AASHTO method for the adjustment of composite pavement modulus has the advantage of computational ease. Because Figure 2 is presented in graphical form only, using it in pavement deflection analysis software requires either interpolation from data files of values read from the figure or the creation of regression equations to simulate Figure 2. Figure 2 also requires some judgement to select the proper curve for deflection adjustment. Equation 10 may be integrated easily into pavement deflection analysis software and has clearly defined inputs.

Although Equation 10 theoretically may be used at any temperature, when used with Equation 8 it is valid only for pavement test temperatures above 35°F. In warm climates, this restriction is not a serious problem. In climates in which high pavement temperatures are not typically encoun-

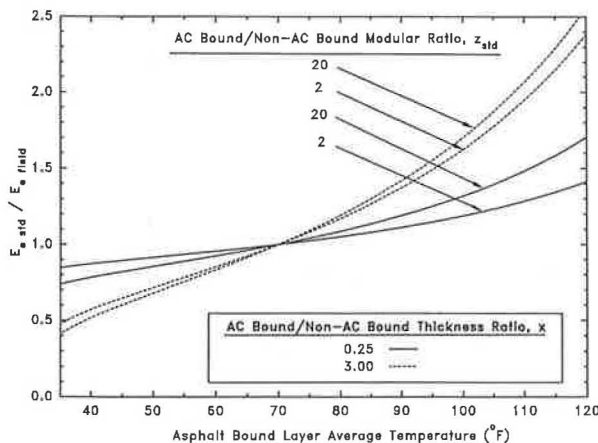


FIGURE 5 Variation of  $E_{e \text{ std}}/E_{e \text{ field}}$  ratio calculated using Equation 10 with temperature.

tered, the use of Equation 6 or another AC concrete modulus-temperature relationship may be more appropriate.

## COMPARISON OF RESULTS USING AASHTO AND PROPOSED METHODS

Theoretically, a perfect temperature correction technique should yield identical corrected pavement moduli ( $E_{e \text{ std}}$ ) when the same site is tested repeatedly at different temperatures. Unfortunately, inaccuracy in the estimation of the actual pavement temperature, complex pavement and subgrade material constitutive properties, variations in as-built pavement thickness, and other factors prevent totally uniform results from being achieved in the field. The removal of the component of variation in backcalculated pavement stiffness and, subsequently, structural number due to the variation of AC bound layer modulus with temperature should reduce the overall observed variation seen with varying temperature. Therefore, to judge the effectiveness of a temperature correction procedure, the overall variation of the results can be analyzed. A superior correction procedure should reduce variation of deflection-based backcalculated pavement stiffness with test temperature.

In order to achieve satisfactory results, any temperature correction procedure must rely on accurate estimation of pavement temperature. Bissada and Guirguis (8) noted that the deflection characteristics of flexible pavements are not only controlled by average pavement temperature, but also by the temperature gradient within the pavement, especially at high temperatures. Dynaflect tests were performed during a 2-year period on test sections in Kuwait, and the most uniform results were achieved under conditions of zero temperature gradient. The difficulty of estimating temperature gradient in uninstrumented pavements illustrates one of many difficulties that practicing pavement engineers must consider before the results from NDT may be used to accurately design overlays for flexible pavements. It should be noted that Figure 1 is based on the typical temperature gradient at 1 p.m. The actual temperature gradient may vary significantly during the day, decreasing the accuracy of the pavement temperature estimates.

Thirteen sites at various locations throughout South Carolina were tested using a Dynatest FWD. Drop heights were selected to give peak impact loadings of approximately 6,000, 9,000, 12,000, and 15,000 pounds. Each test section was 500 ft long and was tested at 50 ft stations on 8 to 10 different dates between January 1989, and June 1990. Most tests were conducted between 9 a.m. and noon. Testing was not conducted under rainy conditions or when the road surface was visibly moist. Pavement surface temperatures were collected using an infrared temperature sensor mounted on the FWD trailer. A summary of the pavement structure at the test sites is presented in Table 1.

Using both the AASHTO and the proposed alternative (Equations 8 and 10) temperature correction methods, values of  $E_{e \text{ std}}$  were computed for each station at each date using the Direct Structural Capacity Method. All Direct Structural Capacity Method computations here are based on FWD loadings of approximately 9,000 pounds. The value of  $z_{\text{std}}$  was

**TABLE 1 Pavement Structure of Test Sites**

Site Number	Road and County	Pavement Structure
1	I-26, Orangeburg Co.	11.3 inches AC Bound 14.0 inches Uniform Earth Base
2	SC-31, Charleston Co.	3.2 inches AC Bound 11.5 inches Fossiliferous Limestone Base
3	US-17, Charleston Co.	3.5 inches AC Bound 6.2 inches Fossiliferous Limestone Base
4	US-17, Charleston Co.	4.9 inches AC Bound 7.4 inches Fossiliferous Limestone Base
5	US-321, Fairfield Co.	6.2 inches AC Bound 3.5 inches Unbound Granular Material 12 inches Cement Stabilized Earth Base
6	SC-9, Chester Co.	10.8 inches AC Bound 6 inches Uniform Earth Base
7	I-26, Newberry Co.	9.0 inches AC Bound 16 inches Unbound Macadam Base
8	I-77, Richland Co.	18.1 inches AC Bound 6 inches Cement Stabilized Earth Subbase
9	S-1623, Lexington Co.	1.3 inches AC Bound 6 inches Unbound Macadam Base
10	I-20, Lexington Co.	12.4 inches AC Bound
11	US-76/378, Sumter Co.	6.6 inches AC Bound 12 inches Uniform Earth Base
12	US-76, Marion Co.	10.2 inches AC Bound
13	US-76/301, Florence Co.	7.0 inches AC Bound 4.5 inches Cement Stabilized Earth Base 8 inches Uniform Earth Base

assumed to be eight for all non-AC bound base pavements tested. The  $E_{e\text{ std}}$  values were converted to structural number using the transfer function in the AASHTO guide (1). This function is

$$SN = 0.0043h_r \sqrt[3]{\frac{E_{e\text{ std}}}{(1 - \mu_e^2)}} \quad (12)$$

The equivalent Poisson's ratio ( $\mu_e$ ) equals 0.35 and  $E_{e\text{ std}}$  is in pounds per square inch. Examples of  $E_e$  backcalculation results are shown in Figures 6 and 7.

Figure 6 compares backcalculated site average uncorrected and corrected composite pavement moduli ( $E_e$  and  $E_{e\text{ std}}$ ) for Site 9. Each data point on this figure represents an estimated average pavement temperature or average backcalculated composite pavement modulus on a testing date. Figure 6 shows a case for which the proposed temperature correction yields  $E_{e\text{ std}}$  values that remain much more stable with fluctuations in temperature. Interestingly, at Site 9, use of the AASHTO temperature correction significantly overcorrects composite pavement modulus. That is, overly high  $E_{e\text{ std}}$  values are predicted for high pavement temperatures (for example, see testing date in June 1989, when the estimated average pavement temperature was higher than 100°F) and overly low  $E_{e\text{ std}}$  values are predicted for low pavement temperatures (for example, see testing date in October 1989, when the estimated average pavement temperature was less than 50°F). Backcalculated site average uncorrected and corrected composite pavement moduli for Sites 8 and 12 are compared in Figure 7. Data from these sites clearly show that the proposed pavement temperature correction tends to yield  $E_{e\text{ std}}$  values less

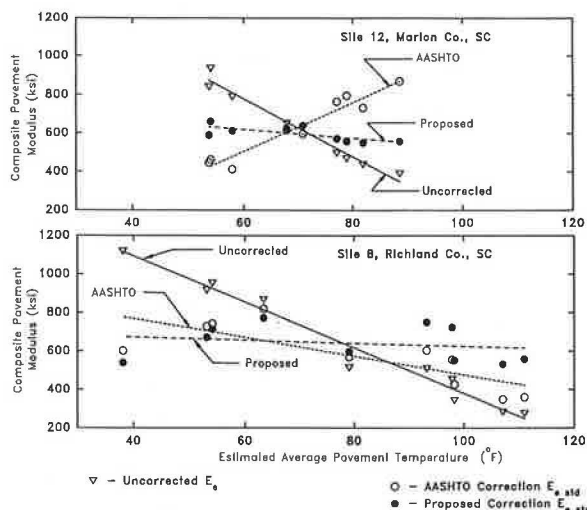


**FIGURE 6 Variation of average backcalculated corrected and uncorrected composite pavement modulus and estimated average pavement temperature with date for Site 9.**

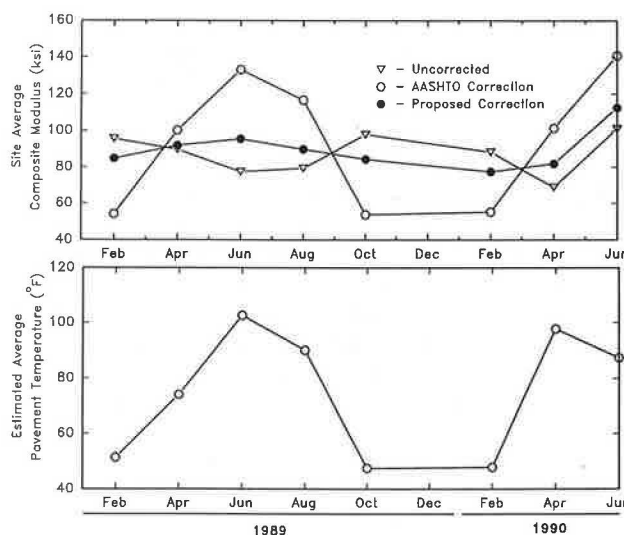


**FIGURE 7 Variation of average backcalculated corrected and uncorrected composite pavement modulus with estimated average pavement temperature for Sites 8 and 12.**

dependent on the average pavement temperature at the time of FWD testing.

For statistical evaluation, the structural number results for each deflection test at all testing dates were grouped according to the site and temperature correction method used and variances were computed. Each group of data was checked for normality using the Shapiro-Wilk statistic; all variances were then combined to compute an overall variance value. A summary is presented in Table 2 of the computed variation in structural number for each site and the results of statistical inferences described here. The assumption was made that the structural number of the sites remained constant during the 18-month test period. In reality, some slight reduction may have occurred as a result of traffic loading at all sites except

**TABLE 2 Summary of Site Structural Number Variances**

Site	$s_2^a$	$s_1^b$	Number of Tests Analyzed	$s_1^b / s_2^a$	Percent Probability $s_1^b < s_2^a$
2	0.18900	0.22351	99	1.18261	79.605
3	0.01478	0.01336	99	0.90383	30.885
4	0.01086	0.00994	99	0.91565	33.179
5	0.04999	0.04582	99	0.91661	33.366
6	0.14491	0.15038	88	1.03778	56.845
7	0.21878	0.23076	88	1.05476	59.789
8	0.13925	0.11994	99	0.86131	23.062
9	0.25595	0.73767	110	2.88209	100.000
10	0.00675	0.03912	88	5.79612	100.000
11	0.06349	0.51971	88	8.18567	100.000
12	0.22503	0.23625	88	1.04989	58.955
13	0.14799	0.26223	99	1.77195	99.749
14	0.14605	0.15554	88	1.06499	61.515
All Sites	0.12356	0.21316	1232	1.72516	100.000

<sup>a</sup>Proposed method site structural number variance  
<sup>b</sup>AASHTO method site structural number variance

Site 8, which was closed to traffic during the test period. Because the visual condition of the sites remained constant throughout the test period, it was concluded that the reduction in structural number during the test period was negligible compared with the observed structural number variation due to temperature effects.

Once all variances were computed, the *F* test for the comparison of the variances of two populations was used to test the null hypothesis that the variance of the proposed method is greater than or equal to the variance of the AASHTO method versus the alternative hypothesis that the proposed method's variance is less than the AASHTO method's variance. The percent confidence that the null hypothesis should be rejected in favor of the alternative is shown in the sixth column of Table 2. The site standard deviations are compared graphically in Figure 8.

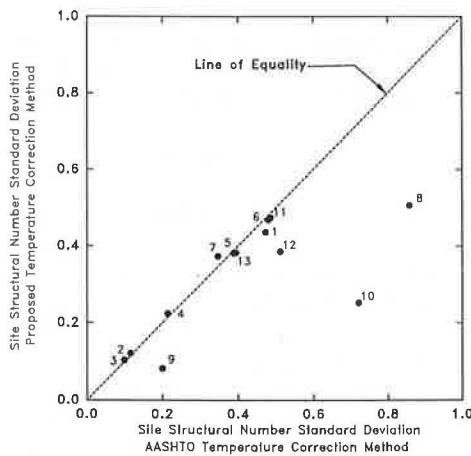


**FIGURE 8 Comparison of site average structural number standard deviation using proposed correction method versus AASHTO correction method.**

It may be inferred from the results in Table 2 that the proposed temperature correction method yielded a lower variance than the AASHTO correction method at 9 of the 13 sites. The confidence level that the proposed method is superior exceeded 99 percent at four of the sites. When all sites are considered together, the variance in structural number values computed using the proposed correction method is clearly lower than those computed using the AASHTO method. However, the proposed method led to greater variances at 4 of the 13 sites—Sites 2, 3, 4, and 7. Examination of the data shows that the variances at Sites 2, 3, and 4 are very low for both methods, so the increase in variance caused by the new method is extremely small.

The observed standard deviation of corrected SN values was found to increase with increasing SN for both correction methods. This relationship is shown in Figure 9 for both the AASHTO and proposed methods. The coefficient of variation (CV) of calculated SN, which expresses the standard deviation as a percentage of the mean, is shown in Figure 10. Although the data are relatively scattered, the trends shown indicate that the average CV values for both methods tend to remain

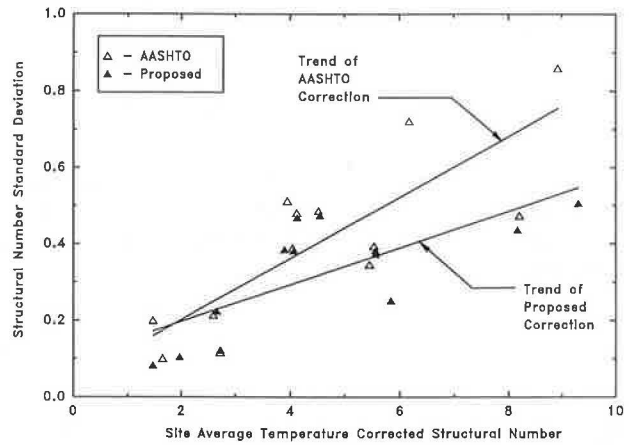


**FIGURE 9 Site average structural number standard deviation versus temperature-corrected backcalculated site average structural number.**

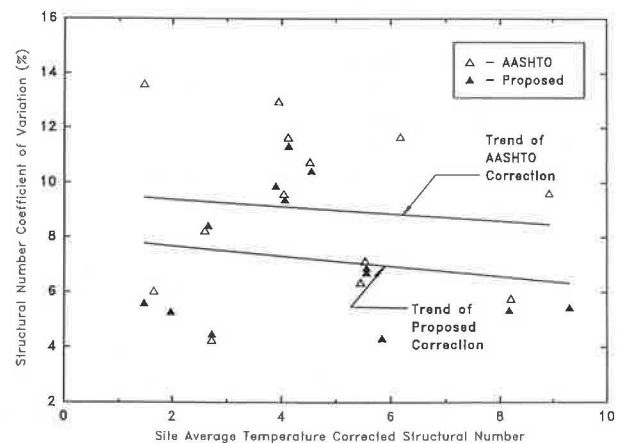


**FIGURE 10 Site average structural number coefficient of variation versus temperature-corrected backcalculated site average structural number.**

roughly constant with increasing SN. Additionally, it is clearly shown that the proposed alternative correction method yields a lower average CV value than the AASHTO correction method.

## CONCLUSIONS

The proposed method to correct composite modulus and structural number values calculated using the Direct Structural Capacity Method for the effect of temperature has been shown to provide more consistent results than the method currently recommended by the AASHTO pavement design guide (1) for conditions observed in South Carolina. The proposed technique requires an estimate of the ratio of AC bound layer stiffness to non-AC bound layer stiffness. Although the AASHTO Direct Structural Capacity Method does not provide any information on individual pavement layers, it was shown that an estimate of the AC/non-AC layer modular ratio is sufficient for most pavement analysis applications.

The equation used for the estimation of AC concrete modulus at varying temperatures, Equation 8, is not recommended at estimated average pavement temperatures of 35°F and below. Although curtailing FWD operations during periods of low pavement temperature is not a problem in warm climates such as South Carolina, in many areas this may not be an acceptable limitation. Additional difficulties may ensue if freezing of water in the base layer alters overall pavement stiffness.

It is likely that the accuracy of either correction procedure would be increased if more accurate estimates of pavement temperature could be made. Although destructive methods of measuring pavement temperature allow more accurate pavement temperature estimates, such tests tend to offset the advantage of the FWD to test large sections of pavement rapidly. As a compromise between rapid testing and accuracy, it may be advisable to perform a single destructive temperature measurement at the beginning of a test section. This direct measurement of temperature could then be com-

pared with the temperature calculated from Figure 1 to determine the estimation procedure's accuracy for that particular pavement.

## ACKNOWLEDGMENTS

This research was funded by the South Carolina Department of Highways and Public Transportation and FHWA. The authors would like to thank Lori Thombs of the University of South Carolina Department of Statistics for her assistance in the analysis of the test results.

## REFERENCES

1. *AASHTO Guide for Design of Pavement Structures*. AASHTO, Washington, D.C., 1986.
2. H. F. Southgate and R. C. Deen. Temperature Distribution Within Asphalt Pavements and Its Relationship to Pavement Deflection. In *Highway Research Record 261*, HRB, National Research Council, Washington, D.C., 1969.
3. *Research and Development of the Asphalt Institute's Thickness Design Manual (MS-1)*, 9th ed. Research Report 82-2, Asphalt Institute, College Park, Md., 1982.
4. R. L. Lytton, F. P. Germann, Y. J. Chou, and S. M. Stoffels. *NCHRP Report 327: Determining Asphaltic Concrete Pavement Structural Properties by Nondestructive Testing*. TRB, National Research Council, Washington, D.C., 1990.
5. *Standard Specifications for Highway Construction*. South Carolina Department of Highways and Public Transportation, Columbia, S.C., 1986.
6. B. E. Seebaly. *Dynamic Models for Pavement Analysis*. Ph.D. dissertation. Arizona State University, Tempe, 1987.
7. P. Ullidtz. *Pavement Analysis*. Elsevier, New York, N.Y., 1987.
8. A. F. Bissada and H. Guirguis. Temperature Dependency of Dynamic Measurements on Asphalt Pavements. In *Transportation Research Record 930*, TRB, National Research Council, Washington, D.C., 1983.

---

*Publication of this paper sponsored by Committee on Strength and Deformation Characteristics of Pavement Sections.*

# Simplified, Rational Approach to Falling Weight Deflectometer Data Interpretation

DIETER F. E. STOLLE AND FRIEDRICH W. JUNG

The authors present a simple elastostatic approach to estimate a suitable subgrade modulus from falling weight deflectometer (FWD) data. An effective surface modulus is defined on the basis of Boussinesq-Newmark equations. Deviations between the model assumptions and actual in situ conditions are reflected in the effective surface modulus variation with radius. The variation indicates which sensor readings are suitable for backcalculation. The presence of a shallow bedrock, increase in subgrade modulus with depth, or anisotropic properties may lead to nonconservative estimates of subgrade modulus. Assuming that the deflections at the subgrade surface (not directly under the load) may be approximated by the surface deflections, the Boussinesq-Odemark equations are used to define an effective subgrade modulus. In order to determine the subgrade modulus, the equivalent thickness of the pavement structure, which reflects pavement stiffness, is estimated by fitting preselected normalized deflections. Given the equivalent thickness, an effective subgrade modulus profile is established, from which a design subgrade modulus may be determined. An example using data of the Canadian Strategic Highway Research Program (C-SHRP) demonstrates the approach. The uniformity of the subgrade at the C-SHRP site is studied by considering the spectral density functions of the FWD time histories. The group velocity is used to define a weighted average profile modulus. The profile moduli of the two sections studied were higher but consistent with subgrade moduli estimated using elastostatic analysis.

Pavements deteriorate gradually over many years. To assist in the decision making with respect to the allocation of funds and resources for the maintenance and rehabilitation of the aging highway network, the highway engineer is finding it necessary to rely more and more on nondestructive testing (NDT) techniques for evaluating the structural integrity of pavement structures. A popular NDT approach is falling weight deflectometer (FWD) testing, together with the interpretation of the surface deflection data via rational analysis. FWD testing is reliable, quick to perform, and its data can provide the engineer with an objective estimate of structural pavement stiffness.

A key component in the interpretation of FWD data for evaluating the structural integrity of pavements is backcalculation analysis. Unfortunately backcalculation problems are often ill-conditioned and their solutions are not unique, even under ideal conditions (1,2). These difficulties are aggravated

by the fact that the mechanical models often used in backcalculation analyses do not properly take into account the material properties and the dynamic nature of the FWD load. Recognizing the analysis limitations, Lytton et al. (3) developed an expert systems environment to help provide more realistic interpretation of FWD data.

It is clear that the use of more realistic mechanical models is most desirable from a fundamental point of view. Although many advanced models are available, the potential gains achieved from these models are most often undermined by the lack of input data, which is required to properly define the boundary-valued problem, and by the increased difficulty to converge to physically admissible solutions. Furthermore, one cannot afford to use computationally intensive models within a pavement management environment in which several thousand calculations may be made using the data collected during FWD testing. Examples of data that are often not available include: accurate thickness of each layer, spatial variation of subgrade materials and moisture content, and stress history of subgrade material.

The objective of this paper is to present a simple, "workhorse" approach for characterizing pavement structures using FWD data. Implicit in the approach is the understanding that insufficient information generally exists to properly define a pavement structure, boundary-valued problem. Consequently, FWD data are interpreted by implicitly taking into account why backcalculated, effective moduli deviate from expected, idealized trends. To provide additional information on the variation of subgrade properties, it is demonstrated how spectral analysis techniques may be used to investigate the uniformity of the subgrade along the road. Although considerable literature exists on backcalculation, only those papers considered to be most relevant to this contribution are referenced.

## MECHANICAL MODELS

A typical pavement structure, shown in Figure 1, consists of a prepared subgrade over which granular base and asphalt concrete courses are constructed. Computer programs developed for pavement analysis, such as BISAR and ELSYM5, generally assume linear elastic theory where the upper, parallel layers extend to infinity in the horizontal plane, and the subgrade is assumed to be semi-infinite. These programs are considered to provide exact solutions. One must remember,

D. F. E. Stolle, Department of Civil Engineering and Engineering Mechanics, McMaster University, Hamilton, Ontario, Canada L8S 4L7. F. W. Jung, Pavements and Roadway Section, Research and Development Branch, Ministry of Transportation of Ontario, Downsview, Ontario, Canada M3M 1J8.

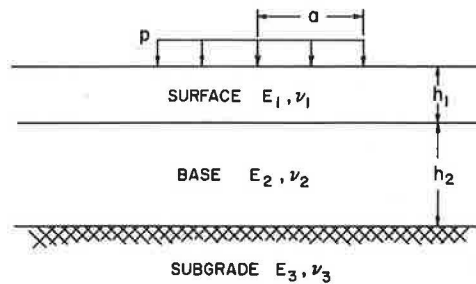


FIGURE 1 Typical pavement structure.

however, that "exact" refers to the solution of idealized problems.

To more realistically take into account the stress-dependent nature of the pavement and subgrade materials, models have been developed within the finite element framework. Although these models help provide a better understanding of a pavement's response to surface loading in a qualitative sense (4), their use within a backcalculation environment will not necessarily provide better quantitative solutions because the input data with respect to distribution of properties within the subgrade must still be assumed. In other words, these models still provide an idealization. Furthermore, because of the nature of the finite element approximation, it is not clear, a priori, how sensitive a backcalculated solution is to discretization.

Realistic analysis of pavement structures, for the purpose of design or evaluation of in situ properties by means of backcalculation, is complicated by the complex properties of the materials and their distribution. All models provide solutions that deviate from the actual in situ behavior. As a model becomes more complex, it becomes more difficult to keep track of the parameter(s) responsible for any deviation between ideal and actual behavior. As a result, the approach described here emphasizes the use of simple models. However, an appropriate mechanical model should reflect the phenomenon being studied, and backcalculation should not attempt to extract more information than is provided by what is actually known from the input data.

The simplest model that was considered is a flexible circular plate of radius  $a$  and uniform pressure  $p$ , supported by a semi-infinite, linear elastic homogeneous half space. Neglecting the friction that may develop between the plate and foundation and assuming isotropic properties it is possible to evaluate an effective surface modulus ( $E_{eff}$ ) (5,6) using

$$E_{eff}(r) = \frac{p(1 - \nu^2)}{w(r)} a \Omega_1(r/a) \quad (1)$$

where

$\nu$  = assumed Poisson's ratio for the half space,  
 $r$  = radius at which the vertical deflection  $w(r)$  is calculated, and

$\Omega_1(r/a)$  = a shape function.

If the in situ measurements correspond to a problem that satisfies all model assumptions exactly,  $E_{eff}$  should be independent of  $r$ . Because the model is only an approximation,  $E_{eff}$  is not constant. The relationship between  $E_{eff}$  and  $r$  pro-

vides the engineer information with respect to the variation of material stiffness with depth.

A second model is introduced that recognizes that the pavement structure is constructed with materials that have elastic moduli higher than that of the subgrade. Using the Boussinesq-Odemark methodology (6), the displacement [ $w_s(r)$ ] at the subgrade level may be approximated as

$$w_s(r) = \frac{P(1 + \nu)}{2\pi E_3 h_e} \Omega_2(r/h_e) \quad (2)$$

where  $h_e$  = equivalent thickness:

$$h_e = 0.9 (h_1^3 \sqrt{E_1/E_3} + h_2^3 \sqrt{E_2/E_3}) \quad (3)$$

$\Omega_2$  = shape function:

$$\Omega_2(r/h_e) = \frac{1}{R^3} + \frac{2(1 - \nu)}{R} \quad (4)$$

where

$R = [1 + (r/h_e)^2]^{1/2}$ ,  
 $P$  = applied load, and  
 $E_3$  = subgrade modulus.

The elastic moduli  $E_1$  and  $E_2$  and thicknesses  $h_1$  and  $h_2$  are defined in Figure 1. The definition for equivalent thickness in Equation 3 assumes that the Poisson's ratio ( $\nu$ ) is the same for all layers. Equation 2 may be used to estimate the surface deflection [ $w(r)$ ], provided that the vertical strains in the pavement structure are small. This is generally true for thin, stiff layers or if deflections are calculated at  $r$  greater than  $2a$ . If Equation 2 is inverted, one may evaluate an effective subgrade modulus ( $E_s$ ), provided that  $h_e$  is known or can be estimated. Similar to  $E_{eff}$ , the functional relationship between  $E_s$  and  $r$  provides the engineer with information on the variation of material stiffness with depth.

## LIMITATIONS OF MODELS

The FWD is an instrument that measures the deflection history at various sensors caused by an impulse load created by a falling weight. The time history of deflections arising from an FWD test is shown in Figure 2. The load is distributed over a circular plate of 30 cm diameter and thus resembles, also in its duration, a passing heavy single-tire wheel load from a truck. The peak deflections measured at various distances from the load only superficially resemble the deflection basin created by an equivalent elastostatic load. Elastodynamic analysis (7,8) indicates that the shape of the deflection bowl defined by peak deflections is different from that corresponding to an elastostatic load. Consequently, a systematic error is introduced to subgrade modulus estimates when elastostatic models are used for backcalculation. A factor not considered with respect to load application is the pressure distribution under the plate. Although the effect of the pressure distribution on effective moduli estimates may be important in the immediate vicinity of a plate resting on a weak pavement structure, its effect is diminished as pavement stiff-

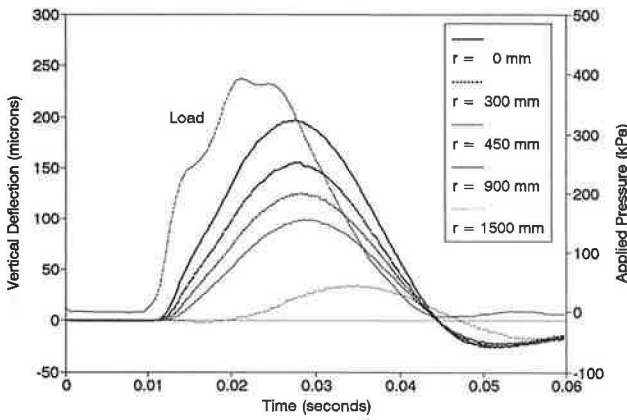


FIGURE 2 Typical FWD load and deflection histories.

ness or the radius at which the displacement is observed increases.

Real pavement and subgrade materials exhibit nonlinear stress-strain behaviors that are sensitive to stress level, temperature, moisture content, and loading history (3,9). To compound analysis difficulties, the properties are not uniform, and continuum mechanics concepts do not apply to the analysis of cracked or broken-up pavements. Consequently, the use of Equations 1 and 2 must be accompanied by the understanding that the moduli associated with these equations are not material properties, but model parameters which vary with time (10). These parameters, which directly reflect material properties, undergo an evolution influenced by environmental factors and traffic history.

The difficulty of incorporating the evolution of properties into a model can be easily appreciated by considering what happens during the development of residual stresses as a result of plastic deformations induced by a heavy load (4) and subsequent stress relief due to creep as temperatures rise. Although it may be possible to follow such a process for one or two load applications, it is not possible to do so for the general random nonlinear loading process that is encountered in practice. Fortunately an NDT program can provide the engineer with some of the information lacking when the evolution details of material properties in a mechanical model are neglected.

**IDEALIZED EXAMPLE**

A comparison of computer-generated and measured deflection bowls clearly indicates that differences exist between actual field conditions and what is assumed for modeling. In order to investigate possible reasons for the observed differences, an idealized two-layer pavement was studied; the effects of bedrock location and dynamic impact loading were taken into account. The problem profile consisted of a pavement with an elastic modulus of 2,250 MPa and Poisson's ratio of 0.35, supported by a homogeneous subgrade with an elastic modulus of 45 MPa and a Poisson's ratio of 0.50. The elastostatic deflection bowls were generated using ELSYM5.

The elastodynamic analyses were completed using a discrete layer approach similar to that described elsewhere (7). The version of the model adopted for this study, however, treated the pavement as a Kirchhoff plate and the subgrade

as a semi-infinite halfspace. The analysis procedure was based on a Galerkin approach in which Burmister's static solution (11), together with a Bessel-Fourier expansion, provided an interpolation function for displacements in the subgrade. The Burmister solution was assumed to be acceptable as an interpolation function because the FWD load is dominated by low frequency content. In order to take advantage of Bessel function orthogonality properties, the load was also expressed by a Fourier series approximation, thereby permitting an uncoupled time-domain solution for each term of the series. The net displacement response at a point was obtained by linearly superimposing the appropriate contribution from each solution. When generating the elastodynamic deflection bowls, the FWD impact load was applied as a half-sine wave over a time interval of 0.025 sec, and a unit weight of 20 kN/m<sup>3</sup> was assumed.

The effective surface modulus profiles using data from the elastostatic analyses are summarized in Figures 3 and 4, and the profiles obtained from deflection bowls generated by the discrete layer model are compared in Figure 5. Figure 3 clearly shows that an increase in effective modulus, when real data are used, can be attributed to the presence of bedrock at shallower depths. The strength of the effective modulus increase with radius depends on the subgrade thickness (*H*). As *H* decreases, both the minimum effective modulus and rate of increase of the distant effective moduli increase.

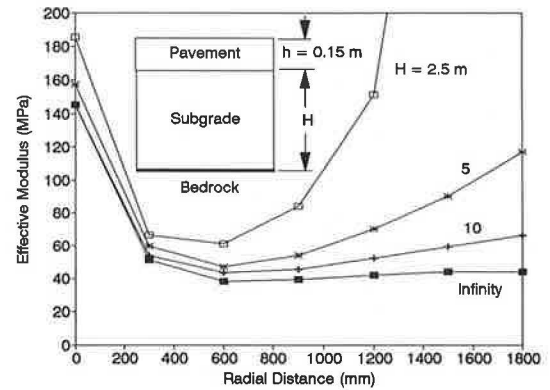


FIGURE 3 Influence of subgrade thickness (*H*) on effective surface modulus.

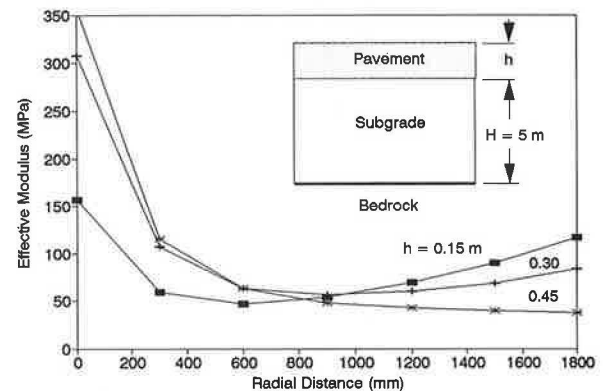


FIGURE 4 Influence of pavement thickness (*h*) on effective surface modulus.

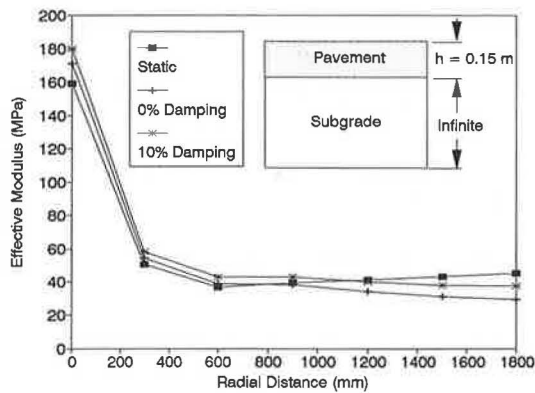


FIGURE 5 Influence of dynamic loading on effective surface modulus.

Although not shown, the increase in effective modulus at larger radii can also be explained if the subgrade modulus increases with depth (6) or if the subgrade properties are anisotropic (12). The presence of bedrock at shallow depths may be regarded as providing a sudden increase in subgrade stiffness. Owing to the sensitivity of the outside sensors to material properties deeper within the subgrade, it is clear that the sensors farther away from the load may not be suitable for estimating an average subgrade modulus that is representative of that portion of the subgrade that has the greatest impact on the life of a pavement.

As expected, the effective modulus profile, for the case in which the subgrade extends to infinity, asymptotically approaches 45 MPa as the radial distance from the load increases. The dip below 45 MPa at  $r = 600$  mm, and the subsequent gradual increase of  $E_{eff}$ , is a result of the Poisson's ratio of the pavement being different from that of the subgrade. A Poisson's ratio of 0.5 was used to estimate all effective surface moduli. Had the Poisson's ratio of the pavement,  $\nu_1 = 0.35$ , been substituted into Equation 2 for the point at  $r = 600$  mm, the effective modulus would have been slightly larger than 45 MPa. If effective moduli are estimated using idealized deflection bowls in which all layers have identical Poisson's ratios, the minimum effective modulus is attained at  $r \rightarrow \infty$  (5).

Figure 4 shows that the minimum effective surface modulus occurs at a larger radial distance as the thickness of the pavement increases. For the idealized two-layer problem the radius at which  $E_{eff}$  is a minimum corresponds approximately to  $h_e$ . As the minimum  $E_{eff}$  is pushed further away from the load, the positive slope at the outer sensors is decreased.

When the deflection bowl data from the elastodynamic analysis are used, the effective surface modulus decreases below 45 MPa as  $r$  increases, as shown in Figure 5. This is not surprising because the decay rate with respect to radius of a deflection bowl defined by a propagating wave is less than that corresponding to an elastostatic deflection bowl (7). Although it is clear that the dynamic nature of the FWD load has an influence on effective moduli predictions, these effects may be quite small when compared with those associated with subgrade modulus increase with depth or anisotropic soil properties.

The results from the idealized two-layer problem suggest that the effective surface modulus variation with radius may

be used to characterize a pavement-subgrade profile: (a) radial distance to the minimum  $E_{eff}$  is proportional to  $h_e$ ; (b) minimum  $E_{eff}$  provides a ballpark stiffness estimate of the average subgrade modulus in the vicinity of the load; and (c) taking into account pavement stiffness,  $dE_{eff}/dr$  at larger values of  $r$  may indicate how subgrade modulus increases with depth. It appears that the effects of the unknowns associated with subgrade modeling and the dynamic nature of the FWD load are relatively small, provided that the sensor readings directly under the load and on the positive  $dE_{eff}/dr$  branch are not used in backcalculation.

The use of the outside sensors can lead to nonconservative estimates in subgrade modulus. To compensate for the differences between the assumed and the actual conditions, Jung (13) developed a curve-fitting strategy to permit the use of outside sensors for backcalculation. The strategy incorporates the peak deflections from the outside three or four sensors by introducing a power law fit

$$\log(E_{eff}) = (\eta - 1) \log(r) + C \quad (5)$$

where  $E_{eff}$  corresponding to radius  $r$  is obtained from the deflection data using Equation 1, and  $\eta$  and  $C$  are constants evaluated from regression analysis. It is suggested that a representative subgrade modulus may be estimated from Equation 5 by calculating  $E_{eff}$  at a radius of 0.75 m (13). Analyses involving actual FWD data indicate that the error of fit obtained, when trying to fit the last three or four sensor readings, may provide a measure of pavement condition (i.e., badly cracked or broken pavements have high errors of fit, whereas pavements in good condition have low errors of fit) (5).

## BACKCALCULATION STRATEGY

Various backcalculation strategies are used for solving the inverse problem. The approach most often adopted involves the following steps:

1. Estimate the seed moduli via some approximate strategy,
2. Predict a deflection basin using estimated moduli,
3. Compare predicted and measured deflection basins,
4. Adjust layer moduli through a search technique to reduce differences between measured and predicted displacements, and
5. Repeat Steps 2 to 4 until error between the two deflection basins is within an allowable tolerance.

Regardless of which procedure is used, solutions are not unique and engineering judgment is required to determine whether the predictions are reasonable.

The backcalculation procedure proposed here is simplified significantly by absorbing the effect of the pavement structure on displacements through a single parameter:  $h_e$ . The solution procedure is based on rewriting Equation 2 as

$$\frac{w(r)}{w(r_n)} = \frac{\Omega_2(r/h_e)}{\Omega_2(r_n/h_e)} \quad (6)$$

where  $r_n$  is the radius corresponding to the sensor for which deflection is used to normalize the deflection bowl data. Tak-

ing into account the results of the idealized example of the previous section and form of Equation 6 leads to the following simple backcalculation strategy:

1. Find the sensor  $n$  at which  $E_{eff}$  is a minimum,
2. Normalize deflections using sensor  $n$ ,
3. Using sensors  $i = 2$  to  $n$ , find  $h_e$  that provides the best root mean square fit to Equation 6,
4. Using optimum  $h_e$ , calculate  $E_s$  at each sensor to provide an effective subgrade modulus profile, and
5. Estimate the design subgrade modulus from the effective subgrade modulus profile.

The purpose of normalizing the data is to eliminate one unknown, the subgrade modulus, which for Figure 1 corresponds to  $E_3$ . Determining optimum  $h_e$  is equivalent to finding a function that best fits the shape of the deflection bowl, which is sensitive to the properties of the pavement structure. It is recommended that the first sensor not be used because a sufficiently large portion of the measured displacement may be due to pavement layer straining that is not taken into account in Equation 2. For pavements with large  $h_e$  it may also be necessary to avoid using the second sensor deflection because the error, associated with the assumption that the surface deflection is approximately the same as the subgrade deflection, may also be greater than 10 percent.

### PROPAGATION OF ERRORS

As indicated previously, although it is tempting to suggest that more realistic modeling could improve the predictions of the layer moduli, the lack of sufficient input data would most likely undermine the accuracies attainable with more realistic modeling. On the other hand, approximations introduce systematic errors to the predictions owing to incompatibility between model and data. Work by Stolle (2) demonstrates that simplifications introduced for material modeling of the subgrade can have a significant influence on the prediction of the pavement structure moduli. This section briefly addresses this theme with respect to Equation 2.

The error analysis is simplified by considering only sensitivities at  $r = 0$  for a two-layer problem. Given that the operator  $\Delta$  refers to an incremental change, first order expressions for error estimates

$$\left| \frac{\Delta h_e}{h_e} \right| = \left| \frac{\Delta w}{w(0)} \right| + \left| \frac{\Delta E_3}{E_3} \right| \quad (7)$$

$$\left| \frac{\Delta E_1}{E_1} \right| = 3 \left| \frac{\Delta w}{w(0)} \right| + 2 \left| \frac{\Delta E_3}{E_3} \right| + 3 \left| \frac{\Delta h_1}{h_1} \right| \quad (8)$$

may be obtained by using a truncated Taylor's expansion for Equation 2. It should be noted that implicit in the error equations is the assumption that  $w(0) \approx w_s(0)$ . From Equation 8 it is clear that an error associated with displacement, subgrade modulus, or layer thickness as a result of the model not fitting the data properly amplifies the relative error associated with the pavement modulus. For example, a 10 percent error in both subgrade modulus and pavement thickness could pro-

vide, to the first order, a 50 percent error in the estimate of  $E_1$ . At the same time, the relative error associated with  $h_e$ , which indirectly provides a measure of pavement stiffness, is no greater than that of the subgrade modulus. This suggests that it may be more advantageous to deal with  $h_e$  instead of  $E_1$ . Besides, an estimate of  $E_1$  is not required to evaluate key diagnostic parameters such as the radial tensile strain at the bottom of the asphalt layer or maximum compressive strain at the surface of the subgrade (13).

### TEMPERATURE ADJUSTMENTS

All primary response parameters should be adjusted to a standard reference state of temperature, moisture condition, and loading frequency (9). Of these three variables, temperature adjustment is most critical because the asphalt concrete temperature can change significantly during the day. This makes it difficult to meaningfully compare pavement stiffness predictions from the various test sections that may be located along the same road. Various relationships exist, however the one adopted by Jung (13) is followed here to demonstrate how the equivalent thickness of an asphalt layer is influenced by temperature changes. Given that the temperature dependence of the elastic modulus of asphalt concrete may be approximated as

$$E_1 = E_1^s \exp[k(T - T_s)] \quad (9)$$

where

$$\begin{aligned} E_1^s &= \text{asphalt concrete modulus at temperature } T_s, \\ T - T_s &= \text{temperature difference (degrees Celsius), and} \\ k &= \text{a coefficient.} \end{aligned}$$

The equivalent thickness of the asphalt concrete  $h_e^a$  varies according to

$$h_e^a \propto \exp\left[\frac{k}{3}(T - T_s)\right] \quad (10)$$

It should be noted that Equation 10 follows naturally from Equation 9 when one considers the definition for equivalent thickness (see, for example, Equation 3). As shown in Equation 10,  $h_e^a$  is not as sensitive to temperature change as the asphalt concrete modulus. Because  $h_e^a$  is only a portion of the overall  $h_e$ , the temperature change effects may, in some cases, be neglected. For cases in which it cannot be neglected (e.g., extreme temperature differences), an assumption must be made with respect to the asphalt concrete modulus, provided that the asphalt concrete is not severely cracked. If a pavement is severely cracked, a temperature adjustment is meaningless.

### CASE HISTORY

One of the C-SHRP test sites is located on Highway 80 south-east of Sarnia. Although the highway was relatively smooth to drive on, the pavement was severely cracked and was therefore rehabilitated with an overlay during the summer of 1989. The pavement profile of Section A consists of a 90 mm bi-

tuminous overlay, 140 mm broken bituminous layer, and 280 mm of Granular A and 560 mm of Granular C sand. The effective modulus profiles at Sections 0.00 and 0.08 are summarized in Figure 6.

The effective moduli were calculated assuming  $\nu = 0.5$ . The equivalent thicknesses at Sections 0.00 and 0.08 were estimated to be 1005.4 mm and 945 mm, respectively. The slightly lower subgrade moduli shown in Figure 6 for Section 0.00 may, in part, be attributed to the slightly higher  $h_e$  at this section. It is clear from this figure that Equation 2 largely filters out the effect of the pavement structure on the effective subgrade modulus estimates. For both these sections, the minimum effective surface modulus, which occurs at  $r = 900$  mm, is close to the effective subgrade modulus. A representative subgrade modulus that is assumed to correspond to the deflection at which  $E_{eff}$  is minimum is approximately 75 to 80 MPa. The lower subgrade moduli in the vicinity of the load are attributed to systematic errors associated with neglecting the strain in the pavement structure. Farther away, both the effective surface and subgrade moduli merge, as anticipated. The positive increase in the effective moduli at the distance sensors is attributed to the stress-dependence of the subgrade modulus, which would increase with depth. The use of correlation techniques for studying the stiffness increase with depth is discussed briefly in the next section.

#### CORRELATION ANALYSIS OF FWD DATA

The analysis methodology up to this point has only made use of the peak deflections. In correlation analysis, more often referred to as spectral analysis, the full time history at each sensor, exemplified in Figure 2, is used in order to extract more information. Owing to the nature of FWD load and location of sensors, some constraints complicate the interpretation of the data: (a) low frequencies (0 to 100 Hz) are excited, and consequently only properties in the subgrade can be adequately characterized; and (b) sensors are located in "near field," where Rayleigh waves are not yet fully developed. Because the waves are not fully developed, models that are advanced and more computationally intensive (14) are required to exploit the information provided by the FWD data.

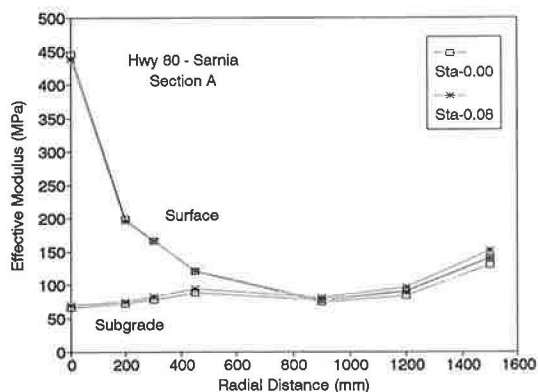


FIGURE 6 Summary of effective surface and subgrade moduli for Sections 0.00 and 0.08, C-SHRP site.

For the purposes of this paper, the objective of correlation analysis is to provide additional information on the uniformity of properties over a region. An important aspect of this approach is that the time lag ( $\tau$ ) in response between two sensors is sensitive to the material properties of the underlying media. Given that the time histories of two sensors are defined by

$$\begin{aligned} x(t) &= w(r_1, t) - \bar{w}(r_1) \\ y(t) &= w(r_2, t) - \bar{w}(r_2) \end{aligned} \quad (11)$$

where  $\bar{w}(r_i)$  refers to average values of the deflection history  $w(r_i, t)$  at sensor  $i$  over a time period  $T$ , a covariance function  $C_{xy}(\tau)$  may be defined as

$$C_{xy}(\tau) = \frac{1}{T} \int_0^T x(t)y(t + \tau) dt \quad (12)$$

or when working with discrete Fourier transforms (15) as

$$C_{xy}(\tau) = \sum_k A_k \cos(2\pi f_k \tau + \theta_k) \quad (13)$$

The amplitude  $A_k$  and phase lag  $\theta_k$  are components of the cross-spectral density function (cross-spectrum). The fundamental frequency is given by  $f_1 = 1/T$ . The correlation coefficient function  $\rho_{xy}(\tau)$ , which is a normalized equivalent of  $C_{xy}(\tau)$ , satisfies the constraint  $|\rho_{xy}(\tau)| \leq 1$  (15). As with the correlation coefficient used in statistics,  $|\rho_{xy}(\tau)| = 1$  implies perfect correlation between two variables that are related through a linear operator.

The phase lag  $\tau_m$ , which maximizes  $\rho_{xy}(\tau)$ , can be used to define the group velocity  $v_G = \Delta r / \tau_m$ , where  $\Delta r$  is the distance between both sensors. Instead of following the usual practice, where the phase velocity  $v_k$  corresponding to frequency  $f_k = k f_1$  is evaluated for each  $k$  in order to estimate the elastic modulus variation with depth (16), the group velocity is used to estimate a weighted average profile modulus

$$E_{av} = 1.21 \bar{\rho} v_G^2 \cdot (1 + \nu) \quad (14)$$

where  $\bar{\rho}$  is the average density of the subgrade.

The analysis of a semi-infinite halfspace indicates that most of the energy associated with a surface (Rayleigh) wave is concentrated in a zone one wavelength wide (17). Assuming that  $v_G$  corresponds to the frequency  $f_G$  whose term dominates  $\rho_{xy}(\tau)$ , then a crude approximation for the zone, to which the average  $E_{av}$  applies, may be defined by  $\lambda_G = v_G / f_G$ . Implicit in Equation 14 is the understanding that  $\lambda_G$  is much larger than the thickness of the stiffer asphalt concrete layer. This constraint is required because the presence of a pavement alters the surface wave velocity. As the wavelength increases the influence of the pavement decreases.

The C-SHRP data were analyzed using the correlation procedure described in this section. The correlation was carried out between Sensors 5 and 7, which were located 900 and 1500 mm away from the load, respectively. The data were sampled at a rate of 0.2 msec for 60 msec. Because discrete Fourier transforms assume that the input is periodic, an additional 724 points consisting of zeros was added at the end of the time-history records to ensure a reasonable transfor-

mation of the nonperiodic data. The results are summarized in Figures 7 and 8.

Figure 7 compares the variation in amplitude and phase angle for both sections. The dominant frequencies for Sections 0.00 and 0.08 are approximately 15 and 10 Hz, respectively. The concave upward increase in phase angle with respect to frequency increase suggests that the elastic modulus increases with depth, which is consistent with the effective modulus profiles. Although the overall phase angle profiles for these sections are similar, the fact that they are not the same indicates that the variations in stiffness with depth may not be identical. The largest differences between the two occur in the frequency range of 35 to 45 Hz, which corresponds to properties close to the pavement structure. The larger phase angle at 44 Hz for Section 0.08 may reflect the fact that the old pavement under the overlay at this section is severely cracked.

Using the data from the correlation coefficient functions shown in Figure 8, the profile modulus  $E_{av}$  for Sections 0.00 and 0.08 are estimated to be 113 and 122 MPa, respectively. These estimates are based on an average unit weight of 20 kN/m<sup>3</sup> and Poisson's ratio of 0.5. If one were to further assume that the sampling depth is approximately  $\lambda_G/2$ , then these moduli would correspond to depths of 4 and 6.5 m, respectively. Although these figures are only approximate, the values for  $E_{av}$  are consistent with the effective subgrade modulus

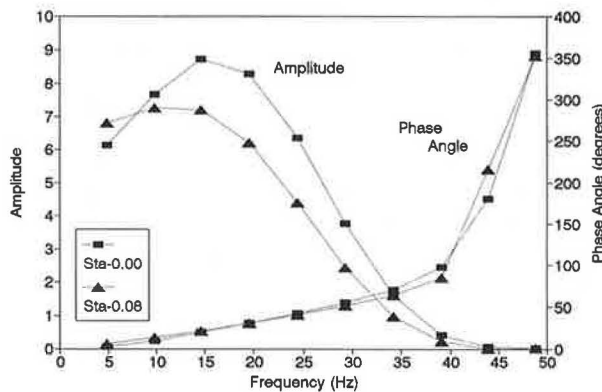


FIGURE 7 Cross-spectrum from FWD data for Sections 0.00 and 0.08, C-SHRP site.

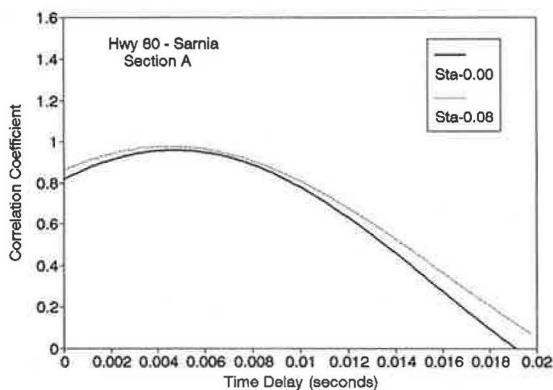


FIGURE 8 Correlation coefficient functions from FWD data for Sections 0.00 and 0.08, C-SHRP data.

predictions shown in Figure 6. For both spectral analyses, the maximum  $\rho_{xy}$  is close to one, which confirms an excellent correlation between the behaviors at the two sensors.

## CONCLUDING REMARKS

Owing to the complex properties of pavements and subgrade materials, a realistic, accurate stress analysis of a pavement structure is difficult. Systematic errors associated with back-calculated moduli are introduced when imperfect mechanical models are forced to fit in situ data. Although it is desirable to accurately model pavements to obtain a better understanding of stress distributions in these structures, more accurate mechanical modeling, when used in a backcalculation environment, will not necessarily lead to better estimates of in situ properties. As a result, the approach advocated here is to use simple models. When these models are used, estimates of appropriate in situ subgrade moduli are possible through recognition of the reasons for the deviations between the expected and actual modulus predictions.

Emphasis has been placed on estimating subgrade modulus and the apparent stiffness of a pavement structure via the concept of equivalent thickness. It has been shown by using the effective modulus profiles and considering the cospectrum that the properties of a real subgrade vary, as expected. Because errors associated with subgrade modeling can amplify errors associated with the pavement structure moduli predictions, these predictions are considered to be unreliable. Taking this into account and the fact that continuum concepts are no longer applicable to cracked pavements, it is suggested that the effective thickness may provide a better measure of a pavement structure's integrity.

## ACKNOWLEDGMENTS

The work reported in this paper was supported by the Ministry of Transportation of Ontario and the National Sciences and Engineering Research Council of Canada. The field data were supplied by D. Hein of Dynatest Canada.

## REFERENCES

1. D. Stolle and D. Hein. Parameter Estimates of Pavement Structure Layers and Uniqueness of the Solution. In *Nondestructive Testing of Pavements and Backcalculation of Moduli* (A. J. Bush III and G. Y. Baladi, eds.). STP 1026. ASTM, Philadelphia, Pa., 1989, pp. 313–322.
2. D. F. E. Stolle. Effect of Mechanical model on Back-calculated Pavement Modulus. *Canadian Journal of Civil Engineering*, Vol. 17, 1990, pp. 494–496.
3. R. L. Lytton, F. P. Germann, Y. J. Chou, and S. M. Stoffels. *NCHRP Report 327: Determining Asphaltic Concrete Pavement Structural Properties by Nondestructive Testing*. TRB, National Research Council, Washington, D.C., June 1990.
4. S. H. Carpenter and T. J. Freeman. Characterizing Premature Deformation in Asphalt Concrete Placed over Portland Cement Concrete Pavements. In *Transportation Research Record 1070*, TRB, National Research Council, Washington, D.C., 1986, pp. 30–41.
5. F. W. Jung and D. F. E. Stolle. Non-Destructive Testing with FWD on Whole and Broken AC Pavements. *Proc., Symposium*

- on *Nondestructive Deflection Testing and Backcalculation for Pavements*, August 19–21, 1991, Nashville, Tennessee (in preparation).
6. P. Ullidtz. *Pavement Analysis*. Elsevier, New York, N.Y., 1987.
  7. D. F. E. Stolle. Modelling of Dynamic Response of Pavements to Impact Loading—Technical Note. *Computers and Geotechnics*, Vol. 11, 1991, pp. 83–94.
  8. B. E. Sebaaly, M. S. Mamlouk, and T. G. Davies. Dynamic Analysis of Falling Weight Deflectometer Data. In *Transportation Research Record 1070*, TRB, National Research Council, Washington, D.C., 1986, pp. 63–68.
  9. F. P. Germann and R. L. Lytton. Temperature, Frequency, and Load Level Correction Factors for Backcalculated Moduli Values. In *Nondestructive Testing of Pavements and Backcalculation of Moduli* (A. J. Bush III and G. Y. Baladi, eds.). STP 1026. ASTM, Philadelphia, Pa., 1989, pp. 431–451.
  10. D. F. E. Stolle, D. Hein, and Y. Wang. Elastostatic Analysis and Backcalculation Estimates of Pavement Layer Moduli. *Proc., 1988 Annual Conference, Roads and Transportation Association of Canada*, Vol. 1, pp. C39–C59.
  11. D. M. Burmister. The General Theory of Stresses and Displacements in Layered Systems I. *Journal of Applied Physics*, Vol. 16, 1945, pp. 89–94.
  12. J. M. Golden. Strains and Displacements in Stochastic Stress Models. *Journal of Engineering Mechanics*, Vol. 114, No. 5, May 1988, pp. 876–886.
  13. F. W. Jung. *Interpretation of Deflection Basin for Real-World Materials in Flexible Pavements*. Report RR-242. Pavements and Roadway Section, Research and Development Branch, Ministry of Transportation of Ontario, Feb. 1990.
  14. A. H. Magnuson. A Comparison Study of Computer Predictions and Field Data for Dynamic Analysis of Falling Weight Deflectometer Data. Paper Prepared for Presentation at 70th Annual Meeting of the Transportation Research Board, Washington, D.C., 1991.
  15. J. S. Bendat and A. G. Piersol. *Engineering Applications of Correlation and Spectral Analysis*. John Wiley and Sons, New York, N.Y., 1980.
  16. S. Nazarian and K.H. Stokoe II. Nondestructive Evaluation of Pavements by Surface Wave Method. In *Nondestructive Testing of Pavements and Backcalculation of Moduli* (A. J. Bush III and G. Y. Baladi, eds.). STP 1026. ASTM, Philadelphia, Pa., 1989, pp. 119–137.
  17. F. E. Richard, J. R. Hall, and R. D. Woods. *Vibrations of Soils and Foundations*. Prentice-Hall Inc., Englewood Cliffs, N.J., 1970.
- 
- Publication of this paper sponsored by Committee on Strength and Deformation Characteristics of Pavement Sections.

# Radar Pavement Thickness Evaluations for Varying Base Conditions

W. M. KIM RODDIS, KENNETH MASER, AND ANDREW J. GISI

Accurate knowledge of pavement layer thicknesses is important in many aspects of pavement management. Often this information is unknown, and records are inaccurate, out of date, or difficult to access. To date, the only method for obtaining pavement layer data has been core sampling. That is time-consuming, labor intensive, intrusive to traffic, and limited in coverage. This study investigated the capability of ground-penetrating radar to provide accurate subsurface pavement profile information. Eleven sites were selected to represent the population of pavement types present in Kansas, with a particular emphasis on variations in base type and road history. The radar results show substantial variations in pavement thickness within each 1,000-ft test section, and in general, higher values of pavement thickness than were reported in available records. These predictions, when correlated with data from 73 ground truth cores, show an accuracy of  $\pm 5$  percent to 10 percent, depending on the treatment of the data. The asphalt thicknesses in this study ranged from 2.5 to 20 in. The radar data were analyzed automatically using software that operated directly on the raw radar waveforms. This software is based on an electromagnetic model of the pavement layer structure. The resulting predictions were correlated with core samples obtained in cooperation with the Kansas Department of Transportation. The results show that a radar system that combines air-launch horn antenna equipment with appropriate software can provide an effective alternative to coring for pavement thickness measurements. In addition, this system provides more information to the agency, is cost competitive, and is safer to use because it does not require lane closures.

Knowledge of asphaltic pavement layer thickness is important in many areas of pavement management. Accurate thickness data are needed throughout the roadway network to improve pavement performance predictions, establish structural load carrying capacities, and develop maintenance and rehabilitation priorities. On a project level, accurate knowledge of pavement thickness is required for overlay design and to interpret the results of structural tests such as dynaflect and the falling weight deflectometer (FWD). For new construction, it is important to ensure that the thickness of materials being placed by the contractor is close to specification.

Accurate project level determination of pavement thickness for overlay design is of particular value for the Kansas road system. Overlays dominate the Kansas Department of Transportation's (KDOT's) current and projected paving activities, with reconstruction and new construction playing a lesser role. A rational project optimization system requires correct pavement thickness data for effective and efficient overlay design.

W. M. K. Roddis, Department of Civil Engineering, University of Kansas, Lawrence, Kans. 66045. K. Maser, Infrasense, Inc., 19-R Brookline Street, Cambridge, Mass. 02139. A. J. Gisi, Kansas Department of Transportation, Materials and Research Center, 2300 Van Buren Street, Topeka, Kans. 66611.

Negative economic effects are the consequence of both underestimates and overestimates of the actual pavement thickness.

For a direct overlay project, an underestimate of existing thickness will result in an overly conservative overlay design with an excessive cost. On the other hand, an overestimate will result in a nonconservative design that will not achieve the desired service-life. For a mill and recycle overlay project, an underestimate of existing thickness may falsely indicate that a direct overlay would be more cost-effective. An overestimate may result in an inadequate amount of material for reuse. Possible equipment breakthrough on the reduced structure of the milled pavement may also occur. The consequences of inaccurate thickness information may thus be seen to be severe, especially for the case of milling and recycling, which is an increasingly common project type.

Layer thicknesses may be determined from historical records. However, records are often highly inaccurate or non-existent. The only acceptable method for pavement thickness measurement at present is through core samples and test pits. These are time-consuming, destructive to the pavement system, dangerous to the field employees, and intrusive to traffic. In addition, they only provide data at the location of the test, and assumptions must be made regarding variations between cores. Recent studies (1,2) at Strategic Highway Research Program (SHRP) sites have shown that variations of up to 2.5 in. in asphalt thickness can be found between cores taken at 50-ft spacing. When such variations exist and are not detected, large errors in dynaflect or FWD test interpretation and in overlay design can occur.

Ground-penetrating radar is a noncontact technique that has the potential for surveying pavement thickness while operating at highway speed. Until recently, the radar data required manual and qualitative interpretation (ASTM D4748-87, 3-5). Recent research has resulted in automated data interpretation and allowed verification (1,2). Radar-generated continuous pavement thickness profiles provide important data for pavement management at network and project levels. These data would lead to better decisions regarding highway safety, use of funds, and life cycle designs for repair and rehabilitation.

The main objective of this study was to assess the applicability of the radar thickness profiling technology to KDOT's pavement evaluation and management program, both at the network and project levels. To meet this objective, it was necessary to establish the capabilities of radar technology for accurately generating continuous pavement profiles for asphalt overlaying a variety of base conditions. The testing for this study consisted of the collection of radar data on in-service pavements and the correlation of the predictions from the

radar data with direct measurement. This work included test site selection, radar data collection, analysis of radar waveforms, selection of direct measurement locations, collection of direct samples, and correlation between radar data and direct measurement.

**SITE SELECTION**

The pavement population of the Kansas road system was considered when determining the site test matrix. The objective of site selection was to ensure that the selected pavement segments would constitute a representative cross-section of the state's asphaltic pavement population. In-service sites were selected from among candidates for which the actual pavement construction and conditions were reasonably well known, so that the range of conditions could be reliably selected.

**Characteristics of Pavement Population**

The pavement management system for the Kansas highway network classifies roads into 23 categories by pavement type, function, traffic level, and width, as illustrated in Figure 1. The pavement types are (a) portland cement concrete (PCC); (b) composite pavement (Comp), PCC pavement or brick that has been overlaid with asphaltic concrete; (c) full-depth bituminous pavement (FDBit), designed and constructed to carry expected traffic; and (d) partial design bituminous pavement (PDBit), not designed or constructed to carry expected traffic. The two functional classifications of the road categories are "Interstate" and "other." The traffic levels are based on annual average daily traffic counts expressed in terms of daily equivalent 18 kip axle loads in one direction and categorize roads as low (L), medium (M), or high (H) use. Widths are categorized as less than 32 ft or 32 ft or greater. These 23 road categories used for the entire Kansas road network were reduced to 10 road categories for inclusion in the radar survey according to the following rationale.

Pavement type is the most important road characteristic for this study because the objective is asphalt thickness determination. In addition, the radar response is most directly affected by the arrangement of the layered materials that make up the pavement cross-section. Only the three pavement types including an asphalt surface are of interest here, eliminating Categories 1, 2, 6, 7, and 8 from further consideration.

Because construction and use for Interstate roads differ from construction and use of other roads, survey sites were selected from both function types.

Traffic levels were not of direct interest for survey site selection. However, traffic level was used as an indirect indicator of road condition and maintenance history, but no systematic link between traffic level and condition resulted. Most pavements surveyed were in good condition with some transverse cracking, typical of KDOT's road population. For each pavement type and function selected, a pair of sites was selected, one from the highest traffic level and one from the lowest traffic level. This eliminated categories 10, 13, 16, 19, and 22 from further consideration. Category 9 was eliminated from the study because the site that had been radared was not available for coring because of ongoing reconstruction work.

Road width does not have a direct effect on radar survey results, but inclusion of narrow and wide roads more completely represented road types in Kansas. The narrow width, high traffic road categories (14 and 20) were not included to mitigate traffic control problems.

The 10 categories shown shaded in Figure 1 are those included in the radar survey. All three pavement types in the state network are included. The functional classifications, different roadway widths, and spectrum of traffic levels encountered in the state network are covered by the categories selected.

**Criteria for Site Selection**

Of primary importance in selecting specific road segments to represent each category was that the in-service segments chosen had well-known construction history, maintenance history, and current condition. This allowed a choice of road segments with the desired range of characteristics. It also facilitated the interpretation of the radar signatures of different sites of varying maintenance histories.

An additional criterion was to have a multiple asphalt overlays in place on several sites so that the ability of the radar to separately measure several asphalt layers could be examined. For the bituminous pavements, the sites selected covered a range of subpavement materials (bituminous treated, lime treated, crushed stone, naturally occurring gravels, cement treated).

The selected sites were chosen to be geographically clustered. This minimized time spent in travel between sites, and thus maximized productive use of the radar survey equipment. The sites were clustered around Topeka in District I in northeast Kansas. This highway district covers a diverse portion of the state, allowing inclusion of all 10 of the selected road categories.

Pavement Type		PCC			Comp			FDBit			PDBit		
Traffic		L	M	H	L	M	H	L	M	H	L	M	H
Function	Width												
Interstate	< 32 ft	1		2		3		4		5			
	32 ft												
Other	< 32 ft	6	7	8	9	10	11	12	13	14	18	19	20
	32 ft							15	16	17	21	22	23

FIGURE 1 Kansas highway network road categories.

**Pavement Structure of Sites Selected for Radar Survey**

Table 1 presents the pavement structure of the 11 sites included in the radar survey. The individual layers that make up the pavement structure are shown according to KDOT's pavement management data base. Two sites of Category 17 were included because of the addition of a SHRP site. Maintenance histories earlier than 1970 are not available. Before 1970 KDOT's standard operating procedure was to apply a

seal coat every 3 years. For this reason, when using data base values to determine asphalt thicknesses, KDOT's rule of thumb is to add 0.1 in. for each year of pavement service before 1970. This accounts for pavement thickness build up as a result of repeated applications of seal coating. Table 1 includes this adjustment.

**Accuracy of Pavement Management System Data Base**

Network planning relies on the information in the pavement data base; therefore, discrepancies between recorded and observed layer information are of interest even though the study was not designed to sample and verify the recorded data. Discrepancies were found between KDOT pavement management data base records and the in-place pavements with regard to pavement type. Of the 11 sites tested, the pavement type differed from that obtained from KDOT records in 2 cases. One site was classified in the records as Category 15, a fully designed bituminous category. In fact, the site is a partially designed pavement. Another site was classified in the records as Category 23, a partially designed bituminous category. In fact the site is a fully designed pavement. Layer data obtained from KDOT records are in general agreement with the core data and thus also contradict the data base road categories for these two sites.

**CONDUCT OF RADAR SURVEY**

**Principles of Ground-Penetrating Radar**

Ground-penetrating radar operates by transmitting short pulses of electromagnetic energy into the pavement using an antenna attached to a survey vehicle. These pulses are reflected back

to the antenna with an arrival time and amplitude that is related to the location and nature of dielectric discontinuities in the material (air/asphalt or asphalt/base, etc). The reflected energy is captured and may be displayed on an oscilloscope to form a series of pulses that are referred to as the radar waveform. The waveform contains a record of the properties and thicknesses of the layers within the pavement. Figure 2 shows the relationship of the layer thicknesses to the radar waveforms. Figure 3 shows typical pavement waveforms collected during this project.

The pavement layer thicknesses and properties may be calculated by measuring the amplitude and arrival times of the waveform peaks corresponding to reflections from the interfaces between the layers (see Figure 2). The dielectric constant of a pavement layer relative to the previous layer may be calculated by measuring the amplitude of the waveform peaks

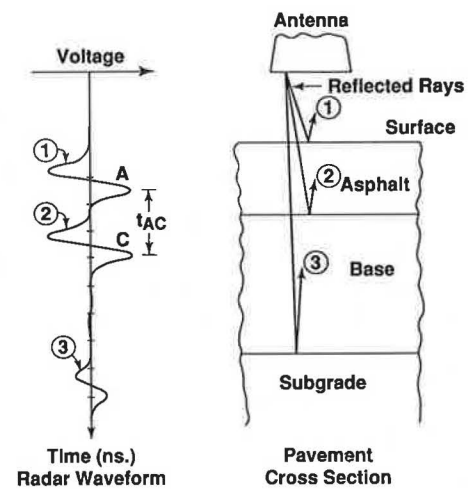


FIGURE 2 Model of radar pavement data.

TABLE 1 Pavement Layers from KDOT Data Base

Road Category	Layer 1			Asphalt			Layer 3			Base Layer		
	(in.) Thick	Material	Year	(in.) Thick	Material	Year	(in.) Thick	Material	Year	(in.) Thick	Material	Year
3	3.0	BM2	1979	1.0	BM1	1979			1950-70	9.0	PCCPAV	1950
4	1.0	BM1	1980	3.0	BM2	1980				9.0	PCCPAV	1956
5	0.75	BM2	1981	1.0	HM31	1973	1.0	HM3	1973	16.0	ACB3	1973
11	1.0	BM1	1984	2.0	BM7	1984				9.0	PCCPAV	1968
12	1.5	BM1	1979							2.0	BITCOV	1979
15	1.5	BM2A	1990	1.5	BM2	1983	2.3	Maint	1947-70	2.0	BITCOV	1947
17	4.0	BM3	1975							9.0	BM4	1975
18	2.0	BM2	1988	0.75	BM2	1988	2.3	Maint	1947-70	6.0	BM2A	1947
21	2.0	BM1B	1990	1.5	BM1	1981	1.8	Maint	1952-70	2.0	BITCOV	1952
23	1.5	BM2	1982	1.0	BITCOV	1950	2.0	Maint	1950-70	6.0	AB	1950
SHRP*	4.0	HM3	1972							7.5	ACB3	1972

Legend

AB	Aggregate binder	HM3	Hot mixture 3
ACB3	Asphalt concrete base mix	HM31	Hot mixutre 31
BITCOV	Bituminous cover	HM6	Hot mix
BM1	Bituminous mixture 1	PCCPAV	Portland cement concrete
BM1B	Bituminous mixture 1B	Maint	Maintenance seal
BM2	Bituminous mixture2		
BM2A	Bituminous mixture2A		
BM3	Bituminous mixture3		

\*SHRP LTPP GPS 201005 Site, Road Category 17

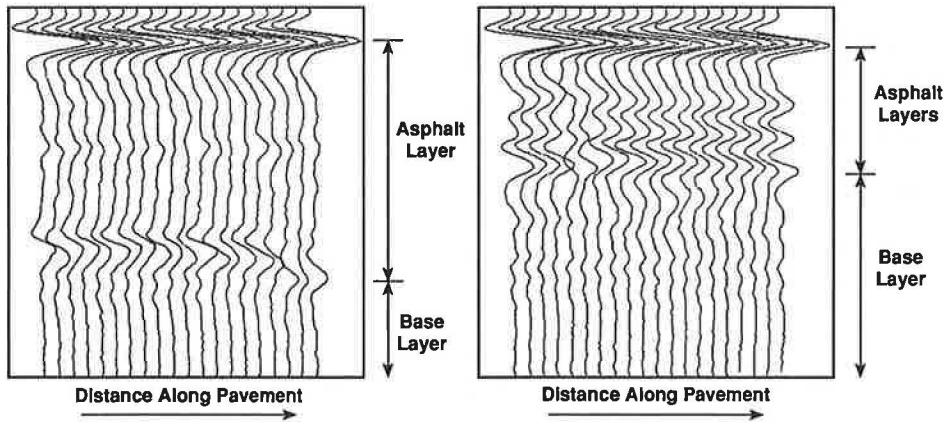


FIGURE 3 Typical waveforms.

corresponding to reflections from the interfaces between the layers. The travel time of the transmit pulse within a layer in conjunction with its dielectric constant determines the layer thickness, as follows:

$$\text{Thickness} = \text{velocity} \times (\text{time}/2) \quad (1)$$

Because the measured time between peaks represents the round trip travel of the radar pulse, the thickness computation is based on the travel time divided by 2. The radar velocity can be computed from the dielectric constant of the medium,  $\epsilon$ , as

$$\text{Velocity} = 11.8/\sqrt{\epsilon} \text{ (inches/nanosecond)} \quad (2)$$

where 11.8 is the radar velocity in free space in inches per nanosecond. The result of combining Equations 1 and 2 is

$$\text{Thickness} = (5.9 \times \text{time})/\sqrt{\epsilon} \text{ (inches)} \quad (3)$$

where time is measured in nanoseconds.

Computation of the surface layer dielectric constant can be made by measuring the ratio of the radar reflection from the asphalt to the radar amplitude incident on the pavement. This ratio, called the reflection coefficient, can be expressed as follows:

$$\begin{aligned} \text{Reflection coef (1 - 2)} \\ = (\sqrt{\epsilon_1} - \sqrt{\epsilon_2})/(\sqrt{\epsilon_1} + \sqrt{\epsilon_2}) \end{aligned} \quad (4)$$

where the subscripts (1 and 2) refer to the successive layers. The incident amplitude on the pavement can be determined by measuring the reflection from a metal plate on the pavement surface because the metal plate reflects 100 percent. Using these data, and noting that the dielectric constant of air is 1:

$$\begin{aligned} \text{Reflection coef (air - asphalt)} &= A/(-A_{pl}) \\ &= (1 - \sqrt{\epsilon_a}) \\ &\div (1 + \sqrt{\epsilon_a}) \end{aligned} \quad (5)$$

where

- $A$  = amplitude of reflection from asphalt,
- $A_{pl}$  = amplitude of reflection from metal plate (= negative of incident amplitude), and
- $\epsilon_a$  = asphalt dielectric constant.

By rearranging Equation 5, one obtains the following expression for the asphalt dielectric constant.

$$\epsilon_a = [(1 + A/A_{pl})/(1 - A/A_{pl})]^2 \quad (6)$$

A similar analysis can be used to compute the dielectric constant ( $\epsilon_b$ ) of the base material. The resulting relationship is

$$\epsilon_b = \epsilon_a[(F - R2)/(F + R2)]^2 \quad (7)$$

where

- $F = (4\sqrt{\epsilon_a})/(1 - \epsilon_a)$ ,
- $R2$  = ratio of reflected amplitude from the top of the base layer to the reflected amplitude from the top of the asphalt, and
- $\epsilon_b$  = base dielectric constant.

Note that in the context of this work, "base" represents any material occurring below the first major asphalt layer. The previous equations serve as the basis for analysis of the data collected during this study.

### Radar Data Collection

Radar data were collected by INFRASENSE, Inc., of Cambridge, Massachusetts, using a van-mounted horn antenna system provided and operated by Pulse Radar, Inc., of Houston, Texas. Data were collected June 8 and 9, 1991, and taken back to INFRASENSE for analysis. Based on the analysis, areas within each site were identified for direct sampling. Extraction of direct samples was carried out jointly by KDOT in association with the University of Kansas.

Radar equipment setup included a number of calibration tests, including an antenna end reflection test, a metal plate reflection test, and a time calibration test. Traffic control was

set up by KDOT to allow for medium speed (5 to 20 mph) radar runs. Data were acquired at longitudinal intervals of 5 ft. These speeds and sampling intervals were selected for convenience, and do not represent radar system limitations. A 3-ft<sup>2</sup> aluminum plate was placed on the pavement surface at the beginning and end of each 1,000-ft test section to provide reference markers in the radar data. Each site was tested with one pass of the radar van, with the antenna positioned in the left wheel path of the outside (low speed) lane.

All radar data were continuously digitized and stored using an IBM compatible 386 computer housed in the van. The radar data were subsequently analyzed by INFRASENSE using its PAVLAYER (Copyright by INFRASENSE, Inc.) customized software for the radar pavement application. The results presented here are based on this analysis.

## RADAR DATA ANALYSIS AND RESULTS

The data analysis was carried out using Equations 1–7. Asphalt pavement thickness is calculated in the following steps: (a) determination of the radar velocity in the asphalt using the asphalt dielectric constant determined from the surface reflection using Equation 6, and (b) computation of the thickness from the velocity and the arrival time of the reflection from the bottom of the asphalt using Equation 3. The base layer thickness was calculated in a similar fashion. The radar velocity in the base material was determined from the base material dielectric constant computed from the magnitude of the reflection at the asphalt/base interface using Equation 7. All of these calculations are automated in the INFRASENSE PAVLAYER software so that a continuous thickness profile with thousands of waveforms can be computed in a few minutes on a 386 machine. Typical asphalt thickness and base thickness profiles obtained from the radar data collected during this study are shown in Figures 4 and 5.

Two different types of radar data analyses were conducted on these tests sections. The first was where the bituminous layers could be treated as a single monolithic layer. The sec-

ond was where the thicknesses of each significant bituminous layer had to be calculated separately. The decision to use one of the two approaches depended on how clearly the individual bituminous layers appeared in the raw data as shown in Figure 3. Figure 3a shows raw radar data that had the appearance of a single monolithic layer; this site was thus analyzed using the single monolithic layer approach.

In other circumstances the data clearly showed successive reflections from multiple asphalt layers as shown in Figure 3b. This was true for the sites with processed data shown in Figures 4 and 5. In Figure 4, the bituminous surface layers were distinguished from a bituminous base layer. In Figure 5, bituminous surface layers placed at different times are distinguished from one another. Discussed in the following sections are comparisons of these predictions with direct core measurements.

## COMPARISONS WITH GROUND TRUTH

### Ground Truth Data Collection

Locations for coring were determined after a preliminary analysis of the radar data. This analysis revealed locations and areas in which significant variations in thickness and dielectric constant occurred. The samples were located such that a reasonable range of values could be obtained at each site. The first 10 field sites listed in Table 2 were cored to determine actual asphalt thickness and pavement layer structure. Cores 4 in. in diameter were wet drilled through the pavement. All cores were photographically documented in the field, and layer data were field recorded to an accuracy of approximately 0.125 in. Cores were then examined in the laboratory to confirm layer thickness measurements. Core and test pit data from the 11th site (the SHRP site) were also used because they were available from the SHRP long-term pavement performance data base.

In addition to coring, soil classification and particle size distribution were tested. At one site, dry samples of the as-

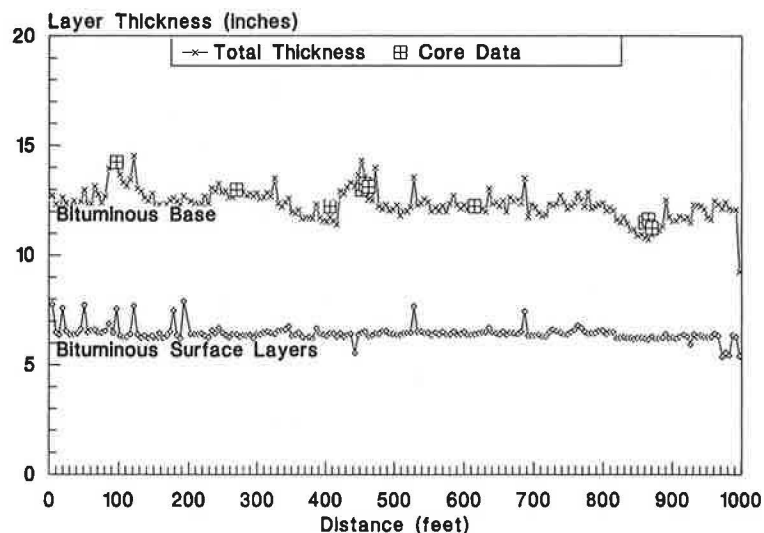


FIGURE 4 Output for two-layer analysis (Category 23).

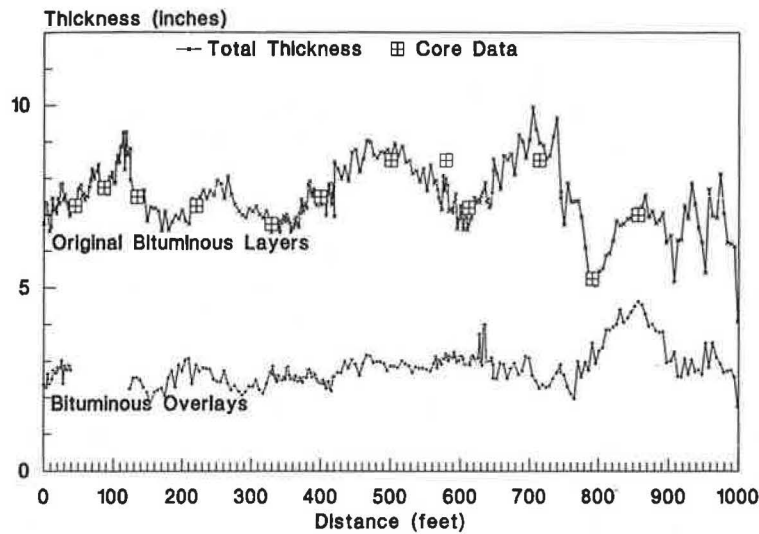


FIGURE 5 Output for two-layer analysis (Category 12).

TABLE 2 Pavement Thickness Data Statistics: Comparison of Radar, Cores, and Data Base

Road Cat.	AVERAGES at Core Sites		DIFFERENCES Between Radar and Cores		STANDARD DEVIATION			KDOT DATA BASE	
	Radar (inches)	Core (inches)	Inches	%	at core sites	complete section	Cores	KDOT Data (inches)	Differences KDOT-Core
3	4.64	4.41	0.23	5.30	0.23	0.40	0.22	4.0	-0.41
4	3.30	2.79	0.51	18.28	0.27	0.24	0.26	4.0	1.2
5	21.66	19.17	2.49	13.00	0.54	0.63	0.76	18.75	-0.42
5 <sup>d</sup>	19.19	19.17	0.02	0.10					
11	2.82	2.63	0.19	7.31	0.22	0.21	0.22	3.0	0.37
12	7.37	7.41	-0.04	-0.57	0.92	0.80	0.87	3.5	-3.91
15	9.60	8.36 <sup>a</sup>	1.23	14.76	0.54	0.38	1.03	7.3 <sup>e</sup>	-1.03
17	14.32	14.03	0.30	2.11	0.86	0.61	0.24	13.0	-1.03
18	11.92	10.12 <sup>b</sup>	1.79	17.70	0.30	0.44	0.11	11.05 <sup>e</sup>	0.93
21	10.91	10.71	0.20	1.87	1.99	1.07	1.04	7.3 <sup>e</sup>	-3.41
23	12.46	12.55	-0.09	-0.70	1.35	0.62	0.89	10.5 <sup>e</sup>	-2.05
17(SHRP)	14.20	13.35	0.85	6.39	0.16	1.3	<sup>c</sup>	11.5	-1.85

Notes: <sup>a</sup>questionable data due to poorly defined asphalt/soil base  
<sup>b</sup>questionable data due to core damage during drilling  
<sup>c</sup>insufficient data (less than 5 cores)  
<sup>d</sup>calibrated by 1 core  
<sup>e</sup>for the period 1950-1970, these figures assume one chip seal every 3 years, with an average thickness of 0.33 inches/chip seal

phalt at various depths were taken to determine moisture contents and hence variations in dielectric constant. For Sites 3, 5, 11, 15, 17, 18, 21, and SHRP, dynaflect tests were performed. This was to evaluate the effect of having such data on KDOT pavement management and overlay decisions.

**Description of Data and Results**

Figure 6 shows a comparison of all of the core data versus the radar predictions at each of the 73 core locations. The number of distinct asphalt layers observed in the cores varied from 1 to 8. Thirteen of the 73 cores were not intact when removed from the hole. These damaged cores were clustered almost entirely among the sites from Categories 5, 15, and 18. Questions regarding the interpretation of the core data occurred for two of the sites, as discussed next.

In Site 15, the cores revealed a consolidated soil/asphalt layer under the main paving layer. The data reported in Figure 6 represent the thickness of what was believed to be the main paving layer. The cores, however, broke at various locations between the top and the bottom of this layer, and the bottom of consolidated bituminous material was not clearly defined. Similarly, the radar data for this site showed several layers, and it was not clear which interface to define as the bottom. From this perspective, the radar data accurately reflected the pavement condition, but the core measurements were not adequate to provide ground truth.

In Site 18, the cores revealed 5 to 8 pavement layers, 4 of which were about 1 in. thick and located between the depths of 4.5 and 8.5 in. All of the cores were damaged during drilling. The thickness measurements on the fragmented cores may not accurately reflect the pavement thickness. Unfortunately, more reliable in-hole measurements were not made

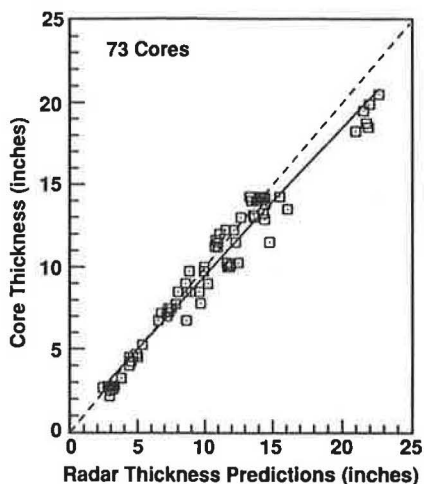


FIGURE 6 Asphalt thickness: radar predicted versus core measurements for 73 cores.

at this site. The radar data for this site suggested a complex layered structure, which was simplified in the analysis as a two-layered structure: the first 6.5 to 7.5 in. thick, the second 4 to 5 in. thick.

#### Discussion of Data

The radar and core data for the 73 core locations are plotted in Figure 6. The regression line through the data is represented by the following equation.

Core data =  $K1 + K2 \cdot (\text{radar prediction})$

The regression results are as follows:

- $R$ -squared = 0.97,
- Standard error = 0.87 in.,
- $K1$  = 0.51,
- $K2$  = 0.90.

This regression includes all the data, including those sites (15 and 18) for which the core data were questionable. A regression analysis with these sites removed shows little change in results. Regressions performed for the three different pavement types result in  $R$ -squared values of 0.90 for composite pavement, 0.97 for fully designed bituminous pavement, and 0.48 for partially designed bituminous pavement. The composite data yielded a good fit, as expected, because of the clear dielectric interface between the asphalt and the concrete and the low variability in asphalt thickness for this pavement type. The fit for fully designed bituminous data was extremely good, showing a systematic tendency to overestimate asphalt thickness for thicker pavements. The reason for this tendency is discussed in the following section with regard to Site 5, the thickest pavement tested. The fit for partially designed bituminous data was the poorest, as expected, because of the questionable core data from Sites 15 and 18, representing 2 out of the 3 sites for this pavement type.

A regression analysis using the site averages in Table 2 instead of the individual data points yields the following values:

- $R$ -squared = 0.99,
- Standard error = 0.61 in.,
- $K1$  = 0.04 in., and
- $K2$  = 0.93.

This also shows an excellent fit. The average difference between the radar predictions and the core data is 0.72 in., or 8.0 percent. When the data for sites with questionable core data (15 and 18) are eliminated, the results show an accuracy of within 0.5 in. in all but two sites. As discussed later, a single core calibration for Site 5, as would be warranted because of the thickness, would further reduce the average difference to 0.275 in., or 4.75 percent.

It is of interest to compare the standard deviations to see if the radar data can provide a measure of the section variability. The standard deviation has been computed for each site using (a) the core values; (b) the radar data at the core site locations; and (c) all of the radar data (approximately 200 points per section). Using a simple threshold of 0.5 in. to categorize variability, the variability as determined by the radar data corresponds to the variability as determined by the core data 70 percent of the time.

The relationship of these results to the pavement condition and to the application of the data for project and network level pavement management will be discussed in the next section.

## DISCUSSION OF RESULTS

### Relationship of the Radar Data to Pavement Condition

Data from 73 cores taken at 11 sites showed that the radar predictions were within 10 percent of the core data. This accuracy was achieved using radar data alone and including questionable core data. When poor quality core data are removed from the data set, and when one calibrating core is used for Site 5, the accuracy is increased to 7.5 percent. These are excellent results and show that radar, when properly used, represents an effective alternative to coring in a variety of pavement engineering and management applications.

The largest deviations between radar predictions and core data occurred in Sites 5, 15, and 18. The deviations for Sites 15 and 18 can be attributed to the poor quality of the core data, as discussed earlier. In Site 5, the core data revealed a total of five asphalt layers adding up to 18 to 20 in. in thickness. The radar data did not show any significant contrast between layers, and therefore the dielectric constant for the top layer was used for the entire thickness computation. Common knowledge of pavement conditions would suggest, however, that there is a gradient of moisture content with depth. This gradient would yield an increased dielectric constant and a reduced velocity with depth, which, if accounted for, would produce more accurate thickness computations.

The use of the surface dielectric constant for a 20-in. layer is not realistic, and there are two possible procedures for implementing corrections. The first is to take a calibration core. This core will provide the average radar velocity for the full pavement, and that velocity can be used to compute the

thicknesses of the remaining points. Table 2 shows the results of such a calibration. The second approach is to use a moisture/depth function for thick layers as part of the normal analysis procedure. Such a function would require further development and verification.

Analysis of the data reveals a level of accuracy that is somewhat less than that observed in a previous study by Maser and Scullion (1,2). In that study, the standard error was  $\pm 5$  percent (0.33 in.) over a thickness range of 2 to 9 in. In the Maser and Scullion study, the four investigated sites were SHRP general pavement study sites, and were of more recent, higher quality construction. The sites in this Kansas study were thicker, older, and more heavily layered than those studied by Maser and Scullion. Efforts were made in the radar analysis to recognize and compute the contrasting layer properties. In some cases this yielded accurate results (e.g., Category 23). In other cases, there were either too many layers to consider (e.g., Category 18) or the layers did not show up in the data (e.g., Category 5). In these cases, the analysis does not accurately model the progressively increasing moisture content and dielectric constant with depth, resulting in an overestimate in radar velocity and in computed thickness.

### Determination of Rutting

One interesting result of this study was a computation of rut depth versus distance using the radar data for Category 3. For that site, radar surveys were conducted in both the left wheelpath and the center of the lane. Analysis of the data showed a uniformly greater asphalt thickness in the center of the lane, as expected, because of rutting. By subtracting the two computed asphalt thicknesses from one another, rut depth versus distance was computed.

Because radar can compute the thicknesses of deeper layers, it is possible to use the above approach to identify the layer in which the rutting is occurring. Investigating this possibility was not in the scope of this program, but could be evaluated in the future.

### Implications for Pavement Management

The results of this work have relevance to both network and project level pavement management. Table 2 compares average thickness of bituminous layers found by the three different methods of radar, cores, and data base records. As may be seen in Table 2, the thicknesses given in the data base may differ significantly from those found by coring, and the data base usually underestimates the actual thickness. At the network level, KDOT does not take cores but relies on the data base records. The data generated in this study show that, on the average, for 1,000-ft sections, the radar predictions are within 7.5 percent of what would be obtained from a series of at least 5 cores. Therefore, for network-level pavement management, the results of a radar survey can improve the accuracy of asphalt thickness values used for pavement management decision making.

At the project level, radar-based thickness data can be used to eliminate backcalculation errors that can occur if incorrect thickness assumptions are used. The data show that radar thickness predictions can be expected to be within 7.5 percent

to 10 percent of core thickness values for use in conjunction with FWD and dynaflect data interpretation. As shown in the data for Site 5, accuracy improvements can be achieved on certain sections by using a single calibration core.

The radar results also showed an ability to characterize the variability of the pavement thickness over potential project sections. This information would be useful in defining the required spacing of structural evaluation tests.

At the project level, the true thickness and its variation is very important. Project decisions consider amounts of cold milling and hot or cold recycling. The closer the milling gets to the bottom of the existing layer, the more construction related problems are encountered. The pavement is generally cracked and is leaking water into the subgrade soils, creating soft or weak spots. Heavy construction equipment breaks through the pavement in these areas. With accurate pavement thicknesses, it would be possible to avoid getting too close to the subgrade. It is also necessary to be able to evaluate the load carrying capacity of a milled surface to carry traffic during construction. The thickness of the pavement remaining after milling needs to be accurately determined so that failure due to insufficient thickness does not occur. Radar data would thus be of value at the project level.

### CONCLUSIONS

The main objective of this study was to assess the application of radar thickness profiling technology to KDOT's pavement evaluation and management program at both the network and project levels. As a result of these and previous studies, the following conclusions can be reached.

1. A radar system that combines air-launch horn antenna equipment with the appropriate software provides an effective alternative to coring for pavement thickness measurements. In addition, this system provides more information to the agency, is cost competitive, and is safer to use because it does not require lane closures.

2. The expected accuracy will range from 7.5 percent to 10 percent for thicknesses from 2.5 to 20 in. The accuracy is improved with the occasional use of a calibration core, particularly in the thicker material.

3. Radar thickness information can be used for the following applications:

- FWD and dynaflect backcalculation,
- Quality control in new construction,
- Thickness estimates for mill and recycle projects,
- Design of overlays, and
- Network-level pavement inventories.

4. It is possible that radar thickness measurement could be used to identify the pavement layer most responsible for rutting. This identification would influence the pavement rehabilitation design.

### ACKNOWLEDGMENTS

This research was funded under the Kansas Transportation Research and New-Developments Program, an on-going, co-

operative, comprehensive research program addressing transportation needs of Kansas. This project represents a cooperative effort between KDOT and the University of Kansas.

#### REFERENCES

1. K. R. Maser. Automated Detection of Pavement Layer Thickness and Subsurface Moisture Using Ground Penetrating Radar. Infrasense, Inc., Cambridge Mass.; Texas Transportation Institute and Texas State Department of Highways and Public Transportation, Nov. 30, 1990.
2. K. R. Maser and T. Scullion. Automated Pavement Subsurface Profiling Using Radar—Case Studies of Four Experimental Field Sites. Presented at 71st Annual Meeting of the Transportation Research Board, Washington, D.C., Jan. 1991.
3. F. Berg, J. M. Jansen, and H. J. E. Larsen. Structural Pavement Analysis Based on FWD, Georadar, and/or Geosonar Data. In *Proc., 2nd International Conference on the Bearing Capacity of Roads and Airfields*, Plymouth, U. K., 1986.
4. R. A. Eckrose. Ground Penetrating Radar Supplements Deflection Testing to Improve Airport Pavement Evaluations. *Non-Destructive Testing of Pavements and Back Calculation of Moduli*, A. J. Bush III and G. Y. Baladi, eds. ASTM STP 1026. ASTM, Philadelphia, Pa., 1989.
5. J. V. Rosetta, Jr. *Feasibility Study of the Measurement of Bridge Deck Overlay Thickness Using Pulse Radar*. Report R-35-80. Geophysical Survey Systems, Inc., Salem, N.H.; Massachusetts Department of Public Works, 1980.

---

*Publication of this paper sponsored by Committee on Pavement Monitoring, Evaluation, and Data Storage.*

# Modeling of Ground-Penetrating Radar Wave Propagation in Pavement Systems

CHUN LOK LAU, TOM SCULLION, AND PAUL CHAN

In recent years considerable attention has been focused on the use of ground-penetrating radar (GPR) to detect a variety of pavement problems. The results to date have been mixed. Information on the electrical properties of highway materials is limited as is the ability to model the propagation of electromagnetic waves in a pavement system. A forward model capable of simulating the signature of GPR waveforms is proposed. A monostatic 1 GHz GPR is used in this study. The pavement system is modeled as a layered medium comprising flat parallel layers of pavement materials laminated together. Physical laws governing electromagnetic wave propagation inside the layered medium are used to calculate the attenuation, dispersion, reflection, and transmission encountered by the pulse. Major reflection paths and some multiple reflection paths are selected that begin from the open tip of the antenna, penetrate into the pavement, and reach the pavement surface again. The analysis is performed in the frequency domain. The transmitted pulses are traced through each of these paths one at a time. The resultant echoes at the pavement surface are then positioned and superimposed together according to the time required for the pulse to travel each of the selected paths. A synthetic waveform is thus formed. This process is called forward modeling. The forward model is tested on data collected on experimental pavements of known layer thicknesses and types. Reasonable agreement was achieved between theoretically calculated and field-measured GPR traces. In predicting the amplitude of the waves reflected from layer interfaces average errors of less than 9 percent were calculated. The error in estimating the time delays between peaks was less than 2.5 percent. More work is required, particularly in the area of measuring the complex dielectric properties of paving materials under a range of operational temperature and moisture conditions.

In recent years several investigators have attempted to use ground-penetrating radar (GPR) to detect subsurface problems in pavement systems. Much of the initial work was focused on manual interpretation of multiple GPR traces collected along a highway. The traces were often color coded, and an expert was needed to locate the problem areas. Sometimes the approach worked; other times poor results were obtained. Highway department personnel who evaluated the technology recognized potential but were often disappointed by the manual interpretation system.

Only relatively recently have automated procedures been applied to estimating layer thicknesses (1) and detecting voids (2,3). These procedures model the pavement as a multilayered system and apply the laws of electromagnetic wave propagation to interpret the results from a single GPR-reflected signal. If a single reflected trace cannot be interpreted, there is little hope of obtaining quantifiable information from mul-

tle traces. It is the authors' opinion that GPR technology shows potential for highway applications. However, the authors' knowledge of the required electrical properties of pavement materials is limited. In addition, few models exist that adequately explain how a GPR wave propagates through a layered system of different complex dielectrics. Such a model is proposed in this paper.

A pavement system is modeled as a layered medium consisting of layers of distinct pavement materials. To GPR signals, different pavement materials are distinguishable electrically in terms of relative permittivity (i.e., dielectric constant), magnetic permeability and conductivity. In highway applications the parameter that has the most influence on these properties is the moisture content of the pavement layer. A list of relative dielectric constants of typical pavement materials measured at room temperature at 1 GHz follows:

- Asphalt: 2–6,
- Crushed limestone: 3–9,
- Hot-mix asphalt: 4–6,
- Concrete: 6–9,
- Air: 1, and
- Water: 81.

Clearly the addition of moisture to a pavement layer will significantly increase the dielectric constant of that layer.

For analysis purposes, a simulation model capable of predicting the signature of a GPR waveform collected under certain pavement subsurface conditions is desirable. Modeling offers several advantages. For example, suppose a section of pavement with a 5-in. layer of Type A asphalt, a 10-in. layer of Type B base, and Type C subgrade is studied by GPR, and a simulated signature of the GPR waveform is obtained successfully. To predict the GPR signature of a pavement with the same materials and with the presence of an air- or water-filled void, it is a simple matter of adding a layer of air or water to the pavement model and to repeat the same simulation procedures. Additionally, a realistic forward model of a GPR trace can potentially provide a way to estimate both the thickness and material properties of each layer in the pavement structure. The idea is to use an iterative procedure that varies the unknown parameters to minimize the sum of squared error between actual and calculated traces.

In this paper a simulation model is established for the prediction of GPR signature as would be collected from a pavement with specified subsurface conditions. The result of a simulation example will be given to demonstrate the feasibility of modeling in assisting pavement subsurface condition assessment. The intermediate results of the modeling process

will also be presented to aid understanding of the propagation characteristics of the GPR signal in a pavement system.

**GPR AND BACKGROUND OF ELECTROMAGNETIC THEORY (4)**

Two types of GPR are commercially available: monostatic and bistatic. As shown in Figure 1, the former uses a single antenna for transmission and reception. The latter uses two separate but identical antennas.

For this study, a Penetradar model PS-24 monostatic GPR (pulse width = 1 nsec; center frequency = 1 GHz) was used. A typical trace from this radar on a pavement is shown in Figure 2. The amplitudes are those reflected from significant layer interfaces. The time delays are related to layer thicknesses and will be discussed further. The aim of this study is to build a theoretical model to simulate reflected GPR traces.

GPR works according to the pulse-echo principle. A narrow electromagnetic pulse is generated by the transmitter and ra-

diated toward the pavement through the antenna. In many cases, the wavefront of the transmitted pulse reaching the pavement surface is approximately a plane wave. Below this surface is a lossy inhomogeneous medium made of pavement materials. However, to a 1-ft radar wave, the medium may appear homogeneous. The propagation of a plane wave along the z-direction, perpendicular to the surface, in a homogeneous medium is governed by the wave equation (5):

$$\frac{\partial^2 E}{\partial z^2} = -\omega^2 \mu \epsilon E \tag{1}$$

where

$E = \text{Re}[E_0 \exp(j\omega t)]$  = sinusoidal time varying electric field vector (V/m),

$E_0$  = amplitude of the electric field vector (V/m),

$\omega$  = angular frequency (rad/sec),

$z$  = distance along the propagation direction (m),

$\mu$  = magnetic permeability,

$\epsilon = \epsilon' - j\epsilon''$  = complex permittivity (F/m),

$\sigma = \sigma' + j\epsilon''$  = conductivity (mho/m).

A solution for  $E$  in Equation 1 is

$$E = E_0 e^{-jkz} \tag{2}$$

with propagation constant

$$k = \omega \sqrt{\mu \epsilon (1 - j \tan \delta)} \tag{3}$$

The loss tangent is defined by

$$\tan \delta = \frac{\frac{\sigma}{\omega} + \epsilon_r''}{\omega \epsilon_r'} \tag{4}$$

where

$\epsilon_0 = 8.854 \times 10^{-12}$  = permittivity of free space (F/m),

$\epsilon_r' = \epsilon'/\epsilon_0$  = real part of the relative permittivity, and

$\epsilon_r'' = \epsilon''/\epsilon_0$  = imaginary part of the relative permittivity.

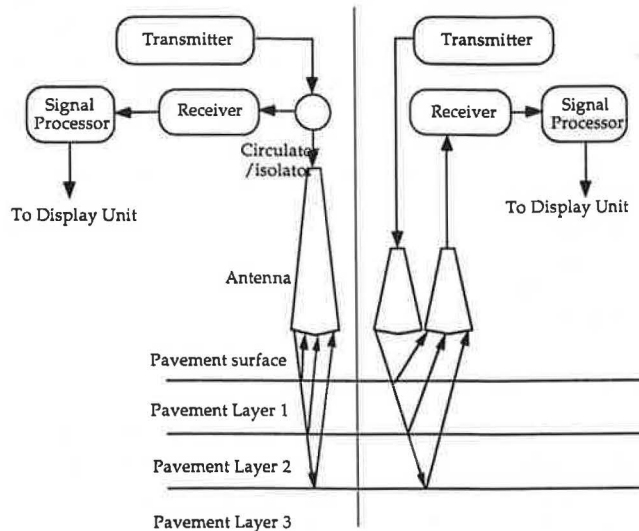


FIGURE 1 Monostatic (left), and bistatic (right) GPR.

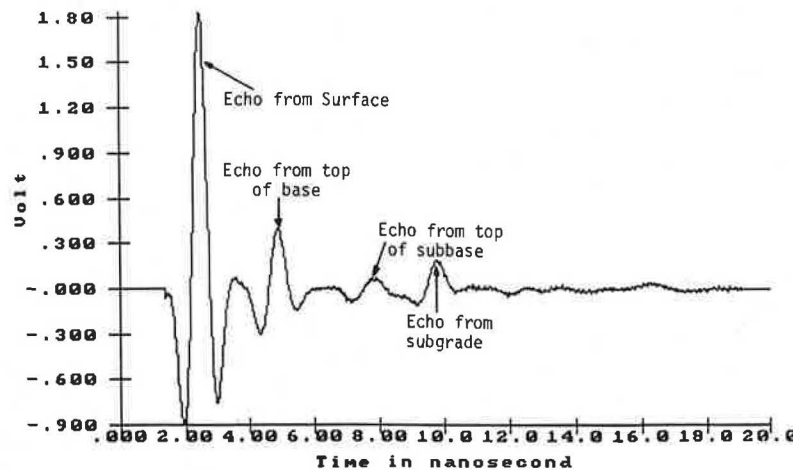


FIGURE 2 Actual GPR traces from four-layered pavement at TTI Research Annex.

If the real and the imaginary parts of  $jk$  are separated and the attenuation parameter  $\alpha$  and the phase parameter  $\beta$  are written as

$$\alpha = \omega \sqrt{\frac{\mu\epsilon}{2} (\sqrt{1 + \tan^2 \delta} - 1)} \left( \frac{\text{neper}}{m} \right) \quad (5)$$

$$\beta = \omega \sqrt{\frac{\mu\epsilon}{2} (\sqrt{1 + \tan^2 \delta} + 1)} \left( \frac{\text{radian}}{m} \right) \quad (6)$$

Equation 2 can be rewritten as

$$E = E_0 e^{-\alpha z} e^{-j\beta z} \quad (7)$$

The amplitude of the GPR pulse decreases as it propagates in the material medium, and the pulse shape is distorted because of the nonlinear phase term  $\beta z$ . Equations 5 and 6 will be used in forward modeling to calculate the attenuation and the dispersion caused by the lossy characteristics of the layered medium.

Equation 7 shows that a negative value of  $\alpha$  will diminish the amplitude of  $E$  of the wave traveling in the  $z$ -direction, and  $\beta z$  is a nonlinear phase term that distorts the shape of the signature in time domain. These phenomena will be shown later.

A GPR pulse propagating inside the multilayer pavement system will encounter the interfaces between the pavement layers where reflection and transmission take place. The parameters that determine the amount of the energy that is reflected back toward the antenna and the remaining portion that travels downward toward the next interface are the reflection and transmission coefficients, respectively. They are defined for Layers 1 and 2 as follows:

$$R \equiv \frac{E_r}{E_i} = \frac{\mu_2 k_1 - \mu_1 k_2}{\mu_2 k_1 + \mu_1 k_2} \quad (8)$$

$$T \equiv \frac{E_t}{E_i} = \frac{2\mu_2 k_2}{\mu_2 k_1 + \mu_1 k_2} \quad (9)$$

For waves propagating through a multilayered medium, the amplitude of the reflected electric field and transmitted electric field can be expressed in terms of the reflection and transmission coefficients, in the  $n$ th layer

$$E_r(n) = R(n) E_i(n) \quad (10)$$

$$E_t(n+1) = T(n) E_i(n) \quad (11)$$

where the subscript  $n$  refers to the  $n$ th interface in a multilayer pavement system. Only the electric field is considered here because the receiver electronics in a GPR detects and processes only voltage waveforms.

Both the reflected and the transmitted energy are attenuated and their spectral characteristics altered by dispersion as determined by Equations 5–7. These events take place at each interface of the pavement system. The pulse is traced through selected paths, and events occurring along the way are calculated. A synthetic waveform can be constructed on the basis of knowledge of the events and times of occurrence.

## FORWARD MODELING

### Assumptions

Forward modeling is based on the following assumptions:

1. Parallel and planar layers. This assumption is generally true for typical pavement systems. The subsurface interfaces may be considered as parallel and smooth for a microwave energy of a wavelength of 1 ft (30 cm).

2. Plane wave. For monostatic GPR, normal incidence and reception is easily achieved. There are good reasons to assume that the wavefront does not deviate significantly from a plane wave. The only obvious cause for deviation from a plane wave will be the geometrical spreading of the wavefronts shown in Figure 3. This may be accounted for by simple manipulation: (a) measure the length of the horn antenna ( $L$ ), (b) divide the distance traveled by a reflection or multiple reflection event by  $L$  and add 1 to the result, and (c) divide the amplitude of the final wavelet amplitude of the corresponding reflection event by the number obtained in (b).

### Selected Paths and Events

The models used in this program are an adaption of those proposed by Duke in 1990 (6). The selected paths of the radar pulse begin at the air-pavement interface and continue into the subsurface of a four-layer medium as shown in Figure 4. The angles of incidence are zero at all interfaces. Oblique rays used are for illustration purpose only. Multiple reflections occur, and their electric field amplitudes may be comparable with that of a major reflection from lower layers. Consequently, their use must be accounted for in the theoretical

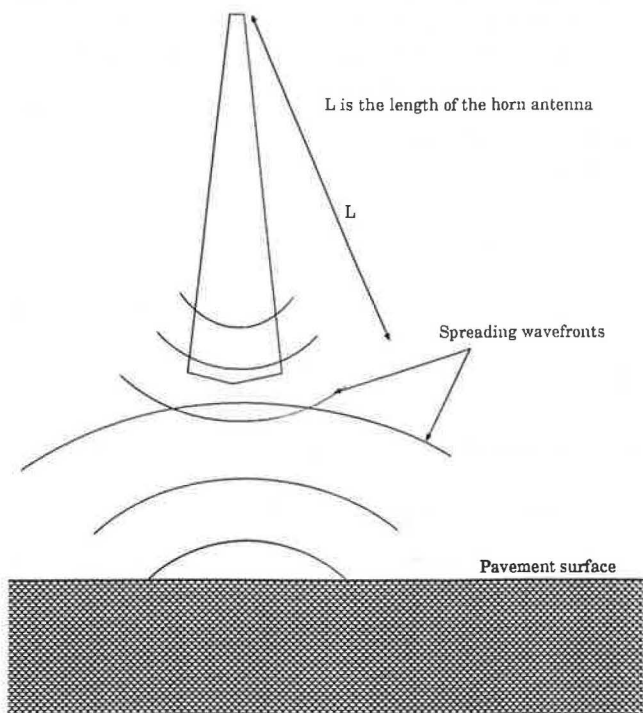


FIGURE 3 Geometric spreading of wavefronts.

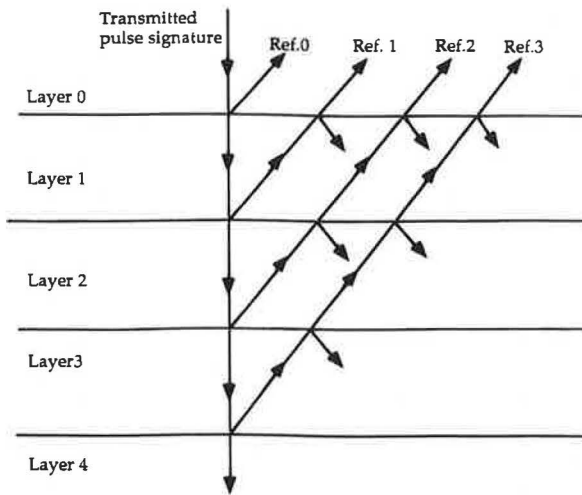


FIGURE 4 Paths of major reflection events.

model. Paths of these multiple reflection/transmission events are shown in Figure 5.

In the model proposed in this paper, no multiple reflections below Layer 2 are used. Layers 3 and 4 are subbase and subgrade in a pavement system; typically they hold significant amounts of moisture. Consequently, they have higher loss, and amplitudes from multiple reflections in these layers are negligibly small and are disregarded in the forward modeling process.

The pavements considered in this study are three-layer pavement systems (with two subsurface interfaces). Nevertheless, a four-layer pavement model is established in this study to account for special cases such as void and delamination between two adjacent layers. A three-layer model can be obtained from a four-layer model simply by using identical electrical parameters on two adjacent layers. Equations 5 and 6 are used to compute the attenuation and phase change on the pulse within each layer.

The amplitudes of the reflected and transmitted waves are determined by Equation pairs 8 and 10, and 9 and 11, respectively.

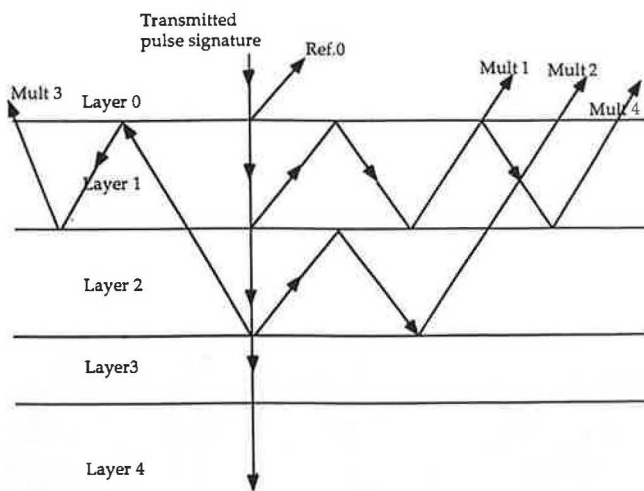


FIGURE 5 Selected paths of multiple reflection events.

Velocity of electromagnetic wave propagation in a medium with electrical parameters

$$\begin{aligned} \sigma &= \sigma' + j\sigma'', \\ \epsilon &= \epsilon' - j\epsilon'', \text{ and} \\ \mu &= \mu_0. \end{aligned}$$

is expressed as (4)

$$v = c \left\{ \frac{\left( \epsilon' - \frac{\sigma''}{\omega} \right)}{2 \epsilon_0} \left[ \sqrt{1 + \left( \frac{\epsilon'' + \frac{\sigma'}{\omega}}{\epsilon' - \frac{\sigma''}{\omega}} \right)^2} + 1 \right] \right\}^{-1/2} \quad (12)$$

where  $\mu = \mu_0$  is used because pavement materials are non-magnetic. Because  $\omega$  is large compared to  $\sigma'$  and  $\sigma''$ , and  $\epsilon''$  is small compared to  $\epsilon'$ , Equation 12 can be approximated by

$$v = \frac{c}{\sqrt{\frac{\epsilon'}{\epsilon_0}}} = \frac{c}{\sqrt{\epsilon_r}} \quad (13)$$

Using the thickness data and Equation 13, round-trip times for the three reflection events and four multiple reflection events can be determined in a three-layer system. Because each event generates a reflected pulse appropriately dispersed and attenuated, if these pulses are properly positioned according to their corresponding round trip times, a linear summation of the pulses produces the resultant synthetic waveform.

**Summary of Forward Modeling Procedures**

1. The GPR system is calibrated to obtain the transmitted pulse signature as it emerges from the antenna. The calibration procedure is as follows:
  - a. Set up the GPR system in an open environment with the antenna pointing to the sky. Record the end reflection signature of the GPR waveform (see Figure 6). This signal is essentially system noise; it will be present on all subsequent traces and should be removed.
  - b. Place a big (4 ft × 4 ft) flat metal plate perpendicularly below the antenna. The antenna should be mounted at the height to be used during normal operation, typically 12 in. Record the metal plate reflection (see Figure 7). The peak before the main peak is the end reflection measured in Step a.
  - c. Align and subtract the signature recorded in Step a from that of Step b. This provides a good approximation of the transmitted pulse of the monostatic GPR (see Figures 8 and 9).
2. Take the fast Fourier transform (FFT) of the transmitted pulse. Because the equations involved in the calculation of the model are frequency dependent, it is necessary to find the frequency components of the transmitted pulse. Figure 10 shows the frequency components of the transmitted pulse.

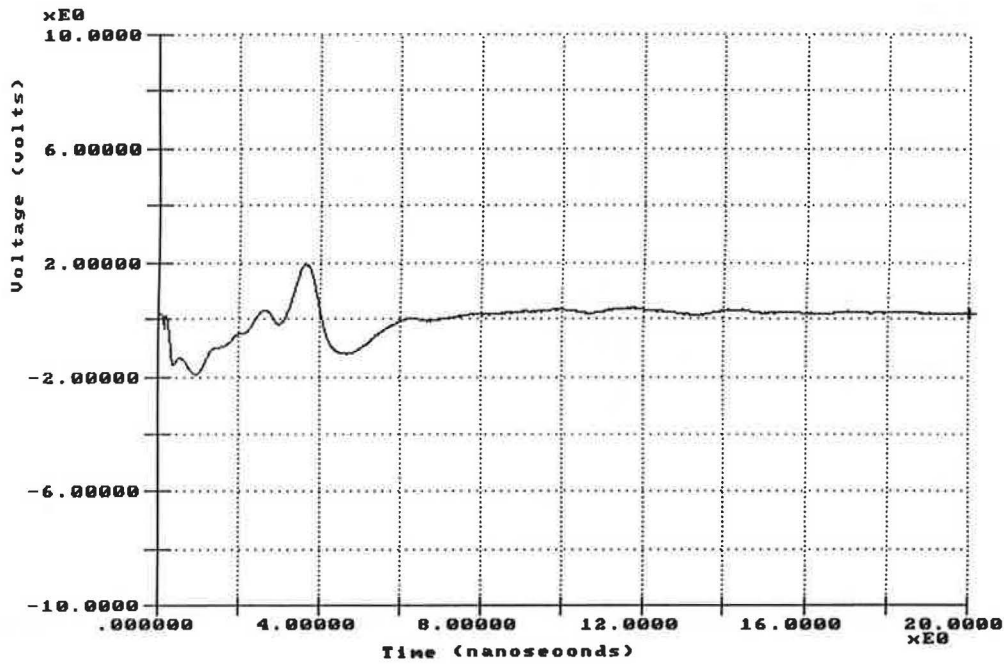


FIGURE 6 Signature of GPR waveform with antenna pointing skyward.

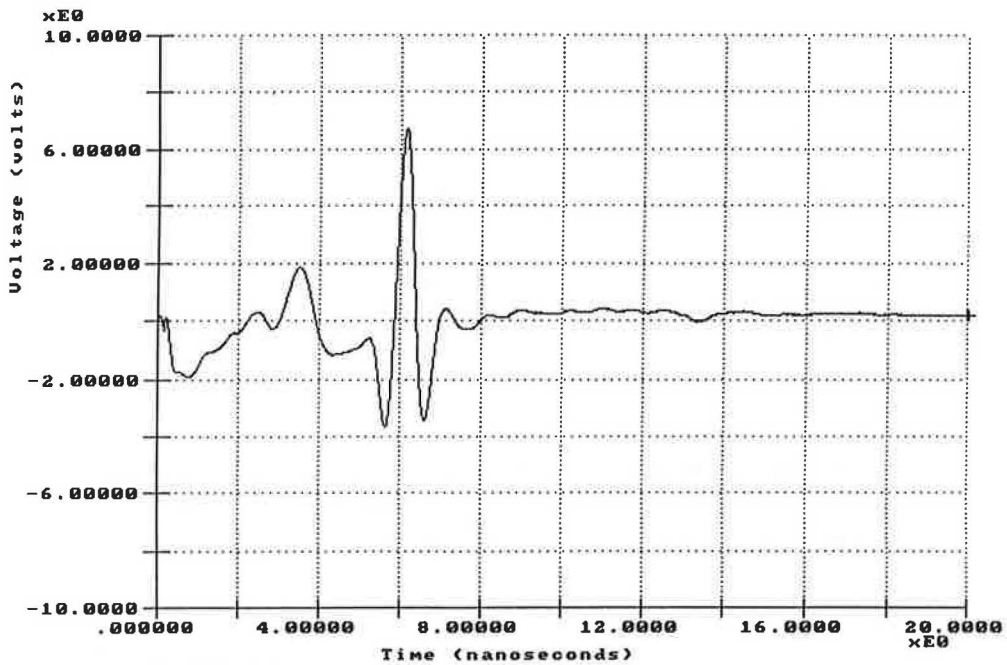


FIGURE 7 Signature of GPR waveform reflected from metal plate.

3. Consider an individual frequency component of the pulse as a continuous sinusoidal wave. Trace this wave through each of the selected ray paths and calculate all reflection, transmission, attenuation, and dispersion events encountered along each path. Do the same for all frequency components for each path. The amplitude and phase of the wave propagated through a path and reaching the pavement surface are expressed as a particular complex number characterizing the component of the pulse at that frequency. Consider these as new spectral

elements of the spectrum. A resultant echo pulse is formed by taking the inverse FFT of the new spectrum.

4. Correct geometric spreading loss as discussed earlier.

5. Use Equation 13 to calculate the velocity of the GPR pulse in each layer. Calculate the time taken to propagate each of the paths in Step 3.

6. Position and superimpose each of the echo pulses according to the time obtained in Step 5 in the voltage versus time plot.

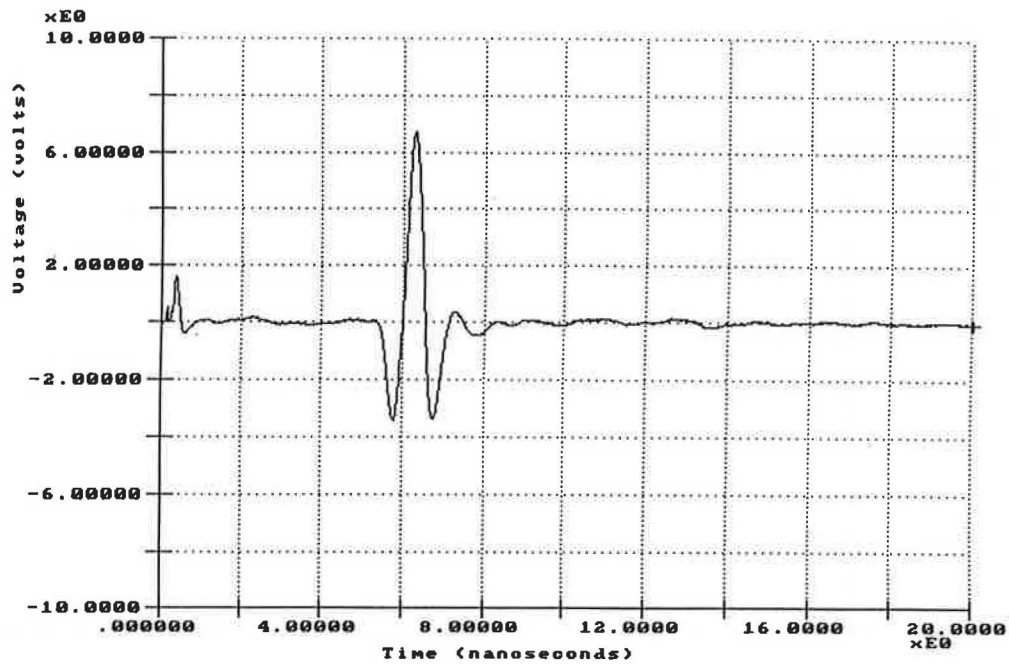


FIGURE 8 Result of waveform by subtracting Figure 6 from Figure 7.

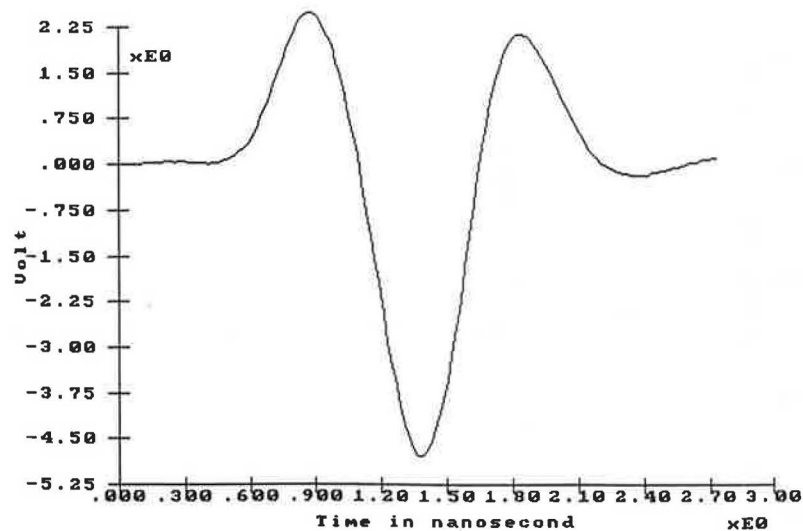


FIGURE 9 Transmitted pulse extracted from Figure 8.

### Case Study

The forward model of a GPR trace provides a way to estimate the thickness of pavement layers. The idea is to objectively match the synthetic GPR trace and field GPR trace by altering iteratively the unknown parameters, which include the thickness of each layer, used in the model. After the synthetic GPR trace is obtained, the layer thicknesses used in the model are then taken to be the true layer thicknesses of the pavement. With some knowledge of the range of electrical parameters  $\sigma$ ,  $\epsilon$ , and  $\mu$  in an individual layer, forward modeling can be an efficient method to determine the layer thickness.

The example field trace (Figure 11) is taken from a section of an experimental test pavement at the Texas Transportation Institute (TTI) Research Annex. The section is a three-layer pavement system. The theoretical and modeled GPR traces are shown in Figures 11 and 12, respectively. The measured and computed amplitudes and time delays between peaks are shown in Table 1 for comparison of these traces. Each amplitude is calculated by averaging the amplitude measured from peak to preceding minimum and peak to following minimum. The time delays are measured between peaks. The average error in predicting amplitudes is less than 9 percent, and in predicting time delays it is less than 2.5 per-

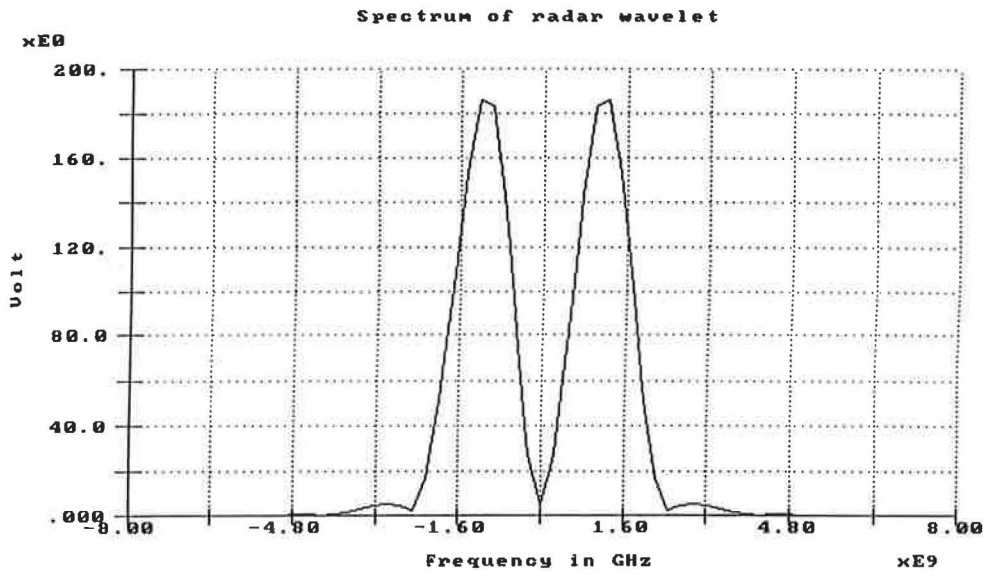


FIGURE 10 Frequency components of transmitted pulse.

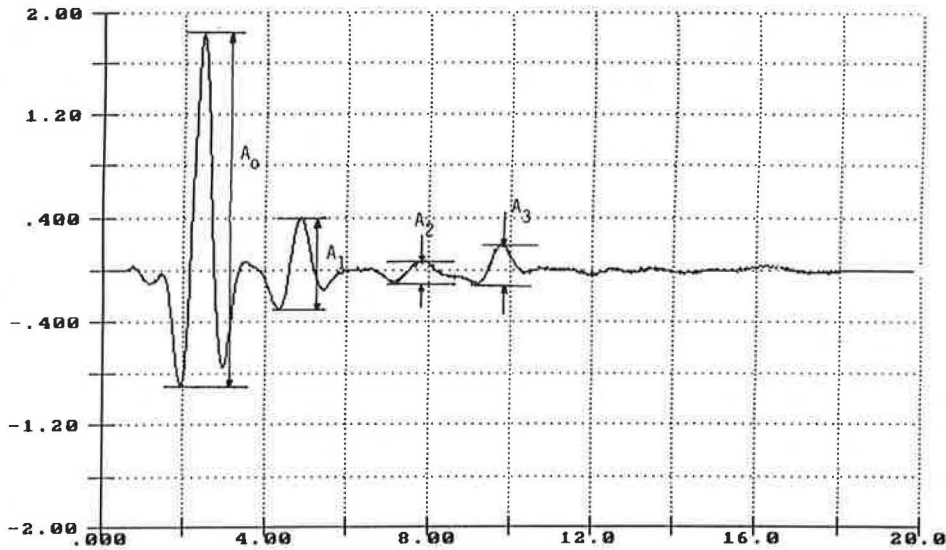


FIGURE 11 GPR field trace.

cent. A flowchart of the forward modeling process is shown in Figure 13.

Forward modeling can also be used to predict the signature of GPR traces taken from experimental or problematic pavement such as those with a void or delamination between two adjacent layers. Both water- and air-filled voids can be modeled. These simulations can be helpful to diagnosis of problematic pavements using GPR. Figure 14 shows the model trace resulting from the simulation of a three-layer pavement with an air void between concrete and base. The thickness of the void is  $\frac{1}{8}$  in. The thickness of the concrete and base layer are each 5 in. The dielectric values of concrete, base, and subgrade are 6.2, 9.6, and 10.5, respectively.

Once a match between the synthetic trace and the field trace is obtained, the electrical properties of the pavement subsurface are known. The synthetic trace is used for obtain-

ing information of pulse amplitudes and round-trip times for layer thickness computations. The estimation of complex electrical properties of pavement materials is also provided by this model. The significance of these dielectric values for pavement engineers is as yet unknown. However, by applying constitutive models it may be possible to convert these values into more traditional items such as moisture content or void contents of pavement layers. This will be the subject of further research.

## CONCLUSION AND RECOMMENDATIONS

A computer algorithm capable of simulating GPR waveforms collected from pavements was established. The pavement was modeled as a layered medium comprising layers of pavement

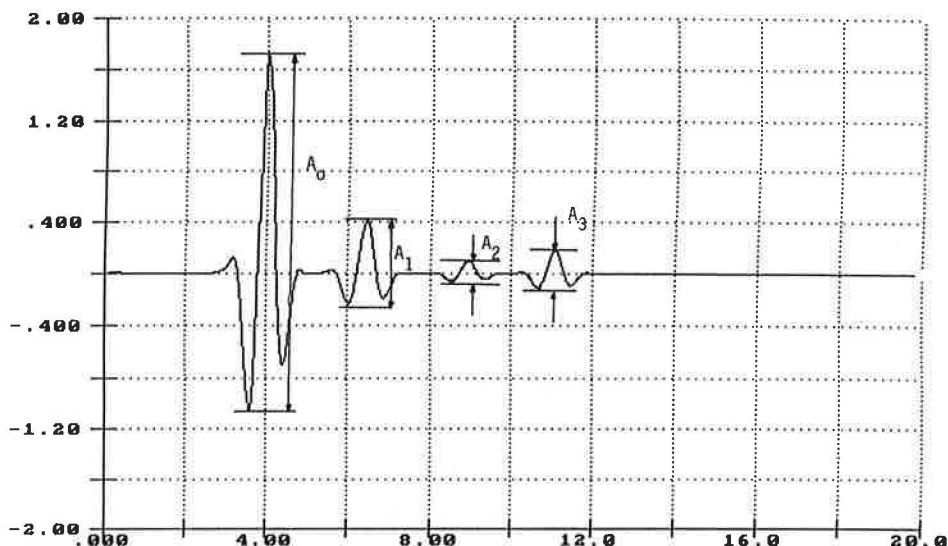


FIGURE 12 Corresponding forward model GPR trace.

TABLE 1 Comparison of Measured and Predicted GRP Traces

	Amplitudes (volts)				Time Delays (nanoseconds)		
	$A_0$	$A_1$	$A_2$	$A_3$	$t_1$	$t_2$	$t_3$
Model Trace	2.65	0.52	0.15	0.295	2.33	2.68	2.0
Field Trace	2.64	0.635	0.18	0.29	2.40	2.80	2.0
% error	0.4	17	16.7	1.7	2.9	4.3	0

where

- $A_0$  is the amplitude reflected from surface.
- $A_1$  is the amplitude reflected from top of base.
- $A_2$  is the amplitude reflected from top of subbase.
- $A_3$  is the amplitude reflected from top of subgrade.
- $t_1$  is the round trip time to travel through the asphalt.
- $t_2$  is the round trip time to travel through the base.
- $t_3$  is the round trip time to travel through the subbase.

materials. Two cases studies were carried out to investigate the feasibility of forward modeling in assisting pavement sub-surface problems diagnosis. In the first case, the forward model was tested on data collected on experimental pavement of known layer thickness and types. Reasonable agreement was achieved between modeled and field traces. In the second case study, a 1/8-in. air void between concrete and base was simulated. These simulations computed ideal signatures of GPR waveforms collected from pavements with voids.

Recommendations for future work on related topics include the following:

1. Develop a least-square fitting algorithm to allow the model parameters (layer dielectrics and thicknesses) to be adjusted automatically by the computer until a satisfactory match between synthetic and field trace is achieved.
2. The accuracy of the complex dielectric constants of pavement materials is essential to the success of forward modeling.

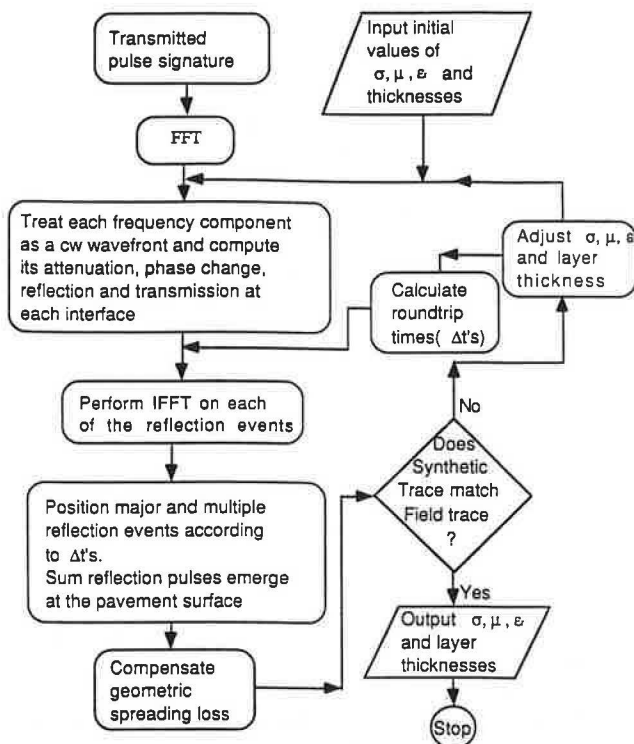


FIGURE 13 Flowchart of forward modeling.

An initial guess that is too far away from the true values will affect the convergence toward a matching trace. Hence, more work is required in the area of measuring the complex dielectric and conductivity properties of paving materials for a range of materials and environmental conditions.

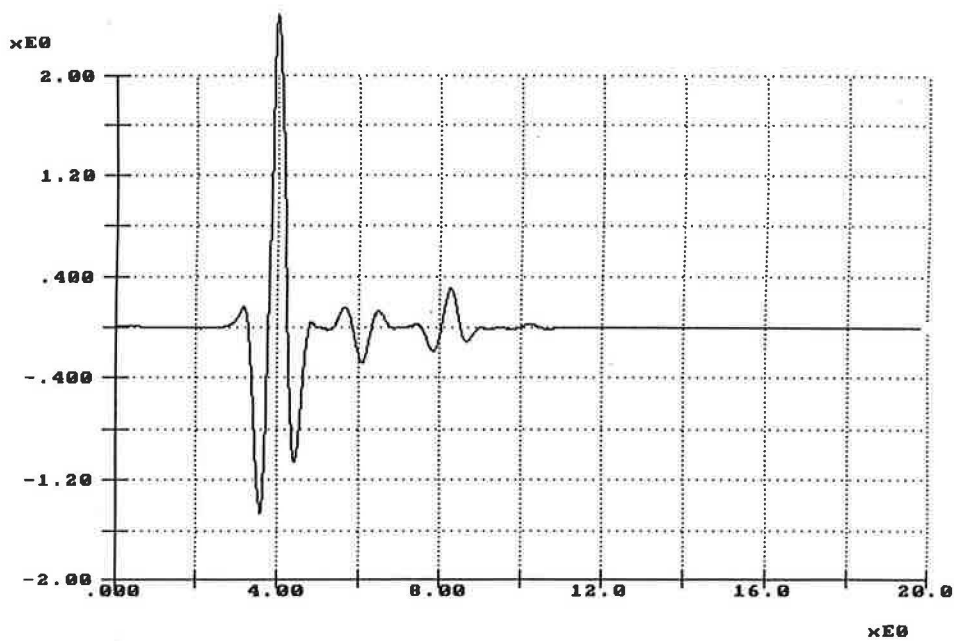


FIGURE 14 Model trace of three-layer pavement with air void between concrete and base.

#### REFERENCES

1. K. R. Maser and T. Scullion. Automated Pavement Subsurface Profiling Using Ground Penetrating Radar—Case Studies of Four Experimental Field Sites. Presented at 70th Annual Meeting of the Transportation Research Board, Washington, D.C., 1991.
2. W. J. Steinway, J. D. Echard, and C. M. Luke. *NCHRP Report 237: Locating Voids Beneath Pavement Using Pulsed Electromagnetic Waves*, TRB, National Research Council, Washington, D.C., Nov. 1981.
3. L. C. Bomar, W. F. Horne, D. R. Brown, and P. E. and J. L. Smart. *A Method to Determine Deteriorated Areas in PCC Pavements*. NCHRP Project 10-28 Final Report. TRB, National Research Council, Washington, D.C., Jan. 1988.
4. D. J. Gunton and H. F. Scott. Introduction to Subsurface Radar. *IEE Proceedings, Part F, Communications, Radar and Signal Processing*, Vol. 135, Aug. 1988, pp. 278–320.
5. R. F. Harrington. *Time-Harmonic Electromagnetic Fields*. McGraw-Hill Book Company, New York, N.Y., 1961, p. 38, Equation 2-8.
6. S. Duke. *Calibration of Ground Penetrating Radar and Calculation of Attenuation and Dielectric Permittivity versus Depth*. M.S. thesis. Colorado School of Mines, Golden, June 1990.

---

*Publication of this paper sponsored by Committee on Pavement Monitoring, Evaluation, and Data Storage.*